Measuring spatial resolution in Mass Spectrometry Imaging

Martin Metodiev

Imperial College London

Department of Metabolism, Digestion and Reproduction

PhD thesis

Statement of originality

The work presented in this document is the product of love and dedication towards the pursuit of the Truth. I therefore state that this is my own work. All other scientific work that appears within this document has been appropriately cited. All collaborators have been explicitly mentioned. In addition, ChatGPT did not contribute to this thesis

Copyright declaration

The copyright of this thesis rests with the author. Unless otherwise indicated, its contents are licensed under a Creative Commons Attribution-Non Commercial-No Derivatives 4.0 International Licence (CC BY-NC-ND).

Under this licence, you may copy and redistribute the material in any medium or format on the condition that; you credit the author, do not use it for commercial purposes and do not distribute modified versions of the work.

When reusing or sharing this work, ensure you make the licence terms clear to others by naming the licence and linking to the licence text.

Please seek permission from the copyright holder for uses of this work that are not included in this licence or permitted under UK Copyright Law.

Abstract

Mass spectrometry imaging (MSI) is a term for a collection of imaging techniques that allow for the spatial distribution of different molecules found natively within thin tissue sections to be visualised. The hyperspectral nature of those imaging techniques makes these methods extremely powerful for the detailed analysis of complex systems, for example characterising living systems. Unfortunately, the concept of image formation, which can be thought of as a set of mathematical rules that describe how information is mapped from an object to an image, has remained unexplored. As a consequence, the definition of spatial resolution has been ill-defined. This thesis introduces a new image formation model which mends the currently ill-defined notion of spatial resolution and at the same time exposes some common misconceptions about it. With the aid of this model the processes that lead to the loss of spatial resolution are identified as blur and noise and the origin of those parameters is derived and demonstrated through computational simulations. Ultimately, a new method for measuring spatial resolution is proposed. The method allows for the study of spatial resolution across different pixel sizes and modalities. Apart from the practical use of measuring spatial resolution, the image formation model also allows for theoretical studies of MSI tissue imaging experiments. As MSI detects hundreds or thousands of ions per pixel and resolution is shown to be intricately linked to the signal intensity as well as blur, resolution in MSI is best described by a range representing resolution calculated for different ion images. The model is used to asses resolution from standard samples and tissue imaging experiments acquired using NanoSIMS, OrbiSIMS, MALDI and DESI.

Acknowledgments

I would like to thank my supervisors – Professor Josephine Bunch and Professor Zoltan Takats for the support and excellent guidance I received while conducting this work.

I thank Professor Josephine Bunch for the wonderful discussions we had on MALDI signal formation, the general nature of MSI and its applications in the field of biology. Furthermore, I would also like to thank Professor Josephine Bunch for guiding this thesis in the direction of resolution measurements based on SNR rather than blur alone. Finally, I would like to thank Professor Josephine Bunch for believing in me and seeing a potential for scientific growth. I would also like to thank Professor Zoltan Takats for the enlightening conversations we had on DESI and DEFFI, cell membranes and MSI in general. I also thank Professor Zoltan Takats for his guidance in blur estimates in DESI imaging.

I thank Dr. Rory T. Steven for all his help and expert guidance on the experimental side of MALDI and DESI MSI and the help I received when investigating appropriate model samples for spatial resolution. I also thank Dr. Yuchen Xiang for the conversations on noise models in MSI and the help he provided in the form of the derivations of the uncertainties of resolution measurements.

I thank my dear friend Dr. Alexander Little for the wonderful friendship we have had. I also thank him for our lively discussions and for providing the ansatz used in the derivation of the image formation model. I would also like to thank my dear friends Alexander Dimitrov, Kaloyan Simeonov, Dr. Peter Hristov and Hristina Tsolova for being amazing friends and being there for me in time of need.

I thank my family – my mother, my father, my brother and my grandparents for all the support, care and unconditional love I received throughout my life. I dedicate this thesis to my mother, who has the soul of an angel.

"Is it the fault of wine if a fool drinks it and goes stumbling into darkness?" – Ibn Sina (Avicenna), father of modern day medicine.

Table of contents

Chapter 1 A general introduction to Mass Spectrometry Imaging 23
1.1 Introduction 23
1.2 MSI Modalities 24
1.2.1 MALDI 25
1.2.2 DESI 37
1.2.3 SIMS 50
1.3 Mass analysers 52
1.3.1 Time of flight (ToF) 53
1.3.2 Magnetic sector 55
1.3.3 Fourier Transform Ion Cyclotron Resonance (FTICR) and Orbitrap 56
1.4 Noise 57
1.5 Spatial resolution 60
1.6 The Rosetta project and the Cancer Grand Challenge 62
1.7 Thesis outline 63
Chapter 2 A new image formation model 64
2.1 Why do we need an image formation model? 64
2.1.1 Problems with the current MSI image formation model 65
2.1.2 A short discussion about picture elements (pixels) 66
2.2 Exploring the Sampling theorem in the context of Mass Spectrometry Imaging 68
2.2.1 The case of ideal sampling 68
2.2.2 The Nyquist frequency 71
2.2.3 Oversampling vs Undersampling (aliasing) 72
2.2.4 Some important remarks about resolution 74
2.2.5 Realistic sampling 77
2.3 Deriving an image formation model 80
2.3.1 Simplifying assumptions: continuous raster mode 80

2.3.2 Finalizing the model 82
2.3.3 A simple example – image of a point source 83
2.4 Noise modelling 85
2.4.1 The instrument response function (IRF) 91
2.4.2 How is noise generated? 91
2.4.3 Investigating the properties of different noise types: A simple simulation 93
2.5 Conclusions 98
Chapter 3 How to measure spatial resolution. 101
3.1 Introduction 101
3.2 Loss of resolution due to blur and noise 101
3.2.1 Scaling the image formation model to two dimensions 101
3.2.2 Applying the model on simple systems: the PSF, the ESF and the MTF 103
3.2.3 Loss of resolution due to blur 109
3.2.4 Loss of resolution due to noise and blur 113
3.3 Calculating spatial resolution 119
3.3.1 The noise spectral density (NSD) 119
3.3.2 Calculating spatial resolution. 123
3.3.3 Resolution model 128
3.3.4 Errors 129
3.4 Resolution of a datacube 130
3.4.1 Data cube simulation 131
3.4.2 Data cube resolution 134
3.4.3 Dependence on number of number of linescans 137
3.4.4 Recovering the resolution equation when reduced 139
3.4.5 Comparing the resolution of different datacubes 143
3.5 Conclusions 149
Chapter 4 Measuring spatial resolution experimentally using a step edge 153

4.1 Introduction 153
4.2 Methods 153
4.2.1 Physical vapour deposition (PVD) 153
4.2.2 Sample preparation 155
4.2.3 Mass spectrometry imaging 155
4.2.4 Computational methods 156
4.3 Results and discussion 159
4.3.1 Edge characteristics 159
4.3.2 Mean spectra 161
4.3.3 Characterising the distribution of intensities across pixel sizes using maximum likelihood estimation (MLE). 163
4.3.4 Noise statistics 169
4.3.5 Spatial resolution 181
4.4 Conclusions. 197
Chapter 5 Applications for tissue imaging 199
5.1 Introduction 199
5.2 Methods 200
5.2.1 Experimental 200
5.2.2 Computational methods 202
5.3 Results and discussion 206
5.3.1 Intensity distributions across different modalities. 206
5.3.2 Noise statistics 211
5.3.3 The blurring parameter 219
5.3.4 Spatial resolution 229
5.4 Conclusions 234
Chapter 6 Conclusions and future work 236
6.1 Summary 236

6.2 Future work 237
6.2.1 Image formation model – ion flux generation 237
6.2.2 Image formation model – noise models 239
6.2.3 Possible applications for the image formation model in its current state 240
6.2.4 Future ways of measuring spatial resolution 243
Bibliography 245

List of figures

Figure 1-1. A diagram depicting a generalised MSI experimental set up. 24
Figure 1-2. A schematic of a typical MALDI laser profile imaging set up. 26
Figure 1-3. An energy level schematic of the thermal ionisation of the photoexcited matrix molecule ionisation model. Solid lines represent optical transitions caused by the absorption of a photon of an electron. $S0, S1, Sp$ and Ip are the ground state, first excited singlet state, a higher energy singlet state and the ionisation potential respectively. Curved lines represent radiationless transitions. The dashed line represents vibronically coupled ionisation. The figure is adapted from[15]. 30
Figure 1-4. A schematic diagram of the $S1 - S1$ pooling process proposed in the CPCD model. $S0$ is the ground state, $S1$ is the first excited singlet state and Sn is a state with double the energy of $S1$. The green circles represent an excitation and the orange arrows represent the movement of the excitation from one molecule to another. Eventually, the energy of two distant molecules can be pooled into a single molecule, resulting in a molecule in the Sn state. 31
Figure 1-5. A schematic diagram of the $Sn - S1$ pooling process proposed in the CPCD model. $S0$ is the electronic ground state, $S1$ is the first excited singlet state and Sn is a state with double the energy of $S1$. The green circles represent an excitation. 32
Figure 1-6. A diagram of a traditional DESI emitter set up. 38
Figure 1-7. (a) – A histogram of primary droplets diameter measured at 5 mm from the emitter. (b) – A histogram of the primary droplet velocities measured at 2 mm from the emitter. (c) – Droplet velocities as a function of distance from the emitter. Adapted from [42]. 39
Figure 1-8. Top – average progeny droplet diameters at different distances and heights from the impact site. Bottom – average progeny droplet velocities at different distance and heights from the impact site. Adapted from [42]. 40
Figure 1-9. (a) – An MD simulation of the nebulising gas effects on droplet transport. (b) – An MD simulation of a droplet – thin liquid layer impact interaction. Adapted from [43]. 42
Figure 1-10. Snapshots from the evolution of a droplet/liquid layer interaction and the generation of progeny droplets. Taken from [40]. 44
Figure 1-11. (a) – An SY curve of the thermometer ions used in the experiment. (b) – The internal energy distribution $P(E)$ of the thermometer ions used in the experiment. Figure adapted from [44]. 46
Figure 1-12. (a) – A schematic of the ion evaporation model (IEM). (b) – a schematic of the charge residue model (CRM). (c) – a schematic of the chain ejection model (CEM). Taken from [47]. 47
Figure 1-13. A diagram showing the reorientation of polar molecules in a small Rayleigh charged droplet. Taken from [47,49] 48

Figure 1-14. (a) – A snapshot from an ejection simulation in IEM. The analyte ion is marked with a blue circle. (b) – The free energy profile $\Delta G*$ computed by the simulation. The transition state is denoted by TS . (c) – radial distance from the centre of the droplet for four different ions. Figure adapted from [47,50]. 49
Figure 1-15. A schematic overview of the SIMS process. 51
Figure 1-16. (a) – definition of mass resolution. (b) – definition of mass accuracy. 52
Figure 1-17. Schematic of ToF mass analyser. Left – without reflectron. Right – with reflectron. 53
Figure 1-18. A diagram of a magnetic sector mass analyser. 55
Figure 1-19 Left – a simplified schematic of an FTICR mass analyser. Right – a simplified schematic of an Orbitrap mass analyser. 56
Figure 1-20. A diagram of an electron multiplier. 57
Figure 1-21. A misinterpretation of noise. Taken from[108]. 59
Figure 2-1 An illustration of how an image formation model works. 64
Figure 2-2. A depiction of the ion flux emanating from the surface due to the beam/matter interaction. 67
Figure 2-3 (a) – A time signal $f(t)$. (b) – The Shah function $\text{Ш}t$. (c) – the sampled signal $fsampled$ 69
Figure 2-4 (a) – a continuous time signal $f(t)$. (b) – the magnitude of the Fourier transform of $f(t)$. 70
Figure 2-5 (a) – a continuous time signal $f(t)$. (b) – the sampled signal $fsampled$. (c) – the reconstructed signal $fsampled$. 71
Figure 2-6. (a) – oversampling in the context of MSI. (b) – oversampling in the context of information theory. (c) – undersampling in the context of MSI. (d) – undersampling in the context of information theory. 72
Figure 2-7. (a) – Original signal (blue) compared to the undersampled (from the point of view of information theory) signal (orange). Sampled at $\Delta t = 1s$. (b) – Original signal (blue) compared to the oversampled (from the point of view of information theory) signal (orange). 74
Figure 2-8 (a) – An array of 18 cells. The density of a particular molecule is alternating between neighbouring cells. (b) – A zoomed in version showing the first six cells. (c) – An oversampled image with a pixel size of $5\ \mu m$. (d) – An undersampled image with a pixel of $15\ \mu m$. 76
Figure 2-9. (a) – duty cycle of 0.9 with a scan time of one second. (b) – duty cycle of 0.3 with a scan time of one second. 78
Figure 2-10 A simulation of a PSF for weak and strong material consumption at three different pixel sizes, corresponding to undersampling and oversampling from the point of view of MSI. 84
Figure 2-11. How to estimate noise. Left or red line – original data[108]. Right of red line – reconstructed histograms using MS PAINT. Note that the identity of the m/z value was not provided by the authors. 86
Figure 2-12. Reconstructed data from[108]. (a) – Poisson noise. (b) – Poisson/Gaussian mixture. (c) – quadratic variance. 87

Figure 2-13. Reconstructed data from[108] excluding the problematic ROI. (a) – Poisson noise. (b) – Poisson/Gaussian mixture. (c) – quadratic variance. 89
Figure 2-14. Possible origin of peak height fluctuations for MALDI and DESI. Left – fluctuations in MALDI laser energy result in slightly different craters. Right – fluctuations in DESI primary droplets size and velocity results in fluctuations of the number of secondary droplets. 90
Figure 2-15. (a) – High intensity image generated from a high intensity mass spectrum corrupted with Poisson noise. (b) – same as (a) but corrupted by amplitude noise. (c) – same as (a) but corrupted with combined noise. (d) – A low intensity image generated from a low intensity mass spectrum corrupted with Poisson noise. (e) – same as (d) but corrupted with amplitude noise. (f) – same as (d) but corrupted with combined noise. 94
Figure 2-16 (a), (b) – Mass spectrum affected by Poisson noise for two randomly selected pixels – (4,5) and (19,23) respectively. (c), (d) – Peak amplitude noise at the same two pixels. (e), (f) – Combined noise for the same two pixels. 95
Figure 2-17. (a), (b), (c) – The variance of Poisson, amplitude and combined noise as a function of the mean intensity I. (d), (e), (f) – The standard deviation of all three types of noise considered here as a function of the mean intensity I. (g), (h), (f) – The image SNR for all three types of noise. 96
Figure 2-18. A summary of the mathematical procedures that produce the image formation model. 99
Figure 3-1 (a) – A beam path for which $vx > 0$ and $vy = 0$. (b) – a zig-zag beam path - vx alternates between positive and negative so the beam switches direction and $vy = 0$. (c) – a beam path for which both $vx > 0$ and $vy > 0$. 102
Figure 3-2 The ground truth objects that are to be imaged. (a) – A ground truth point source. (b) – a ground truth edge source. (c) – a ground truth device. 105
Figure 3-3. A snapshot of the image formation simulation. (a) – weak material consumption at $t = 23s$ from the start of the experiment. (b) – strong material consumption at $t = 23s$ from the start of the experiment. 106
Figure 3-4 (a), (b), (c) – subpixel shifted point source. (c), (d), (f) – the obtained PSFs. 107
Figure 3-5 (a) – ground truth PSF in the case of weak material consumption. (b) – ground truth PSF in the case of strong material consumption. (c) – ground truth MTF in the case of weak material consumption. (d) – ground truth MTF in the case of strong material consumption. 108
Figure 3-6 (a) – ESF obtained in the case of weak material removal. (b) – ESF obtained in the case of strong material removal. (c) – device imaged with weak material consumption. (d) – device imaged with strong material consumption. 109
Figure 3-7 (a) – An average profile of a resolution device imaged with weak material removal. (b) – an average profile of a resolution device imaged with strong material removal. 110
Figure 3-8 Comparing different approaches to computing an MTF to a ground truth MTF for (a) – weak material removal, (b) – strong material removal. 111

Figure 3-9 (a), (b), (c) – In increasing order of intensity – resolution device imaged under weak material consumption conditions and corrupted with Poisson noise. (d), (e), (f) – In increasing order of intensity – resolution device imaged under weak material consumption conditions and corrupted with combined noise. (g), (h), (i) – In increasing order of intensity – strong material consumption, Poisson noise. (j), (k), (l) – In increasing order of intensity – strong material consumption, combined noise. 115
Figure 3-10 (a) – the $23rth$horizontal linescan of image Figure 3-9 (j). (b) – average profile cancels noise out and signal is recovered. 118
Figure 3-11. (a) – image of a homogeneous area. (b) – histogram of the image, black horizontal line shows the standard deviation and black vertical line is the average. 120
Figure 3-12 (a) – image of a sharp step edge with a homogeneous surface. (b) – an average profile resulting in a 1D ESF. (c) – histogram acquired from the edge surface. (d) – NSD computed from all the linescans of the edge surface. 121
Figure 3-13 (a) – image of a sharp step edge with a homogeneous surface. (b) – average profile resulting in a 1D ESF. (c) – PSF approximation obtained after numerical differentiation. (d) – MTF obtained after computing the magnitude of the Fourier transform of the PSF. 124
Figure 3-14 (a) – high intensity edge image. (b) – MTF and $NSD/2$ at a high intensity. (c) – low intensity edge image. (c) – MTF and $NSD/2$ at a low intensity. 126
Figure 3-15 (a) – log-skew normal distribution of intensities. (b) – same but plotted after computing the logarithm of intensities – skew normal distribution. 132
Figure 3-16 (a), (b) – Poisson noise, weak material consumption, low and high intensity ESFs. (c), (d) – Combined noise, weak material consumption, low and high ESFs. (e), (f) – Poisson noise, strong material removal, low and high intensity ESFs. (g), (h) – Combined noise, strong material removal, low and high intensity ESFs. 133
Figure 3-17(a) – Resolution distance in the case of weak material removal (maximised blur). The solid magenta and dashed black curves represent the theoretical prediction for Poisson noise and combined noise respectively. The blue circle and red triangle scatter points depict the experimentally measured resolution with the aid of Algorithm 2. The vertical grey lines are the errors in the resolution measurement. (b) – same but in the case of strong material removal (minimised blur). 135
Figure 3-18 Image blur as a function of intensity for (a) – weak material removal and Poisson noise. (b) – weak material removal and combined noise. (c) – strong material removal and Poisson noise. (d) – strong material removal and combined noise. 136
Figure 3-19 Resolution measurements with reduced number of linescans. (a) – resolution distance in the case of weak material removal (maximised blur). The solid magenta and dashed black curves represent the theoretical prediction for Poisson noise and combined noise respectively. The blue circle and red triangle scatter points

depict the experimentally measured resolution with the aid of Algorithm 2. The vertical grey lines are the errors in the resolution measurement. (b) – same but in the case of strong material removal (minimised blur). 137
Figure 3-20. Blur parameter estimates when a reduced number of linescans is used. (a) – weak material removal and Poisson noise. (b) – weak material removal and combined noise. (c) – strong material removal and Poisson noise. (d) – strong material removal and combined noise. 138
Figure 3-21 Resolution measurements with reduced number of linescans. Only red scatter points with a fractional error less than 0.23 are plotted. (a) – resolution distance in the case of weak material removal (maximised blur). The solid magenta and dashed black curves represent the theoretical prediction for Poisson noise and combined noise respectively. The blue circle and red triangle scatter points depict the experimentally measured resolution with the aid of Algorithm 2. The vertical grey lines are the errors in the resolution measurement. (b) – same but in the case of strong material removal (minimised blur). 140
Figure 3-22 (a) – measured blur vs intensity for datacube 4. Shaded cyan region represents the high intensity region from which the blurring parameter is obtained. (b) – a histogram representing the distribution of blurs. Dashed cyan line is the median value obtained from the shaded cyan region in (a). (c) – same as (a) but for datacube 2. (d) – same as (b) but for datacube 2. 141
Figure 3-23 (a) – SNR for datacube 4. (b) – SNR for datacube 2. 142
Figure 3-24. (a) – recovering the resolution equation for datacube 4. Red scatter points – measured with Algorithm 1 and 2. Dashed Black curve – ground truth. Violet solid curve – recovered using the procedure describe here. (b) – same but for datacube 2. 143
Figure 3-25 A violin plot of the intensity distributions of the four datacubes. The plot is presented on a semi-natural log scale. 144
Figure 3-26 Comparing resolution estimates for each datacube obtained with the different methods. x-axis – Algorithm 2 with 129 linescans, Algorithm 2 with 30 linescans, recovery method and ground truth. Black vertical line in each plot is the ground truth median value. (a) – resolution estimates for datacube 1. (b) – resolution estimates for datacube2. (c) – resolution estimates for datacube 3. (d) – resolution estimates for datacube 4. 146
Figure 4-1 A schematic representation of the PVD process. 154
Figure 4-2 (a) – A bright field microscopy image of the matrix/step edge obtained via bright field microscopy after an MSI experiment. The MSI experiment was set to 75 μm pixel size. (b) – A two dimensional ESF of the most intense ion image acquired at 75 μm pixel size. Here M denotes the matrix molecule – the ion signal displayed is a matrix/silver adduct. 159
Figure 4-3. Mean spectra from silver region acquired at different pixel sizes. (a) – 90 μm pixel size. (b) – 75 μm pixel size. (c) – 60 μm pixel size. (d) – 45 μm pixel size. (e) – 30 μm pixel size. (f) – 15 μm pixel size. 161
Figure 4-4. Base silver peak at different pixel sizes. (a) – 90 μm pixel size. (b) – 75 μm pixel size. (c) – 60 μm pixel size. (d) – 45 μm pixel size. (e) – 30 μm pixel size. (f) – 15 μm pixel size. 162

Figure 4-5. The most intense ion images across the six datacubes. (a) – 90 μm pixel size. (b) – 75 μm pixel size. (c) – 60 μm pixel size. (d) – 45 μm pixel size. (e) – 30 μm pixel size. (f) – 15 μm pixel size. 163
Figure 4-6 The distribution of intensities across all pixel sizes. (a) – intensity distribution at 90 μm pixel size. (b) – intensity distribution at 75 μm pixel size. (c) – intensity distribution at 60 μm pixel size. (d) – intensity distribution at 45 μm pixel size. (e) – intensity distribution at 30 μm pixel size. (f) – intensity distribution at 15 μm pixel size. 164
Figure 4-7 The natural logarithm of the intensity distributions across various pixel sizes. (a) – natural log of the intensity distribution at 90 μm pixel size. (b) – natural log of the intensity distribution at 75 μm pixel size. (c) – natural log of the intensity distribution at 60 μm pixel size. (d) – natural log of the intensity distribution at 45 μm pixel size. (e) – natural log of the intensity distribution at 30 μm pixel size. (f) – natural log of the intensity distribution at 15 μm pixel size. 165
Figure 4-8 (a) – the skew-norm PDFs describing the intensity distributions. Plotted on a natural semi-log scale. (b) – the skew-norm CDFs describing the intensity distributions. Plotted on a natural semi-log scale. The black line represents the 0.5 threshold. 167
Figure 4-9 A violin plot of the intensity distributions at different pixel sizes. The plot is presented on a log scale. 168
Figure 4-10 Noise variance as a function of intensity plotted across all pixel sizes. (a) – 90 $\mu m\ pixel\ size$ datacube. (b) – 75 $\mu m\ pixel\ size$ datacube. (c) – 60 $\mu m\ pixel\ size$ datacube. (d) – 45 $\mu m\ pixel\ size$ datacube. (e) – 30 $\mu m\ pixel\ size$ datacube. (f) – 15 $\mu m\ pixel\ size$ datacube. 171
Figure 4-11 SNR as a function of intensity plotted across all pixel sizes. (a) – 90 $\mu m\ pixel\ size$ datacube. (b) – 75 $\mu m\ pixel\ size$ datacube. (c) – 60 $\mu m\ pixel\ size$ datacube. (d) – 45 $\mu m\ pixel\ size$ datacube. (e) – 30 $\mu m\ pixel\ size$ datacube. (f) – 15 $\mu m\ pixel\ size$ datacube. 173
Figure 4-12 The functional relationship between the combined noise model parameters and pixel size. (a) – a parameter plotted against pixel size. (b) – b parameter plotted against pixel size. (c) – maximum achievable SNR as a function of pixel size. 174
Figure 4-13 Loss of resolution for two signals at 15 μm pixel size. (a) – high intensity signal. (b) – low intensity signal. (c) – ESF fit on high intensity signal; SNR=2.5. (d) – ESF fit on low intensity signal ; SNR = 0.7. (e) – the MTF and scaled NSD intersect at a critical frequency of 0.18. (f) – the MTF and scaled NSD never intersect....177
Figure 4-14 The SNR distributions for all pixel sizes. The red horizontal line cutting through all distributions shows an SNR value of unity. 178
Figure 4-15 (a) – median intensity as a function of pixel size. (b) – median SNR as a function of pixel size. (c) – median SNR as a function of median intensity. (d) – the percentage of images with SNR less than unity. 180
Figure 4-16 The 86-14% criterion plotted as a function of intensity across all pixel sizes. (a) – effective image blur vs intensity for the 90 μm datacube. (b) – effective image blur vs intensity for the 75 μm datacube. (c) –

effective image blur vs intensity for the 60 μm datacube. (d) – effective image blur vs intensity for the 45 μm datacube. (e) – effective image blur vs intensity for the 30 μm datacube. (f) – effective image blur vs intensity for the 15 μm datacube. 182
Figure 4-17. Distribution of the effective blur parameter for all pixel sizes. The cyan vertical line represents the median blur obtained from high intensity images and the black vertical dashed line is the median of the entire distribution. (a) – distribution of the measured blurring parameter for the 90 μm datacube. (b) – distribution of the measured blurring parameter for the 75 μm datacube. (c) – distribution of the measured blurring parameter for the 60 μm datacube. (d) – distribution of the measured blurring parameter for the 45 μm datacube. (e) distribution of the measured blurring parameter for the 30 μm datacube. (f) – distribution of the measured blurring parameter for the 15 μm datacube. 184
Figure 4-18. (a) – The blurring parameter used as a resolution metric across all pixel sizes. The black diagonal line depicts the Sampling theorem minimum and the blue dots are the measured blur. (b) – the estimated blurring parameter in Fourier space σ. 185
Figure 4-19 log-log plots of measured resolution using Algorithm 2 (red scatter points) and the recovery method (continuous black curve). The vertical grey bars are the errors. The green vertical line is the median intensity. (a) – resolution measurement for 90 μm datacube. (b) – resolution measurement for 75 μm datacube. (c) – resolution measurement for 60 μm datacube. (d) – resolution measurement for 45 μm datacube. (e) – resolution measurement for 30 μm datacube. (f) – resolution measurement for 15 μm datacube.....187
Figure 4-20. Distributions of resolution estimates using the recovery method and Algorithm 2 for (a) – the 90 μm datacube. (b) – the 15 μm datacube.....190
Figure 4-21. (a) – median resolutions acquired from both methods and computed in microns plotted as a function of pixel sizes. (b) – median resolutions acquired from both methods and computed in pixels plotted as a function of pixel sizes (c) – Difference between resolution estimates normalised to the pixel size of each estimate.....192
Figure 4-22 (a) – median resolution acquired through the recovery method as a function of pixel size. Blue scatter points is the data and the continuous black curve is a fourth degree polynomial fit to the data. (b) – derivative of median resolution with respect to the pixel size as a function of pixel size. Blue scatter points is the data and the continuous black curve is a third degree polynomial fit to the data. 195
Figure 4-23. Resolution distributions across all pixel sizes. 196
Figure 5-1 The use of watershed segmentation to separate tissue from background. (a) – original image. (b) – tissue segmentation and separation from background. (c) – image histogram of the original image. (d) – image histogram of the tissue only region.....207
Figure 5-2 Natural logarithm of the median tissue intensities for each datacube. The black curve is a probability density function estimated with MLE. (a) – natural log median tissue intensity in NanoSIMS. (b) – natural log median tissue intensity in OrbiSIMS. (c) – natural log median tissue intensity in uMALDI. (d) – natural log

median tissue intensity in DESI Lab A. (e) – natural log median tissue intensity in DESI Lab B. (f) – natural log median tissue intensity in DESI LAB C. 208
Figure 5-3. (a) – PDFs describing the distribution of the median tissue signals for different modalities. (c) – the corresponding CDFs; black vertical line is the 50^{th} percentile. 210
Figure 5-4. Detection of homogeneous blocks for different modalities. (a) – a single ion image from the DESI Lab C datacube. (b) – a single ion image from the uMALDI datacube. (d) – a single ion image from the OrbiSIMS datacube. (c) – a single ion image from the NanoSIMS datacube. (e), (f), (g), (h) – the detected homogeneous blocks for (a), (b), (c), (d) respectively. 212
Figure 5-5. Noise variance as a function of intensity measured across different modalities. The black/coloured curves are different noise models fitted to the data (a) – NanoSIMS. (b) – OrbiSIMS. (c) – uMALDI. (d) – Orbitrap DESI Lab A. (e) – XevoToF DESI Lab B. (f) – XevoToF DESI Lab C. 213
Figure 5-6 Local image SNR as a function of intensity measured across different modalities. The black/coloured curves are different noise models fitted to the data (a) – NanoSIMS. (b) – OrbiSIMS. (c) – uMALDI. (d) – Orbitrap DESI Lab A. (e) – XevoToF DESI Lab B. (f) – XevoToF DESI Lab C. 217
Figure 5-7 Global (median) image SNR as a function of intensity measured across different modalities. The black/coloured curves are different noise models fitted to the data (a) – NanoSIMS. (b) – OrbiSIMS. (c) – uMALDI. (d) – Orbitrap DESI Lab A. (e) – XevoToF DESI Lab B. (f) – XevoToF DESI Lab C. 218
Figure 5-8. A high intensity single ion image from each of the modalities. The red square in each subplots represents the selected 'edge' ROI. (a) – NanoSIMS. (b) – OrbiSIMS. (c) – uMALDI. (d) – Orbitrap DESI Lab A. (e) – XevoToF DESI Lab B. (f) – XevoToF DESI Lab C. 220
Figure 5-9. Zoomed in 'edge' ROIs. (a) – NanoSIMS. (b) – OrbiSIMS. (c) – uMALDI. (d) – Orbitrap DESI Lab A. (e) – XevoToF DESI Lab B. (f) – XevoToF DESI Lab C. 222
Figure 5-10. Performance of Algorithm 1 on three ROIs. Goodness of fit estimates for Orbitrap DESI Lab A. (a) – ROI 1 - overfitting to noise: reduced $\chi 2 \ll 1$. (b) – ROI 2 - fit not capturing data: $reduced\ \chi 2 \gg 1$. (c) – ROI 3 - good fit: reduced $\chi 2 \approx 1$. 223
Figure 5-11 Performance of Algorithm 2 on ROI 1, ROI 2 and ROI 3. (a), (b), (c) – tissue images; red boxes are the edge ROI. (d), (e), (f) – masked tissue images. (g), (h), (i) – the MTF/NSD intersections computed with Algorithm 2. 224
Figure 5-12 (a) – log base 10 reduced chi squared plotted against intensity. (b) – log base 10 blurring parameter plotted against intensity. (c) – log base 10 blurring parameter plotted against log base 10 the reduced chi squared statistic. 226
Figure 5-13. The distribution of blurring parameters acquired from different modalities after thresholding the reduced chi squared values. Median vertical line is the median. (a) – Nano SIMS. (b) – OrbiSIMS. (c) – uMALDI. (d) – Orbitrap DESI Lab A. (e) – XevoToF DESI Lab B. (f) – XevoToF DESI Lab C. 228

Figure 5-14. Resolution as a function of intensity for different modalities. (a) – NanoSIMS. (b) – OrbiSIMS. (c) – uMALDI. (d) – DESI Lab A, DESI Lab B and DESI Lab C. 229
Figure 5-15. Violin plots depicting the resolution distributions of the different modalities. (a) – NanoSIMS. (b) – OrbiSIMS. (c) – uMALDI. (d) – the three DESIs. 230
Figure 5-16. The MSI resolution ruler.....233
Figure 6-1. Image formation model that incorporates DESI. 238
Figure 6-2. A Voronoi tessellation simulating a tissue structure.....240
Figure 6-3 The image formation model in action. Top – first isotope. Bottom – third isotope. 241
Figure 6-4. (a) – A terribly noisy low intensity image. (b) – denoised image. (c) – ground truth. 242
Figure 6-5 Denoising effects on PCA. Left – PCA on denoised datacube. Right – PCA on original data. 243

List of tables

Table 2-1. A summary of the parameters used in the simulation of a PSF. 83
Table 2-2. A summary of the resolution measurements derived from the PSF simulations. 85
Table 2-3. A summary of the equations that describe the variance, standard deviation and image SNR for the three different types of noise model 97
Table 2-4. The value of the coefficients a, b derived from curve fitting.....97
Table 3-1. A summary of the experimental parameters used in this simulation. 106
Table 3-2. A summary of the parameters for the two noise models applied on the images of the resolution device. 114
Table 3-3 Pseudocode for real space estimates of blur and noise 127
Table 3-4. Pseudocode for inverse space estimates of blur and noise and a measurement of resolution....128
Table 3-5. Comparison of resolution frequencies calculated from the resolution model (Equation 3.20) and the experimental method outlined in Algorithm 2. Uncertainty calculated using Equation 3.22....130
Table 3-6. A summary of the noise and blur parameters used in the data cube simulation. 132
Table 3-7. Median values for the resolution of each datacube. Standard errors derived from bootstrapping. 147
Table 4-1. A summary of the MSI parameters used in this MALDI experiment. 155
Table 4-2. Variations in crater area for nine randomly selected craters. 160
Table 4-3. A summary of the $\alpha, \mu I, \sigma I$ parameters obtained from MLE for each of the six data sets. 167
Table 4-4. Parameters of the combined noise model extracted from curve fitting the variance as a function of intensity for each datacube. 172
Table 4-5. Parameters of the combined noise model extracted from curve fitting the SNR as a function of intensity for each datacube. 174
Table 4-6. Comparison between the empirically estimated SNRs and those predicted from the noise model curve fitting. 179
Table 4-7 The percentage of unsuccessfully estimation of Algorithm 2 due to pre-set fractional error threshold for each datacube. The number of linescans is also listed....189
Table 4-8. Polynomial coefficients describing the median resolution as a function of pixel size. 196
Table 5-1. Summary of the modalities investigated in this chapter in their relative pixel sizes. 202
Table 5-2. A quick comparison between the performance of Algorithm 2 and the recovery method with the right blurring parameter. 226
Table 5-3. Median tissue image spatial resolution from different modalities. 232
Table 5-4. A table showing the ability of NanoSIMS to resolve different cell organelles. 233

List of abbreviations

Abbreviation	Definition
a.u.	arbitrary units
ADC	Analogue to ditigital converter
CDF	Cumulative Distribution Function
CEM	Chain Ejection Model
CFD	Computational Fluid Dynamics
CHCA	α-Cyano-4-hydroxycinnamic acid
CPCD	Coupled Physical and Chemical dynamics
CRM	Charge Residue Model
DESI	Desorption Electrospray Ionisation
DHB	2,5-DIHYDROXYBENZOIC ACID
DI	Desorption Ionisation
ESF	Edge Spread Function
ESI	Electrospray Ionisation
ESSI	Electrosonic Ionisation
FFT	Fast Fourier Transform
FTICR	Fourier Transform Ion Cyclotron Resonance
FWHM	Full Width at Half Maximum
GoF	Goodness of Fit
IEM	Ion Evaporation Model
IRF	Instrument Response Function
LAMMA	Laser Microprobe Mass Analyser
LSF	Line Spread Function
m/z	mass to charge ratio
MALDI	Matrix Assisted Laser Desorption/Ionisation
MD	Molecular Dynamics
MK Test	Mann-Kendall test
MLE	Maximum Likelihood Estimation
MS	Mass Spectrometry
MSI	Mass Spectrometry Imaging
MTF	Modulation Transfer Function
NLF	Noise Level Function
NPS	Noise Power Spectrum
NSD	Noise Spectral Density
PCA	Principal Component Analysis
PDF	Probability Density Function
PDPA	Phase Doppler Particle Analyser
PI	Postionisation
ppm	parts per million
PSD	Power Spectral Density
PSF	Point Spread Function
PVD	Physical Vapour Deposition

ROI	Region Of Interest
SIMS	Secondary Ion Mass Spectrometry
SNR	Signal to Noise Ratio
SY	Survival Yield
ToF	Time of Flight

Chapter 1 A general introduction to Mass Spectrometry Imaging

1.1 Introduction

Characterising the behaviour and properties exhibited by living systems is the main task of biology and life sciences. Such systems are incredibly complex and a full scientific description of their nature is often the product of interdisciplinary research. There are two famous examples from history which come to mind. The first one is the discovery of cells by Robert Hooke in 1665, which would be impossible had the microscope not been invented. The second is the use of X-ray crystallography by Rosalind Franklin to obtain images of the diffraction pattern of the DNA molecule. Her data later inspired Watson and Crick to produce their double-strand DNA model.

Cells, which can be considered the building blocks of life, are comprised of a large number of different types of molecules and atoms. Different cell types perform different functions, and as such their chemical composition differs. The use of scientific instrumentation for the purpose of identification and quantification of molecules and atoms in matter is referred to as analytical chemistry. On the other hand, characterising the full molecular profile of living matter is referred to as 'omics'. For example, genomics is concerned with the profiling the genome of a cell, while lipidomics aims to describe the lipid profile of a cell. One of the main tools used in analytical chemistry is mass spectrometry (MS). MS allows for the structural identification and quantification of charged particles. When applied to living matter MS becomes an incredibly powerful tool. The ability of MS to detect and identify a large set of molecules fits the needs of lipidomics, metabolomics and proteomics perfectly. In addition, MS can also provide information about the spatial distribution of molecules. This is referred to as mass spectrometry imaging (MSI).

MSI stands out from other imaging techniques, such as bright field microscopy, because it derives information by probing and consuming material from the sample of interest. Because of this destructive nature, the object which is being imaged changes as the image is acquired. Generally, imaging techniques can be characterised by their resolution capability. Spatial resolution relates the ability of an imaging system to faithfully obtain information from the object, which is being imaged. In particular, spatial resolution is the minimal distance between two features in an object, such that those features can be distinguished from each other in the image of the object. So far neither a reliable definition, nor a standardised methodology for measuring spatial resolution has been accepted in the MSI community. This is mostly due to the lack of a mathematical model, which can describe the process of mapping information from the object to the image of the object. Developing such a model and a methodology for measuring spatial resolution that follows from the model is the main focus of this work. The motivation for this can be viewed from two different angles. The first one is the optimistic, long-term angle. Similar to how a fundamental theory of X-ray diffraction was crucial to the discovery of DNA, a theory of image formation in MSI can further develop the

field. The second view point is based on practical reasons. In fact, there are many different practical benefits to measuring spatial resolution. For example, if interested in imaging a certain feature, selecting the right pixel size can save tremendous amounts of time and hardware storage space. This can be crucial for optimising large scale biological studies.

1.2 MSI Modalities

Now that the main focus of this work has been established and justified, a generalised description of an MSI experiment is provided, followed by a description of the different type of MSI modalities. A generalised description of a typical MSI set up is now provided.

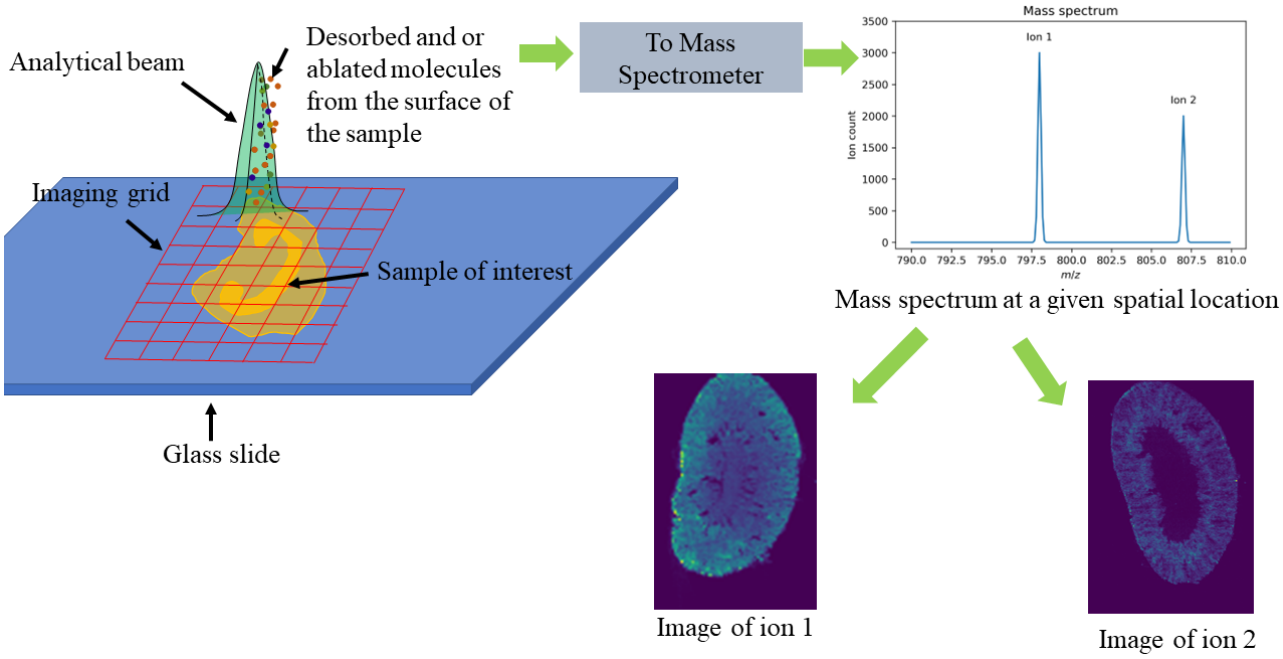


Figure 1-1. A diagram depicting a generalised MSI experimental set up.

An MSI set up can be broken down into two parts – an ion source and a mass analyser. A generalised schematic of an MSI set up is shown in Figure 1. In the ion source a sample of interest, typically a thin tissue section, is often thaw mounted on a glass slide. The glass slide is attached to a motorised stage. An analytical beam is then used to probe the sample of interest. The movement of the stage and the rate at which the mass spectrometer records data is defined experimentally. Thus, a sampling path for the analytical beam is established. The sampling path is later converted to a discretised array of pixels, or an imaging grid. As the analytical beam moves across the sampling path, once the beam/sample interaction occurs, molecules are energised and leave the surface of the sample through desorption and or ablation. A set of chemical reactions occur that allow for the soft ionisation of biomolecules.

These ions are then captured by a mass spectrometer. The mass analyser then measures the mass to charge ratio (referred to as an m/z value) of all ions associated with a particular spatial location. Thus, for a single pixel a large number of signals can be detected. As the analytical beam probes the sample, the chemical composition of the sample changes. In turn, the mass spectrum changes and so do the image intensities. This way a hyperspectral imaging data set is created.

MSI modalities are defined by the nature of the analytical beam used in the ion source. If a laser beam is used in combination with a thin organic crystal coating the sample, the resultant modality is referred to as Matrix Assisted Laser Desorption/Ionisation (MALDI). In the case of an electrospray beam the modality in question is Desorption Electrospray Ionisation (DESI). When an ion beam is used to probe the sample, the modality is named Secondary Ions Mass Spectrometry (SIMS). MALDI, DESI and SIMS are three of the most common MSI modalities used to obtain images of the molecular composition of biological samples. Each modality can be coupled with a different mass analyser to create an MSI set up. The characteristics of an analytical beam used by a given modality, such as beam width and energy, in combination with the mass analyser used determine the arising mass spectra for each pixel. The MSI modality is crucial to an image formation model. To help us establish such a model for the purpose of measuring resolution an overview of the three most commonly used modalities now follows.

1.2.1 MALDI

MALDI was first described by Karas and Hillenkamp in 1985 [1]. Two years later Koichi Tanaka demonstrated that it is possible to ionise and detect protein molecules [2]. Roughly ten years later after, Richard Caprioli published an article that described the use of MALDI for the purpose of imaging the spatial distribution of biomolecules [3]. While MSI already existed in the form of SIMS MSI, it was used for the characterisation of non-organic materials [4]. Another form of MSI described at the time of MALDI's discovery was the Laser Microprobe Mass Analyser (LAMMA) [5]. LAMMA was shown to be capable of imaging biological specimens. However, only elemental spectra could be obtained. On the other hand, combining MALDI's capability to softly ionise large biomolecules with an MSI set up was revolutionary and opened up a whole new area of research.

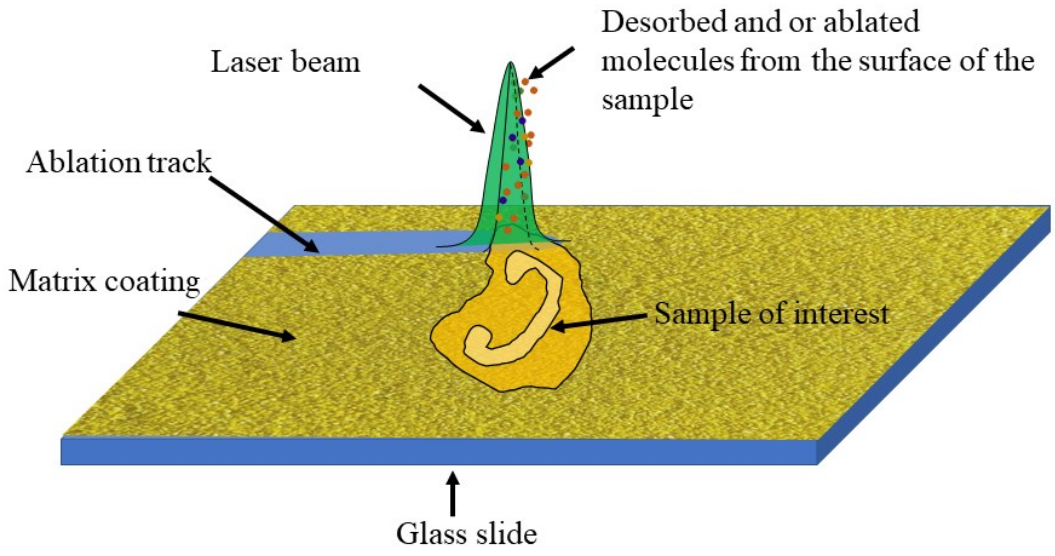


Figure 1-2. A schematic of a typical MALDI laser profile imaging set up.

The MALDI process can be broken down into two parts. The first one is the desorption and/or ablation process. The second one is the ionisation process. Generally, a laser with a wavelength that matches the absorption spectrum of the matrix is used. Typically, matrix molecules with a benzene ring are used and the phenol group absorbs light at around 337 nm. This way the analyte molecules, which can be large and fragile biomolecules, are protected from fragmentation by the matrix from the high intensity laser. The matrix coating not only helps keep the analyte molecules intact but also ionises them through a set of interactions. A generalised MALDI MSI set up is depicted in Figure 2.

1.2.1.1 The Desorption/Ablation process in MALDI

There exist several different models that describe the MALDI desorption/ablation process. Some of the early work done on the MALDI desorption process was carried out by Hillenkamp et al [6,7]. In their first publication on the matter a quasi-thermal Arrhenius-like equation was used to describe the number of desorbed particles [6]. The functional dependence of desorption counts on experimental parameters such as laser intensity and spot size. The proposed equation for the number of desorbed molecules is given by:

$$N_{des} = Pf(A)\exp\left[-\frac{E_A}{k_B(T_0+\eta H)}\right] \qquad \text{Eq. (1.1)}$$

Where P is a pre-exponential factor, $f(A)$ is a function that describes the desorption area, E_A is an activation energy for desorption, k_B is the Boltzmann constant, η is a conversion constant describing the transformation of the laser

beam energy into matrix temperature and H is the laser fluence. While the proposed equation models the desorption counts well the ionisation mechanism is not accounted for. In order to decouple ionisation effects from material ejection effects a secondary laser pulse is used for the photoionisation of the expanding plume. The quasi-thermal desorption model provided by Hillenkamp et al. fits the data well at lower laser fluences and suggests thermal desorption as a primary ejection mechanism. At higher fluences deviations from Equation 1.1 are observed. The authors attribute those deviations to non-equilibrium effects having an effect on the spot size dependence $f(A)$. In particular it was noticed that a small beam would require a larger laser fluence for desorption to occur. In their second publication on the matter the temperature dependence of desorption was investigated [7]. Once again, for lower fluences the predicted temperature dependence was corroborated by the experimental results.

A completely different approach to the MALDI desorption problem was taken by Garrison et al [8,9]. Molecular dynamics (MD) simulations of the laser/matrix crystal simulations revealed new information that analytical models had failed to see. While Garrison *et al.* were not the first to study the MALDI desorption process through the lens of MD, previous work on the topic was computationally intensive due to the large number of degrees of freedom. For example, previous MD simulations by Bencsura and Vertes modelled the desorption process for 202 matrix molecules and studied the breaking of the hydrogen bonds due to the temperature jump induced by a laser pulse [10]. This is a very small model corresponding to roughly $2\,nm$, which could have an effect on the validity of the calculations. However, Garrison et al. introduced a breathing sphere model, which approximated the internal molecular degrees of freedom. This is done by replacing molecules with a single particles and the interparticle interaction potential is chosen such that it matches the material properties. Each particle has an internal degree of freedom (breathing mode) that is meant to approximate the internal molecular degrees of freedom. This in term allowed for calculations to be performed on much larger ensembles [8,9]. The MD simulations performed by Garrison et al. revealed that there exist two different material ejection regimes, separated by a threshold fluence. At lower fluences the MD simulations agree with the thermal desorption model. At higher fluences thermal desorption still occurs, but the dominant material ejection mechanism is ablation [11]. The MD simulations reveal that while the desorption regime is characterised by single molecules leaving the crystal surface at high velocities, in the ablation regime a collective behaviour of particles/molecular clusters is observed. The ejected clusters have a much lower velocity and can further disintegrate into single molecules when they are in the gaseous phase. Generally, ablation is a very complex phenomenon arising from the interplay between the physicochemical properties of the matrix organic crystal and the laser beam. Some of the proposed mechanisms at play include inertial confinement [12] and phase explosion [13]. The precise contribution from each mechanism is still unclear. In the MD simulations provided by Garrison et al. ablation arose in a scenario where a pressure wave induced by the laser melting the sample propagates through the crystal to the substrate boundary. This pressure wave is then reflected and causes a material ejection of large, low velocity molecular clusters. The proposed model for the ablative process, which occurs above a critical energy threshold is given by:

$$N_{abl} = n_m L_p \ln\left(\frac{H}{L_p(E_v^* - CT_0)}\right) \quad \text{Eq. (1.2)}$$

The logarithmic term is explained by the exponential decrease of laser intensity as per the Beer-Lambert law. Thus, this model is sometimes referred to as the *ln* model or the photoablation model. This model applies for fluences larger than the threshold fluence $H > H_{thr}$. Here n_m is the molecular density, L_p is the laser penetration depth, C is the specific heat capacity, T_0 is the initial crystal temperature and E_v^* is a critical energy. Equation 1.2 provides a good fit for the data derived from the MD simulations.

Another approach to modelling the ablation process in molecular crystals was investigate by Rohlfing et al [14]. The authors used photoacoustic data to study the phase MALDI phase transition. While the data presented by Garrison et al. was derived from MD simulations, in this study the number of ejected particles was recorded experimentally. A discrepancy between the photoablation model and experimental data was observed. Rohlfing et al. suggested another model, which follows a linear form :

$$N_{abl} \propto N - N_{thr} \quad \text{Eq. (1.3)}$$

The linearity suggests that above the threshold value excess energy is deposited into the latent heat of vaporisation. The model suggested by Rohlfing et al. modelled the experimental data better than the photoacoustic model. In a more recent study Niehaus and Soltwisch used laser postionisation (PI) complemented by the acoustic method to investigate MALDI material ejection [15]. Two commonly used MALDI matrices were studied at a range of different laser beam sizes and a range of different laser fluences. The matrices were 2, 5 – dihydroxybenzoic acid (DHB) and 4-chloro-α-cyanocinnamic acid (CHCA). The laser beam sizes ranged from $200 - 20\ \mu m$, aiming to replicate the typical MALDI MSI and MALDI MS experimental conditions. They calculated the velocity distribution for ejected particles. The results show that for larger beam sizes ($\approx 200\ \mu m$) the dominant material ejection mechanism is thermal desorption across all fluences used (highly energetic single molecules). This is consistent with the experimental results of Hillenkamp et al[6,7]. However, at medium sized beam widths a bimodal distribution was observed across intensities, indicating that both thermal desorption and ablation can be responsible for material ejection, the slower velocity distribution being attributed to ablation. At small beam sizes ($\approx 20\ \mu m$), which are also typical for modern day MALDI MSI set ups, the predominant material ejection mechanism is governed by ablative processes. The results from the photoacoustic experiments are striking. Once the data is normalised to the beam area, the counted ejected material across all beam sizes fall on the same curve. This indicates that the desorption/ablation process is independent of the beam size used and solely depends on the laser fluence. The photoacoustic data also revealed that below a certain threshold the material ejection mechanism is thermal

desorption. Above that threshold they tested the *ln* model and the linear model (Equations 1.1 and 1.2). They observed a slight discrepancy between the photoacoustic model and the data, while the linear model provided a good fit for the data. This is in agreement with Rohlfing et al [14]. The apparent effects of beam size on the ejected material count were explained by the expanding plume dynamics having a possible effect on the MS signal. However, another explanation for this can also be provided. To understand this we need turn our gaze towards the other important aspect of the MALDI process – ionisation mechanisms.

1.2.1.2 Ionisation mechanisms in MALDI

Roughly speaking MALDI ionisation models can be divided into two broad categories. The first of those consists of models which rely on primary ion generation from photoexcited molecules. In general, for most matrices at a laser wavelength of $337\ nm$, a three photon scattering event is required to ionise the matrix molecule. However, a three photon scattering event is very unlikely, even for very high intensity beams. Thus, a common theme among photoexcitation models is the conversion of three separate scattering events into another form that can later be reconverted into an ionised molecule. A notable example is the thermal ionisation of the photoexcited matrix molecule model proposed by Allwood et al[16,17]. The model assumes ionisation occurs in the gaseous phase and requires a very hot and dense plume. Ionisation is explained by vibronic coupling with an excited singlet state electron.

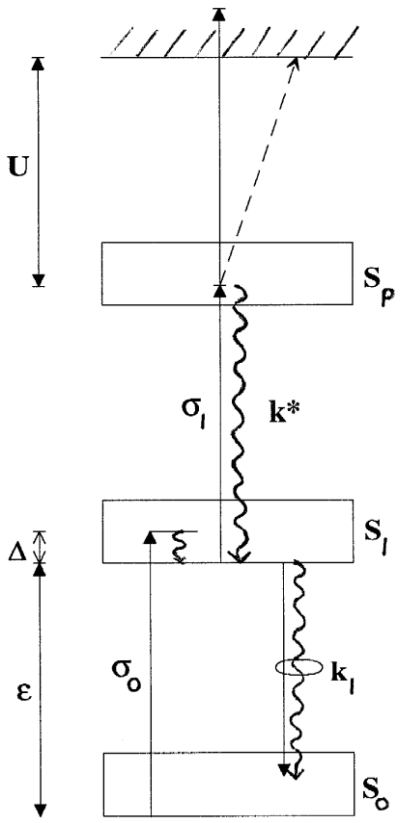


Figure 1-3. An energy level schematic of the thermal ionisation of the photoexcited matrix molecule ionisation model. Solid lines represent optical transitions caused by the absorption of a photon of an electron. S_0, S_1, S_p *and* I_p *are the ground state, first excited singlet state, a higher energy singlet state and the ionisation potential respectively. Curved lines represent radiationless transitions. The dashed line represents vibronically coupled ionisation. The figure is adapted from*[15].

In simpler terms, optical excitation of electrons to a higher singlet state occurs. The excited electron can then decay to a lower state via radiationless transition; the energy is converted to a higher molecular vibration state (vibronic state). The excited electron may also be elevated to an upper energy state through another photon scattering event. However, if previous radiationless transitions have occurred, the molecule will have enough energy to 'shake off ' this electron. Thus, three separate photon scattering events can be converted to an ionised molecule and an ejected electron through vibronic coupling. While this mechanism can plausibly explain the primary ion generation mechanism in MALDI, it requires plasma-like plume behaviour. In particular, in order to explain the observed ion intensities observed the model would require temperatures at least twice as high as typical MALDI plume temperatures [18]. Nevertheless, even at typical MALDI plume temperatures this process could be generating ions, albeit those ions would be a small portion of the observed signal.

Another example of a photoexcitation ion generation mechanism was proposed by Knochenmuss [19–21]. The model in question is referred to as the Coupled Physical and Chemical Dynamics (CPCD) model or the energy pooling model. In the CPCD model primary ionisation occurs before the desorption/ablation event takes place.

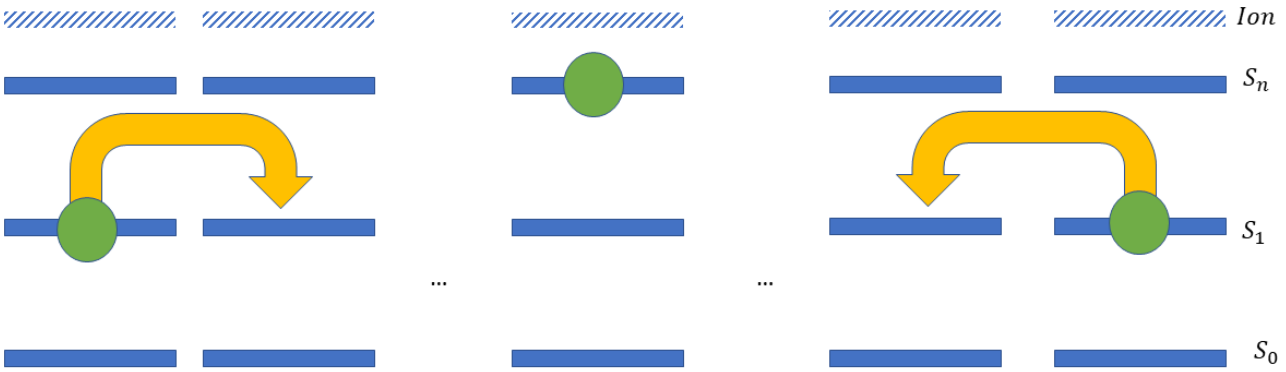


Figure 1-4. A schematic diagram of the $S_1 - S_1$ pooling process proposed in the CPCD model. S_0 is the ground state, S_1 is the first excited singlet state and S_n is a state with double the energy of S_1. The green circles represent an excitation and the orange arrows represent the movement of the excitation from one molecule to another. Eventually, the energy of two distant molecules can be pooled into a single molecule, resulting in a molecule in the S_n state.

It invokes the beautiful idea of excitons. When an electron in an molecules is excited to a higher energy state it leaves a hole in the lower state. The electron-hole pair forms a hydrogen-like structure within the molecules itself called an exciton. The exciton can hop around from one molecule to another in the crystal. Thus, when a molecule is excited that excitation is not localised but instead can roam around in the crystal. This roaming process is illustrated schematically by the orange arrows in Figure 4. When two excitons 'collide' an $S_1 - S_1$ annihilation event occurs. The two original S_1 molecules return to the ground state S_0 and the molecule 'experiencing' the pooling event is promoted to a higher excitation state S_n.

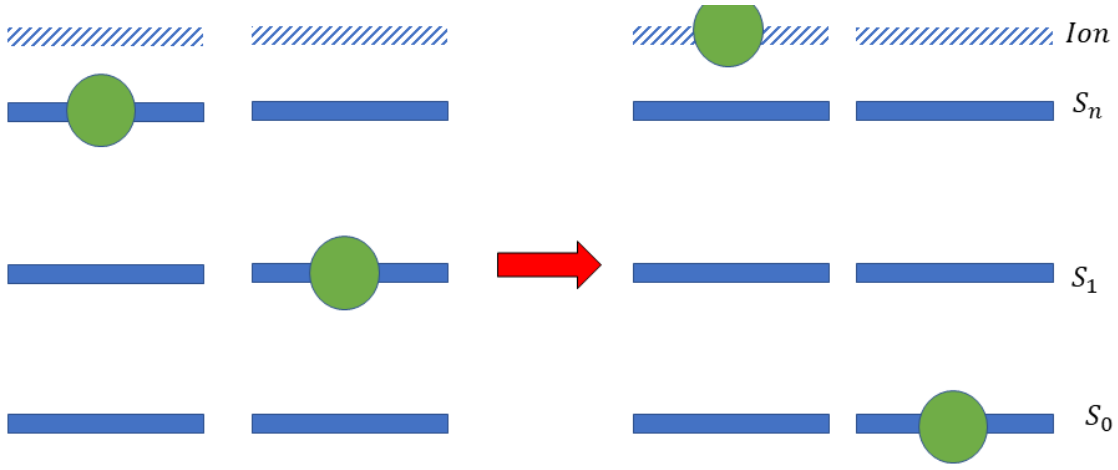


Figure 1-5. A schematic diagram of the $S_n - S_1$ pooling process proposed in the CPCD model. S_0 is the electronic ground state, S_1 is the first excited singlet state and S_n is a state with double the energy of S_1. The green circles represent an excitation.

Of course the S_n excitation is also free to move around the crystal. As it propagates from molecule to molecule it may encounter an S_1 excitation. An $S_n - S_1$ pooling event occurs, which results in an ionised molecule, an ejected electron and a molecule in the ground state. The ionised molecule and the ejected electron can then produce the secondary analyte ions observed in typical MALDI spectra. Once again, the energy of three photons has been converted to an ionised molecule, this time via a pooling scheme. Experimental evidence of $S_1 - S_1$ pooling was shown by Setz and Knochenmuss [22]. These phenomena occur at a timescale of nanoseconds, whereas the desorption/ablation event leading to plume expansion is of the order of microseconds. In this model material ejection is also taken into account in the form of thermal desorption – a sample layer changes phase when a critical temperature is reached. However, as described earlier, the MD model developed by Zhigilei and Garrison [8,9,11] predicts that low temperature clusters can also be ejected. Taking these into account is important when describing the MALDI signal quantitatively. To this end Zhigilei and Knochenmuss produced a fully quantitative MALDI MD model which takes into account ionisation, desorption and ablation [23,24].

The second category of MALDI ionisation models attributes primary ion generation to molecules in the ground state. In these models ion generation occurs due to temperature effects rather than light/matter interactions. One worthy example is the solid state thermodynamic model [25]. As an ionisation model it stands out from some of the previously discussed models because it also incorporates the desorption process. While the thermal ionisation of the photoexcited matrix molecule model assumes chemical equilibrium in the gas phase here chemical and thermal equilibrium are assumed in the solid state, before desorption occurs. In order to invoke thermally induced chemical reactions, rather than photochemical reactions, the assumption that thermal energy is confined within the irradiated volume is crucial. There is a sufficient amount of evidence that this is the case, as the time required for heat

dissipation is several order of magnitudes lower than the relaxation times for chemical and thermal equilibrium [26,27]. The proposed reaction pathway starts with a chemical reaction prompted by the laser:

$$M_s + nh\nu \overset{K_1'}{\leftrightharpoons} M_s^{\bullet} + e^- \quad \text{Eq. (1.4)}$$

Where M_s is a matrix molecule in the solid state and K_1' is an equilibrium constant. Thus, according to Equation 1.4, under the influence of the laser a matrix radical and an electron are created. Then, this is followed by:

$$M_s + M_s^{\bullet} \overset{K_1''}{\leftrightharpoons} [M+H]_s^+ + [M-H]_s^{\bullet} \quad \text{Eq. (1.5)}$$

The matrix radical produced in Equation 1.4 reacts with a neutral matrix to create the protonated matrix ion. Combining Equations 1.4 and 1.5 together, the overall reaction takes the following form:

$$2M_s + nh\nu \overset{K_1}{\leftrightharpoons} [M+H]_s^+ + [M-H]_s^{\bullet} + e^- \quad \text{Eq. (1.6)}$$

Finally, the radical $[M-H]_s^{\bullet}$ may react with the freed electron to produce a negative ion :

$$2M_s + nh\nu \overset{K_1}{\leftrightharpoons} [M+H]_s^+ + [M-H]_s^- \quad \text{Eq. (1.7)}$$

The authors suggest that the reactions described by Equation 1.4 to 1.7 as possible pathways, although different pathways maybe be possible for different matrices. The equilibrium constant is assumed to take the same value in both pathways. In the heart of the model a transition state theory approach for the desorption of the solid state ions formed by the reaction pathway is used:

$$k_{desorb}(T) = \frac{k_B T}{h}\frac{Q^*(T)}{Q(T)} e^{-\frac{\Delta E_a^*}{RT}} \quad \text{Eq. (1.8)}$$

With ΔE_a^* being the sublimation enthalpy, T being the temperature, k_B is the Boltzmann constant, h is Planck's constant. Q^* and Q are the vibrational partition functions of the desorbed molecule and the crystal-bound molecule respectively. Using the approach taken by Hillenkamp et al[6,7], the surface temperature may be described linearly. The ratio of the two partition function can also be simplified. Thus, according to the solid state thermodynamic model[25], Equation 1.8 becomes:

$$k_{desorb}(T) = \frac{k_B(T_0+\eta H)}{h}\left(1 - e^{-h\nu/k_B(T_0+\eta H)}\right) e^{-\frac{\Delta E_a^*}{R(T_0+\eta H)}} \quad \text{Eq. (1.9)}$$

The ion signal observed by the mass spectrometer is proportional to the surface ion concentration and the desorption constant:

$$I_p \propto k_{desorb}[P] \qquad \text{Eq. (1.10)}$$

Using transition state theory to model for desorption as described by Equation 1.8 and the proposed chemical reaction pathways in Equation 1.4 through 1.7, the observed signal for the protonated matrix molecule can be written as:

$$I_{[M+H]^+} = A\frac{k_B T}{h}\left(1 - e^{-h\nu/k_B T}\right) e^{-\frac{\Delta E_a^*}{RT}}\left(\frac{\sqrt{K_1}}{1+2\sqrt{K_1}}\right) \qquad \text{Eq. (1.11)}$$

Where A is a pre-exponential normalisation constant and the term $\left(\frac{\sqrt{K_1}}{1+2\sqrt{K_1}}\right)$ is a prediction of the ion concentration derived from the proposed pathways seen in Equations 1.4 through 1.7. The authors observed a significant deviation from the data when the ion concentration was excluded from Equation 1.11, indicating that the proposed pathways are viable explanations for the primary ion formation mechanisms. The effects of temperature were also studied, leading to a good agreement with theoretical predictions. It should be noted that the value for the equilibrium constant K_1 was derived from ion to neutral ratios reported in literature. These values typically range from 10^{-9} to 10^{-4}. The authors just assumed an ion to neutral ratio of 10^{-5}, without experimental or theoretical justification for their matrix of choice. Furthermore, the model does not take ablative processes into account.

The review of MALDI ionisation models will now be concluded with the thermal proton transfer model proposed by Ni et al [28,29]. It is one of the more recently developed models. As the name suggests, here the primary ionisation mechanism is due to thermally induced proton transfer reactions. The role that the laser serves here is to heat the sample enough so that such reactions may occur; photoionisation effects are not important at all. In this model, primary ionisation also occurs before the desorption/ablation event takes place. While in the solid-state thermodynamic model primary ionisation was taking place in the solid state and sublimation then leads to the desorption event, here the matrix molecules are assumed to have more degrees of freedom. In fact, as described by the authors, the matrix molecules are neither in the solid nor in the liquid phase, but instead somewhere in between – phase equilibrium is not achieved. These extra degrees of freedom are needed to account for the more frequent collisions between molecules, so that a thermally induced proton transfer reaction may occur. The transition of the solid to the liquid-like state is well justified by the fact that matrix molecules undergo fast internal conversion – the optically excited electrons return to the ground state and the energy is converted into molecular vibrational energy during times much shorter than the laser pulse duration [30,31]. The highly energetic molecule then relax to lower vibrational states by transferring its energy to the surrounding molecules. This leads to the transition from the solid to liquid state. Again, it is important to mention that this happens before desorption/ablation occurs. In this model a calculation of the matrix temperature is crucial and once material ejection starts the temperature will drop as the molecules are leaving the surface. In addition, thermal confinement is also crucial and it can be seen that it is a

plausible assumption from the calculations proposed by Ni et al. The thermally induced proton transfer reaction can be described as:

$$M + M \rightarrow [M + H]^+ + [M - H]^- \qquad \text{Eq. (1.12)}$$

This is the primary ionisation reaction – under the influence of temperature two matrix molecules can exchange a proton. Secondary investigating reactions are also studied by the authors. For the purpose of brevity we will focus on the primary reaction only. By definition the equilibrium constant for reaction 1.12 can be expressed as follows:

$$K = \frac{[M + H]^+[M - H]^-}{M^2} = e^{-\frac{\Delta G}{RT}} \qquad \text{Eq. (1.13)}$$

Where ΔG is the Gibbs free energy of reaction 1.12, R is the universal gas constant and T is the temperature. Using charge conservation we can assert that the number of protonated matrix ions must be equal to the number of deprotonated matrix ions $[M + H]^+ = [M - H]^-$. Thus, the ion to neutral ratio can be easily calculated as follows:

$$\frac{ion}{neutral} = \frac{protonated}{neutral} = \frac{deprotonated}{neutral} = \sqrt{K} = e^{-\frac{\Delta G}{2RT}} \qquad \text{Eq. (1.14)}$$

The beauty of this model is its simplicity – the only thing needed to predict the number of primary ions formed is knowledge on the Gibbs free energy of reaction 1.12 and the temperature of the matrix. However, this is easier said than done. In previous models the temperature change due to the laser heating up the matrix crystal was calculated using a simple linear relation. However, Ni et al use the heat equation coupled with a term that describes the laser induced heat generation:

$$\frac{\partial T}{\partial t} = \frac{\kappa}{\rho_0 c_p}\nabla^2 T + \alpha/\rho_0 c_p(1 - \Phi)I \qquad \text{Eq. (1.15)}$$

Where κ is the matrix thermal conductivity, ρ_0 is the mass density before irradiation, c_p is the specific heat capacity at constant pressure, α is the matrix absorption coefficient, Φ is the fluorescence quantum yield, I is laser beam intensity and ∇^2 is the Laplace operator. The heat diffusivity given is given by $\frac{\kappa}{\rho_0 c_p}$ and is typically a small number for organic materials. This suggests that thermal energy is confined withing the irradiation volume. Thus, Equation 1.15 may be approximated by setting $\frac{\kappa}{\rho_0 c_p}\nabla^2 T = 0$. Ni et. al demonstrate that this is a suitable approximation, especially for large beam sizes. However, really small beam sizes (below $50\ \mu m$ or so) the term cannot be neglected and heat will flow from the irradiated area to the rest of the matrix crystal.

This also explains the effects of beam size and the apparent need for a higher laser fluence at smaller beam diameters reported by Hillenkamp et al [6,7], Rohlfing et al [14] and Niehaus and Soltwisch[15]. Taking this approximation into account, Equation 1.15 simplifies to:

$$\frac{\partial T}{\partial t} = \alpha/\rho_0 c_p (1-\Phi) I \qquad \text{Eq. (1.16)}$$

By definition, the laser fluence between times t_0 and t_1 is given by:

$$H \equiv \int_{t_0}^{t_1} I dt \qquad \text{Eq. (1.17)}$$

Thus, the solution to Equation 1.16 can be written as

$$H = \int_{t_0}^{t_1} I dt = \frac{\rho_0}{\alpha(1-\Phi)} \int_{T_0}^{T} c_p(T) dT \qquad \text{Eq. (1.18)}$$

Thus, a very commonly used experimental parameter – the laser fluence – has been linked to the evolution of heat in the matrix crystal. Calculating the ion to neutral ratio requires knowledge on the Gibbs free energy and the temperature; the temperature may now be estimated provided that mass density, absorption coefficient, the fluorescence quantum yield and the specific heat capacity at constant pressure are known. The only thing left is the specific heat capacity and while it can be measured experimentally it is a function of temperature and it will change as the laser is heating up the matrix. Thus, an analytical expression of the specific heat capacity as a function of temperature is required. In order to calculate the specific heat capacity at constant pressure, Ni et al first calculate the specific heat capacity at constant volume using a modified Einsteinian solid model:

$$c_v = 3R\left(\frac{h\nu}{k_B T}\right)^2 \frac{e^{h\nu/k_B T}}{(1-e^{h\nu/k_B T})^2} + \frac{3}{2}R + \sum_{i}^{3N-6-m} R\left(\frac{h\nu}{k_B T}\right)^2 \frac{e^{h\nu/k_B T}}{(1-e^{h\nu/k_B T})^2} \qquad \text{Eq.(1.19)}$$

Here the first term is the traditional Einstein model, the second term represents contributions from molecular rotation and the third term takes into account molecular vibrations. The two added terms model the matrix molecules in the liquid state described earlier in this section. Below the melting point the second term is neglected. The third term takes into account all possible vibrational modes. Ab initio calculations were used for the vibrational frequencies were performed [28,29]. From here the specific heat capacity at constant pressure can be estimated using the following relation:

$$c_p = c_v + VT\frac{a^2}{b} \qquad \text{Eq. (1.20)}$$

Where a is the coefficient of thermal expansion and b is the isothermal compressibility. Once the specific heat capacity at constant pressure is calculated, Equation 1.18 can be used to calculate the temperature increase of the matrix crystal due to laser irradiation.

The only thing left to estimate the ion to neutral ratio is an estimate of the Gibbs free energy of reaction 1.12. This is also tricky to do, as the Gibbs free energy itself is a function of temperature. To do this ab initio quantum chemistry calculations were performed. Finally, once the temperature is calculated as a function of laser fluence using Equation 1.18 and the Gibbs free energy of the thermally induced proton transfer reaction as a function of temperature is obtained, the ion to neutral ratio can be predicted as a function of laser fluence. The theoretical prediction for the ion-neutral ratio does not match the experimental data perfectly. However, while other models rely on adjusting unknown physical parameters to fit the data, here all of the parameters are either experimentally determined or obtained from ab initio calculations. This is a great advantage as adjusting the values of physical parameters to fit the data is not appropriate for model validation. The model presented by Ni et al is elegant and it assumes the simplest ionisation mechanism. While the thermal proton transfer model cannot explain all of the features observed in a MALDI mass spectrum, such as the existence of matrix radicals, it certainly suggests that thermally induced proton transfer reactions play an important role for the formation in the MALDI signal. In a later publication Ni et al demonstrate an application of their model to several analytes to correctly predict the ion intensities of secondary ionisation reactions of amino acids [32]. More recently, a well-designed experiment that measured both desorbed neutrals and ions at different temperatures was carried out [33]. The experiment showed good agreement with the predictions of the model, further validating the importance of thermally induced proton transfer reactions.

To conclude this section, the MALDI desorption/ablation process was reviewed in depth. A detailed description of some of the most commonly accepted MALDI ionisation mechanisms was provided. This is important for the task that lies ahead – setting up an imaging model for the purpose of measuring the spatial resolution. In particular, inspiration will be drawn from the simple desorption model described here. Because a qualitative image formation model will be set up, ionisation models can be set aside. Nevertheless, they can still be incorporated in the modelling.

1.2.2 DESI

Now that signal formation in MALDI was investigated a similar review for DESI is provided. DESI belongs to a family of techniques based on Electrospray Ionisation (ESI). ESI was first described by Masamichi Yamashita and John Fenn in 1984 [34]. In 1989 John Jenn reported the use of ESI for the analysis of large biological molecules [35]. ESI stands out from other methods that can softly ionise large molecules (such as MALDI) in two ways. Firstly,

ESI can produce multiply charged particles and secondly ESI can only be used to analyse samples in the liquid state. In 2004 Zoltan Takats and Graham Cooks described the first Desorption Electrospray Ionisation (DESI) experiment, in which a pneumatically assisted electrospray was used to analyse different surfaces [36]. This was important because it showed that a Desorption Ionisation (DI) step can be used to investigate samples in the solid phase, while ESI can only be used in the liquid phase. An in vivo application of DESI was also provided in this work. A schematic of a typical DESI sprayer is shown in the figure below.

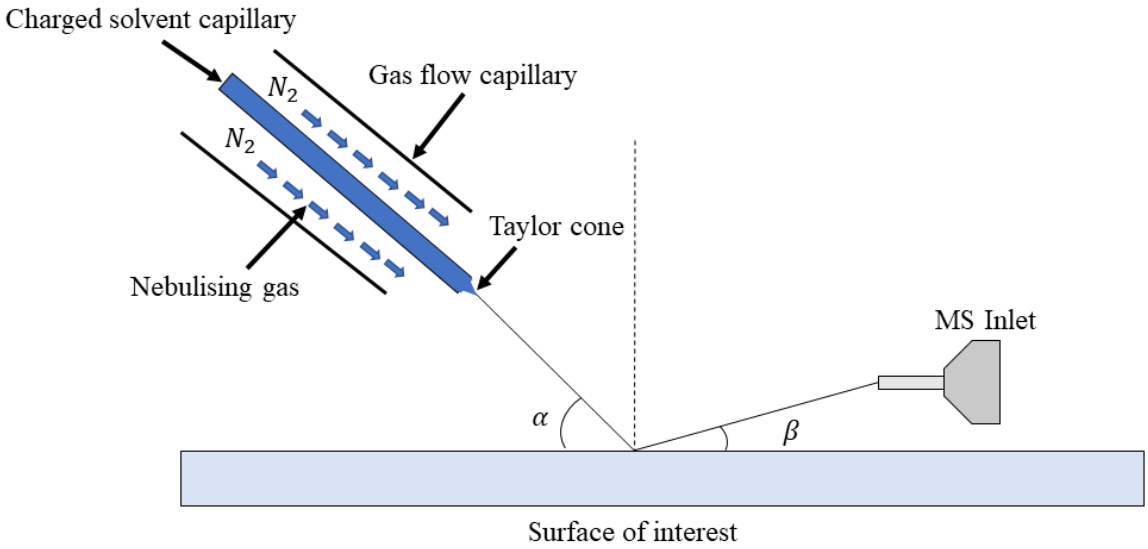


Figure 1-6. A diagram of a traditional DESI emitter set up.

The DESI emitter consists of an outer capillary, which is used to carry a nebulising gas – usually nitrogen. The inner capillary carries a solvent which is also subjected to a high voltage. At the tip of the inner capillary a Taylor cone is formed and the electrostatic forces there break down the liquid and emit tiny droplets of charged liquid [37]. This is process is further aided by the nebulising gas, which helps direct the droplets towards the surface of interest. The nebulising gas also plays an important role when it comes to helping the MS inlet collect secondary droplets generated from the surface of interest. The DESI sprayer and the MS inlet are oriented at an angle α and β respectively, with regards to the surface of interest. These angles generally vary from one set up to another, however a typical angle used for α is $\approx 55°$. For this geometry it has been observed that the signal is maximised for angles $\beta < 10°$.

1.2.2.1 The desorption process in DESI

The DESI desorption process has yet to be fully understood. In fact referring to the main matter collection mechanism as desorption may be slightly misleading. The dominant mechanism responsible for material collection is thought to be the droplet pickup mechanism [38]. The existence of a thin liquid surface layer deposited by the

electrospray is crucial for this model. This thin liquid layer serves two purposes. Firstly, a solid-liquid extraction step occurs. This allows analytes of interest to be desorbed from the solid state into thin liquid layer deposited by the spray. Secondly, the thin liquid layer is continuously bombarded by a stream of droplets generated by the electrospray. This bombardment causes secondary (progeny) droplets to be thrown away from the thin liquid surface. It is important to mention that the properties of this thin liquid layer have not been studied thoroughly. Generally, these properties will depend on the electrospray solvent composition, the surface which will host the thin liquid layer and the physicochemical interaction between the liquid layer and the surface. For example, a thin liquid layer can be observed on a glass surface but not on a porous Teflon surface [39,40]. The presence of such a thin liquid layer is crucial to the droplet pickup mechanism. Even though the properties of the liquid layer are not understood well, there is evidence that it plays an important role in the desorption/ionisation step. For example, a solvation delay in the signal intensities can be observed when the DESI spray is switched on [41].

While the formation and the properties of the thin liquid layer are still to be elucidated, there is ample evidence that supports the droplet pickup mechanism. One study uses a Phase Doppler Particle Analyser (PDPA) set up to measure the velocity distribution and particle size of the primary droplets generated by the DESI source and also the progeny droplets [42]. The particle size was deduced by using Mie scattering theory, which assumes that the droplets are perfect spheres. This assumption does not hold in the case of electrically charged droplets near the Rayleigh limit. Deformations may also be present for very large drops and can also be caused by the drag forces induced by the nebulising gas. In addition, progeny droplets close to the impact site may also be deformed. Finally, the PDPA technique is limited to measuring droplets with a diameter larger than $0.5\ \mu m$. A summary of the results for the primary droplets is presented in the following graph

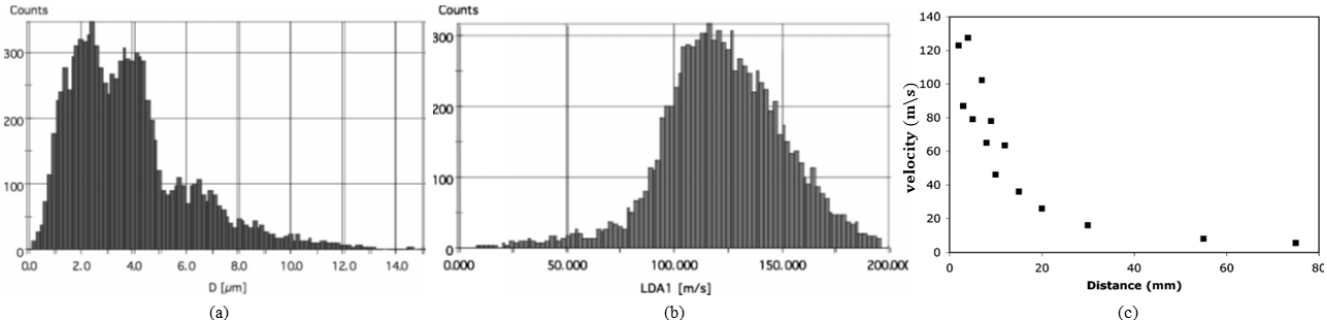


Figure 1-7. (a) – A histogram of primary droplets diameter measured at $5\ mm$ *from the emitter. (b) – A histogram of the primary droplet velocities measured at* $2\ mm$ *from the emitter. (c) – Droplet velocities as a function of distance from the emitter. Adapted from* [42].

Figure 7 (a) depicts the distribution of droplet diameters. The histogram may be interpreted as three different droplet populations centered at 2, 4 and 6 μm. The authors attribute this heterogeneity to the nebulising gas shearing of the solvent liquid at the capillary orifice and thus obstructing the formation of a stable Taylor cone. Another reason

provided by the authors is an asymmetry in the internal solvent capillary – as the solvent cappilary is not perfectly centered in the outer nebulising gas capillary the interaction between the nebulising gas and the solvent will not be uniform. Cooks et al. also argue that the time required for a droplet to evaporate is much larger than the travel time required to reach the impact surface. Thus, it can be expected that the droplets will remain constant in diameter, unless they are near the Rayleigh limit, in which case they will disintegrate.

The distribution of droplet velocities measured at 2 mm from the emitter is shown in Figure 7 (b). The average velocity at this position is 120 m/s. The relationship between average velocity and distance from the emitter can be seen in Figure 7 (c). The average velocity tapers off with increasing distance due to drag forces. For distances between 2 and 10 mm, which correspond to typical DESI set ups, the average droplet velocity will range from 120 to 40 m/s. This measurement allows the authors to perform a valuable calculation. For example, when the sample is placed at 3 mm from the emitter droplets will arrive at the surface with a velocity of 100 m/s. Cooks et al. estimate that the kinetic energy per impacting water molecule is 0.6 meV. This discards sputtering as a material removal mechanism as at this energy sputtering through momentum transfer is highly unlikely. This calculation also supports the droplet pickup mechanism as the main mechanism for material removal.

The PDPA measurements on the secondary droplets also support the droplet pickup mechanism. A summary of these is presented in the following figure.

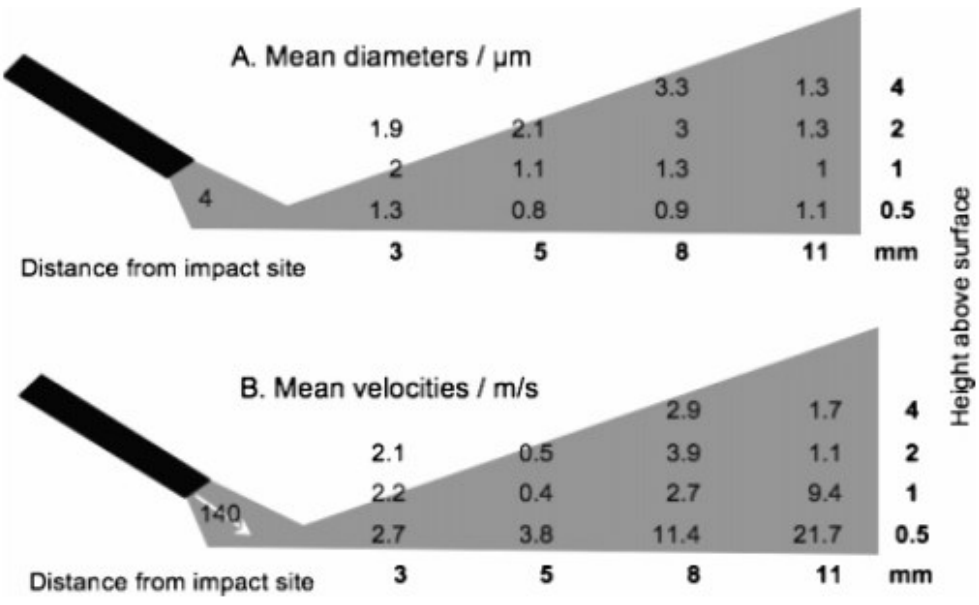


Figure 1-8. Top – average progeny droplet diameters at different distances and heights from the impact site. Bottom – average progeny droplet velocities at different distance and heights from the impact site. Adapted from [42].

While the PDPA technique failed to obtain measurements of progeny droplets below a height of $0.5\ mm$ because light was reflected from the surface, the data still reveals interesting information. Very peculiarly, it appears that droplets closer to the surface are being accelerated. This increase in velocity is attributed by the authors to the gas flow pushing the droplets. However, one may argue that the pressure drop from the MS inlet helps accelerate them. Notably, these droplets have a smaller diameter (around $1mm$) as can be seen in the top panel of Figure 8. Droplets that leave the impact site at a larger angle are observed to have a larger diameter. These larger droplets also slow down as they get farther away from the impact site. This measurement explains why the MS inlet angle β is positioned at values smaller than $10°$ – the flux of droplets is much higher for lower angles due to the high droplet velocities, which leads to a higher signal intensity.

There are a few more studies that interrogate the DESI material consumption mechanism. These are based on MD simulations and support the experimental data discussed above. One of these studies investigates two DESI phenomena: the effects of the nebulising gas on droplet transport and a simulation of the droplet – thin liquid surface layer impact [43]. To achieve this computational fluid dynamics (CFD) was used to model the system. The results from this study are summarised in the following figure.

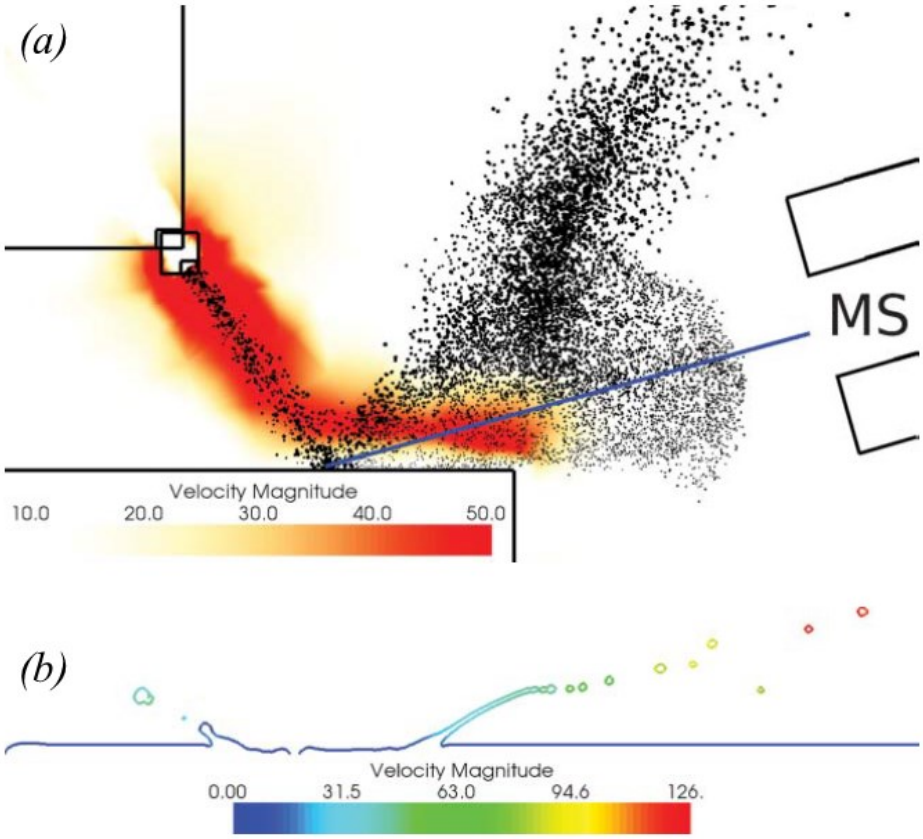


Figure 1-9. (a) – An MD simulation of the nebulising gas effects on droplet transport. (b) – An MD simulation of a droplet – thin liquid layer impact interaction. Adapted from [43].

The results from the simulation which explores the effects of the nebulising gas on droplet transport can be seen in Figure 9 (a). In this simulation the inner capillary has an inner diameter is set to $100\ \mu m$ and an outer diameter of $190\ \mu m$. The outer capillary has its inner diameter set to $250\ \mu m$. The sprayer position is set to $2mm$ away from the surface and the incident angle is set $55°$. These values correspond to a typical DESI set up and are in line with the experimental conditions in [42]. There are two major simplifications in this study that can be outlined. The first simplification is that electrostatic forces are neglected. Thus, the actual electrospray formation is not accounted for. For example, a Coulomb repulsion force between individual droplets may widen the spray. This also means that the atomization process, which is caused by the nebulising gas shearing the electrically charged solvent at the orifice, is not accounted for. In order to mitigate this and still produce a realistic droplet size and velocity distributions the initial conditions for the droplet size and velocities were taken from the PDPA experiments [42]. The droplet size distribution is generated using a Rossin-Rammler distribution and the initial droplet velocity is set to $180\ m/s$. The second simplification invoked is that the pressure drop due to the presence of the MS inlet is disregarded. The authors reason that ignoring the pressure transport effects will allow for the evolution of the spray itself to be tested.

However, pressure transport effects are certainly a critical element of the material collection process and will also change the evolution of the spray.

Droplets are represented as black circles in Figure 9 (a), the relative size of the droplets is proportional to the size of the circles. The colour scale represents the speed of the nebulising gas. Interestingly, the nebulising gas shows a Coanda-like effect and appears to follow the surface. Thus, as indicated by the red region, the nebulising gas has a significantly higher velocity near the surface. The simulation also shows that most of the droplets near the surface are small and fast moving. Because they are small, the nebulising gas carries them across the surface and eventually they obtain the same velocity as that of the moving gas. At higher altitudes larger droplet sizes are observed. The larger droplets have a greater mass, and thus momentum, which means they can escape the horizontal nebulising gas flow near the surface. These larger droplets also exhibit a lower velocity. The simulations discussed here are in close agreement with the experimental results discussed previously [42].

The results from the second simulation are shown in Figure 9 (b). It summarizes the results from a simulation in which progeny droplets are produced by the primary spray droplets bombarding a thin liquid layer. Cooks et al. chose to simulate a $1\ \mu m$ water layer which will be impacted by a $3\ \mu m$ diameter water droplet moving with $120\ m/s$ at a $55°$ incident angle. While the spray droplet diameter, velocity and incident angle are derived from experimental measurements, the choice of $1\ \mu m$ water layer is arbitrary. As discussed previously, the properties of the liquid layer will depend on the solvent and substrate. Nevertheless, the results from this simulation are informative enough. Figure 9 (b) is a snapshot of the system's evolution taken at $t = 4.5\ \mu s$. It can be seen that the sprayer droplet/liquid layer collision produces a lot of progeny droplets with high velocities. The velocities of the progeny droplets can range up to the velocity of the velocity of the impact droplet $120\ m/s$. A jetting effect is also observed, where a series of small progeny droplets is emitted. While the velocities of the generated droplets are somewhat higher than the experimental measurements, a take-off angle between 0 and $15°$ is observed and the droplet diameter is around $1\ \mu m$. Thus, the take-off angle and the droplet diameter is in close agreement with the experimentally verified angles and diameters.

Both simulations shown in this report strongly suggest that a droplet pickup mechanism is the primary matter removal mechanism. The authors' choice to neglect electrostatic interactions between individual droplets and also to ignore droplet-field interactions can be easily justified. However, the presence of the MS inlet and the pressure differential induced by it could significantly alter the progeny droplet velocities calculated in this study. For example, assuming that the MS atmospheric pressure sits at $500\ mbar$ and treating the nebulising gas flow as an incompressible fluid flow one may invoke Bernoulli's equation to estimate the velocity of the gas flow. Assuming a static pressure of 1 atmosphere and using the density of nitrogen, the dynamic pressure term can allow us to estimate the velocity of the nebulising gas near the MS inlet. While this is a crude, back of the hand calculation, the velocities one can obtain after performing it are around $290\ m/s$. Thus, the droplet velocities near the MS inlet can

be more than one order of magnitude higher than the experimentally measured velocities. This indicates that for a full investigation of the droplet pickup mechanism the MS inlet should be considered. Another critique that can be added is that the methodology used in this report does not allow for the two simulations to be ran together so that the effects of the nebulising gas and the generation of progeny droplets can be considered simultaneously. However, from the discussion on a later publication that will follow immediately, it will become apparent that using Stokes' law is sufficient to determine the behaviour of progeny droplets in the nebulising gas environment.

In a later publication a refined model for the generation of progeny droplets is provided [40]. This includes a full three dimensional treatment of the droplet/liquid layer interaction. The results from this simulation are presented in the following figure.

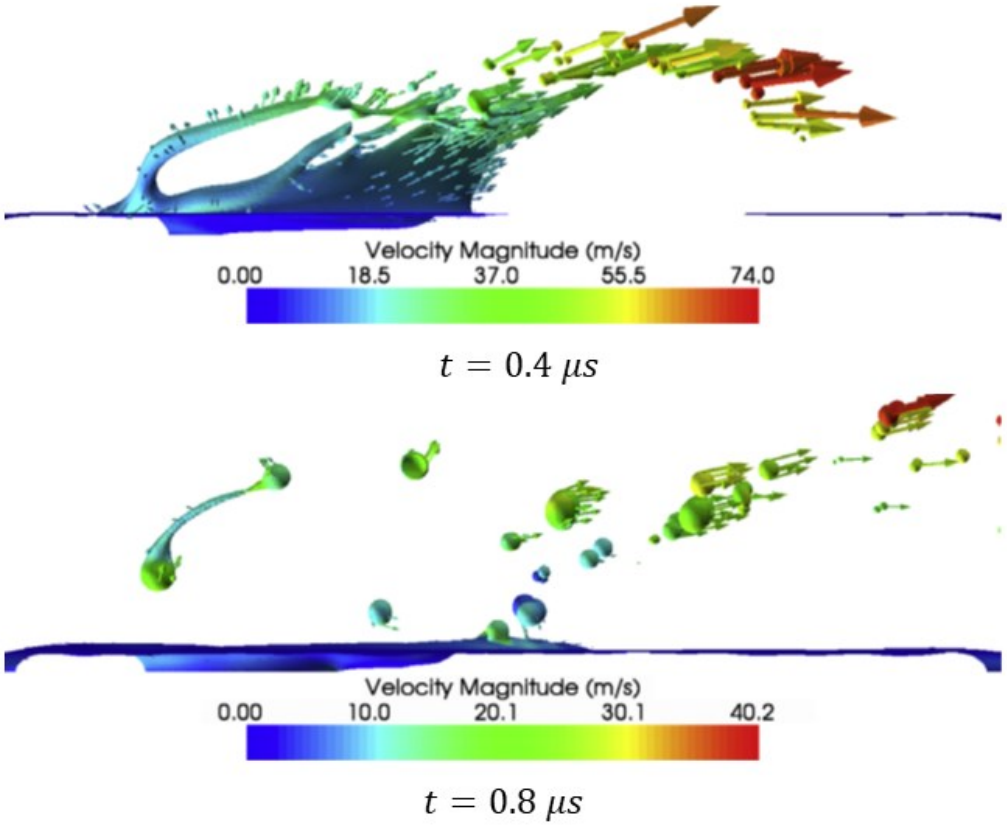


Figure 1-10. Snapshots from the evolution of a droplet/liquid layer interaction and the generation of progeny droplets. Taken from [40].

The authors investigated the behaviour of progeny droplets at different angles α, including $\alpha = 90°$. The data displayed in Figure 10 is for $\alpha = 55°$. The top panel is a snapshot from $t = 0.4\ \mu s$ and the for the bottom panel $t = 0.8\ \mu s$. The velocity and diameter initial conditions for the sprayer droplet are similar to those seen in the previous study [43] and are derived from the experimental data shown in [42]. For the velocity a value of $120\ m/s$ was chosen and the diameter was set to $3.7\ \mu m$. As for the progeny droplets, the results from the simulations are in close

agreement with experimental data [42] and previous MD simulations [43]. In particular, droplets with a small diameter and large velocities are initially generated, followed the ejection of large, slower droplets. The take-off angle for the large droplets is much larger than that of the small and fast-moving droplets. An interesting argument presented in this work aims to address the relaxation times of droplets that exhibit Stokes flow. The authors argue that the Reynolds number for the progeny droplets is small (<50). Thus Stokes' law can be used to model the behaviour of progeny droplets. The relaxation time is proportional to the diameter squared. Thus smaller droplets will have a small relaxation time and will equilibrate quickly to the nebulising gas flow, which will carry them towards the MS inlet. On the other hand, larger droplets will have a relaxation time which is several orders of magnitude larger. Thus, the larger droplets, which are also leaving at a higher take-off angles, may escape the gas flow.

The studies reviewed so far provide experimental and computational insights into the main DESI matter collection mechanism. While MALDI is characterised by a thermal desorption process for low energies and a mixture of thermal desorption and ablation at higher energies, DESI is characterised by a droplet pickup mechanism. In particular, the DESI spray deposits a thin liquid layer on top of the sample of interest. This allows for analytes to desorb into the thin liquid layer. As the DESI sprayer continuously bombards the thin liquid layer progeny droplets containing analytes are generated. The size, velocity and take-off angles of these progeny droplets were thoroughly discussed in the past few pages. A large majority of these droplets swept by the nebulising gas, which carries them towards the MS inlet, where the mass to charge ratio can be measured by the mass analyser. However, this means that an ionisation step must also occur. DESI's ionisation mechanisms are discussed next.

1.2.2.2 Ionisation mechanisms in DESI

DESI spectra can be similar to ESI spectra where the same molecule appears in multiple charged states. Thus, the main ion formation mechanisms are attributed to be the same as those for ESI. One study conducted by Cooks et al. provides some experimental clues as to why this is the case [44]. In this study a survival yield (SY) method was used to probe the internal energy distributions of DESI, ESI and electrosonic spray ionisation (ESSI). By comparing the internal energy distributions for those techniques it is possible assert that the final steps of the DESI ion formation process are similar to the ionisation mechanisms seen in ESI. The SY method involves using a set of thermometer ions which fragment at a known critical energy E_0. Thermometer ions below this critical energy are observed as intact ions and thermometer ions with an internal energy greater than the critical energy are observed as fragments. Thus, the survival yield is defined as the total number of ions below the critical energy. The SY can be calculated using the following equation:

$$SY = \frac{I_M^+}{I_M^+ + I_F^+} \qquad \text{Eq. (1.21)}$$

Where I_M^+ denotes the intensity of intact molecular ions and I_F^+ is the *sum* of the intensities of fragmented ions. The distribution of internal energies $P(E)$ can be thought of as the probability of finding an ion with an internal energy E. Thus, the survival yield can also be expressed as the integral of $P(E)$ from 0 to $E = E_0$. This gives the means of obtaining $P(E)$ experimentally simply by taking the derivative of the SY curve generated from Equation 1.21. It is interesting to point out that in the case of ESI, $P(E)$ has been shown to be approximately equal to a thermal energy distribution [45]. It is also important to mention that $P(E)$ can be affected by ion-source parameters. For example, the internal energy can be raised by increasing the temperature of the MS transfer capillary [46]. Thus, in order to avoid the effects of in-source disassociation when comparing the internal energy distributions of DESI, ESI and ESSI, Cook et al. took care in making sure that the in-source conditions are the same [44]. The survival yield obtained from Equation 1.21 can then be used to compute $P(E)$ by fitting a logistic curve using the following equation:

$$SY = \frac{a}{1 + \exp\left(-\frac{b - E}{c}\right)} \qquad \text{Eq. (1.22)}$$

While it would be interesting to understand the physical significance of the parameters a, b and c the authors do not comment on what that might be. For example, dimensional analysis shows that a must be unitless, while b and c must have units of energy. The results for the SY curves and the $P(E)$ distributions are presented in the following figure.

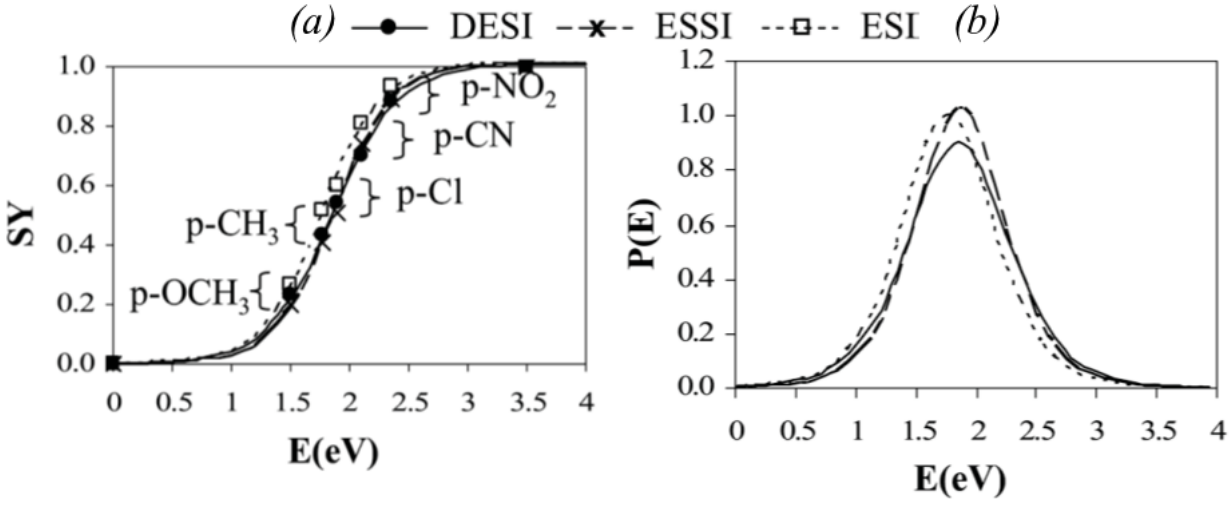


Figure 1-11. (a) – An SY curve of the thermometer ions used in the experiment. (b) – The internal energy distribution $P(E)$ of the thermometer ions used in the experiment. Figure adapted from [44].

Now that the methodology behind the SY approach for measuring the internal energies of different ionisation techniques has been discussed, the results of these measurements can be interpreted. In particular, it can be seen on Figure 11 (b) that the shape and mean values of $P(E)$ for DESI, ESI and ESSI are very similar. This result implies

two things. Firstly, the differences in droplet properties between DESI, ESI and ESSI appear to have a minimal effect on the distribution of internal energies. This is somewhat counterintuitive, as ESI and ESSI are characterised by faster moving analyte containing droplets compared to DESI. Secondly, this result suggests that the desolvation process that leads to the liberation of free ions for all three ionisation techniques can be considered the same. This is an important conclusion as ion formation in ESI has already been studied extensively. Therefore, the desolvation events that lead to ion formation in DESI can be identified as the ion evaporation model (IEM), charge residue model (CRM) and the chain ejection model (CEM). A schematic for these is presented in the following figure.

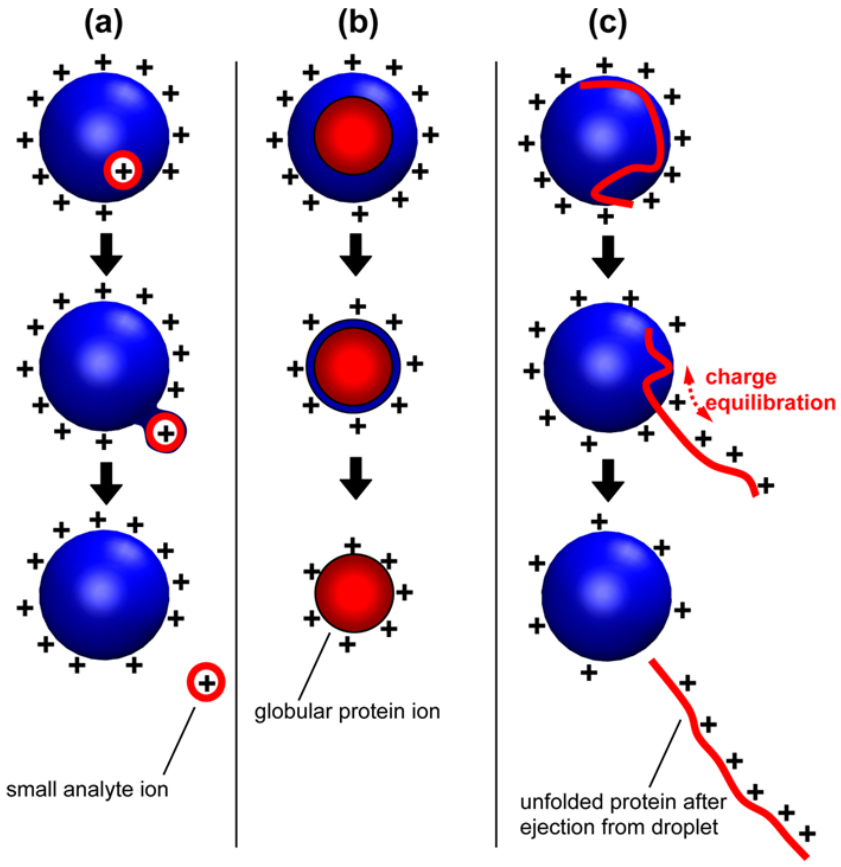


Figure 1-12. (a) – A schematic of the ion evaporation model (IEM). (b) – a schematic of the charge residue model (CRM). (c) – a schematic of the chain ejection model (CEM). Taken from [47].

The proposed mechanism for the release of low molecular weight ions into the gas phase is the IEM and a schematic can be seen in Figure 12 (a). Low molecular weight analytes can form ions while still in the liquid phase. This happens due to protonation events. When the droplet is sufficiently small (radius in the *nm* range) the electric field created by the droplet can be strong enough to expel solvated ions. This is the basic idea behind the ion evaporation model [48]. It is interesting to point out that the experimental and theoretical methods that addressed the properties of DESI progeny droplets lacked the resolution to study droplets in the *nm* range [40,42,43]. However, the fact that DESI ions exhibit a very similar internal energy to ESI ions suggests that an IEM process takes place. One very plausible

explanation on how such small droplets can be produced from the micron sized droplets seen in [40,42,43] is that droplets near the Rayleigh limit can emit smaller droplets via jet fission. An ejection rate constant k can be described using transition state theory:

$$k = \frac{k_B T}{h} \exp\left(-\frac{\Delta G^*}{k_B T}\right) \qquad \text{Eq. (1.23)}$$

Here T denotes the temperature, ΔG^* is the height of the activation energy barrier and k_B and h are Boltzmann's constant and Planck's constant respectively. Using Gauss' law one may assert that all of the charge in the droplet *must* be located at the surface of the droplet. However, it is more energetically preferable for solvated ions to remain within the droplet interior. An MD simulation by Ahadi and Konermann reveals how Gauss' law can be satisfied while an analyte ion still remains solvated [49]. In their simulation a small water droplet with a radius $\approx 2\,nm$ containing ten Na^+ analyte ions was probed.

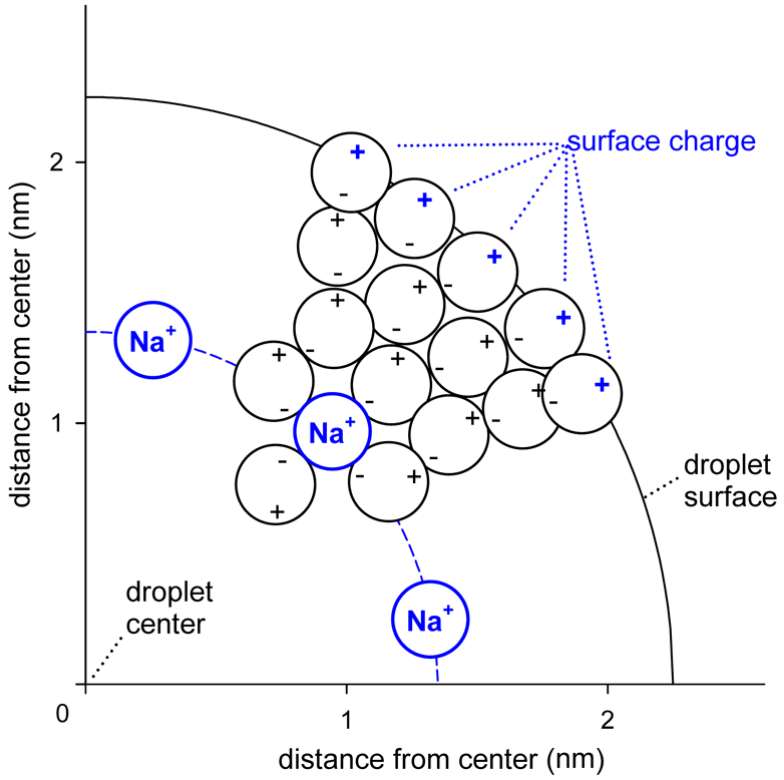


Figure 1-13. A diagram showing the reorientation of polar molecules in a small Rayleigh charged droplet. Taken from [47,49].

In particular, as can be seen in Figure 13, the presence of a Na^+analyte ion in the interior of the droplet causes the polar solvent to reorientate in such a way that the analyte charge is projected at the surface of the droplet. Thus, the analyte ion remains solvated while all the charge is still localised at the surface, as per Gauss' law. Another

interesting point of discussion is the activation energy barrier ΔG^*. Initially it was thought that once the analyte ion is expelled a mirror charge is projected, which tries to pull back the analyte, while the electric field from the droplet is trying to accelerate it farther from the droplet. Thus, an energy barrier can arise. However, another MD simulation by Ahadi and Konermann provides insight into the exact mechanism that causes this barrier [50].

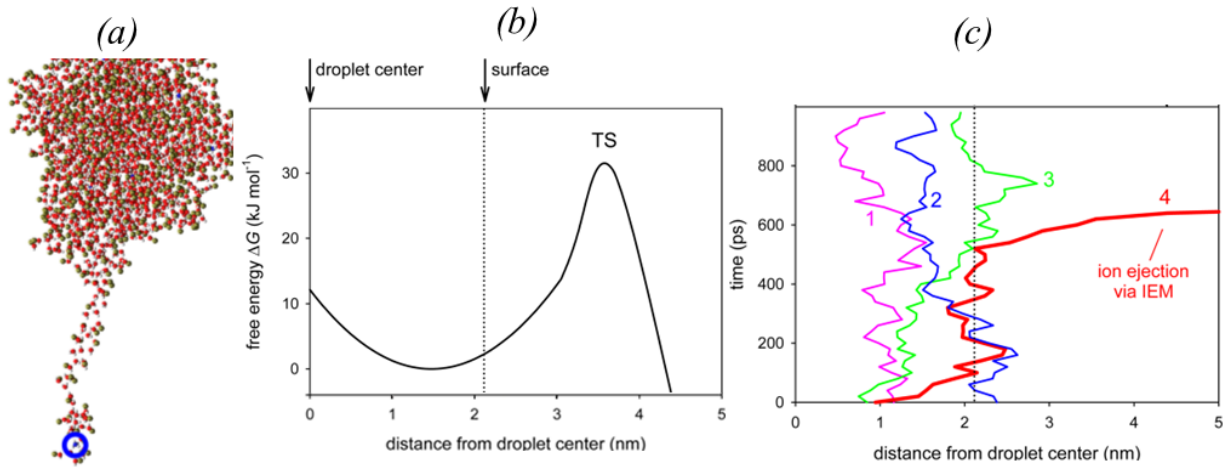


Figure 1-14. (a) – A snapshot from an ejection simulation in IEM. The analyte ion is marked with a blue circle. (b) – The free energy profile ΔG^* computed by the simulation. The transition state is denoted by TS . (c) – radial distance from the centre of the droplet for four different ions. Figure adapted from [47,50].

As it can be seen in Figure 14 (a) a bridge of solvent ions appears. This is due to adhesive/surface tension forces. Thus, the free energy barrier originates from this bridging effect. The arising free energy profile is shown in Figure 14 (b). An interesting question that can be asked is if there are no electric fields within the droplet, as per Gauss' law, what causes the analyte ion to be ejected? Depending on the polarity and the overall charge of the analyte it may prefer a different position in the droplet interior. However, the analyte will still undergo a random walk and it may eventually be pushed to the surface, where strong electric fields are present. This process is depicted in Figure 14 (c) where the path of four different ions is shown. It can be seen that ion 3 emerges at the surface but then it is pulled back by adhesive forces so that the solvation energy can be minimised. However, ion 4 successfully crosses the energy barrier and is ejected from the droplet.

While the IEM can explain the ionisation step responsible for small molecular weight it is energetically unfavourable for large species such as proteins to undergo this mechanism. Instead, the preferred ion release mechanism is the charge residue model. A schematic of the CRM is shown in Figure 12 (b). In the CRM a single globular protein is contained within a charged droplet, which is near the Rayleigh limit. As the droplet shrinks it remains close to the Rayleigh limit. At the Rayleigh limit, the number of elementary charges present in the droplet is:

$$z_R = 8\pi/e\sqrt{\epsilon_0 \gamma R^3} \qquad \text{Eq. (1.24)}$$

Where R is the droplet radius, ϵ_0 is the permittivity of free space, γ is the surface tension and e is the elementary charge. Thus, it can be seen from Equation 1.24 that for the droplet to remain near the Rayleigh limit as it is shrinking it must also expel charge. This charge expulsion can happen via an IEM of protons and small ions. The droplet completely evaporates when its radius reaches that of the globular protein. However, this also means that the globular protein has been charged by an amount of charge that can be predicted by Equation 1.24. For example, for a globular protein with a radius of $5nm$ that was contained in a water droplet, the final charge state of the protein is ≈ 44. This can be generalised in the following way: for a globular protein M the expected molecular ion observed in an ESI spectrum is $[M + z_R H]^{z_R+}$. There is ample experimental evidence that confirms the validity of this model [51–53]. The CRM is also supported by computational simulations, which confirm that the a globular protein remains trapped within the droplet interior as the droplet is evaporating[54].

It should be noted that while the CRM can predict the behaviour of folded, globular proteins quite well it does not apply to unfolded proteins. Instead, the chain ejection model is used to describe the release of molecular ions into the gas phase for unfolded proteins. A schematic of the CEM is shown in Figure 13 (c). The CEM was described in an MD simulation [54]. For an unfolded protein in a Rayleigh charged droplet the hydrophobic chains are drawn towards the surface of the droplet. Once at the protein emerges at the surface the chains that contain a charge experience a force from the strong electric fields emanating from the droplet. Thus, a sequential ejection of the protein begins.

To conclude this section, the DESI process was reviewed in depth. The strong evidence for a droplet pickup mechanism reported in literature was summarised and discussed. In particular, the velocity and size distribution of progeny droplets and their take-off angles were considered from experimental measurements [42]. Two computational simulations that seek to validate the experimental measurements were also reviewed [40,43]. Then, a report inspecting and comparing the internal energies of DESI, ESI and ESSI provided a clue that the same ionisation steps occur for all three techniques [44]. Since the mechanisms that lead to the formation of gas phase analyte ions in ESI have been studied extensively a short review of those mechanisms was then provided.

1.2.3 SIMS

A short review of Secondary Ion Mass Spectrometry will follow now. SIMS is the oldest MSI technique. It operates in ultra-high vacuum conditions, which are required for the primary ion beam to be formed. Different primary ion beams may be employed –$Ar_n^+, Bi_n^+, C_{60}^+, Cs^+, O^-, O_2^-$, etc [55]. A diagram of the SIMS process is provided in the following figure.

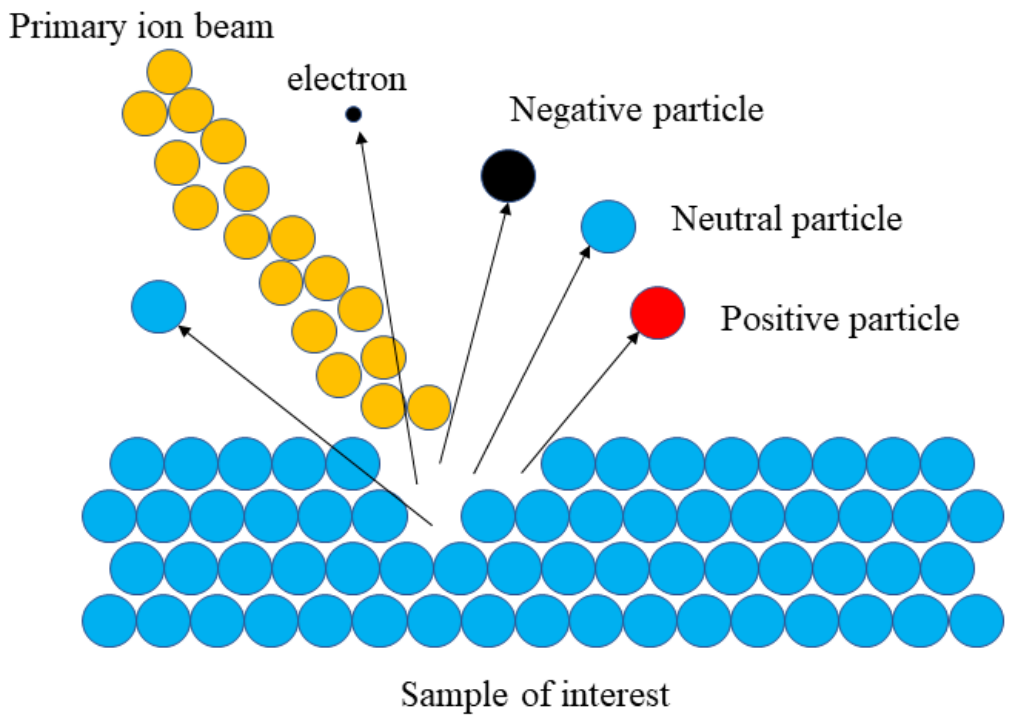


Figure 1-15. A schematic overview of the SIMS process.

As the surface is bombarded by the high energy particles that constitute the primary ion beam, secondary ions are ejected from it. This ejection is caused by the fact that the energy of the primary ions gets dissipated in a collision cascade. Neutral particles and electrons are also ejected [56]. The secondary ions can then be collected by a mass analyser where their mass to charge ratio is measured. There are some SIMS properties that need to be highlighted. The high kinetic energy of the primary ion beam often causes biomolecules to fragment. Thus SIMS spectra may not be as rich as MALDI or DESI spectra. However, the SIMS primary beam can be have a much smaller diameter than that of the laser beam used in MALDI (which is diffraction limited) or the electrospray beam used in DESI. Thus, SIMS can offer information on a smaller length scale and is capable of achieving subcellular resolution [57]. The highest resolution available in the SIMS family is offered by nanoscale SIMS (NanoSIMS), where the primary ion beam can have a diameter smaller than $30nm$ [58]. Of course, this comes at the expense of high fragmentation and only elemental or small functional groups can be detected.

Generally, SIMS a beautiful technique that is much more mature than MALDI or DESI and as such the physical processes that lead to signal formation have been studied and quantified more thoroughly. For example, there is only one MD model used to study the process of material removal in MALDI (the breathing sphere model)[9] and only one MD model used to study the generation of secondary droplets in DESI [40], but there are several MD models for SIMS[59–62]. Furthermore, the sputter yield can be predicted with an universal equation[63–66], while making a prediction of the total ion signal in MALDI and DESI remains a topic of hot debate. Spatial resolution and depth resolution have also been studied thoroughly[67–74], whereas spatial resolution remains understudied in MALDI and

DESI. As it stands, MALDI and DESI are routinely used in largescale biological studies, such as the Cancer Research Grand Challenge one [75–77]. Therefore, there is a natural need to characterise the imaging performance of MALDI and DESI MSI instruments. Thus, SIMS will not be reviewed as thoroughly as MALDI and DESI in this thesis. Nevertheless, resolution will still be measured in some SIMS modalities (NanoSIMS in particular) in Chapter 5.

1.3 Mass analysers

Now that the three main modalities used in MSI have been discussed the attention of the reader is shifted towards the actual measurement process. While the modality was concerned with generating ions, the task of the mass analyser is to measure the mass to charge ratio of those ions. The basic idea is to use electric or magnetic fields to induce some trajectory of the collected ions. Typically this trajectory depends on the mass to charge ratio and from it the mass to charge ratio can be extracted. A brief discussion of some of the most common mass analysers is provided in this section. First some basic definitions are provided. To help visualise these the following figure is provided.

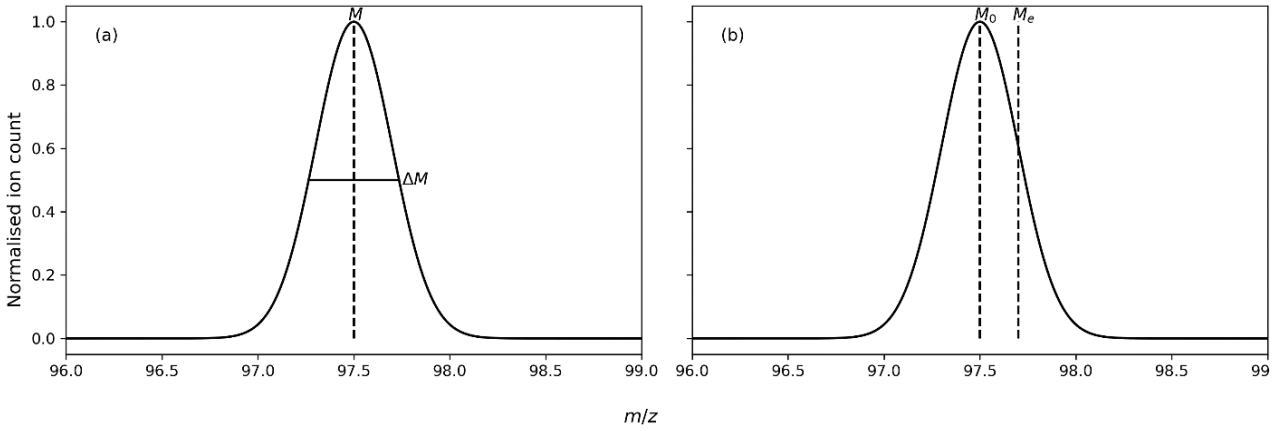


Figure 1-16. (a) – definition of mass resolution. (b) – definition of mass accuracy.

As per the recommendations of the International Union of Pure and Applied Chemistry (IUPAC) mass resolution is defined as [78]:

$$R = \frac{M}{\Delta M} \qquad \text{Eq. (1.25)}$$

Where M is the measured mass and ΔM is the fullwidth at half maximum (FWHM) of the observed peak. This is illustrated in Figure 16 (a). Another useful definition that may be used is the mass accuracy:

$$mass\ accuarcy = \frac{|M_0 - M_e|}{M_e} \qquad \text{Eq. (1.26)}$$

Here M_0 is the theoretical mass (accurate mass) and M_e is the experimentally observed mass (exact mass). Thus, the mass accuracy is the ratio of the absolute value of the difference between the accurate mass and exact mass to the exact mass. In other words, the mass accuracy is the fractional error of the observed mass. Notice that Equation 1.26 on its own is dimensionless. However, very often the mass accuracy is quoted in parts per million (*ppm*). In this case Equation 1.26 can simply be multiplied by a factor of 10^6. It should be pointed out that the Equation 1.25 is rather awkard; much more convenient would be to provide ΔM as the spectral resolution of the instrument.

1.3.1 Time of flight (ToF)

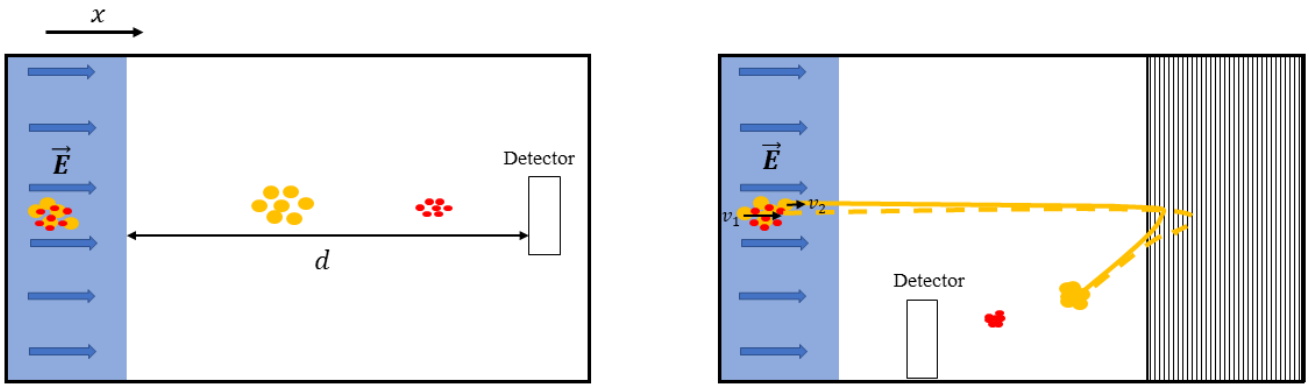


Figure 1-17. Schematic of ToF mass analyser. Left – without reflectron. Right – with reflectron.

The principle of operation of a ToF mass analyser is quite simple[79]. The mass analyser is divided in two regions – acceleration region and a drift region. The acceleration region is represented with a blue region in the diagram above. Upon entering this region ions collected from the sample experience an electric field (indicated by blue arrows). This causes them to accelerate. The force they experience is given by the Lorentz equation:

$$\vec{F} = q\left(\vec{E} + \vec{v} \times \vec{B}\right) = q\vec{E} \qquad \text{Eq. (1.27)}$$

Where q is the charge, $\vec{E}$ is the electric field and $\vec{B}$ is the magnetic field. Since there are no magnetic fields the cross product term vanishes. By definition, the electric potential energy is therefore:

$$U_E(r) = -\int_{-\infty}^{r} q\vec{E} \cdot d\vec{r}' \qquad \text{Eq. (1.28)}$$

Since everything is aligned in the x direction an the electric field may be considered constant we may drop the vector notation. The potential energy then becomes:

$$U_E = qV \qquad \text{Eq. (1.29)}$$

Where V is the voltage in the acceleration region. Once the ions are accelerated they enter the drift region. They transverse a distance d before they reach a detector. Their kinetic energy at the detector will be:

$$K_E = \frac{1}{2}mv^2 = \frac{1}{2}m\left(\frac{d}{t}\right)^2 \quad \text{Eq. (1.30)}$$

Where t is the time of arrival. Invoking the Law of conservation of energy and solving for time:

$$t = \frac{d}{\sqrt{2V}}\sqrt{m/q} \quad \text{Eq. (1.31)}$$

The time of flight is proportion to the root of the mass to charge ratio. As heavier ions (represented as yellow circles in diagram) acquire a smaller velocity, they lag behind the lighter ions (represented as red circles) and arrive at the detector later. This separation allows for ions with different mass to charge ratios to be measured.

There exists a natural spread in velocities. At a given temperature and at thermal equilibrium this is described by the well-known Maxwell-Boltzmann distribution. Therefore, there will be a spread in the kinetic energies of different ions of the same kind; this will result in a spread of time of arrivals. To deal with this a reflectron is utilised[80,81]. This is depicted on the right hand side of Figure 1-17. The reflectron region is represented by the continuous lines at the end of the drift region. The spread in velocities v_1 and v_2 is indicated by small black arrows . Their corresponding trajectories are shown with dashed and continuous line. Since v_1 will result in a higher kinetic energy after acceleration, this ion penetrates the reflectron deeper than the ion with velocity v_2. This causes them to arrive at the detector at the same time. The reflectron also increases the flight path *d* and thus it further improves the mass resolution. Generally, the mass spectrum of a ToF instrument can be simulated with the aid of an instrument response function (IRF)[82].

1.3.2 Magnetic sector

A magnetic sector relies on a magnetic field to change the trajectory of charged particles.

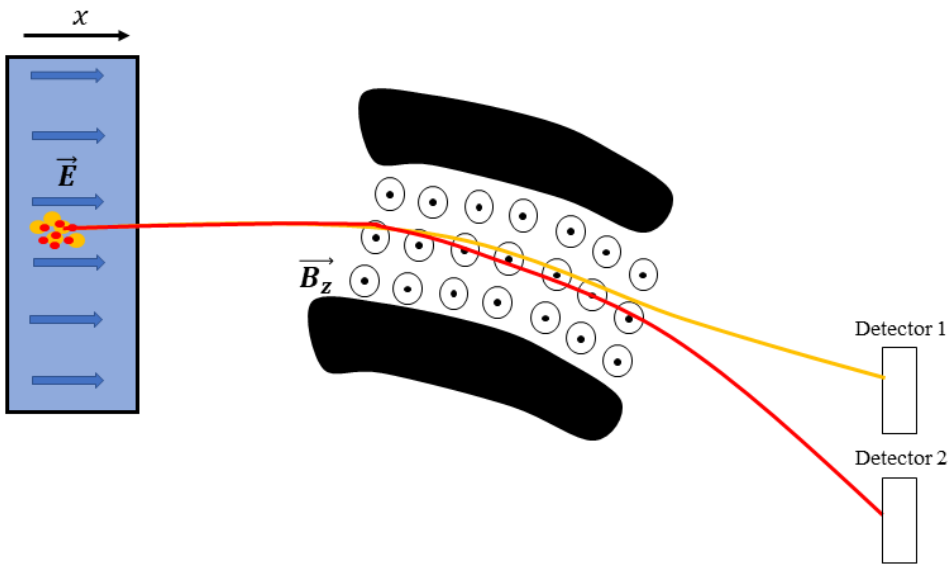


Figure 1-18. A diagram of a magnetic sector mass analyser.

Such a mass analyser typically consists of an acceleration region and deflection region. The acceleration region works in a similar principle to that of a ToF analyser. In particular, ions are accelerated through an electric field with a kinetic energy of $\frac{1}{2}mv^2 = qV$. However, once they enter the deflection region, they encounter a magnetic field; in the diagram above the magnetic field is coming out of the page as indicated by the arrowhead symbol. The ions will be deflected by the magnetic field $\overrightarrow{B_z}$. Coming back to the Lorentz equation, there is no electric field in this case and the force that acts on them is:

$$\overrightarrow{F_L} = q\left(\vec{E} + \vec{v} \times \vec{B}\right) = qvB_z \qquad \text{Eq. (1.32)}$$

Where the cross product reduces qvB_z as the velocity vector has only an x component and the magnetic field vector has only a z component. This force is balanced by the centrifugal force:

$$\overrightarrow{F_c} = \frac{mv^2}{r} \qquad \text{Eq. (1.33)}$$

Therefore, after equating the two forces one may write:

$$\frac{mv^2}{r} = qvB_z \qquad \text{Eq. (1.34)}$$

And rearranging for the mv^2 term:

$$mv^2 = qvB_z r \qquad \text{Eq. (1.35)}$$

Invoking the Law of conservation of energy again:

$$\frac{1}{2}mv^2 = qV \qquad \text{Eq. (1.36)}$$

After substituting the expression for mv^2 from Equation 1.35 and solving for m/q one obtains:

$$m/q = \frac{B_z^2 r^2}{2V} \qquad \text{Eq. (1.37)}$$

And thus the mass to charge ratio may be measured based on the deflection that a charged particle experiences in the presence of a magnetic field. Such mass analysers are not common today but are used in some MSI modalities such as NanoSIMS[58].

1.3.3 Fourier Transform Ion Cyclotron Resonance (FTICR) and Orbitrap

A type of mass analysers which obtain a mass spectrum from frequency space also exist. This is done by inducing an orbital motion with a certain frequency.

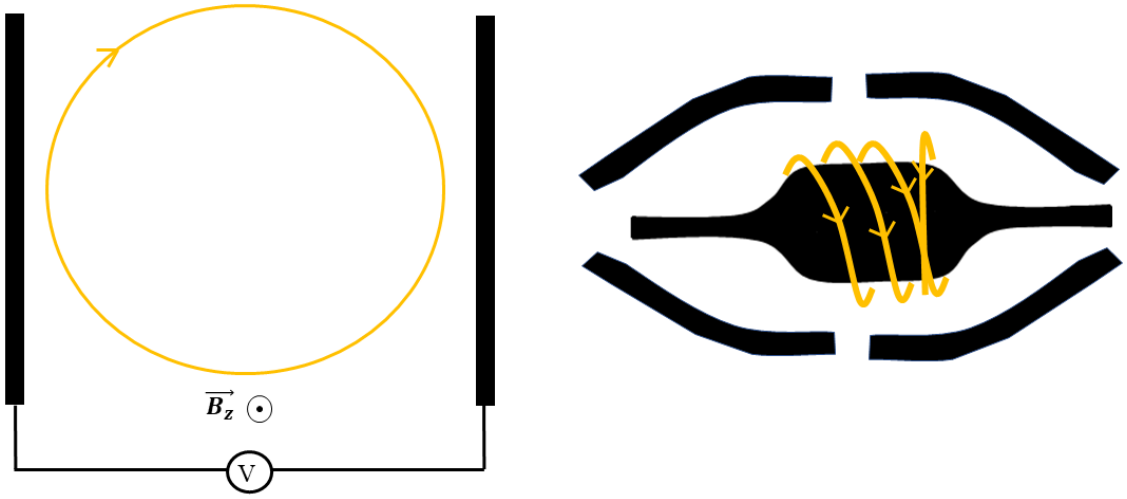


Figure 1-19 Left – a simplified schematic of an FTICR mass analyser. Right – a simplified schematic of an Orbitrap mass analyser.

Such mass analysers measure the mass to charge ratio by obtaining the Fourier transform of an image current induced by the orbital motion of ions. On the left hand side of Figure 1.19 a simplified diagram of an FTICR mass analyser[83]. A strong magnetic field causes ions to undergo a circular motion. As the ion moves close to the plates an image charge is induced in each plate. Using the Lorentz equation and balancing it against the force in uniform circular motion (Equation 1.32 and Equation 1.33) one may compute the angular frequency of such an ion $\omega_c \equiv v/r = qB_z/m$. In practice an electric field is also used to trap the ions in the axial direction and as a consequence the angular frequency is different. The picture presented here is simplified but still provides a basic idea of how the

FTICR mass analyser operates. How things change when an electric field is introduced to trap ions is not discussed here; the curious reader is referred to this wonderful summary instead[84].

On the right hand side of Figure 1-19 an Orbitrap mass analyser is shown[85–88]. It consists of a spindle-like inner electrode which attracts ions but due to their inertia they experience an orbital motion around the spindle. The frequency of back and forth motion among the spindle is dependent on the mass to charge ratio. This back and forth motion induces an image current which is the Fourier transformed to obtain a mass spectrum. Orbitraps are an incredibly elegant type of mass analysers and they are require much less space than an FTICR. While FTICR typically also needs incredibly strong magnetic fields (stronger than Earth's own magnetic field), Orbitraps operate based on electric fields alone. A characteristic of both type of mass analysers is the incredibly high mass resolution.

1.4 Noise

The topic of image noise in MSI remains largely understudied. Nevertheless, there are some brilliant efforts to study and quantify image noise. In general, the community seems to be interested in quantifying 'chemical noise'[89–91] as selecting unwanted peaks can have an impact on the downstream analysis of biological data. The term 'chemical noise' is put in quotation marks as this is not really noise but rather unwanted signals that interfere with biological signals. The actual noise may be described as variations of the signal intensity due to various processes such as an uncertainty of counting discrete particles. In fact, quantifying the variance of intensity (noise) is arguably more important than quantifying chemical noise in the context of clinical studies. As the reader shall be convinced, this limits spatial resolution and is therefore in our interest to review the possible types of noise that can arise. Since all of the information in an MSI image comes from a mass spectrum, one would expect the image noise to be directly related to the mass spectrum itself. In particular, apart from the mass analysers that measure *m/z* from the frequency domain, most mass spectrometers measure the signal intensity by using a device that counts individual particles such as an electron multiplier.



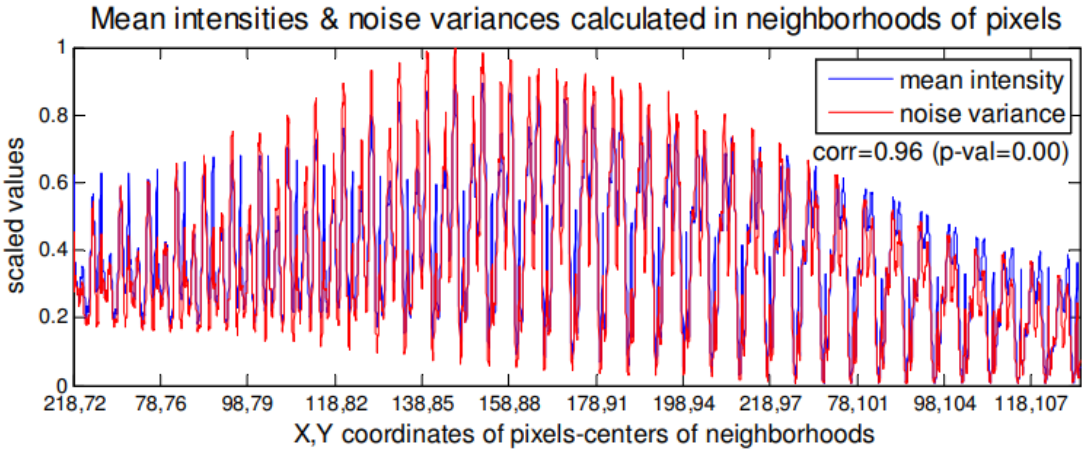
Figure 1-20. A diagram of an electron multiplier.

The electron multiplier consists of a series of dynodes that have a potential difference applied between each other[92]. When an ion strikes the first dynode secondary current is emitted and attracted towards the secondary dynode. The process repeats and the result is a cascade of electrons that greatly multiply the original signal. Let m be the average number of secondary electrons emitted when a primary charge strikes a plate. Since this is a random process, any number of secondaries from 0 to N may be emitted. Thus, the number of secondaries may be modelled as a binomial distribution. The probability that a given value of secondaries is emitted is m/N. If one keeps m constant while N is allowed to approach infinity, one would obtain the Poisson distribution[93]. There also exist other type of detectors, such as the continuous dynode electron multiplier, microchannel plates[94,95], the Daly detector[96] and the Faraday cup[97]. Studying those goes well beyond the scope of the current work, although Poisson statistics may be expected for all those. It is worth mentioning that the Faraday cup has no gain and is therefore less sensitive. To deal with this issue, the gain is often added electronically, which will result in a different noise distribution.

While one may expect Poisson noise to be a contributing factor to the overall noise (and therefore spatial resolution) in MSI, that does not mean that Poisson noise will be the dominant type of noise. In particular, it has been known for a long time that the analogue to digital converter (ADC) can introduce noise as well – thermal, quantisation and flicker noise in particular[98]. Another major source of noise introduced by electron multipliers is caused by the pulse height distribution and the fact that it can behave randomly. Those were reported previously[99] and in a more recent publication this was modelled quite beautifully where the mean value and the variance of intensities in a mass spectrum were derived from first principles[100]. The final distribution describing the expected value of the peak intensity and the variance of intensities is certainly not a Poisson distribution. What is incredibly impressive about this work is that the author has considered the instrument architecture and found a mathematical description independent of the ion optics. This behaviour also affects the distribution of mass centroids, which the author models in a subsequent paper[101]; taking the variance of a mass centroid into account when trying to identify a biomarker can be incredibly useful in biological studies. In another study that involved the noise in MALDI, the power spectrum density of the noise was studied and it was reported that $1/f$ or flicker noise was observed[102]. Thus, more evidence is amounted to the fact that Poisson noise may not be the dominant noise source in MSI. Noise has also been studied in electrospray ionisation (ESI) coupled with liquid chromatography (also known as LCMS)[103–105]. It is a well-known fact that the expected value is equal the variance for the Poisson distribution. However, the empirically measured variance was reported to be quadratic[105]. The authors of this discovery rightfully point that this is incredibly important for clinical applications. They demonstrate the importance of this by showing how estimating the noise model increases the power of t-tests. Therefore, establishing an accurate noise model is not only useful for spatial resolution but could add immense value to the application of MSI in clinical studies. As for MALDI, deviations from Poisson noise have also been reported[106]. The authors model noise as a multinomial distribution combined with Poisson noise. Admittedly, their model does not fit the data well and the authors suggest that the Gamma function could be a good candidate to fix this. Coincidentally, the gamma function also exhibits a

quadratic variance, which seems to agree with the proposed noise model for ESI[105]. Therefore, one should not be too surprised if MALDI and DESI end up deviating from the well accepted Poisson noise model.

Despite this evidence, some authors still insist that Poisson noise is the only type of noise exhibited in MSI[107–109]. While it is true that Poisson noise is a part of the noise mechanisms, there is evidence that other mechanisms may contribute to the variance of the signal[102,105,106]. Some authors even go as far as to state that their calculations confirm the hypothesis that Poisson noise is the dominant noise source[108,109]. The following figure shows their calculation:



Supplementary Figure 1. Relation between peak intensity and noise variance. Blue line: mean intensity, red line: noise variance. Both characteristics are calculated in neighborhoods of diameter of 20 pixels and scaled to [0,1]. 7,000 subsequent pixels are taken as centers of neighborhoods. High correlation (0.96) between these characteristics confirm the multiplicative nature of noise (the noise variance is linearly proportional to the peak intensity).

Figure 1-21. A misinterpretation of noise. Taken from[108].

The original figure caption is intentionally left so the reader may verify that the authors claim that their calculation reveals that noise variance is linearly proportional to the pixel intensity[108,109]. This of course implies Poisson noise. In their publications they also refer to Poisson noise as multiplicative noise. This is wrong as Poisson noise is neither multiplicative nor additive. However, it can be approximated as additive noise at sufficiently high intensities due to the fact that the Poisson distribution can be approximated by a normal distribution. Their calculation involves computing the mean and variance of the intensity within a particular region of interest (ROI). Instead of plotting the variance as a function of intensity and demonstrate that the observed relation is linear, they chose to provide the figure above as proof that variance is linear with intensity. The observant reader will notice that both variance and signal have been forcefully normalised to unity. This forces the measured correlation to be high and they report a value of 0.96. If the variance was truly linear there would be no need to normalise to unity. Thus, the authors of[108,109] have misinterpreted their results and the only thing they have demonstrated is that the noise is signal dependant

(noise correlates with intensity). That is somewhat obvious anyway, as when looking at any MSI image one would immediately notice that noise only manifests where a signal appears.

1.5 Spatial resolution

Much like noise, spatial resolution remains understudied, especially in MALDI in DESI. In fact, spatial resolution is often mistaken with the pixel size/pixel spacing[110–124]. Some authors have defined spatial resolution as the product hardware average (H.A. - average number of laser shots per pixel) and the ratio of stage velocity and laser repetition rate[121,125].

$$d = H.A.\frac{v_{stage}}{f_{rep}} \qquad \text{Eq. (1.38)}$$

Where d is the spatial resolution, v_{stage} is the stage velocity and f_{rep} is the pulsing frequency of the laser. Presented as such, this applies only to imaging systems that use a continuous stage motion. The hardware average may easily be computed if a constant repetition rate is assumed together with a pixel spacing of $p = v_{stage}\Delta t$, with Δt being the scan time spent per pixel:

$$H.A. = \int_0^{\Delta t} f_{rep}\,dt = f_{rep}\int_0^{\Delta t} dt = f_{rep}\Delta t = p\frac{f_{rep}}{v_{stage}} \qquad \text{Eq. (1.39)}$$

Upon substituting the value for the hardware average derived in Equation 1.39 in the authors' definition of spatial resolution provided by Equation 1.38 one quickly finds that the stage velocity and laser repetition rate cancel each other out and the spatial resolution is thus equated to the pixel size. Unfortunately, spatial resolution cannot be equal to the pixel size as this will violate the Shannon Sampling theorem[126]. This will be proven in Chapter 2. Other approaches to defining spatial resolution invoke the degree of homogeneity of the analyte-matrix co-crystallites and the laser ablation diameter[127–129]. However, using the laser ablation diameter as a resolution metric can also violate the Sampling theorem in scenarios where the pixel spacing is greater than the ablation diameter. In cases where the pixel spacing is smaller than the crater diameter and in the presence of strong material removal it is possible to resolve features finer than the width of the beam[130]. This mode of imaging is referred to as 'oversampling'. It shall be shown in Chapter 2 that oversampling has another meaning and this could cause a clash of terminology.

As for SIMS, the SIMS community is well aware of the fact that resolution is not equivalent to the pixel size. A convolution model is employed to describe image formation[67–69]. When the pixel spacing is smaller than the width of the sampling probe resolution has been shown to be limited by the width of the sampling probe[67,68] and therefore image resolution is limited by blur induced by the beam. The way this is typically measured is by looking at the 86-14% quantile of a step edge image. The image of a step edge is referred to as an edge spread function (ESF). It has been theoretically (assuming a Gaussian shaped beam probe) and experimentally shown that this matches the width of the sampling probe[67–69]. Thus, when oversampling in SIMS, which typically involves weak material

consumption, resolution is limited by blur induced by the width of the analytical beam. However, employing the same image formation model in MALDI, where strong material consumption is utilised, the 86-14% criterion can lead to subpixel or single pixel resolution distances[131,132]. As it shall be proven in Chapter 2, this directly contradicts the Sampling theorem[126]. This contradiction needs to be resolved and it suggests that there is something not quite right with the image formation model. A need for a unified approach for measuring spatial resolution is therefore needed and thus the entire point of this thesis[133].

Some approaches for measuring spatial resolution in MALDI recognise that spatial resolution is not equivalent to pixel size and that information can be lost due to noise. The proposed method for measuring spatial resolution involves the production of a resolution device that consists of a series of bars with decreasing widths and sitances[134,135]. There are some disadvantages. Firstly, this is a costly and time consuming way of measuring resolution. Secondly, the resolution threshold is an arbitrary number; it would be better if the resolution distance reflects the average signal strength and the average noise strength. The ratio of the average signal and the noise standard deviation is often referred to as the signal to noise ratio (SNR). A modified SNR metric coupled with a resolution device has been proposed previously[136]. Unfortunately, while this method proposes a methodology for encapsulating the noise and signal strength it does not predict any resolution numbers.

With the aid of a resolution device a modulation transfer function (MTF) can be computed[67,69,137]. This is an excellent way of characterising the signal strength as a function of spatial frequencies. It also provides a good starting point for thinking about how to measure resolution adaptively and as a function of noise and signal strengths. An effective resolution frequency is selected based on the Rose criterion[138] and the assumption that the noise is Poissonian is made in[69]. The other approach for adaptively computing spatial resolution assumes flicker noise[137]; this assumption was made without verifying that flicker noise is the dominant noise source. Flicker noise manifests in low spatial frequencies and has a reciprocal behaviour when plotted against frequency. Therefore, at high frequencies, flicker noise should not be dominant if there are other noise sources. As it stands, both of those methods[69,137] can be identified as the current best practice for measuring spatial resolution in MSI. One of those methods is also an international ISO standard[139,140].

However, it was already mentioned that quadratic variance has been reported in MALDI and ESI[105,106]. Therefore, a good resolution metric should not make assumptions of the nature of the noise or at least the given noise model should be confirmed before making that assumption. Ideally, a good resolution metric would not care about the noise model and should be able to deal with different noise models. This is what this thesis aims to offer to the field of MSI.

Finally, it was mentioned that when oversampling with strong material removal (typically utilised in MALDI), it is possible to detect features finer than the width of the beam[130]. However, when a smaller pixel spacing is used, a

smaller amount of material is also probed and therefore the average pixel intensity drops. Thus, one would expect an interplay between resolution gain due to material removal and resolution loss due to SNR weakening to exist. The adaptive methods described in[69,137] require the use of a special resolution device that is time consuming and expensive to prepare. In order to investigate the change of resolution across different pixel sizes multiple devices would have to be prepared, one for each pixel size. The resolution model proposed in this thesis will provide a simpler method for measuring spatial resolution that also does not make explicit assumptions about the nature of the noise. It will therefore be used to answer the question of interplay between resolution gain due to material removal and resolution loss due to SNR weakening. Ultimately, the characterisation of noise will also allow for this method to be extended in tissue imaging and the spatial resolution of different tissue imaging data sets acquired with different modalities will be compared.

1.6 The Rosetta project and the Cancer Grand Challenge

This work was funded by Cancer Research UK. Several different Grand Challenges have been proposed over the past few years. The particular Challenge addressed here is Challenge 5: find a way of mapping tumours at the molecular and cellular level[141]. The image formation model provided here can help bridge the gap between the physical and life sciences. Cancerous cells exhibit genetic instability and that leads to them to occupy highly heterogeneous states. This happens on a molecular level and on a morphological level[142]. An example of how cancer cells differ on a morphological level is the fact that they exhibit a depolarised cell membrane potential[143]. Cell membranes are incredibly important as they serve not only to separate a living system from the outside world but play an essential role in cell signalling[144]. Some physicists even offer the cell membrane potential as a basis for the definition of life itself using non-equilibrium thermodynamics[145]. An example of how cancerous cells differ from normal ones on a molecular level is the fact that they obtain energy through fermentation; a phenomenon known as the Warburg effect. Rapid advancements in the study of genetical changes in a cancerous cell have been made. Such changes ultimately manifest as a morphological change. However, molecular mechanisms (and thus molecular heterogeneity) have yet to be understood in more detail. The Rosetta project, as the name may suggest, aims to map the metabolic network of tumours and thus provide a better understanding of tumour heterogeneity [75–77]. This is done by establishing a multiscale, multi-omics approach that involves a wide range of MSI modalities (MALDI, DESI, SIMS). The multimodal imaging pipeline allows for correlating the molecular heterogeneity of tumours with underlying genetic alterations.

Having knowledge on whether or not certain biological features can be resolved by an MSI set up can help select the right pixel size, which in turn can save hours, if not even days of acquisition time, especially in the context of large biological studies such as the Rosetta project. MSI is a hyperspectral technique, thus MSI data sets require a large amount of hardware space for storage. Selecting the right pixel size can also minimise storage space, as recording unneeded information can be avoided. In addition, the hyperspectral nature of MSI means that an imaging

experiment can be optimised for a different set of signals. The ability to quantify the change in spatial resolution for a given MSI data set can help with imaging optimisation experiments. This can be especially useful in the context of instrument development and achieving single cell spatial resolution. Finally, MSI consists of a large family of different techniques and this work can provide the means for comparing the performance of different techniques and help select the right modality for a given task.

1.7 Thesis outline

In order to discover a methodology for spatial resolution a new image formation model will be described. This is done in Chapter 2. Chapter 2 itself may be subdivided into three parts: discretisation of continuous signals, ion flux generation and noise generation. The first part defines what pixels are and proves that the smallest resolvable feature is two pixels. The second part explains how image blur arises. The third part is concerned with how noise propagates from the mass spectrum to the image. In Chapter 3 the model is scaled to two dimensions and is used to study how resolution deteriorates due to noise and blur. A method for measuring spatial resolution is outlined. In Chapter 4 this method is tested on a real system and the resolution gain/loss due to material removal/SNR weakening is described. In Chapter 5 these methods are extended to tissue imaging.

Chapter 2 A new image formation model

2.1 Why do we need an image formation model?

Some of the main processes that lead to signal formation in MSI were reviewed thoroughly in the previous chapter. This will be used as the groundwork for the task that lies ahead – building a simple image formation model. Let us now clarify what is meant by image formation in the context of MSI. The following figure is used to help visualise our task.

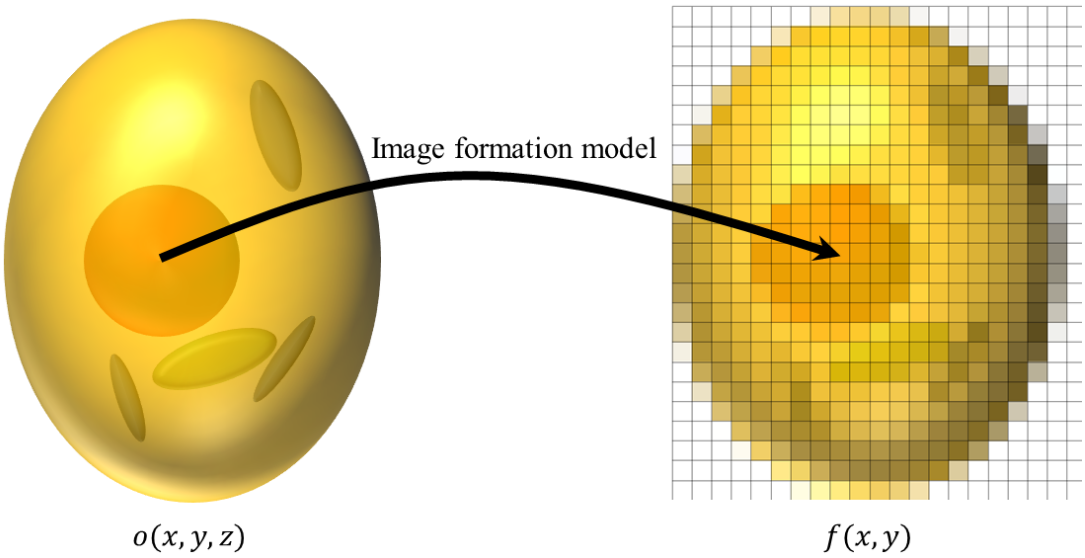


Figure 2-1 An illustration of how an image formation model works.

As depicted in Figure 2-1 image formation is the process in which the information in every point of an object $o(x, y, z)$ is mapped to a two dimensional digital imaging plane $f(x, y)$. The word digital here is important as implies that $f(x, y)$ is somehow discretized. Thus, an image formation model can be thought of as some mathematical rule (or a set of rules) that for every point in the object $o(x, y, z)$ prescribes a particular value to the image $f(x, y)$. In the context of MSI the information that is being mapped from the object to the image is the presence of a set of molecules and their relative concentrations at a particular spatial location. This allows us to immediately identify the object in an MSI experiment as the number of molecules in some region of space. Equivalently, and perhaps more conveniently, the imaging object can be equated to the density of some chemical species.

There are several reasons why establishing an image formation model is useful. Firstly, such a model can help disentangle some of the parameters that govern the resolution of an image in MSI. In particular, with the aid of

Figure 2-1, the concept of resolution can be defined easily. Spatial resolution is the smallest distance between two features in an object $o(x, y, z)$ such that those features appear separated in the image of the object $f(x, y)$. For example, it can be seen in Figure 2-1 that some of the features merge together in the discretized image $f(x, y)$, while others appear to be separated. Thus, it is obvious that having a set of mathematical rules that describe the image formation process can aid measure spatial resolution in MSI.

Secondly, there already exists a model for image formation in MSI and it has been used to measure resolution, as discussed in Chapter 1. Thus, the reader may ask what is the point of going through the trouble of constructing a new model, when a model that has been widely accepted in literature can be used. To illustrate why such a need arises consider the currently used image formation model:

$$f(x, y) = \rho(x, y) * h(x, y) \qquad \text{Eq. (2.1)}$$

Where the object has been replaced with the density of a given chemical species $\rho(x, y)$. The observed MSI image is then the convolution (represented by $*$) of the density $\rho(x, y)$ with some kernel $h(x, y)$ called the point spread function (PSF). In fact, the PSF is often equated to the shape of the analytical beam sampling over the object[67,68,139].

2.1.1 Problems with the current MSI image formation model

There are several problems with this image formation model. The first, and most obvious one is that it lacks a mathematical description of discretization. In other words, the output image is completely continuous and the mapping into individual picture elements (pixels) is not considered.

For this model to hold the output MS image would also need to be continuous. Let us now try to envision one way to achieve a continuous MS image. This would require us to return back to the old days of MS where a photographic plate was used as means of detecting the presence of a signal. Historically, this set up is referred to as a mass spectrograph[146]. If the photographic plate were to be moved simultaneously as the sampling beam, a continuous (analogue) raster image of the density of molecules would be developed on the photographic plate. However, the response of the photographic plate and the ability of the mass analyser to focus the ion beam on that photographic plate are not considered and need to be included in Equation 2.1 as separate convolution terms. Therefore at least two more response functions need to be introduced to Equation 2.1 – on for the ability of the instrument to focus the signal on the photographic plate and one for the response of the photographic plate itself.

Now, even if one were to go through the effort of setting up an analogue imaging system like the one described above just so one can justify the image formation process described by Equation 2.1, one would quickly stumble into another problem and that is that there is no time dependence. In fact, Equation 2.1 cannot take into account that the beam is moving across the surface in order to sample new points. It describes a static beam and the convolution term just describes the smearing that arises due to the fact that the beam has a finite width. Thus, it can be seen that

Equation 2.1 is much more appropriate for the description of a stigmatic mass spectrometry imaging set up (sometimes referred to as microscope MSI), rather than a microprobe imaging set up [147]. In stigmatic MSI the beam remains stationary while the ion optics allow for signals to be detected in a spatially resolved manner.

Another issue is that for an MS imaging system to detect a signal it must consume some of the molecular density at a given spatial location. Therefore, the object of the image, $\rho(x, y)$, is changing as the image is being recorded. This of course is not described by Equation 2.1 – the density always remain constant in time, despite the fact that the analytical beam is consuming it as it moves along. This leads to some practical problems when trying to measure spatial resolution. It was discussed in Chapter 1 that a standard experimental approach for measuring spatial resolution is to image a sharp step edge[67,68,131]. The blur in the image of the sharp step edge is used as a resolution metric. It has been shown in literature that this blur matches the width of the beam sampling the object in some modalities such as SIMS[67–69]. However, in other modalities, such as MALDI, this resolution metric fails and can yield resolution numbers that violate the Sampling theorem[131,132]. Thus, in order to measure resolution, a more realistic image formation model needs to be established.

In order to accomplish this task the issues addressed thus far need to be taken into account. Firstly discretization must be taken into account and a review of the Sampling theorem will be provided. This overview shall explore the applications of the Sampling theorem in MSI. Along the way some important remarks and conclusions about resolution will be made. The case of ideal sampling will be reviewed and from there the case of realistic sampling will be derived. Secondly, the path that the beam takes and the way the beam alters the object as an image of the object is being recorded will be considered. It will become apparent that the object of MSI is not the density itself but a flow of ions emanating from the surface. This quantity shall be dubbed the ion flux. This will allow to describe how image blur is generated. As the ion flux is a time signal, the discussions of discretisation will then allow for an appropriate image formation that matches the MSI process better than Equation 2.1 to be established. Finally, the origin of noise will be discussed.

2.1.2 A short discussion about picture elements (pixels)

Since discretization is one of the main issues that needs to be tackled it is worthwhile discussing some of the aspects of discretization and what digital images are. The object of MSI was identified as the spatial distribution of the density of chemical species of a particular material A single ion image depicts the spatial distribution (in terms of relative concentration) of a particular $\rho_i(x, y)$ where i is an index labelling the molecule of interest. A typical MSI data set is a collection of several thousand $\rho_i(x, y)$. While Equation 2.1 suggests that a mass spectrometer discretises the density $\rho_i(x, y)$, it is important to realise that in MSI a continuous time signal is discretised. This is the flux of particles emanating from the surface, induced by the beam/matter interaction. The desorption/ablation process was

described in Chapter 1. This quantity will be referred to as the ion flux ϕ_i. This is precisely the object that will be discretised, rather than the density itself.

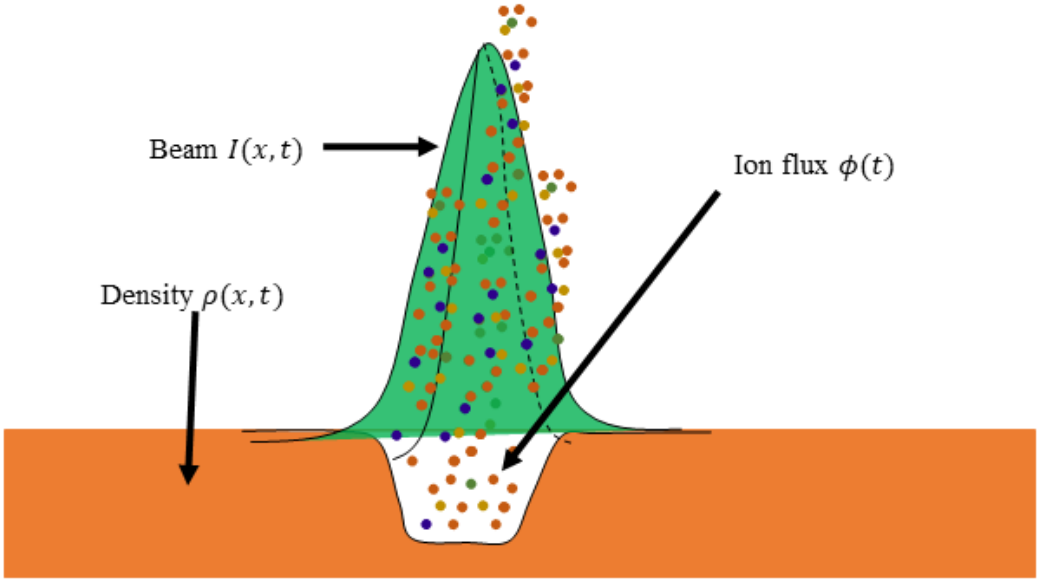


Figure 2-2. A depiction of the ion flux emanating from the surface due to the beam/matter interaction.

The total amount of particles of a given type N_i collected by the mass spectrometer between times t_1 and t_2 can be expressed as:

$$N_i = \int_{t_1}^{t_2} \phi_i(t)dt \qquad \text{Eq. (2.2)}$$

Where $\phi(t)$ is the ion flux. It is apparent that the ion flux $\phi_i(t)$ emanating from a particular spatial location is related to the density $\rho_i(x,y,t)$ at that spatial location. Equation 2.2 can be seen as the beginning of the discretisation process. This will become apparent when the case of realistic sampling is reviewed later on.

Once the mass spectrometer discretises the ion flux (which can be thought of as continuous time signal) that emanates from different spatial locations, a value for the amount of ions detected at these locations can be assigned. Specifically, this happens via the generation of a mass spectrum. Thus, a pixel is created. The author of this document would like to emphasize that pixels are not little squares. Instead, a pixel is a point sample and associating a point (which has no dimensions) with a square area is not right. However, a convenient way of displaying digital images is to do so on square grids – which in turn has caused the misconception that pixels are squares (in MSI and a lot of other imaging fields) [148]. Indeed, there are other ways of displaying a digital image – one could use dots (but then the images would not be very pretty), lines (such is the case for cathode-ray tube television.) , hexagons [149,150],

etc. However, the most natural way of representing an image is to use a reconstruction filter. The Shannon Sampling Theorem proves that a digital signal can perfectly reconstruct a continuous signal, provided that the signal has been sampled at a sufficiently high frequency and that the signal is bandlimited. While image reconstruction is widely used in other imaging fields (and is especially important in medical imaging), it has not found its place in MSI as a regular practice. Instead, no reconstruction filter is used.

2.2 Exploring the Sampling theorem in the context of Mass Spectrometry Imaging

Now a brief description of the Shannon-Nyquist sampling theorem is provided. This is needed for the derivation of the image formation model described later in this chapter. The Shannon-Nyquist sampling theorem is concerned with how continuous signals are mapped to discrete (digital) signals and how a continuous signal can be recovered (reconstructed) from its digitised version. The Sampling theorem is not proven here, only an overview is provided.

2.2.1 The case of ideal sampling

A continuous signal $f(t)$ that is also bandlimited, with a maximum frequency ν_{max}, can be reconstructed if it is sampled at a sampling frequency $\nu_s \geq 2\nu_{max}$.

First, let us clarify what a bandlimited signal means. The Fourier transform of a bandlimited signal has a bounded support. The support of a function is defined as the subset of the domain of $f(t)$ which contains the elements that are not mapped to zero. Thus, a bandlimited signal is a signal whose Fourier transform vanishes above a certain frequency ν_{max}. The Sampling theorem assures us that if such a signal is sampled at a sufficiently high frequency ($\nu_s \geq 2\nu_{max}$), the original signal can be reconstructed from its samples. Now, let us sketch out the sampling process. Ideal sampling can be represented with the aid of delta pulse train or the Shah function $\text{Ш}(t)$ (or sometimes referred to as the *comb* function):

$$\text{Ш}(t) = \sum_{n=-\infty}^{\infty} \delta(t - n\Delta t) \qquad \text{Eq. (2.3)}$$

Where Δt is the sampling interval. One can think of the sampled signal $f_{sampled}$ as the product of original continuous function $f(t)$ and the delta pulse train $\text{Ш}(t)$.

$$f_{sampled} = f(t)\text{Ш}(t) = \sum_{n=-\infty}^{\infty} f(n\Delta t)n\delta(t - n\Delta t) \qquad \text{Eq. (2.4)}$$

This procedure is demonstrated in the following figure

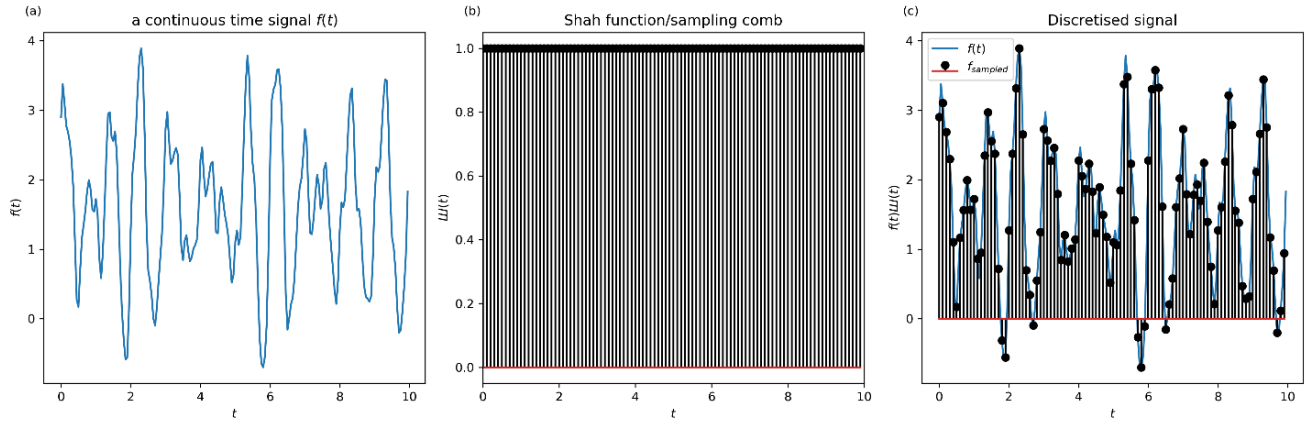


Figure 2-3 (a) – A time signal $f(t)$*. (b) – The Shah function* $\text{Ш}(t)$*. (c) – the sampled signal* $f_{sampled}$

In this picture it can be seen that the sampling interval Δt is an important quantity – if a signal is not sampled at a sufficiently small interval Δt, then faster changes in the signal will not be captured. Indeed the sampling frequency is defined as $\nu_s = 1/\Delta t$ and with the help of the Sampling theorem an appropriate sampling interval can be selected – all that needs to be done is take the Fourier transform of the object that is to be sampled and select a sampling frequency higher than $2\nu_{max}$. The Fourier transform is defined as:

$$\mathcal{F}[f(t)](\nu) = \int_{\infty}^{\infty} f(t)e^{-2\pi i\nu t}\,dt \qquad \text{Eq.(2.5)}$$

And the inverse Fourier transform:

$$\mathcal{F}^{-1}[\mathcal{F}(\nu)](t) = \int_{\infty}^{\infty} \mathcal{F}(\nu)e^{2\pi i\nu t}\,dt \qquad \text{Eq.(2.6)}$$

Now, if the Fourier transform of $f(t)$ is computed and its magnitude plotted a sampling frequency an appropriate sampling frequency can be chosen. This can be seen in the following figure:

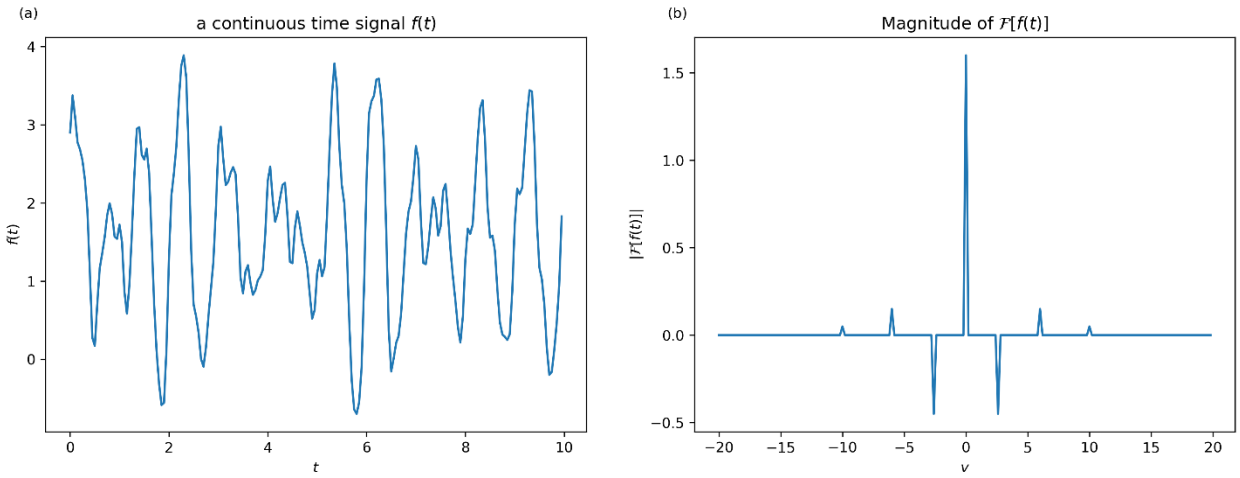


Figure 2-4 (a) – a continuous time signal $f(t)$. (b) – the magnitude of the Fourier transform of $f(t)$.

Figure 2-4 (b) shows that the spectrum of $f(t)$ consists of discrete peaks. The spectrum of a signal can also be continuous rather than discrete. It can be seen that the spectrum is zero for frequencies above $\nu_{max} = 10$. Thus, in order to be able to capture the fastest change in $f(t)$, the Sampling theorem assures us that a sampling interval of $\nu_s > 2\nu_{max} = 20$ is sufficient. This corresponds to a sampling interval of $\Delta t = 0.05s$. Finally, in order to fully explore the wonders of the Sampling theorem, it should be mentioned that the continuous signal can be recovered (reconstructed) from the discretised signal using the Shannon-Whittaker reconstruction formula:

$$f(t) = \sum_{n=-\infty}^{\infty} f_{sampled} sinc\left(\frac{t - n\Delta t}{\Delta t}\right) \qquad \text{Eq. (2.7)}$$

Where here $sinc\left(\frac{t-n\Delta t}{\Delta t}\right)$ is an idealised reconstruction filter that is being weighted by the samples of $f(t)$. To illustrate this process the following figure is provided:

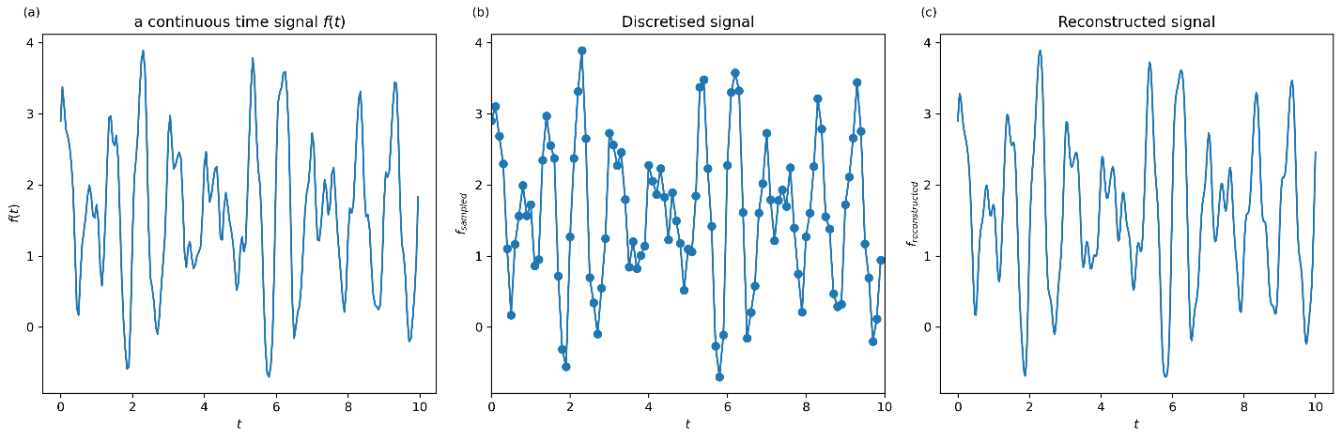


Figure 2-5 (a) – a continuous time signal $f(t)$. (b) – the sampled signal $f_{sampled}$. (c) – the reconstructed signal $f_{sampled}$.

As shown in Figure 2-5 (b) and (c) the discretised signal can be interpolated in order to reconstruct the original continuous signal seen in Figure 2-5 (a). While the *sinc* filter is an idealised filter that assumes a signal with an infinite domain, other reconstruction filters that mitigate this assumption can be used such as the Lanczos filter or the Mitchell filter. As to why pixels should not be thought of as squares but instead as points – the answer can be seen in Figure 2-5 (b), where the digitized signal is shown. Using a box filter to resample the digital image into little squares is a valid depiction of the signal, but a lot less accurate than using one of the more sophisticated filters, such as the *sinc* filter shown in Figure 2-5 (c). These filters could have an important experimental application, especially when trying to upscale an MSI image to the sampling frequency of other higher resolution imaging methods, such as microscopy. For example, when trying to register an MSI image with a higher resolution microscopy image, one would need to either downsample the higher resolution image to match the sampling frequency of the MSI image, or upsample the MSI image to match the sampling frequency of the microscopy image.

2.2.2 The Nyquist frequency

Another important concept that will be used when establishing a procedure for measuring spatial resolution is the Nyquist frequency. Given a sampling rate ν_s the Nyquist frequency ν_N is defined as:

$$\nu_N = \frac{1}{2}\nu_s \qquad \text{Eq. (2.8)}$$

It has a particularly important meaning – it gives us the highest available frequency component that can captured during a sampling process. This is the highest frequency that a measurement at a sampling rate ν_s will preserve. It corresponds to an interval $2/\nu_s$ – this is the shortest duration that one can use to record a change in a signal. If the signal that is sampled has a bandlimiting frequency ν_{max} smaller than the Nyquist frequency ν_N the discretised signal will successfully capture all of the frequency content of the original signal. On the other hand, all information above the Nyquist frequency is lost. Thus, if the original signal has a bandlimiting frequency ν_{max} greater than the

Nyquist frequency ν_N the resultant discretised signal will be distorted. This distortion is referred to as undersampling or aliasing.

2.2.3 Oversampling vs Undersampling (aliasing)

A short discussion on what happens when the sampling frequency is not sufficiently high follows. If ν_s does not satisfy $\nu_s \geq 2\nu_{max}$ aliasing occurs. This is equivalent to $\nu_N > \nu_{max}$. In other words, if the Nyquist frequency of the image is smaller than the bandlimiting frequency, the recorded image will be aliased (undersampled). It was discussed that frequencies higher than ν_N are going to be missed out when sampling. Even worse, these frequencies get mapped to lower frequencies – hence the term aliasing. Thus, the undersampled image will be distorted as the high frequency content will get mapped to low frequency content. It is important to distinguish what undersampling and oversampling means in the context of information theory and in the context of MSI.

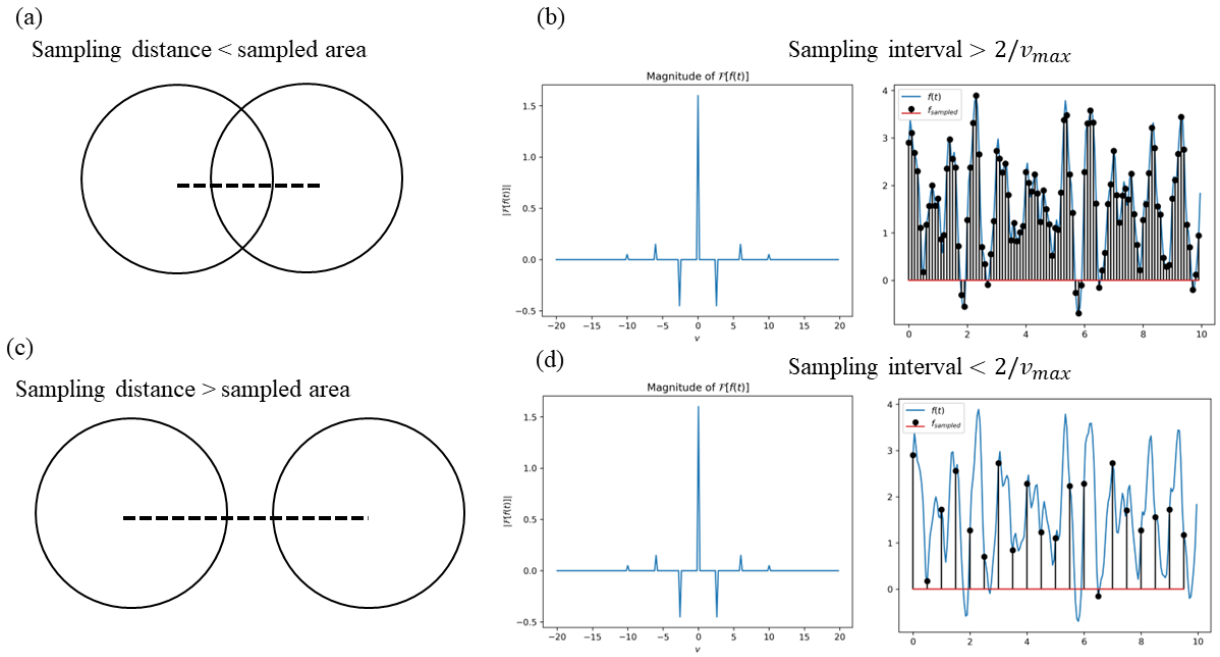


Figure 2-6. (a) – oversampling in the context of MSI. (b) – oversampling in the context of information theory. (c) – undersampling in the context of MSI. (d) – undersampling in the context of information theory.

In MSI, an image is said be to oversampled if the sampling distance (also referred to as pixel size*) is smaller than the sampled area. This scenario is depicted in Figure 2-6 (a). On the other hand, undersampling in the context of MSI is said to arise when the sampling distance is greater than the pixel area, which is depicted in Figure 2-6 (c).

*Pixel size is not a good term. Instead sampling interval, sampling distance or pixel pitch are more appropriate. However, the term is used very often in MSI. In this section it is important to understand that a pixel cannot have any size a pixel is only a point sample (see Figure 2-3). Further on in this document the author may refer to the sampling interval as pixel size and the reader is invited to think of pixels as points instead of little squares.

From the point of view of information theory oversampling is defined in situations where the sampling interval corresponds to a Nyquist frequency greater than the bandlimiting frequency v_{max} (Figure 2-6 (b)). Undersampling occurs when the sampling interval has a Nyquist frequency smaller than v_{max} (Figure 2-6 (d)). The sampling interval in Figure 2-6 (b) satisfies the Sampling theorem and in Figure 2-6 (d) it does not. It is really important to distinguish between the two as they can imply completely different things. An illustration of this clash of terminology will be provided shortly. From now on, in order to avoid confusion, these sampling regimes will be referred to by their full names. The definitions of oversampling and undersampling from the point of view of information theory provide more information about the discretized signal as they consider whether or not the Sampling theorem has been obeyed. Those definitions take into account the object of the image and the sampling distance of the image (pixel size), while the MSI definitions are only concerned with the sampling distance. Thus, a situation can arise where the sampling distance is not sufficiently small to satisfy the Sampling theorem (and hence it will not capture all of the high frequency content of the object) but still be smaller than the sampled area. In such instances the resulting image will be said to be oversampled from the point of view of MSI but undersampled from the point of view of information theory. In fact this happens quite often in MALDI where complete material removal is used to detect features finer than the width of the beam. For example, in the case of a tissue imaging experiment, one might expect the highest frequency content to correspond to the changes of density between individual cells. If $\bar{d}$ denotes the average cell diameter and one is interested in resolving the change in the distribution of molecules between two cells, one would assert that this change in signal corresponds to $2\bar{d}$. Therefore, the Sampling theorem suggests that a sampling distance of $2\,\bar{d}/2$ should be chosen. For a typical animal cell $\bar{d} \approx 10\ \mu m$. Thus, the change in signal between two cells would be $\approx 20\ \mu m$ and according to the Sampling theorem, a sampling interval smaller than $10\ \mu m$ should be chosen – any sampling interval (also referred to as pixel size) larger than that would give rise to an undersampled (aliased) image. However, from the point of view of MSI undersampling will occur when the sampling interval is larger than the width of the sampled area. For example, if in a MALDI experiment a crater has a diameter of $50\ \mu m$ all sampling intervals smaller than that would be said to be oversampled from the point of view of MSI. However, if a tissue section is being imaged and the average cell diameter is $\bar{d} \approx 10\ \mu m$, then all sampling intervals larger than $10\ \mu m$ will be undersampled from the point of view of information theory. Thus, if a sampling interval of $20\ \mu m$ is chosen someone from an MSI background would assert that the image is oversampled, while someone from an information theory background would argue that the image is undersampled. Only at sampling intervals smaller than $10\ \mu m$ would both practitioners agree that the image is oversampled and only at sampling intervals larger than $50\ \mu m$ would both practitioners agree that the image is undersampled.

This clash of terminology is unfortunate and it is important to be aware of it. When the Nyquist frequency corresponds to a frequency smaller than the bandlimiting frequency the discretised signal will be aliased (Figure 2-

6 (d)). Aliasing means that higher frequencies get mapped to lower frequencies. In the context of imaging this gives rise to spurious artifacts and jagged images.

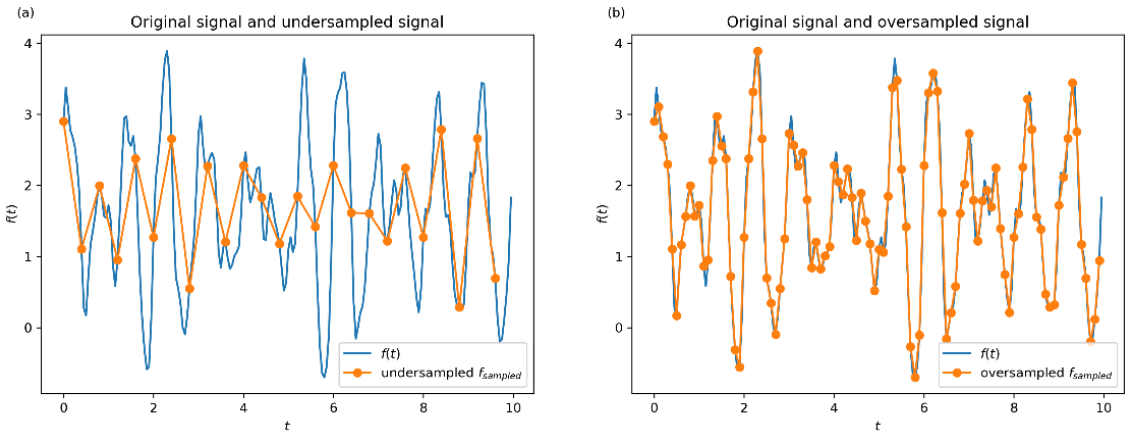


Figure 2-7. (a) – Original signal (blue) compared to the undersampled (from the point of view of information theory) signal (orange). Sampled at $\Delta t = 1s$. (b) – Original signal (blue) compared to the oversampled (from the point of view of information theory) signal (orange).

Thus, an undersampled image from the point of view of information theory will contain spurious artifacts and jagged edges. This can be seen on Figure 2-7 (a), where spurious features appear that are not present in the original signal. Because the Sampling theorem has not been satisfied, perfectly recovering the original signal would also be impossible. On the other hand, an oversampled signal is displayed in Figure 2-7 (b) where the higher frequency content of the original signal captured. This is why it is important to distinguish between the different terminologies.

2.2.4 Some important remarks about resolution

A point has now been reached where an important realisation can be made. One might ask what does sampling a signal in time have to do with microprobe MSI? Well, this is precisely how a microprobe MSI image is generated. Upon realising that spatial sampling occurs at equidistant intervals created by a moving stage with velocity v_{stage} and a mass spectrometer sampling over time with a sampling interval of Δt some very important remarks can be made. The pixel size in an MSI experiment is determined by:

$$\Delta p = v_{stage}\Delta t \qquad \text{Eq. (2.9)}$$

Where Δp is the pixel size and v_{stage} and Δt are the stage velocity and the mass spectrometer scan time respectively and the sampling frequency is $\nu_s = 1/\Delta t$. The first important remark related to image resolution to be made is that, as per the Sampling theorem and the definition of the Nyquist frequency, the smallest resolvable distance in an MSI image will be related to the highest available image frequency. This distance is given by $(2/\nu_s)$. Thus, the smallest resolvable distance is simply.

$$v_{stage}(2/\nu_s) = 2v_{stage}\Delta t = 2\Delta p \qquad \text{Eq. (2.10)}$$

In other words, no feature that is part of the object that is smaller than twice the pixel size will ever be captured in the image. Thus, under idealised conditions the highest achievable resolution is just twice the pixel size. While this statement sounds intuitive here a formal mathematical treatment of the sampling process has been used to arrive at this conclusion. Therefore, the common misinterpretation that resolution and pixel size are equivalent[110,111,120–124,112–119] has been proven wrong.

The second remark that can be made that relates to resolution is slightly more subtle and it has to do with what the resolution of the image would be when the conditions are not idealised. In particular, one would expect that the finite width of the beam and the stage motion can introduce some amount of image blur. This implies that two features belonging to the object can be blurred into a single feature in the image of the object. For this to be possible this blurring parameter must be greater than $2\Delta p$. In order to explain how blur is generated consider oversampling from the point of view of MSI (shown in Figure 2-6 (a)). Intuitively one would expect the amount of blur to depend on how much material is removed. For example, if a small portion of the density is removed at a given spatial location, subsequent scans would still pick up a signal from previous pixels resulting in a blurrier image. The scenario described here corresponds to a typical SIMS experiment. Therefore it can be expected that the resolution of the image in this case would be limited by blur and not $2\Delta p$. As discussed in Chapter 1 a standard experimental approach used to measure blur is to image a sharp step edge. In fact, in MSI modalities that do not fully remove material when oversampling* it has been shown that the experimentally measured blur obtained from the edge image corresponds to the width of the sampling probe. Consequently, in such a scenario resolution is said to be limited by the width of the sampling probe. This is a well-established resolution metric that has been shown to work and has been used as the standard way of measuring resolution in some MSI modalities.

On the other hand, if all of the material is removed at a particular spatial location, subsequent scans will not pick up a signal from previous pixels when oversampling†. Therefore, image blur will be minimised. The scenario described here corresponds to a typical MALDI experiment. Because of this it is possible to detect features finer than the width of the beam. In this situation, when the standard edge method for measuring blur is applied, the blurring parameter will be smaller than $2\Delta p$. In this scenario resolution is not limited by the width of the beam and blurring parameter smaller than $2\Delta p$ is non-physical. Consequently, resolution cannot be measured using this method. At this point, because the measured image blur is smaller than $2\Delta p$, one might be tempted to say that the resolution in such a scenario would simply be $2\Delta p$. This would be completely true if two conditions are satisfied – there is no aliasing and no noise.

* In this paragraph oversampling from the point of view of MSI is considered.
† Same in this paragraph.

Earlier on it was explained why aliasing is problematic. In the context of tissue imaging when complete material removal is used to oversample (from the point of view of MSI), unless a pixel size smaller than $10\ \mu m$ is used, the obtained image would still be undersampled (from the point of view of information theory). Therefore the image would contain spurious features/artifacts. These should be considered when estimating resolution because they will not be faithful representations of the original object. If the spectrum of the ground truth object is known one can calculate the aliased frequencies using the following equation:

$$\nu_a = |m2\nu_N - \nu_s| \qquad \text{Eq. (2.11)}$$

Where ν_a is the aliased frequency, ν_N is the Nyquist frequency, ν_s is the sampling frequency and m is an integer such that $\nu_a < \nu_N$. While this equation is applied for a single frequency it can be extended to multiple frequencies. For example, consider a scenario where the density of a given molecule is constant over the whole cell. Also, assume this density alternates between neighbouring cells, as depicted in the following figure

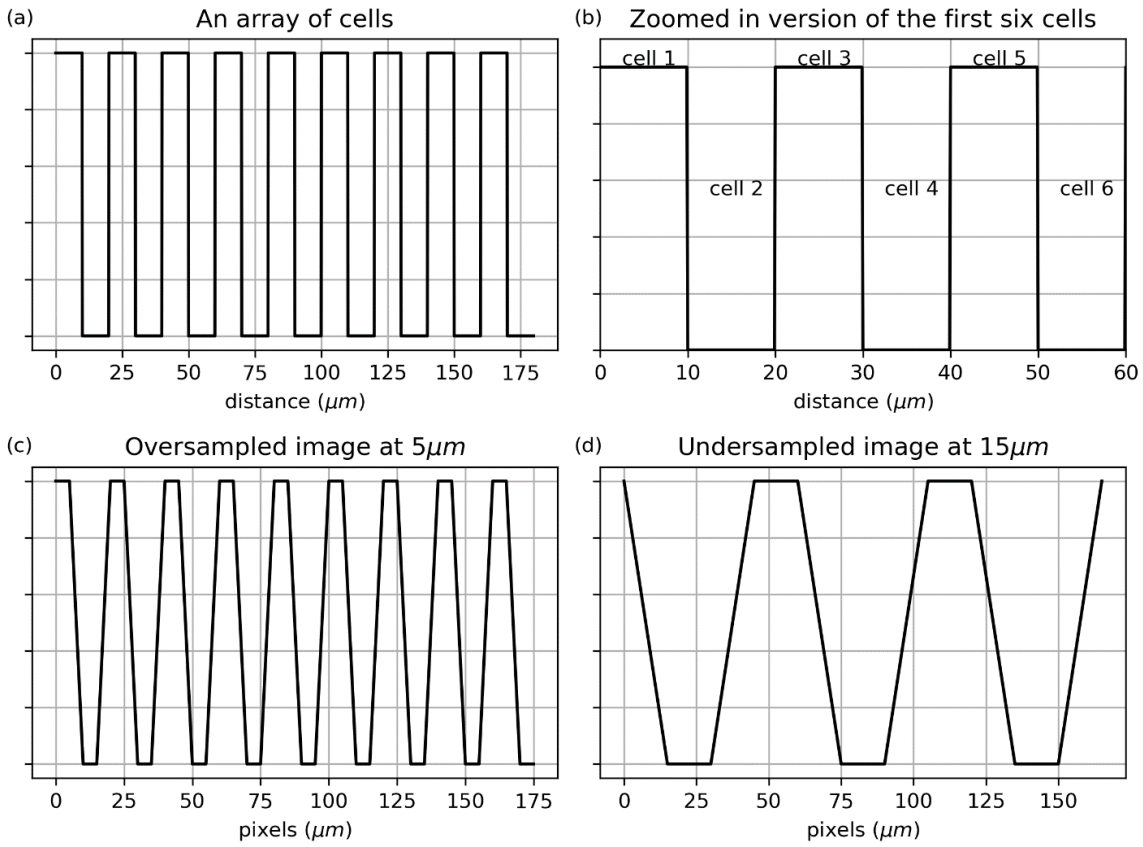


Figure 2-8 (a) – An array of 18 cells. The density of a particular molecule is alternating between neighbouring cells. (b) – A zoomed in version showing the first six cells. (c) – An oversampled image with a pixel size of $5\ \mu m$. *(d) – An undersampled image with a pixel of* $15\ \mu m$.

For simplicity, let us assume that the cells all have the same diameter $\bar{d} = 10\ \mu m$. This idealised scenario is shown in Figure 2-8 (a) and (b). It is well known that the pulse wave used to represent the molecular density can be written as a Fourier series:

$$\rho(x) = C_0 + \frac{4}{\pi} \sum_{i=1,3,5\ldots}^{\infty} \frac{1}{n} \sin\left(\frac{n\pi x}{\bar{d}}\right) \qquad \text{Eq. (2.12)}$$

Equation 2.12 reveals that $\rho(x)$ is not bandlimited in this case – no matter what sampling interval is chosen, there will always be higher frequency components that will be missed out. Equation 2.11 can be applied in order to calculate the aliased components. If a pixel size of 5 µm is chosen, equation 2.11 reveals that all frequencies above the Nyquist frequency will get mapped to the fundamental $\sin\left(\frac{\pi x}{\bar{d}}\right)$. Thus, the image of the cell array can be considered free of distortions and referred to as oversampled, as the Sampling theorem has been (somewhat) satisfied. This can be seen in Figure 2-8 (c) where all 18 cells can be resolved. On the other hand, if a sampling interval of 15 µm is chosen applying Equation 2.11 shows that all of the frequencies in $\rho(x)$ will be mapped to an alias of $0.01666\ldots$. This aliased frequency corresponds to a distance of $60\ \mu m$, or four pixels. This can be seen in Figure 2-8 (d), where a new structure with this frequency arises. Despite the fact that a pixel larger than the smallest change was chosen (15 µm pixel size, 10 µm change in density between cells), the output image appears to show well resolved features with the size of $60\ \mu m$. Thus, even though when blur is minimised because of material removal one might be tempted to assume resolution is $2\Delta p$, one also needs to consider aliasing, as those features will be larger than $2\Delta p$. This is perfectly demonstrated in Figure 2-8 (d).

Unfortunately, the real $\rho(x)$ in a tissue imaging experiment is not known. Therefore, there is nothing one can do in order to put a limit on the size of aliased features in a real tissue imaging experiment. The only thing one can do is to acknowledge that for pixel sizes greater than the average cell diameter, when oversampling from the point of view of MSI, there will be aliasing, despite our perfect resolution limit of $2\Delta p$. The other limiting factor that will prevent a perfect resolution of $2\Delta p$, as mentioned earlier is noise. Luckily, noise can be modelled from empirical observations and resolution can be constrained as a function of noise. Later on it will be shown how our ability to distinguish features deteriorates in an image corrupted by noise and we will derive a resolution metric based on this. In fact, our resolution metric will consider blur, discretization (smallest limit $2\Delta p$) and noise.

2.2.5 Realistic sampling

It was already established that a mass spectrometer is sampling a flux of ions emanating from the surface at different times $m\Delta t$, where Δt is the sampling interval. This allowed for to use the Sampling theorem to arrive at some important conclusions about resolution and the nature of MSI. These include the size of the smallest resolvable features in an image, aliasing and reconstruction was also mentioned. However, when arriving at these conclusions a sampling comb $Ш(t)$ that was constructed with the aid of delta functions was used. This implies that the mass

spectrometer samples the signal with infinitesimal quickness. In practice this is impossible as how quickly the mass spectrometer samples is limited by physical factors. The ratio of the time over which the mass spectrometer is actively collecting information and the overall time scan is known as the duty cycle. For example, if one second is needed to produce a spectrum and the scan time is two seconds, then the duty cycle is 0.5 (or 50%). This concept is further elaborated on in the following figure:

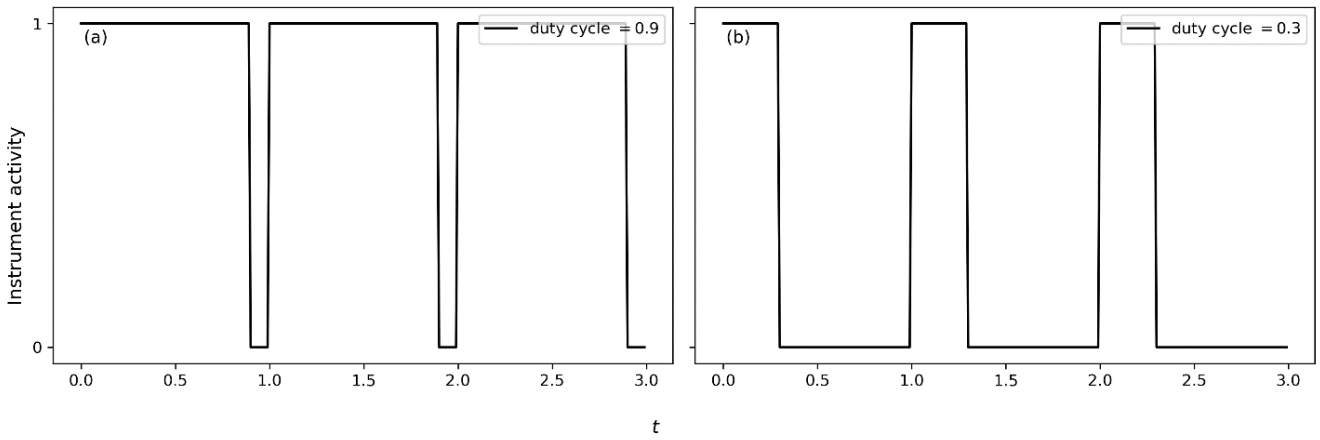


Figure 2-9. (a) – duty cycle of 0.9 with a scan time of one second. (b) – duty cycle of 0.3 with a scan time of one second.

The y axis on Figure 2-9 shows the instrument activity, where one denotes that the instrument is active and collecting data and zero denotes that the instrument is inactive, and the x axis shows time. It is clear that the idealized sampling used earlier on does not match the sampling process described here as a delta function has an infinitesimal width (for a delta function the duty cycle would be approaching zero). Thus the sampling comb needs to be adapted to a more realistic one – instead of a series of delta functions one can think of a it as a series of pulses over which the instrument is actively sampling the data. As mentioned earlier, the MS samples a flux of ions in time. The flux of ions coming off the surface can be denoted with $\phi(t)$ and a single sampling event can be described with a rectangle function $rect\left(\frac{t-m\Delta t_s}{t_a}\right)$ where m is the m^{th} measurement, Δt_s is the scan time (or sampling interval) and t_a is the time over which the mass spectrometer is actively collecting data. Thus, the duty cycle is $D = t_a/\Delta t_s$. The signal in the m^{th} measurement can be written down as:

$$\phi_m = \int_{-\infty}^{\infty} \phi(t)\, rect\left(\frac{t - m\Delta t_s}{D\Delta t_s}\right) dt \qquad \text{Eq. (2.13)}$$

More conveniently, a new variable $\tau = t/(D\Delta t_s)$ can be introduced. Thus, one can write down ϕ_m as

$$\phi_m = D\Delta t_s \int_{-\infty}^{\infty} \phi(\tau) rect\left(\tau - \frac{m}{D}\right) d\tau \qquad \text{Eq. (2.14)}$$

Which is a convolution with respect to the sampling function $rect\left(\tau - \frac{m}{D}\right)$:

$$\phi_m = D\Delta t_s \phi(\tau) * rect\left(\tau - \frac{m}{D}\right) \qquad \text{Eq. (2.15)}$$

As a whole, the realistically sampled signal $\phi_{sampled}$ can be written as a multiplication of the continuous $\phi(t)$ and a impulse train constructed of $rect$ functions instead of delta functions. Let this realistic impulse train be written as $p(\tau)$

$$p(\tau) = \sum_{n=\infty}^{\infty} rect\left(\tau - \frac{n}{D}\right) \qquad \text{Eq. (2.16)}$$

Then, the realistically sampled signal can be written as:

$$\phi_{sampled} = \phi(\tau)p(\tau) = \sum_{m=\infty}^{\infty} \phi(\tau)\, rect\left(\tau - \frac{m}{D}\right) = rect\left(\tau - \frac{n}{D}\right) * \sum_{n=\infty}^{\infty} \phi(\tau)\, Ш(\tau) \qquad \text{Eq. (2.17)}$$

And finally, recognizing that $\sum_{n=\infty}^{\infty} \phi(\tau)\, Ш(\tau)$ is just the idealized sampled signal discussed previously:

$$\phi_{sampled} = \phi_{ideal} * rect\left(\tau - \frac{m}{D}\right) \qquad \text{Eq. (2.18)}$$

Where ϕ_{ideal} is the idealized sampled signal using delta functions. Thus, it can be seen that the effect of realistic sampling will have the effects of 'blurring' the time signal $\phi(\tau)$. In particular, since the integration window increases for a high duty cycle measurement, the measured signal will have a higher intensity. For a perfect duty cycle of 1 all of the ions that left the surface during the experiment will be captured. While noise has not been discussed yet, a higher intensity measurement is less corrupted by noise. An additional benefit of a higher duty cycle measurement is that the $rect\left(\tau - \frac{m}{D}\right)$ function can act as a antialiasing filter. On the other hand a low duty cycle measurement will miss ions that leave the surface while the instrument is not actively sampling. More importantly, it was just demonstrated that realistic sampling can be thought of as idealized sampling convolved by an appropriate sampling window $rect\left(\tau - \frac{n}{D}\right)$. This implies that all of the key notes about resolution and digitization performed by a mass spectrometer in the case of ideal sampling still hold in the case of realistic sampling. Roughly speaking, a third of the image formation model has now been derived. The other two thirds consist in establishing an equation for the ion flux $\phi(t)$ and establishing a noise model. However, even with this work done one is capable of arriving at important statements about resolution, aliasing and other phenomena related

to the digitization of a continuous time signal. In the next section, the model will be further advance by introducing an equation for $\phi(t)$.

2.3 Deriving an image formation model

It is peculiar that image blur can be used to measure resolution for SIMS but can completely fail and yield non-physical answers for MALDI. However, this apparent discrepancy is what this piece of work resolves. On a more fundamental level, this success/failure is a consequence of the image formation model described by Equation 2.1. Now, an image formation model will derived for the purpose of measuring spatial resolution.

As described earlier, in order to amend the image formation model one needs to consider how the object of the image changes because of the beam interaction over time and the discretization of the signal. It was already discussed that a mass spectrometer samples an ion flux that emanates from the surface over time and described some basic properties of the sampling process in the previous chapter. Now considerations are to be made of how this ion flux is generated due to the beam/matter interaction. This will provide a notion of how image blur is generated.

2.3.1 Simplifying assumptions: continuous raster mode

Let $\rho(x,t)$ be a one dimensional density of a given molecule at a time t. The initial density can be described as $\rho(x,0) = \rho_0(x)$. In Chapter 1 the difference between absorption and ablation was clarified[6–9,14,15]. According to the literature discussed in Chapter 1, in the case of MALDI lower beam fluences are well described by thermal desorption and ablation is minimal[6,7,11,14]. Inspiration is drawn from this fact. Let us assume that the probability for a molecule to be thermally desorbed from the surface is proportional to the beam intensity at that point (and not ρ), with a proportionality constant k. Furthermore, let us assume that the beam $I(x,t)$ moves with a constant velocity v_{stage} (such is the case in a real MSI experiment). Thus, $I(x,t) = I(x - v_{st}t)$. These assumptions can be written down as (see Figure 2-2 for an intuitive description):

$$\frac{\partial \rho(x,t)}{\partial t} = -kI(x - vt)\rho(x,t) \qquad \text{Eq. (2.19)}$$

Assuming a Gaussian beam:

$$I(x,t) = \frac{I_0}{\sqrt{2\pi\sigma^2}} \exp\left(-\frac{(x - v_{st}t)^2}{2\sigma^2}\right) \qquad \text{Eq. (2.20)}$$

Then, Equation 2.19 can be solved easily:

$$\rho(x,t) = \rho_0(x)\exp\left(-\frac{kI_0}{2v_{st}}\left[erf\left(\frac{x}{\sigma\sqrt{2}}\right) - erf\left(\frac{x - v_{st}t}{\sigma\sqrt{2}}\right)\right]\right) \quad \text{Eq. (2.21)}$$

With equation 2.19 one is able to describe a simple beam/density interaction, given that some assumptions about the shape of the beam and the desorption process were made. In an MSI experiment, the mass spectrometer will sample the ion flux $\phi(t)$ that emanates from the surface at the location of the beam and at time t. This ion flux $\phi(t)$ is created by the change of density induced by the beam/material interaction. A simple formula for the change in density was established with Equation 2.19. The ion flux per unit time emanating from the surface is:

$$\phi(t) = -\frac{\partial}{\partial t}\gamma \int_{-\infty}^{\infty} \rho(x,t)dx \quad \text{Eq. (2.22)}$$

Where here the ionisation coefficient γ discussed in Chapter 1 is now included[16,17,20,21,23,25,28,32,47]. Depending on which ionisation model one subscribes to, one can include an appropriate γ. The task at hand is to measure spatial resolution and therefore in the simulations later on γ will be set to unity. To proceed with the computation, assume that γ is a constant over time and space. This allows us to propagate the derivative operator inside the integral:

$$\phi(t) = -\gamma \int_{-\infty}^{\infty} \frac{\partial}{\partial t}\rho(x,t)dx \quad \text{Eq. (2.23)}$$

Now, using the simplifying assumptions, encapsulated by Equation 2.19, one can rewrite $\phi(t)$ as:

$$\phi(t) = -\gamma k \int_{-\infty}^{\infty} I(x - vt)\rho(x,t)dx \quad \text{Eq. (2.24)}$$

Finally, using the fact that the beam is Gaussian and thus symmetric:

$$\phi(t) = -\gamma k \int_{-\infty}^{\infty} I(vt - x)\rho(x,t)dx = k\gamma(I *_x \rho)(v_{st}t, t) \quad \text{Eq. (2.25)}$$

Where with $*_x$ one denotes a convolution operation with respect to the spatial variable x. Thus we have arrived at an expression for the ion flux discussed in the previous section. The ion flux can be written as a spatial convolution with respect to the variable $x = v_{st}t$.

2.3.2 Finalizing the model

Using Equation 2.2, the total number of particles recorded by the mass spectrometer in the m^{th} pixel, corresponding to a location $v_{st}(\mathrm{m}\Delta t)$ is given by:

$$I_m = \int_{m\Delta t}^{(m+1)\Delta t} \phi(t)dt = \int_{-\infty}^{\infty} \phi(t)\, rect\left(\frac{t - m\Delta t_s}{D\Delta t_s}\right) dt$$

$$= \phi(t) * rect\left(\frac{t - m\Delta t_s}{D\Delta t_s}\right)$$

$$= k\gamma\big((I *_x \rho)(v_{st}t, t)\big) * rect\left(\frac{t - m\Delta t_s}{D\Delta t_s}\right) \qquad \text{Eq. (2.26)}$$

Using the notion of realistic sampling established earlier, the final digitized image can be written as:

$$image = \left(\sum_{n=\infty}^{\infty} \phi(\tau)\, Ш(\tau)\right) * rect\left(\tau - \frac{m}{D}\right) \qquad \text{Eq. (2.27)}$$

Where $\phi(\tau)$ can be computed using Equation 2.23. Thus, now two thirds of the model have been established. The final notion left to tackle is noise. Assuming that noise can be modelled as additive noise, the pixel intensity derived in Equation 2.26 can be expressed as:

$$I_m = k\gamma\big((I *_x \rho)(v_{st}t, t)\big) * rect\left(\frac{t - m\Delta t_s}{D\Delta t_s}\right) + \eta \qquad \text{Eq. (2.28)}$$

Where I_m is the pixel intensity of the m^{th} pixel, k is a constant related to the probability of desorbing an ion, γ is an ionisation coefficient, $I(x - v_{st}t)$ is the beam intensity at location x with v_{st} being the stage velocity, t is the time from the beginning of the imaging experiment, $rect\left(\frac{t-m\Delta t_s}{D\Delta t_s}\right)$ is a term that describes the digitization process η is a random variable that accounts for noise. At this point it could be said that the image formation model is finalized. However, the properties of the random variable η still need to be explored. This is particularly important for resolution.

2.3.3 A simple example – image of a point source

The model may also be expressed as:

$$I_m = -\int_{m\Delta t}^{(m+1)\Delta t}\int_{-\infty}^{\infty}\frac{\partial\rho(x,t)}{\partial t}dxdt$$

$$= \int_{-\infty}^{\infty}\rho(x,m\Delta t)-\rho(x,(m+1)\Delta t)dx \qquad \text{Eq. (2.29)}$$

Where I_m is the pixel intensity at the m^{th} pixel and the noise function has been set to zero; $\eta = 0$. Allowing for the density to be distributed as a point mass, namely $\rho_0(x) = D\delta(x)$, one obtains the image of a point source, which is also referred to as a point spread function (PSF).

$$I_m = D\left[\exp\left(-\frac{\gamma kI}{2v}\operatorname{erf}\left(\frac{vm\Delta t}{\sqrt{2v}}\right)\right) - \exp\left(-\frac{\gamma kI}{2v}\operatorname{erf}\left(\frac{v(m+1)\Delta t}{\sqrt{2v}}\right)\right)\right] \qquad \text{Eq. (2.30)}$$

Now envision the following thought experiment. Let a point source be $\rho_0(x) = D\delta(x)$ be placed at $x = 2000\ \mu m$ away from the start of the beam path. Let a beam $I(x - vt)$ move with velocity v and interact with the source point with a desorption probability k and ionisation coefficient γ and let the mass spectrometer sample at a time interval Δt. Two opposing scenarios can be pictured – in the first one the point source is not fully destroyed as the beam swipes over and in the second one the point source is destroyed as the beam swipes over. With the aid of Equation 2.30, which models the PSF, the effects of material consumption on resolution can be studied. These two opposing scenarios can also be studied at a range of pixel sizes. Using Python the PSF can be plotted, with the aid of the numpy, scipy and matplotlib packages. The following table summarizes the variables used in this simple simulation:

	Weak material consumption	Strong material consumption
Beam width 2σ (μm)	$32\mu m$	$32\ \mu m$
γ	1	1
k	10^{-6}	1.2×10^{4}
Scan time Δt (s)	$0.5s$	$0.5s$
Stage velocities $v(m/s)$	$80,20,10\ m/s$	$80,20,10\ m/s$
Pixel sizes Δp (μm)	$40,10,5\ \mu m$	$40,10,5\ \mu m$

Table 2-1. A summary of the parameters used in the simulation of a PSF.

For simplicity the ionisation coefficient γ is set to one but the desorption coefficient is adjusted to allow for strong and weak material consumption. For both weak and strong material consumption three different pixel sizes were investigated. The beam width for both situations is $32\ \mu m$. The lowest pixel size used is $40\ \mu m$, corresponding to undersampling from the point of view of MSI (crater diameter > pixel size). The other two pixel sizes (10 and $5\ \mu m$

correspond to oversampling from the point of view of MSI (crater diameter < pixel size). The results from these simulations are presented in the following figure:

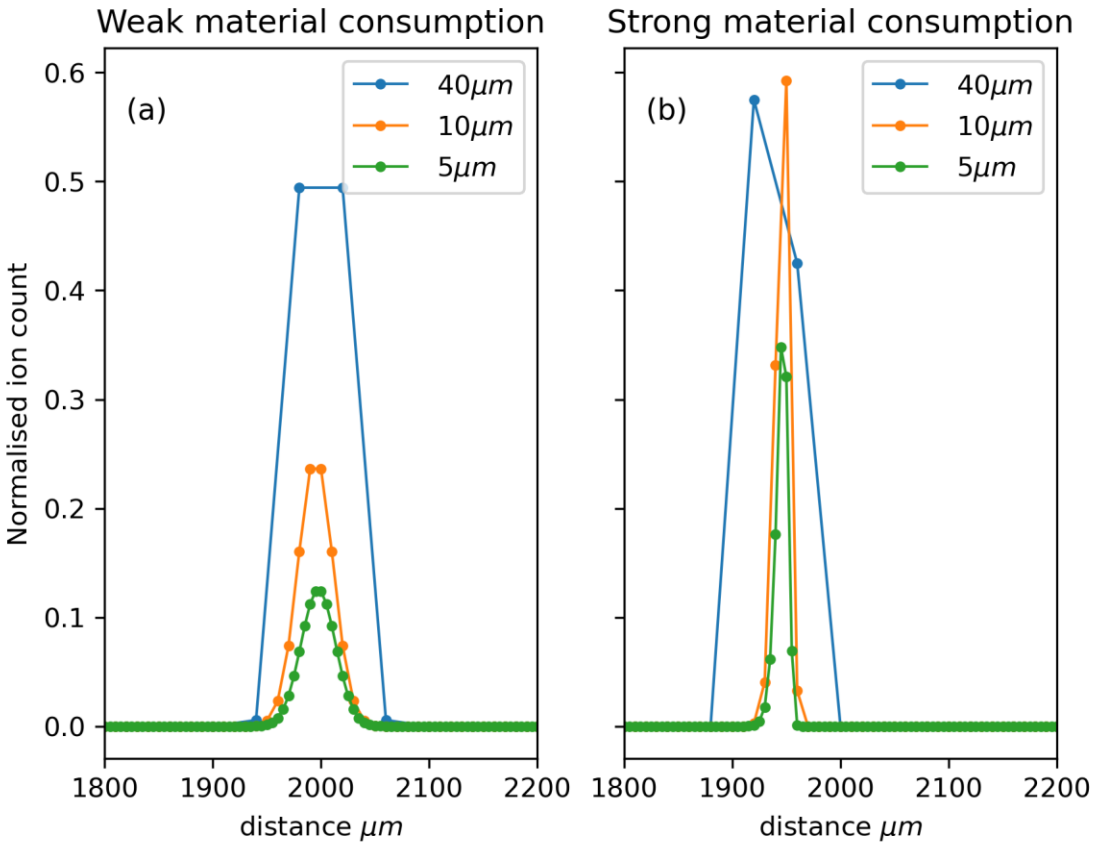


Figure 2-10 A simulation of a PSF for weak and strong material consumption at three different pixel sizes, corresponding to undersampling and oversampling from the point of view of MSI.

In Figure 2-10 (a) and (b) it can be seen that material consumption has a profound effect on the PSF. When material consumption is weak more blur is generated, whereas in the case of strong material consumption blur is minimised. Furthermore, in the case of strong material consumption the PSF appears to be centred at a different position, as the point is consumed before the beam can fully swipe over it. The PSF appears to be centred at a distance of 1950 μm, which corresponds to a shift of around one pixel for the 40 μm PSF, four pixels for the 10 μm PSF and eight pixels for the 8 μm PSF.

When measuring resolution, the width of the PSF is taken as a resolution metric. Since a point source is difficult to produce in a real world scenario, often the profile of a step edge is measured instead. In this case the $86-14\%$ quantile would correspond to the twice the standard deviation of a gaussian beam. However, the simulation here allows us look at a PSF. It is also possible to look at the image of a sharp line (line spread function, LSF), and a sharp edge (edge spread function, ESF) using this model. It should be noted that this was already explored in our

previous work[133]. Thus, the traditional approach for measuring resolution is based on blur. Then, curve fitting can be used to measure the width of each of the PSFs, which serves as a resolution metric. The results from the curve fitting are shown in the following table:

	PSF width as a resolution metric: weak material consumption	PSF width as a resolution metric: strong material consumption	Sampling theorem minimum
40 μm pixel size	37.5 μm	12 μm	80 μm
10 μm pixel size	32 μm	15 μm	20 μm
5 μm pixel size	32 μm	10 μm	10 μm

Table 2-2. A summary of the resolution measurements derived from the PSF simulations.

It is apparent that in the case of weak material consumption resolution is limited by the width of the beam when oversampling from the point of view of MSI (pixel size < crater size). In particular, the resolution measurements derived from the PSF widths for pixel sizes 10 and 5 μm accurately recover the width of the analytical beam used in these simulations, which is 32 μm. This has been well known for modalities that utilise weak material removal such as SIMS[67,68,139]. On the other hand, when undersampling the measured resolution is 37.5 μm, which contradicts the Sampling theorem – it was already shown that no feature smaller than twice the pixel size can ever be captured in an image (80 μm in this case). In fact, this resolution measurement is smaller than the pixel size itself. Thus, because the pixel size is greater than the width of the sampled area, blur cannot be used as a reliable resolution metric. More interestingly, the results shown in Table 2-2 show that in the case of strong material consumption almost all of the resolution metrics violate the Sampling theorem. This has been reported experimentally in modalities that utilise strong material removal[131,132]. Even when oversampling from the point of view of MSI, the measured PSF width turns out to be smaller than twice the pixel size for the 10 μm pixel size. As for the 5 μm pixel size, the resolution metric just barely satisfies the Sampling theorem. Notice that neither the 10 μm nor the 5 μm PSF recovers the original beam width. Thus, one cannot use the traditional resolution metrics in MSI modalities with strong material consumption such as MALDI. This was already discussed previously in **Section 2.2.4** of this chapter. Now, a formal mathematical treatment has proven this. Thus, in the case of strong material consumption a new resolution metric should be derived. As discussed in **Section 2.2.4** aliased features may still be problematic. However, noise can also limit resolution. In the next section noise is studied.

2.4 Noise modelling

As mentioned in Chapter 1, establishing an appropriate noise model can add immense value for clinical applications; in this study there is a practical need to establish a noise model in order to measure spatial resolution. Now some numerical simulations are used to help establish two noise models that have been reported in literature. One is the obvious Poisson noise and the other is the elusive noise that exhibits a quadratic variance. This is important because some authors claim that Poisson noise is the only noise source in MSI[107–109], while evidence of quadratic variance

has been clearly demonstrated[105,106]. To begin this section, the claims that Poisson noise has been confirmed will be examined closely[108,109]. This was already discussed in **Chapter 1.4,** Figure 1-21, where it was shown that the authors have misinterpreted the meaning of the correlation coefficient and confused it with a proof that variance is linearly proportional to intensity. The authors provide histograms of four ROIs. Calculating the average and variance from those would be sufficient to demonstrate that variance and intensity are linearly dependant. Unfortunately, the authors did not perform such analysis, but it is possible to reconstruct those histograms by measuring the widths and heights of the binned pixel intensities and then scaling the x axis.

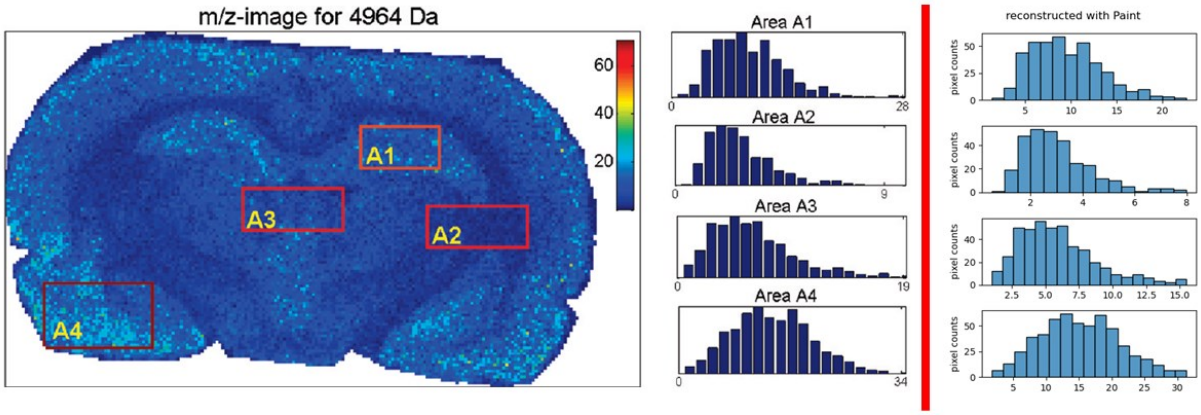


Figure 2-11. How to estimate noise. Left or red line – original data[108]*. Right of red line – reconstructed histograms using MS PAINT. Note that the identity of the m/z value was not provided by the authors.*

Left of the thick red line is the original figure as presented in[108]. The four ROIs are highlighted by red rectangles and are labelled as A1, A2, A3 and A4. It should be pointed out that some of the highest intensities bins were not considered in our reconstruction. Nevertheless, the histograms on the right hand side of the thick red line seem to match those of the original paper. From those histograms one can manually compute the average intensity and the variance. One can then plot those against each other to see if a linear relation is observed. The results, which the authors of[108] should have presented, are presented in the following graph.

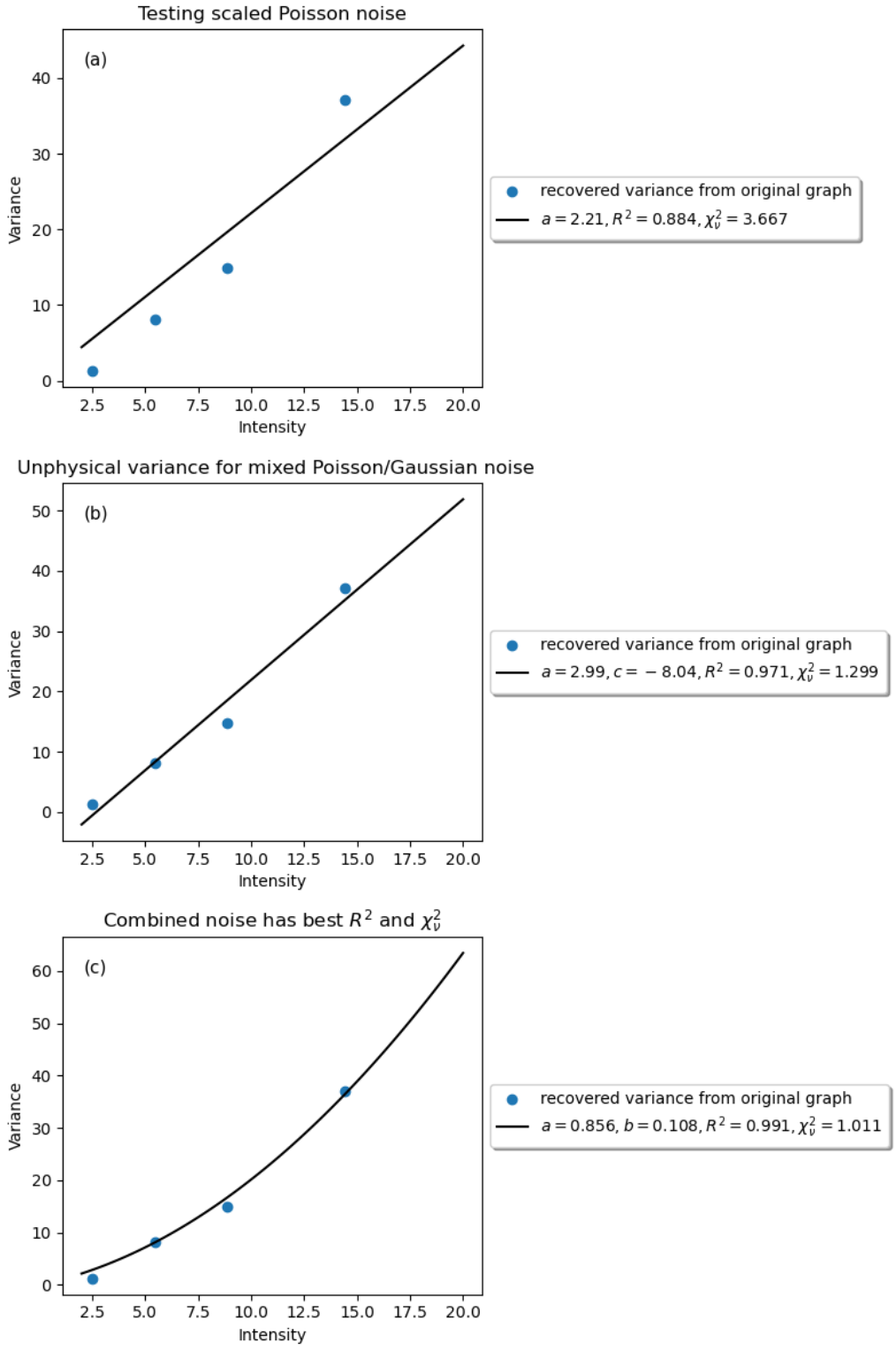


Figure 2-12. Reconstructed data from[108]*. (a) – Poisson noise. (b) – Poisson/Gaussian mixture. (c) – quadratic variance.*

The reduced chi squared values (defined in Chapter 5) and coefficient of determination for the reconstructed data is reported in our analysis. Figure 2-12 (a) shows that Poisson noise is a poor fit for the observed data. Figure 2-12 (b) shows that a Poisson/Gaussian mixture might be a better noise model, but the measured Gaussian component ends up having a negative variance, which is unphysical. Finally, Figure 2-12 (c) shows that quadratic variance is a better noise model candidate than Poisson noise. The observant reader will notice that ROI A4 is not a homogeneous ROI. This is problematic as the signal gets misinterpreted as noise and therefore the variance will be higher. In general, measuring noise in tissue images is a difficult task but some strategies will be proposed for how to deal with this in Chapter 5. Since ROI A4 is problematic in the next graph the same analysis is presented but with that data point excluded.

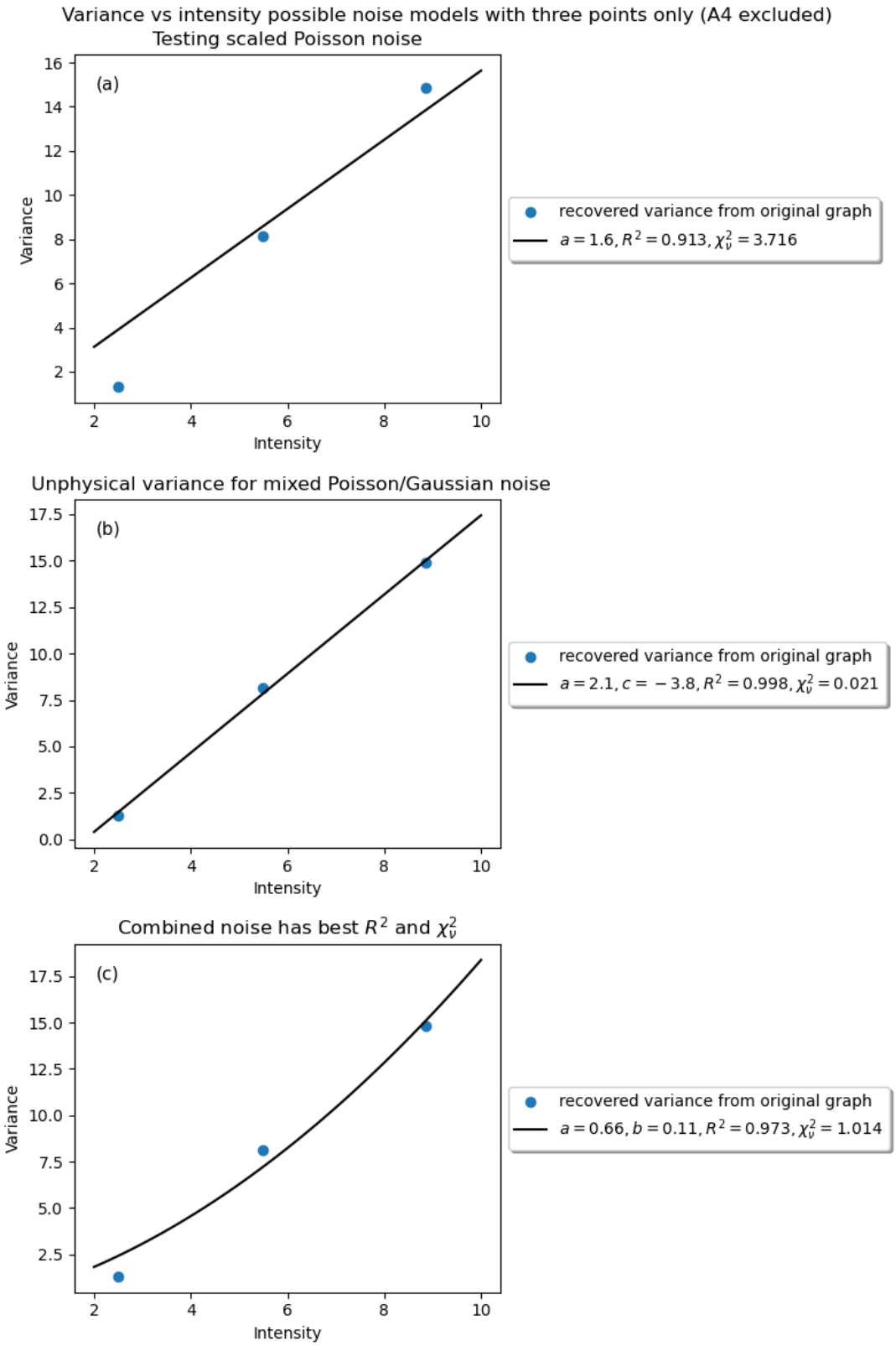


Figure 2-13. Reconstructed data from[108] *excluding the problematic ROI. (a) – Poisson noise. (b) – Poisson/Gaussian mixture. (c) – quadratic variance.*

Much of the results remain the same; the Gaussian Poisson mixture still remains unphysical and the quadratic variance seems to be a better fit than the scaled Poisson noise model according to the reduced chi squared and R^2 goodness of fit metrics. It should be pointed out that performing those goodness of fit estimates with only three datapoints available is not great. Nevertheless, the origin of quadratic variance will be shown through computational simulations in this section. From now on, this noise shall be dubbed as combined noise as it is a combination of Poisson noise and a noise source which causes the peak amplitudes to fluctuate. The following figure suggests the origin of the peak amplitude fluctuations in MALDI and DESI.

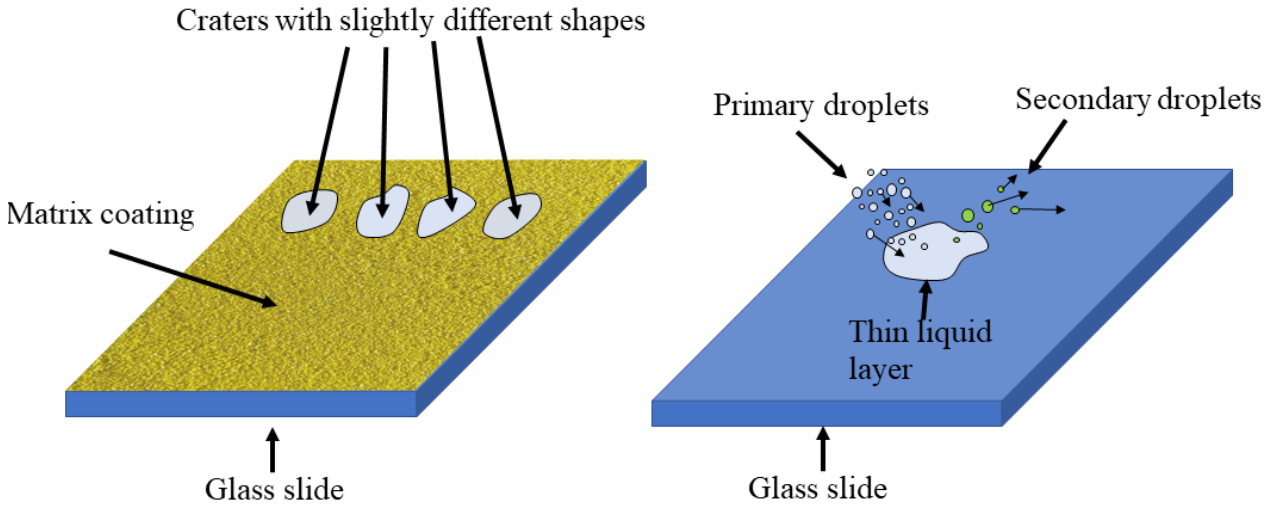


Figure 2-14. Possible origin of peak height fluctuations for MALDI and DESI. Left – fluctuations in MALDI laser energy result in slightly different craters. Right – fluctuations in DESI primary droplets size and velocity results in fluctuations of the number of secondary droplets.

It shall be shown that the combined noise model arises when ones combines Poisson noise, arising from the detector[93], with random fluctuations of the mass spectra peak heights . A possible source of this randomness for both MALDI and DESI is shown in Figure 2-14. On the left hand side MALDI is considered. MALDI is known for its shot-to-shot fluctuations[30]. Fluctuations in the laser energy may result in craters with slightly different shapes and therefore a different ion flux arises from the surfaces. This ultimately manifests as peaks with different heights in the mass spectrum. Natural variations in the matrix crystal sizes will certainly contribute to this as well. As for DESI, shown in the right hand side of Figure 2-14, studies have demonstrated that the primary droplets exhibit a natural variation in their size and velocities[42,43]. This has been experimentally and theoretically been shown to result in a variation of the number of secondary droplets leaving the surface[40,43] (shown as green circles in Figure 2-14). Therefore, the ion flux will also fluctuate and the final peak heights will be affected by this. In this section it will be shown that the parameter that governs the fluctuations of the peak amplitudes will directly lead to quadratic variance. This will later be confirmed experimentally in **Chapter 4** and **Chapter 5**.

The process of forming a mass spectrum and detecting a signal is discussed next. In fact, this is where noise mostly arises and it will have an impact of the properties of the noise function η. Unfortunately, providing a detailed mathematical model of the generation of mass spectra, such as the one seen in[100,101], lies well outside the scope of

this thesis. However, a very basic approach will be provided and this will serve the purpose of demonstrating that η can be treated as an additive noise parameter. Furthermore, this really simple approach will allow us to characterise the properties of η.

2.4.1 The instrument response function (IRF)

Let $N_{m,i}$ be the total number of particles that have left the surface between times $m\Delta t$ and $(m+1)\Delta t$ and consequently collected by the mass spectrometer, with m being the pixel acquired at location $mv_{stage}\Delta t$ and i is an index used to label the molecular identity. The ideal spectrum can be thought of as a delta function centred at m/z_i with a weight of $I_{m,i}$ The instrument response function is a function that maps the ideal mass spectrum $I_{m,i}\delta(m/z - m/z_i)$ to the observed mass spectrum[82]:

$$f(m/z_i) = \int_{-\infty}^{\infty} f(m/z) I_{m,i}\, \delta(m/z - m/z_i) d\, m/z \qquad \text{Eq. (2.31)}$$

Where $f(m/z)$ is the instrument response function and $f(m/z_i)$ is the observed peak. The functional form of the IRF will depend on the mass analyser used and all of the parameters that govern the process of separating charged particles[100,101]. For the purpose of this work a simple Gaussian function shall suffice:

$$f(m/z) = \frac{1}{\sqrt{2\pi\sigma^2}} \exp\left(\frac{m/z^2}{2\sigma^2}\right) \qquad \text{Eq. (2.32)}$$

Where here σ determines the width of the IRF and is related to the mass resolution of the instrument – see Equation 1.25 and Figure 1.16 (a). Thus, in this model system the mass spectrum of the i^{th} molecular species is given by:

$$f(m/z_i) = \frac{I_{m,i}}{\sqrt{2\pi\sigma^2}} \exp\left(\frac{(m/z - m/z_i)^2}{2\sigma^2}\right) \qquad \text{Eq. (2.33)}$$

Where $I_{m,i}$ can be calculated using the image formation model using Equation 2.28. Typically, when constructing an MSI image the peak of the molecular species m/z_i, described by Equation 2.31, is integrated in order to obtain the total number of particles.

2.4.2 How is noise generated?

When Equation 2.31 is integrated the total number of particles $N_{m,i}$ is recovered. This offers a doorway into modelling the noise function η. At this point the discretisation of the mass spectrum can also be considered – one

could go through the exercise of applying the Sampling theorem on the mass spectrum $f(m/z_i)$. However, as mentioned previously this falls outside the scope of this thesis. It is worth pointing out that the discretization process can also introduce noise – for example quantization noise and thermal noise derived from the analogue to digital converter. Therefore, while the spectral discretization is not considered, it can be seen how considering the mass spectrum $f(m/z_i)$ can be useful in establishing a noise model. However, what is considered in this section is the fact that process that leads to signal detection can also introduce noise in $f(m/z_i)$. In particular, the process of single particle counting is described by Poisson statistics. Thus, each observed data point $f_n(m/z_i)$ can be said to be distributed as a Poisson distribution:

$$f_n \sim Pois(N) \qquad \text{Eq. (2.34)}$$

Where here f_n stands for the n^{th} observed data point in the mass spectrum and N is the true number of particles that arrived at the detector that correspond to this data point. Thus, after integrating Equation 2.31 to recover the total number of particles it can be seen that an uncertainty has been introduced in the measurement process. This uncertainty manifests as image noise. In practice the Poisson distribution can be approximated as a normal distribution with its mean and variance equal to N. This is particularly appealing as this can be modelled as additive noise. Therefore, the noise function η that appears in Equation 2.28 can be written as a normal distribution centred at 0 with variance that is linearly proportional to the signal intensity:

$$\eta_{Pois} \sim \mathcal{N}(0, aI) \qquad \text{Eq. (2.35)}$$

Where here a is a simple scaling parameter and I is the pixel intensity obtained from Equation 2.28 and Equation 2.31. Another source of noise considered here is random variations in the peak amplitude $N_{m,i}$. These can be caused by multiple different factors – differences in the collected volume of sampled material due to fluctuations of the analytical beam, variations of the transmissivity of the ion signal through the mass spectrometer, fluctuations of the chemical reactions that lead to ion formation, etc. Overall, this will give rise to a multiplicative type of noise. To model this variation of the peak amplitude, $I_{m,i}$ is assumed to be distributed as a normal distribution centred at I and variance that is related to I^2.

$$A \sim \mathcal{N}(I, bI^2) \qquad \text{Eq. (2.36)}$$

This is great news, because in this case the noise function can also be described as an additive one. In particular:

$$\eta_{Ampl} \sim \mathcal{N}(0, bI^2) \qquad \text{Eq. (2.37)}$$

Where here b is a scaling parameter describing the fluctuations of the peak amplitude (caused by the factors described in the previous paragraph) and I is the pixel intensity obtained after applying Equation 2.28 and Equation 2.31.

Finally, a mixture of the two models can be considered. This arises when the uncertainty due to the detection is combined with the fluctuations in the peak amplitude (which themselves can arise due to the several reasons or combination of those reasons described previously). In this case the mass noise can also be described as additive noise and the noise function takes the form of:

$$\eta_{Comb} \sim \mathcal{N}(0, aI + bI^2) \qquad \text{Eq. (2.38)}$$

2.4.3 Investigating the properties of different noise types: A simple simulation

Thus, in this thesis three different noise models are proposed. For the purpose of this work a simple numerical computation using Python was used in order to study the arising of noise in an image obtained after integrating a mass spectrum. The numpy, scipy and matplotlib packages were used in these simulations. A hundred images with dimensions of 30×30 pixels were created. The images spanned a large range of intensities ($10^0 - 10^4$). Within each image, each pixel contained a mass spectrum of a single peak generated with the aid of Equation 2.33. In order to mimic the distributions of intensities observed in a typical MSI experiment, only a few high intensity peaks were generated (≈ 10) and the majority of peaks (≈ 90) were lower intensity (smaller than 10^4).

The peaks were corrupted with the three types of noise described in the previous paragraphs. After integrating the mass spectrum a noisy image was recovered. The variance $\sigma^2(I)$, standard deviation $\sigma(I)$ and the signal to noise ratio (SNR) of each image were plotted as a function of the average pixel intensity $\bar{I}$. This allowed for the characterisation and investigation of each noise model. The image average is defined as:

$$\bar{I} = \frac{1}{n_x n_y} \sum_{i}^{n_x} \sum_{j}^{n_y} I_{ij} \qquad \text{Eq. (2.39)}$$

Where n_x, n_y are the number of pixels in x and y. Image variance $\sigma^2(I)$ is defined as:

$$\sigma^2(I) = \frac{1}{n_x n_y} \sum_{i}^{n_x} \sum_{j}^{n_y} \left(I_{ij} - \bar{I}\right)^2 \qquad \text{Eq. (2.40)}$$

And image standard deviation $\sigma(I)$ is:

$$\sigma(I) = \sqrt{\sigma^2(I)} = \sqrt{\frac{1}{n_x n_y} \sum_{i}^{n_x} \sum_{j}^{n_y} \left(I_{ij} - \bar{I}\right)^2} \qquad \text{Eq. (2.41)}$$

Thus, image SNR is defined as:

$$SNR = \frac{\bar{I}}{\sigma(I)} \qquad \text{Eq. (2.42)}$$

The mass spectra were centred at $m/z = 50\,Da$. The distance between data points used was $\Delta m/z \approx 3.5 \times 10^{-5} Da$ and Gaussian function with a standard deviation of $2 \times 10^{-4} Da$ was used to generate the mass spectra. This corresponded to a mass resolution of $\approx 100\,000$. Next, after a mass spectrum was generated for each pixel, the mass spectrum was corrupted by noise. Three type of noise models were investigated: Poisson noise, amplitude noise and a mixture of the two. Parameters of $a = 1, b = 0.02$ were chosen. After the mass spectra were generated, the signal was integrated and the value of the signal was assigned to that particular pixel as intensity. It should be noted that in the absence of noise all pixels would have the same intensity (no noise would be present).

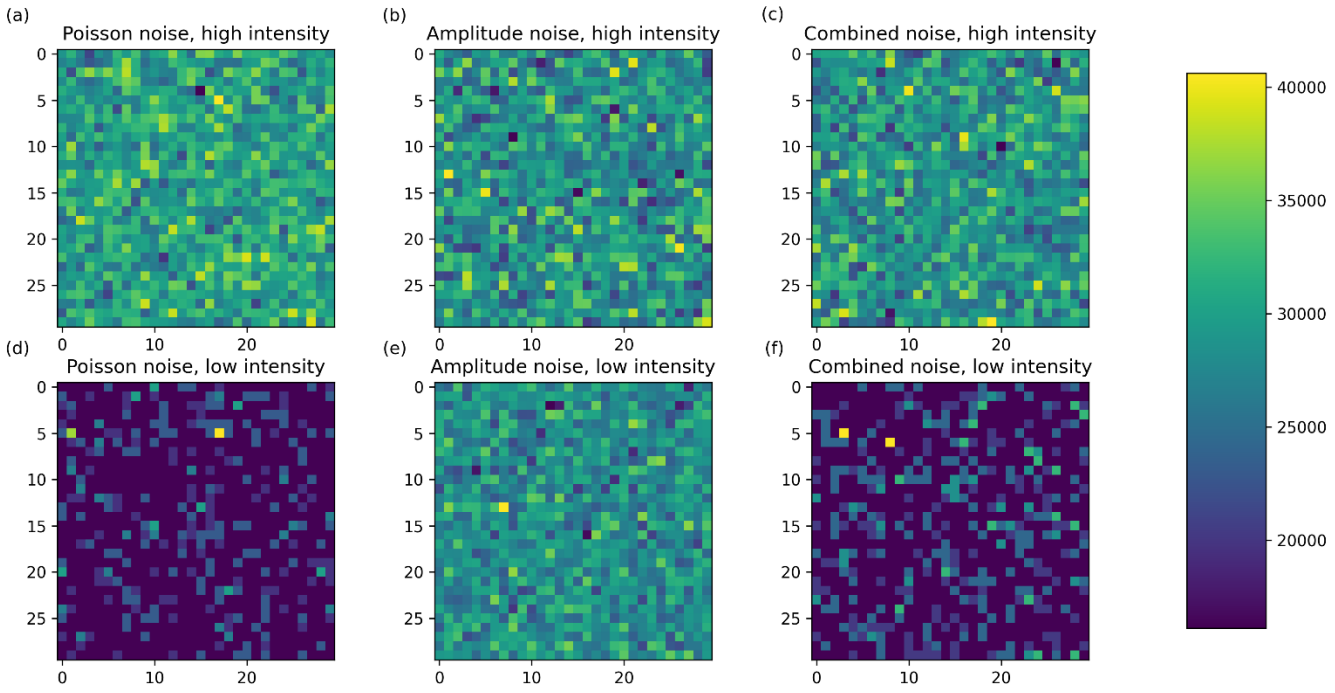


Figure 2-15. (a) – High intensity image generated from a high intensity mass spectrum corrupted with Poisson noise. (b) – same as (a) but corrupted by amplitude noise. (c) – same as (a) but corrupted with combined noise. (d) – A low intensity image generated from a low intensity mass spectrum corrupted with Poisson noise. (e) – same as (d) but corrupted with amplitude noise. (f) – same as (d) but corrupted with combined noise.

The results from this simulation are presented in Figure 2-15, where examples of high and low intensity images affected by the three types of noise can be seen. As for the actual mass spectra, they can are shown in the following figure:

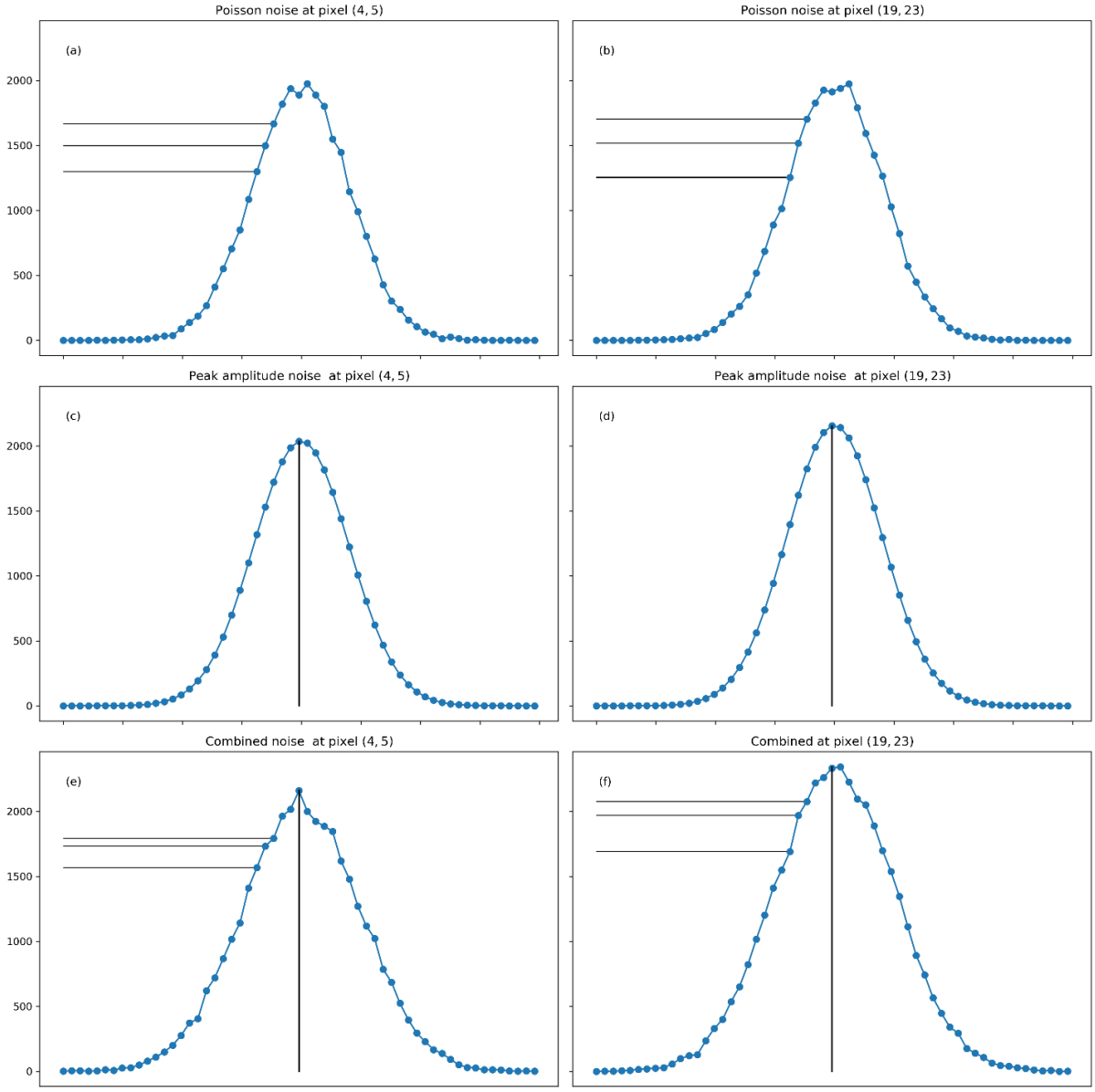


Figure 2-16 (a), (b) – Mass spectrum affected by Poisson noise for two randomly selected pixels – (4,5) and (19,23) respectively. (c), (d) – Peak amplitude noise at the same two pixels. (e), (f) – Combined noise for the same two pixels.

The effects of each type of noise is clearly demonstrated in the figure above. In Figure 2-16 (a) and (b) it can be seen that each data point is affected by an uncertainty introduced by the detector when counting the number of arriving ions. To highlight this, three horizontal black lines are used to track the positions of three data points across the two randomly selected pixels. In the absence of Poisson noise the highlighted data points would always be measured at the same position. Next, in Figure 2-16 (c) and (d) the noise generation of amplitude noise is depicted. To show how this type of noise arises, a vertical black line centred at the middle of the peak is drawn. As mentioned previously, this randomness can be caused by the variations in crater size in MALDI, thin liquid layer size in DESI,

randomness due to ion transmissivity, randomness from ion generation, or the combination of all of these. It can be seen that the amplitude is in each mass spectrum is slightly different in each pixel, while the data points are unaffected by Poisson noise. Finally, in Figure 2-16 (e) and (f) the combination of both types of noise is considered and thus both vertical and horizontal lines are included.

After the mass spectra were generated, images were generated (shown in Figure 2-15). The average intensity, variance, standard deviation and SNR were computed for each noise type. The results of this study are presented in the following graph:

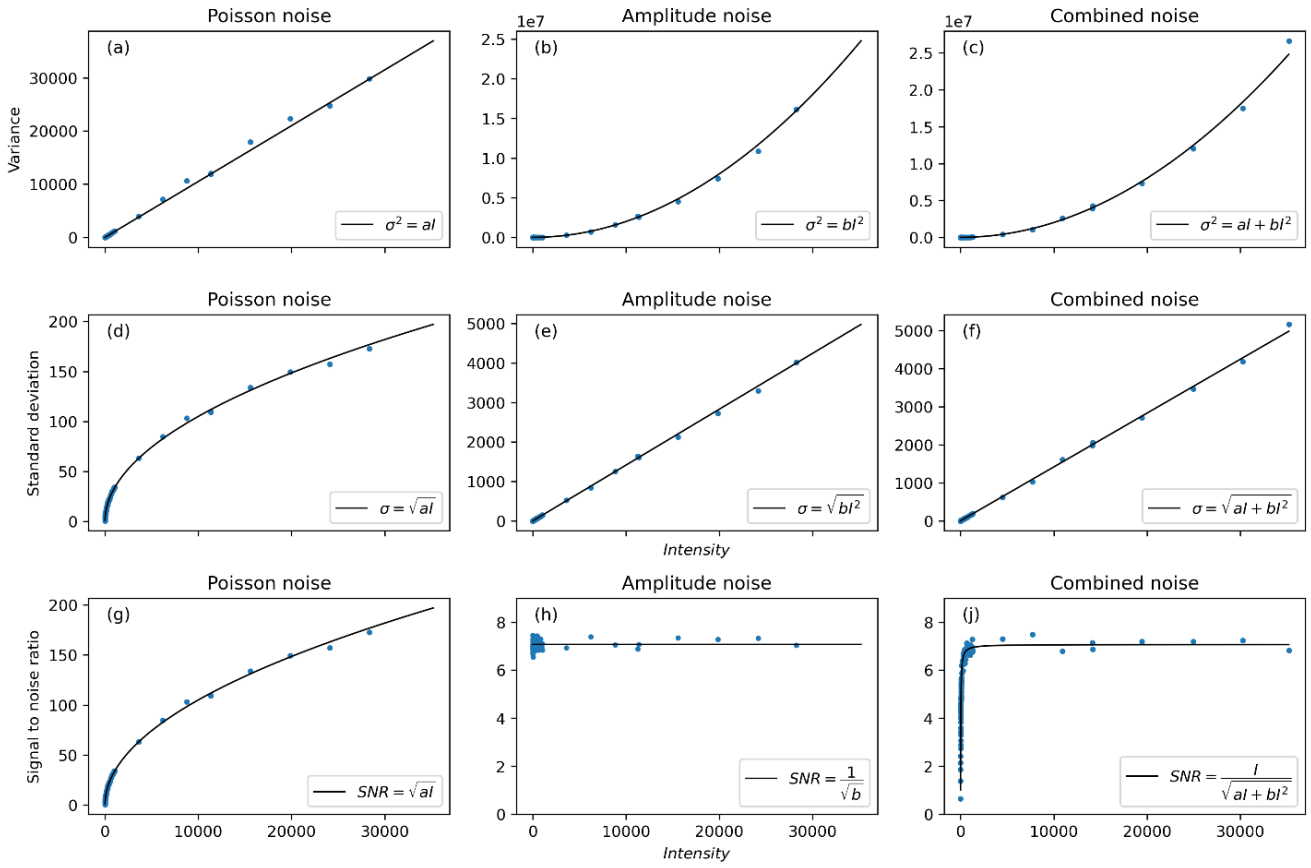


Figure 2-17. (a), (b), (c) – The variance of Poisson, amplitude and combined noise as a function of the mean intensity $\bar{I}$. (d), (e), (f) – The standard deviation of all three types of noise considered here as a function of the mean intensity $\bar{I}$. (g), (h), (f) – The image SNR for all three types of noise.

The variance of all three types of noise is shown in Figure 2-17 (a), (b) and (c). It can be seen that Equation 2.35, Equation 2.37 and Equation 2.38, which describe the noise function η as distributed as Poisson, amplitude and combined noise respectively, predict the variance with good accuracy. Each noise model also fits the standard deviation curves seen in Figure 2-17 (d), (e), (f) and SNR curves seen in Figure 2-17 (g), (h), (j). The equations that describe the variance, standard deviation and SNR are summarised in the following table. More notably, the

simulation here predicts that the combination of Poisson noise, due to detector uncertainties, and peak height fluctuations gives rise to the previously reported quadratic variance[105,106].

	Poisson noise	Amplitude noise	Combined noise
$\sigma^2(I)$	aI	bI^2	$aI + bI^2$
$\sigma(I)$	$\sqrt{aI}$	$\sqrt{b}I$	$\sqrt{aI + bI^2}$
SNR	$\sqrt{aI}$	$1/\sqrt{b}$	$I/\sqrt{aI + bI^2}$

Table 2-3. A summary of the equations that describe the variance, standard deviation and image SNR for the three different types of noise model

It can be seen that in the case of Poisson noise variance increases linearly with signal intensity. This leads to a standard deviation that grows as the square root of the intensity and an SNR that also grows as the square root of the intensity. Thus, at high intensities Poisson noise has little to no impact on the overall image. At low intensities however, noise is significant and one can expect it to affect the resolution capabilities of an imaging system. Amplitude noise here servers as a vessel to transition to the combined noise model. Nevertheless, it is still interesting to point out that its variance has a quadratic dependence on intensity, with the linear coefficient a being equal to zero. This leads to an SNR that is constant with respect to intensity. Combining the Poisson noise model with a term that describes the fluctuations in peak heights has resulted in the combined noise model. It exhibits quadratic variance, which was previously reported in literature[105,106] and a computational simulation has been used to describe its origin. The combined noise model has several interesting properties. At very low intensities the SNR grows as the square root as the Poisson noise term dominates (typically $a \gg b$ as shall be seen in Chapter 4 and Chapter 5). However, for large intensities the quadratic term takes the lead and the SNR curve plateaus. No matter how much the intensity is increased, the SNR remains constant. This also has a significant implication for resolution – in the case of Poisson noise high intensities have negligible noise levels, where as in the case of combined noise high intensities will have a much lower SNR. To confirm the validity of these tests curve fitting was used in order to extract the a, b coefficients for each noise model. As a remainder, when the mass spectra were simulated values of of $a = 1, b = 0.02$ were chosen. The extracted coefficients are shown in the following table:

	Poisson noise	Amplitude noise	Combined noise
a	1.09 ± 0.02	≈ 0	1.2 ± 0.4
b	≈ 0	$0.0201 \ +/ \ 0.001$	0.019 ± 0.002

Table 2-4. The value of the coefficients a, b derived from curve fitting.

The two main types of noise that one should expect to see in a real MSI experiment are Poisson noise and the combined noise model. Amplitude noise was only used as a transition point in this simulation. While Poisson noise has been described in literature previously, the combined noise model has been reported previously[105,106] and not its origin has been explained. Thus, these simulations have equipped us with the necessary tools to deal with different

types of noise that can be encountered. In particular, assessing the average intensity, variance, standard deviation and SNR of a homogenous region would allow us to quantify the noise statistics that govern a particular MSI instrument. Furthermore, it would be possible to compare the performance of different instruments by comparing the coefficients a, b and/or the variance/standard deviation/SNR curves. The a parameter should be related to the detector and instrument itself, while the b describes peak height fluctuations. Finally, these noise models will also be used in order to calculate resolution.

2.5 Conclusions

In this chapter an image formation model appropriate for microprobe MSI was developed. The work needed to establish such a model can be divided into three parts. The first part is signal digitisation. This was in **Chapter 2.2** where the origins of signal digitisation and its implications for resolution were investigated. The main discussion there revolved around the idea that a mass spectrometer samples a flux of ions emanating from the surface, which can be thought as a continuous time signal that is to be discretised by the instrument. It was established that the smallest resolvable feature in a digital image should be $2\Delta p$, with Δp being the pixel spacing. Thus, practitioners in the field of MSI should avoid confusing pixel size with spatial resolution[110,111,120–124,112–119]. Aliasing (undersampling) and why it is problematic for resolution was also discussed. In particular, an example in which a subpixel feature manifested as a structure that is several pixel sizes wide was shown.

The second third of this work, outlined in **Chapter 2.3**, combined the ideas of discretisation of an ion flux with an idealised equation that allows for the computation of the ion flux at a given beam intensity, stage velocity, desorption coefficient and sampling time. The underlying assumption there was that the probability of desorbing a molecule is linearly proportional to the beam intensity. The equation of a PSF was also derived and plotted at several different scenarios to show the failure of the traditional blur based approach for measuring resolution. It became apparent that when undersampling from the point of view of MSI, or when oversampling from the point of view of MSI but with strong material removal, using image blur as a resolution metric yields subpixel answers. This of course contradicted our earlier assertion that the smallest resolvable feature in a digital image should be $2\Delta p$. On the other hand, when oversampling from the point of view of MSI in scenarios where material consumption is weak, it was shown that blur is a suitable resolution metric. Moreover, the model showed that this blur converges to the width of the beam, which has been demonstrated experimentally in SIMS[67,68,139]. Thus, by considering the effects of material removal, our model explains why using blur as a resolution metric is suitable for some MSI modalities[67,68,139] and not for other[131,132]. Thus, when seeking to construct a suitable resolution metric, one should take this into account. A natural way of measuring image blur is to obtain an image of a point like feature – a point spread function. However, this is often impractical and other routes for measuring image blur are discussed in **Chapter 3**.

The other limiting factor for spatial resolution is noise. The origin of noise was thoroughly investigated in **Chapter 2.4**, where it was suggested that noise in the image arises from the mass spectrum. To construct a mass spectrum a simple IRF was invoked and corrupted with different types of noise. The mass spectrum was then integrated to

obtain a pixel intensity. Using empirical statistics, the different types of noise were characterised. While in literature Poisson noise is thought to be the dominant type of noise, in this work a mixture of Poisson and peak amplitude noise was considered. The variations of the peak heights could arise from different factors: slight differences in the crater size in MALDI/ thin liquid layer size in DESI, variations in the transmittivity of the mass spectrometer, variations in the chemical reactions that lead to ion formation, etc. This lead to a noise model which significantly deviates from Poisson statistics. Quadratic variance has been reported previously[105,106] and now computational simulations points to the origin of this behaviour. After reviewing the experimental data in later chapters, the reader should be convinced that some MSI modalities show this deviation from the Poisson noise model (namely a quadratic variance) and that the proposed noise model here is a good candidate for this behaviour. The tools developed in this chapter will also be used to measure resolution. To conclude this chapter the following figure is provided:

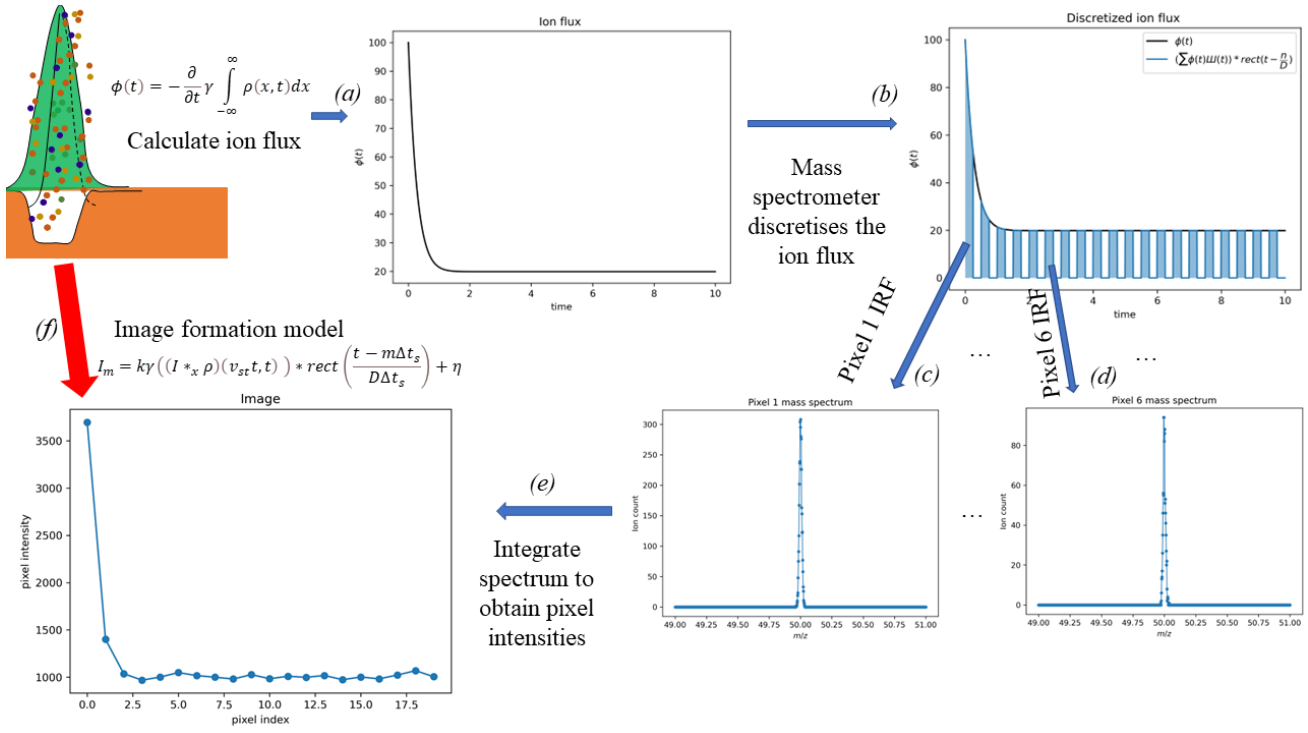


Figure 2-18. A summary of the mathematical procedures that produce the image formation model.

In Figure 2-18 the one dimensional image formation model is described pictorially. A beam moving with a constant velocity is sampling over a uniform surface. A scenario of oversampling with strong material consumption is considered. Molecules are released from the surface resulting in a flux of particles. The blue arrow *(a)* shows the computed ion flux as a function of time. Arrow *(b)* shows the process of discretising the ion flux by a mass spectrometer with a duty cycle of $D = 0.5$. The shaded blue areas under the ion flux are to be integrated to obtain the total number of particles that emanated from the surface during the acquisition time for that given pixel. Arrows

(d) and *(f)* show the use of an IRF to produce a mass spectrum. Due to uncertainties arising from the detection process, when the mass spectrum is integrated to obtain the final pixel intensity, noise is propagated from the mass spectrum to the digital image. This is shown in arrow (e) where the one dimensional digital image of a constant surface is obtained. Alternatively, the red arrow (f), where a single equation (which encapsulates all of these processes – this is the image formation model), can be used.

Some final remarks – the image formation model here is not a quantitative model but a qualitative one. This means that pixel intensities cannot be predicted. This would require knowledge on the ionisation coefficient γ, which itself requires knowledge on the ionisation mechanisms discussed in Chapter 1. As for the desorption coefficient k, it should be pointed out that while it covers the process of thermal desorption in MALDI (typically at lower laser fluences, described in Chapter 1), it does not cover the process material removal in DESI (also described in Chapter 1). The image formation model also does not take into account solvent washing effects observed in DESI, or analyte delocalisation effects. It also assumes that all of the particles that left the surface enter the MS. However, often there is an inlet capillary which collects only a portion of all particles that leave the surface. To calculate this would require knowledge on the velocity distribution of the particles leaving the surface. None of these things are taken into account here and it therefore must be pointed out that the model does not make predictions on the pixel intensities. Rather, only qualitative aspects of MSI are captured by the model. For example, the fact that the first row and column of the digital image are much higher in intensity when oversampling with material consumption (see Figure 2-18). It was also useful in showing that some MSI modalities have a spatial resolution limited by the width of the beam, while other modalities can detect features finer than the width of the beam (see Figure 2-10 and Table 2-2). In the next Chapter the model will be used to study the loss of resolution due to blur and noise. Consequently, this will help us derive a resolution metric, which will then be used to measure the resolution of MSI data sets.

Chapter 3 How to measure spatial resolution.

3.1 Introduction

In the previous chapter it was shown that image blur performs well when material removal is weak but fails in modalities with strong material removal, such as MALDI. In this chapter a methodology for measuring spatial resolution will be formulated. This methodology will not only take blur into account, but also discretization and noise. Blur, discretization and noise were already described thoroughly in the previous chapter. The image formation model derived previously will be applied to study a few simple model systems. Using this approach, in this chapter it will be shown that the ability to differentiate between features (resolution) in an image can deteriorate in the presence of blur and noise. It will also be shown how to calculate what the minimum distance between features should be such is that those features appear to be distinguished in the digital image. The procedure for calculating this distance is the heart of this thesis. Once the new resolution metric is tested on these model systems it will be used in real data sets in order to assess the resolution performance of MSI systems.

3.2 Loss of resolution due to blur and noise

In order to arrive at a resolution metric applicable across a wide range of MSI modalities the image formation model derived in the previous chapter will be utilised to simulate the images of a few simple model systems. The systems under investigation will be: a point source (point spread function, PSF), an edge source (edge spread function, ESF) and a device with decreasing bar widths and distance. Such a device has been previously used to obtain a modulation transfer function (MTF) in order to characterise the loss of resolution due to blur and noise in MSI[67,69]. With the aid of the image formation model, an approach for obtaining an MTF from a sharp step edge will be obtained. It will be shown that this approach gives the same results as the traditional approach used.

3.2.1 Scaling the image formation model to two dimensions

Before the model is applied on these systems it is worth extending it to two dimensions. Fortunately, this is not too difficult. Firstly, the ion flux is now related to the rate of change of the two dimensional density:

$$\phi(t) = -\frac{\partial}{\partial t}\gamma \iint_{-\infty}^{\infty} \rho(x,y,t)dxdy \qquad \text{Eq. (3.8)}$$

Secondly, the same ansatz as before is used. This time instead, the rate of change of the density is linearly proportion to a two dimensional beam:

$$\frac{\partial}{\partial x}\rho(x,y,t) = -kI(x - v_x t, y - v_y t)\rho(x,y,t) \qquad \text{Eq. (3.2)}$$

Where v_x, v_y are the stage velocities in x and y respectively. At this point care should be taken when specifying the path that the beam takes.

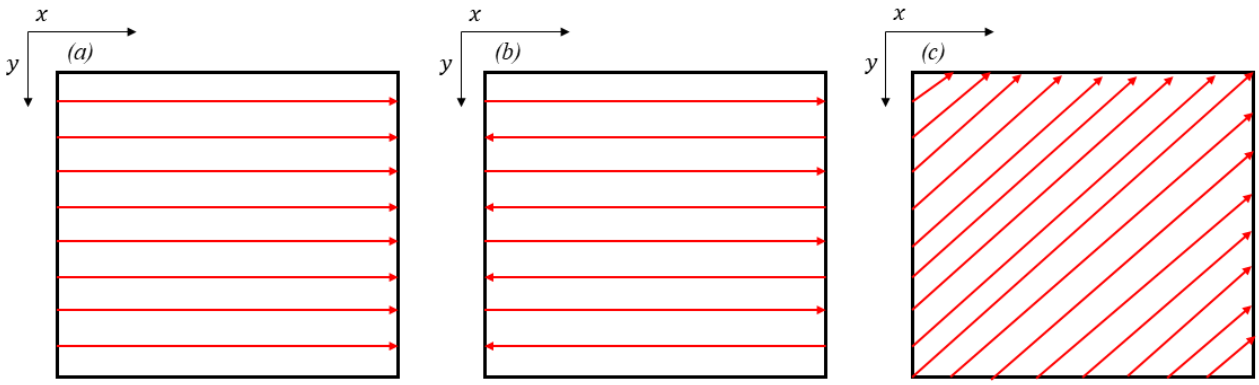


Figure 3-1 (a) – A beam path for which $v_x > 0$ and $v_y = 0$. (b) – a zig-zag beam path - v_x alternates between positive and negative so the beam switches direction and $v_y = 0$. (c) – a beam path for which both $v_x > 0$ and $v_y > 0$.

In Figure 3-1 several possible beam paths are shown. In Figure 3-1 (a) a very typical scenario is shown where the beam moves in a straight line. This corresponds to continuous raster mode. Figure 3-1 (b) depicts a zig-zag path, which can also be utilised in some imaging systems and Figure 3-1 (c) shows a beam path for which the beam has a non-zero velocity in both x and y. It should be noted that such scenarios can be reduced to the scenario in Figure 3-1 (a) by transforming to a reference frame in which $v_y = 0$. In each of the three cases a coordinate system is attached to show the directions of x and y. The origin of the coordinate system is at the first acquired pixel. There also exist more complicated beam paths that involve curved paths. In this work such scenarios are not considered and for simplicity only the simple scenario shown in Figure 3-1 (a) is examined. Thus, Equation 3.2 becomes:

$$\frac{\partial}{\partial x}\rho(x,y_n,t) = -kI(x - v_x t, y - y_n)\rho(x,y,t) \qquad \text{Eq. (3.3)}$$

Where here y_n is the vertical distance from the origin corresponding to the n^{th} linescan. Assuming a Gaussian beam:

$$I(x - v_x t, y - y_n) = \frac{I_0}{2\pi\sigma_x\sigma_y}\exp\left(-\frac{(x - v_x t)^2}{2\sigma_x^2}\right)\exp\left(-\frac{(y - y_n)^2}{2\sigma_y^2}\right) \qquad \text{Eq. (3.4)}$$

With σ_x, σ_y describing the width of the beam in x and y. The solution to Equation 3.3 is now given by:

$$\frac{\partial}{\partial x}\rho(x,y_n,t) = \rho_0(x,y)\exp\left(-\frac{kI_0}{2v_{st}}\left[erf\left(\frac{x - v_{st}t}{\sigma_x\sqrt{2}}\right) - erf\left(\frac{x}{\sigma_x\sqrt{2}}\right)\right]\right)\exp\left(-\frac{(y - y_n)^2}{2\sigma_y^2}\right) \qquad \text{Eq. (3.5)}$$

This then allows a calculation of the ion flux in Equation 3.1 to be performed. From there the ion flux can be discretised in a similar fashion as in Chapter 2. The Sampling theorem still hold, however now there is an additional dimension to consider. The smallest resolvable feature in x, y is given by $2\Delta p_x, 2\Delta p_y$ respectively, where Δp_x and Δp_y are the pixel spacings in x, y respectively. In the x direction this is $\Delta v_x \Delta t$ and in the y direction this is y_n. It should be noted that if a more complicated sampling pattern was chosen, such as the one shown in Figure 3-1 (c), the Sampling theorem needs to applied accordingly. For example, if $v_x = v_y$ and thus the beam is moving at a $45°$ angle path with respect to the coordinate system shown in Figure 3-1 (c), then the minimum distance between pixels in x, y will no longer be $2\Delta p_x, 2\Delta p_y$, but a value greater than that.

3.2.2 Applying the model on simple systems: the PSF, the ESF and the MTF

Now that the model has been extended to two dimensions it can be applied to simple systems in order to study resolution. The systems that will be investigated are a point source, an edge source and a device with decreasing bar widths and distances. A new mathematical object called the modulation transfer function (MTF) is also introduced. The image of a point source is referred to as a point spread function (PSF) and the image of a line source is referred to as an edge spread function (ESF)[67,69]. The MTF is defined as the magnitude of the Fourier transform of a PSF.

$$MTF = |\mathcal{F}[PSF]|(v) \qquad \text{Eq. (3.6)}$$

The MTF is a function of spatial frequencies. The highest available frequency of the MTF is given by $2/\Delta p_x$, which of course is the Nyquist frequency of the image, as discussed in Chapter 2. For simplicity, in the analysis presented in this thesis the MTF will be presented on a normalised frequency scale where unity corresponds to the Nyquist frequency. The MTF allows for the characterisation of resolution and information loss in frequency space. It describes how the imaging instrument maps the frequencies of the original object to the image. The shape of the MTF reveals important information about the loss of spatial information due to blur. For example, an MTF that decays to zero quickly suggests that the imaging systems blurs out higher frequency components, whereas a sharp MTF suggests that the imaging system allows for high frequency components to pass through. Unfortunately, engineering a perfect point source is a difficult task for MSI. In these scenarios one could instead look at the image of a sharp edge source. Then, the obtained ESF can approximate the ground truth PSF by taking the derivative of the PSF:

$$PSF_x \approx \frac{\partial}{\partial x} ESF \qquad \text{Eq. (3.7)}$$

As will be shown later on in this Chapter this approximation holds quite well. One disadvantage of this approach is the loss of spatial information in the y direction. Thus, if one wishes to recover the PSF in the y direction, the orientation of the edge source should be aligned in the y direction. Nevertheless, this allows for a cheap and easy measurement of a PSF and consequently an MTF.

$$MTF_x \approx \left| \mathcal{F}\left[\frac{\partial}{\partial x} ESF \right] \right| \qquad \text{Eq. (3.8)}$$

Again, if one wishes to calculate the vertical response of the MTF, one should do so with an edge aligned in the y direction. Finally, an alternative approach for calculating the MTF is by obtaining an image of a device with a decreasing bar widths and distances. Then, the change in contrast between different frequencies is calculated. This allows for a practical computation of the amplitude of the frequencies that make up the MTF. The contrast is calculated with the aid of the following equation[67,69,137]:

$$C = \frac{I_{max} - I_{min}}{I_{max} + I_{min}} \qquad \text{Eq. (3.9)}$$

The MTF can then be calculated by looking at the ratio of the contrast change of the image and the object at a given frequency[67,69,137]:

$$MTF_x = \frac{C_{image}(\nu)}{C_{object}(\nu)} \qquad \text{Eq. (3.10)}$$

Where the frequencies ν are simply the reciprocal values of the distances between bars. Thus, three different approaches can be taken in order to compute an MTF[*], with the only approach investigated so far in MSI literature is the one given by Equation 3.10. In this thesis it is claimed that using a sharp step edge can yield better results, and it is a cheaper experimental approach than producing the device required by Equation 3.10. As a ground truth, an image of a point source is obtained and the MTF is computed using Equation 3.6. This is the benchmark against which Equation 3.8 (proposed method) and Equation 3.10 (conventional method) will be tested against. While it would also be useful to do this experimentally, it is really difficult to manufacture a PSF. In fact, several different PSFs would need to be manufactured, as shall be seen shortly. Furthermore a device with decreasing bar widths and distances are costly, time consuming and for this comparison several of those would be needed as well. Luckily, the truthfulness of this claim can put to a test with a simulation obtained from the image formation model. The ground truth objects studied that are to be imaged with the image formation model are presented in the following figure:

[*] Only three are discussed here, but there are more.

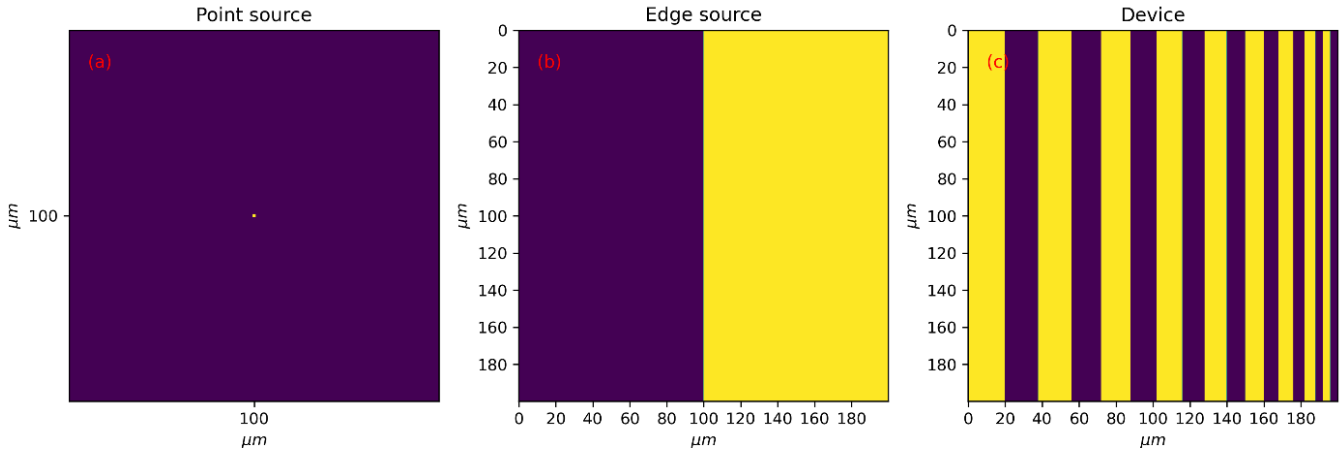


Figure 3-2 The ground truth objects that are to be imaged. (a) – A ground truth point source. (b) – a ground truth edge source. (c) – a ground truth device.

For this simulation, a $200\mu m \times 200\mu m$ field of view was chose. The point source in Figure 3-2 (a) is zoomed in so that it can be easily seen. In a similar fashion to the PSF simulation shown in Chapter 2, the effects of weak and strong material consumption will be investigated. Once the point source (seen in Figure 3-2 (a)) is imaged a PSF is obtained. The point source was placed at a position $(100\mu m, 100\mu m)$ away from the origin (see Figure 3-1 for a definition of the coordinate system used). After the PSF is created, a ground truth MTF is computed with the aid of Equation 3.6. Similarly, once the edge source (seen in Figure 3-2 (b)) is imaged an ESF is obtained. The approximation provided by Equation 3.8 can then be compared to the ground truth MTF. Finally, once the device is imaged an MTF can be derived with the aid of Equation 3.10. The distance between bars is $18,16,14,12,10,8,6$ and $4\ \mu m$. The width of the different bars is $20,18,16,14,12,10,8$ and $6\ \mu m$. The three MTFs will be compared in the case of weak and strong material consumption. Now, a table with the experimental conditions for this simulations is provided:

	Weak material consumption	Strong material consumption
Beam width 2σ (μm)	$14.8\mu m$	$4\ \mu m$
Width of sampled area	$\approx 12\ \mu m$	$\approx 12\mu m$
γ	1	1
k	2.3	3.3×10^3
Scan time Δt (s)	$0.5s$	$0.5s$
Stage velocities $v(m/s)$	$6\ m/s$	$6\ m/s$
Pixel sizes Δp (μm)	$3\ \mu m$	$3\ \mu m$

Table 3-1. A summary of the experimental parameters used in this simulation.

Two simulations are performed on each of the three objects shown in Figure 3-2 – one in the case of weak material consumption and in the case of strong material consumption. In order to keep the MTF calculations consistent, each of the objects is imaged at the same pixel spacing of $3\mu m$ in both x and y. For this to happen a stage velocity of $6\ \mu m/s$ was chosen combined with a scan time of $\Delta t = 0.5\ s$. The difference between strong and weak material consumption wis simulated by setting the desorption coefficient $k = 2.3$ in the case of weak material consumption and to $k = 3.3 \times 10^3$ in the case of strong material consumption. It should be noted that that different beam widths were used in this simulation as well. For the case of weak material consumption a beam width of $2\sigma = 15\ \mu m$ was chosen and strong material consumption was simulated with a beam width of $2\sigma = 4\ \mu m$. This is because the extremely high value of the desorption coefficient causes the beam to desorb material from the tails of the Gaussian distribution, resulting in a much wider crater size. Thus, in order to keep the horizontal and vertical widths of the sampled areas similar in both cases, the beam width was adjusted.

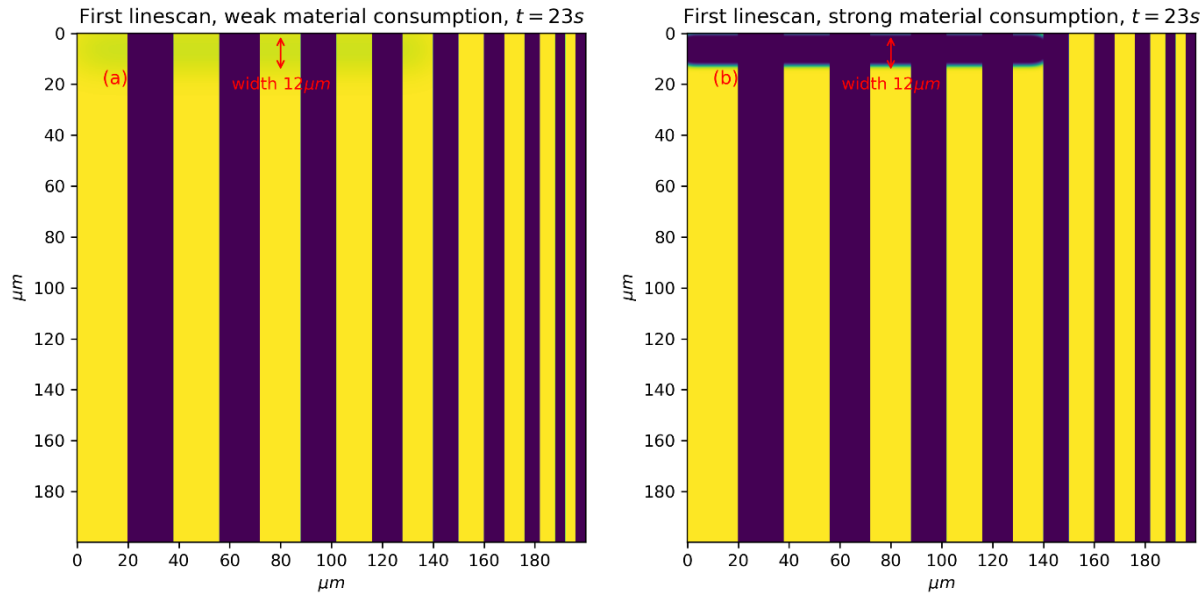


Figure 3-3. A snapshot of the image formation simulation. (a) – weak material consumption at $t = 23s$ from the start of the experiment. (b) – strong material consumption at $t = 23s$ from the start of the experiment.

This is illustrated in Figure 3-3 (a) and (b) where the red arrow shows the width of the sampled area in the y direction. This figure is a snapshot of the image formation simulation for the device shown in Figure 3-2 (c) taken

at $t = 23s$ from the beginning of the experiment. The difference between weak and strong material removal is also clearly illustrated – it can be seen in Figure 3-3 (a) that the device is only very slightly altered after interacting with the beam, whereas in Figure 3-3 (b) it is obvious that a large portion of the material was removed. It should also be pointed out that when strong material removal was studied it was noticed that the placing of the PSF was very important. Subpixel shifts in the location of the point source altered the output PSF. Thus, in the case of strong material removal, three different point sources were used, each shifted by a subpixel amount (roughly half a pixel). The final PSF was the average of the three subpixel shifted point sources. This is illustrated in the following figure.

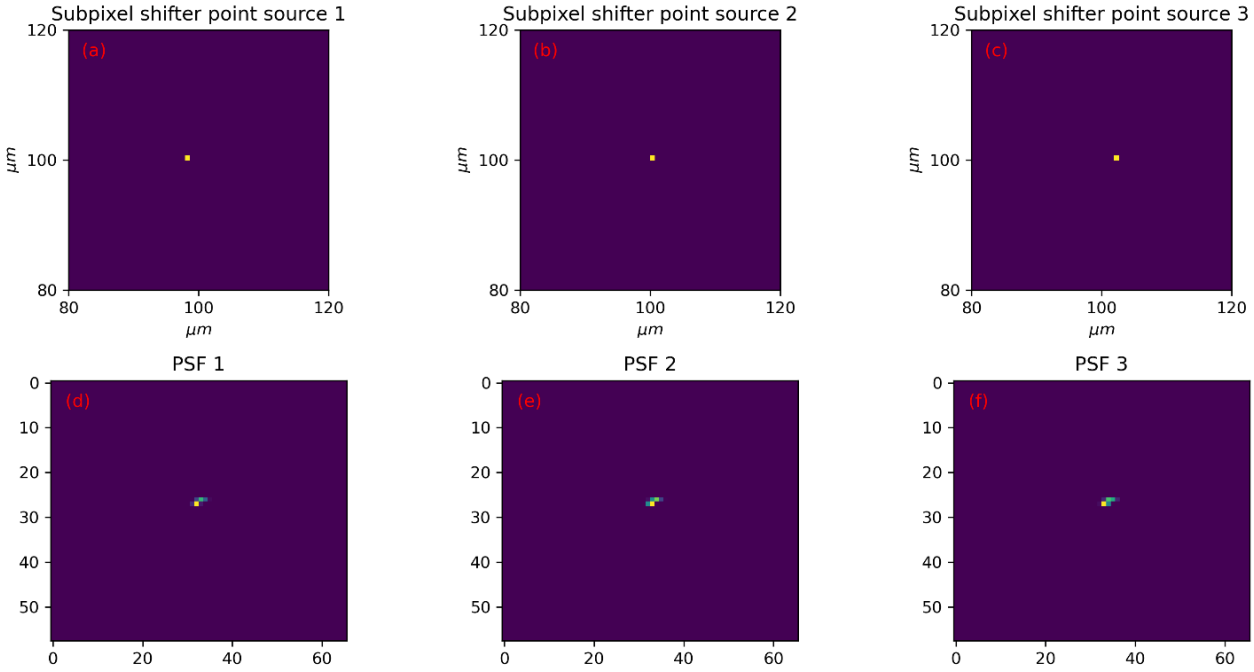


Figure 3-4 (a), (b), (c) – subpixel shifted point source. (c), (d), (f) – the obtained PSFs.

One can infer from the figure above that each of the PSFs appears to have a slightly different shape. Thus, to obtain a more accurate ground truth PSF estimate, all three PSF are averaged. There was no need to do this in the case of weak material removal, as the effect of a subpixel shift there was the opposite – after a short investigation it was found that PSFs generated in the case of weak material removal have almost identical shapes but just appear to be slightly shifted. Now, using Equation 3.6 the ground truth MTFs can be computed. The results are shown in the next figure:

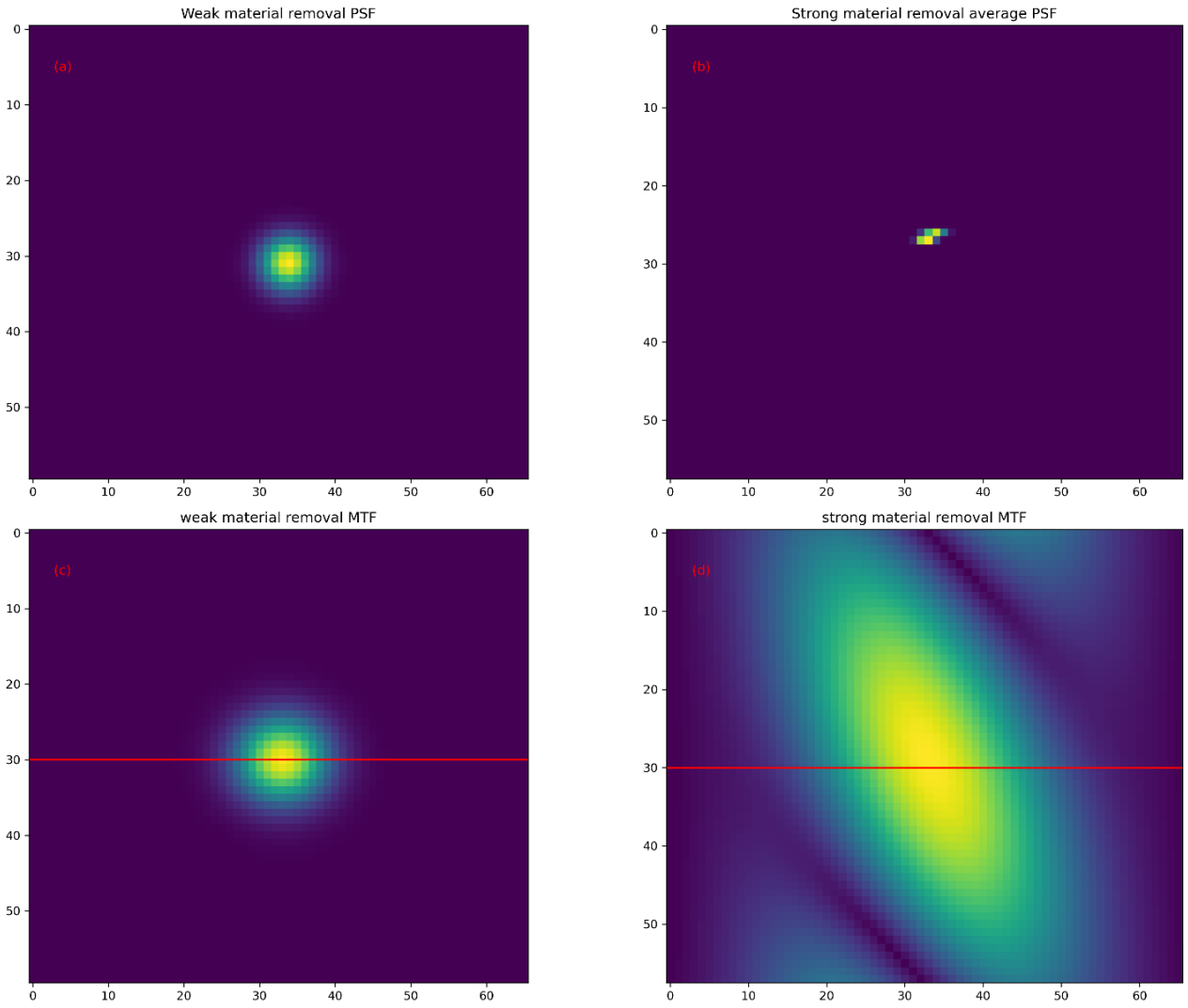


Figure 3-5 (a) – ground truth PSF in the case of weak material consumption. (b) – ground truth PSF in the case of strong material consumption. (c) – ground truth MTF in the case of weak material consumption. (d) – ground truth MTF in the case of strong material consumption.

The obtained PSFs for weak material removal and strong material removal can be seen in Figure 3-5 (a) and Figure 3-5 (b) respectively. The PSF in Figure 3-5 (b) is the averaged PSF from the previous slide. As for the MTFs calculated by Equation 3.6, those are shown in Figure 3-5 (c) and Figure 3-5 (d), corresponding to weak and strong material consumption. The red line in the middle indicates MTF_x that appears in Equation 3.8 and Equation 3.10. Thus, since this line is of particular interest as it will be used to compare the performance of the method for measuring an MTF proposed in this thesis (encapsulated by Equation 3.8) and the traditional approach (described by Equation 3.10). This figure also demonstrates the benefit of measuring resolution through an MTF obtained from a PSF measurement – the resolution capabilities can be measured in any desired direction as the output MTF is two dimensional. Unfortunately, both Equations 3.8 and 3.10 can only measure resolution in one particular direction. Thus, if for example an asymmetric beam is used, resulting in a non-symmetric MTF and therefore a different

resolution response in x and y, several different edge/device imaging experiments need to be performed, whereas only one PSF experiment is sufficient*

3.2.3 Loss of resolution due to blur

Next, the results from the edge source and device are presented. The results reveal why resolution is limited by beam blur in the case of weak material consumption and why features finer than the width of the beam can be detected when material removal is strong. Strong material removal are the typical experimental conditions used in MALDI[151], while weak material removal is a well-known condition in SIMS[68].

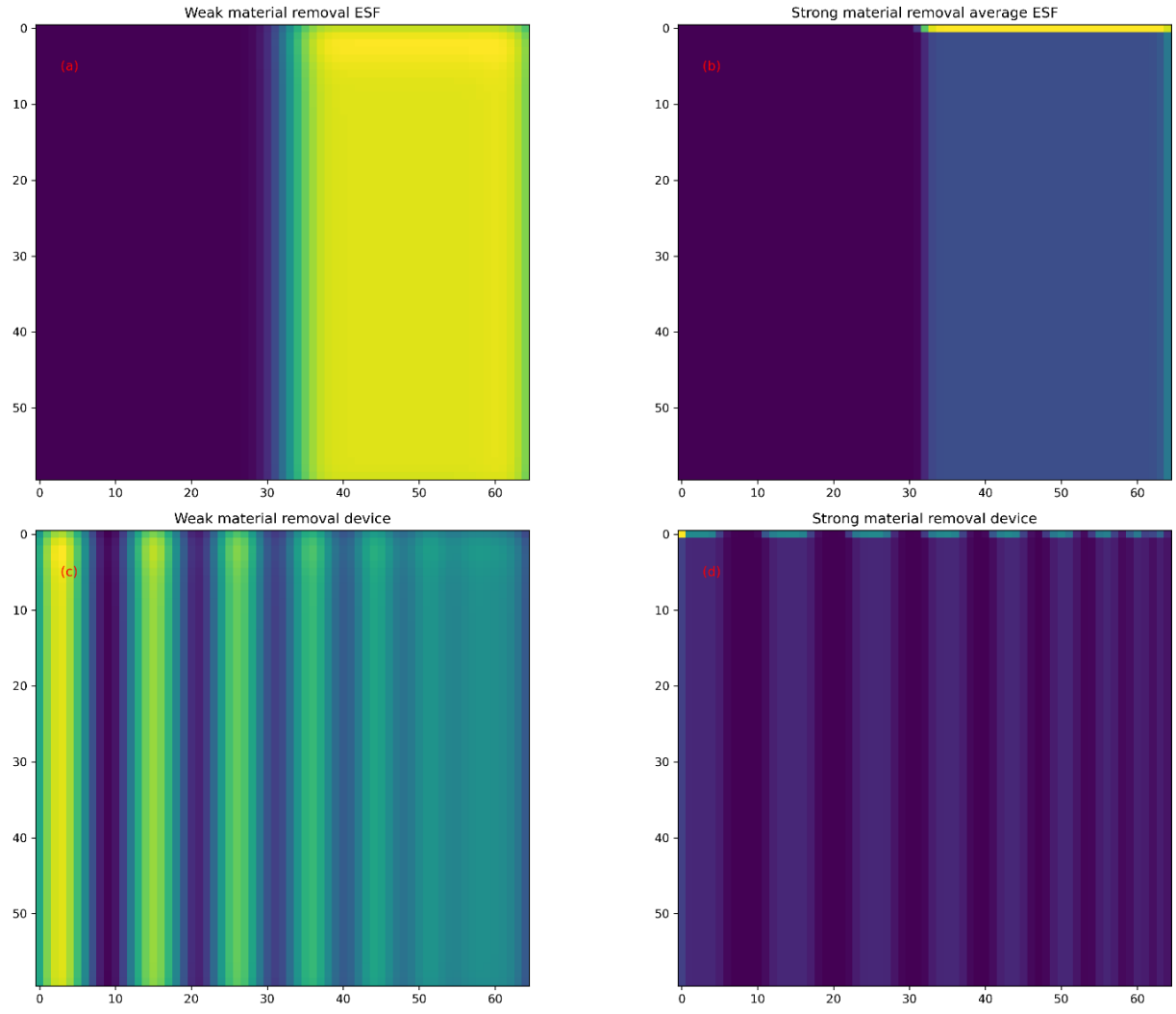


Figure 3-6 (a) – ESF obtained in the case of weak material removal. (b) – ESF obtained in the case of strong material removal. (c) – device imaged with weak material consumption. (d) – device imaged with strong material consumption.

* Excluding the fact that several subpixel shifted PSFs are needed in the case of strong material removal.

The ESF shown in Figure 3-6 (a) has a noticeable blur, while the ESF imaged under the conditions of strong material consumption, shown in Figure 3-6 (b), has a very sharp transition. Concurrently, the image of the device in Figure 3.6 (c), which was obtained using weak material consumption, has noticeable blur. The reader will notice that some of the bars that are close to each other are no longer distinguishable. Thus, resolution has been lost due to blur. On the other hand, the image of the device acquired with strong material consumption (shown in Figure 3-6 (d)) has all of its bars distinguishable. Thus, it is possible to detect features finer than the width of the beam. Notice that the first row and column in both Figures 3-6 (b) and (d) are much brighter than the rest of the image. This is because, due to material removal effects, for these sets of pixels much more material was collected compared to the pixels that belong to the rest of the image. These artifacts are always observed in real experimental data that corresponds to oversampling (from the point of view of MSI) with strong material removal. They are typically removed so that the rest of the image can be seen much clearer. Nevertheless, the author of this document has decided to keep them so that the qualitative aspects of the image formation model can be demonstrated. However, when Equation 3.8 is to be used for the purpose of calculating an MTF, the problematic pixels will be omitted. It should be noted that in order to calculate the MTF from an ESF, the ESF is averaged over all linescans in the vertical direction. This is a particularly important step, as averaging allows for noise to be removed which makes the numerical differentiation step and subsequent curve fitting steps to be perform better. In fact, for curve fitting to perform well it is vital to obtain as many linescans as possible for low SNR images. This will be demonstrated later. However, these images have not been corrupted by noise averaging in this case is not that important but later on it will be of great importance to obtain a sufficient amount of linescans so that an MTF can be computed accurately.

Next, a demonstration of how to compute an MTF from Equation 3.10 is provided

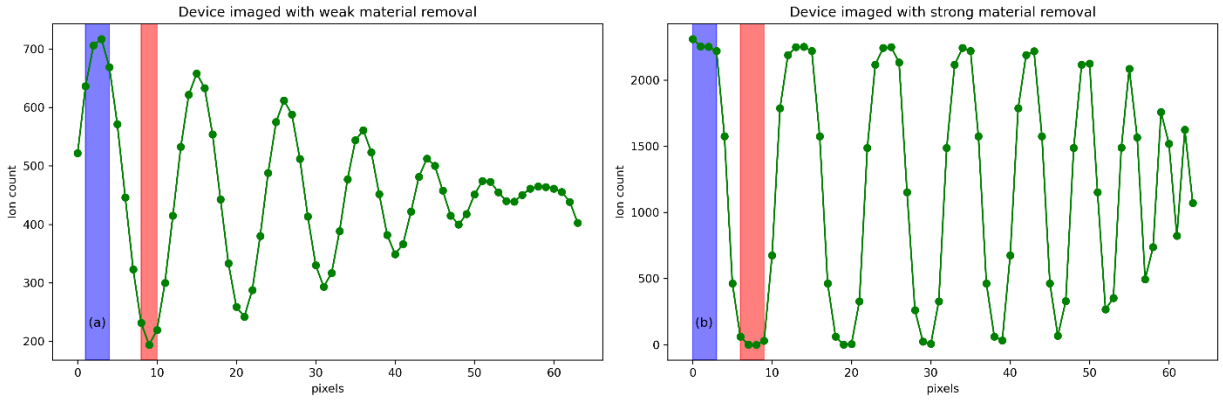


Figure 3-7 (a) – An average profile of a resolution device imaged with weak material removal. (b) – an average profile of a resolution device imaged with strong material removal.

The data shown in Figure 3-7 (a) and Figure 3-7 (b) is a an average profile of the resolution device imaged with weak and strong material consumption respectively. The shaded blue and red shaded rectangles show how the contrast is computed at a given frequency, where the contrast was defined by Equation 3.9. In particular, the average

of all the data points within the blue area corresponds to I_{max} and the average of all the data points withing the red area is I_{min}. Once the contrast is computed for this frequency, it needs to be computed for all the other frequencies – these correspond to the contrast change between the next pair bars, etc. It was already mentioned that the frequency is simply the reciprocal of the distance between bars – this needs to be computed as well. It is apparent in Figure 3-7 (a) that resolution is lost due to blur as the last set of three bars are no longer resolved, while they appear to be resolved in Figure 3-7 (b). This should manifest in the MTFs of the respective experiments. Once the contrasts have been computed, the contrast change as a function of frequency needs to be computed for the ground truth object as well. In this simulation the contrast change of the ground truth device is unity.

Now, the proposal that the edge method can perform better than the conventional method for recovering the MTF is verified. The ground truth MTF were already computed with Equation 3.6 and presented in Figure 3.5. The only thing needed is to apply Equation 3.8 on the edge images. As for the images of the resolution device, Equation 3.10 and the methodology outlined in the previous paragraph are applied. The results are summarised in the following figure:

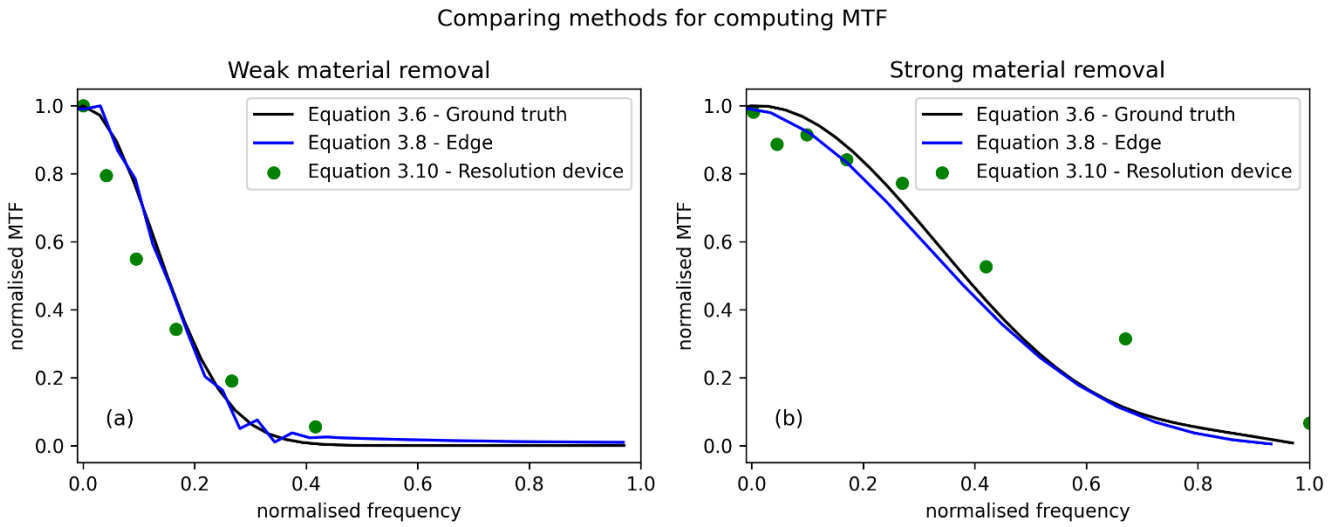


Figure 3-8 Comparing different approaches to computing an MTF to a ground truth MTF for (a) – weak material removal, (b) – strong material removal.

It is clear from Figure 3-8 (a) that the edge method (drawn in blue) provides a really good approximation to the ground truth MTF (drawn in black). The two solid curves are almost identical. The green data points represent the result obtained from the traditional approach for an MTF computation using a resolution device. This is the current best practice used in the field[67,69,137]. While they follow the same general behaviour as the ground truth (solid black curve), it is clear that they do not accurately capture the MTF. Notice that both solid curves vanish (the green scatter points almost vanish as well) at a frequency of 0.4. This is the resolution frequency – the imaging system cannot transmit frequency from the object higher than this critical point f_c .The distance corresponding to this frequency is

$d = \Delta p2/f_c$, which this case turns out to be $15\ \mu m$. This almost matches the beam width used in this simulation, which was $14.8\ \mu m$ (see Table 3.1). Thus, it has once again been demonstrated that under the conditions of weak material removal resolution is limited by the width of the beam. While this is a well-known fact[67–69], it is a good sign that our image formation model can also confirm this.

At the same time the image formation model can explain what happens in the presence of strong material consumption. This scenario is shown in Figure 3-8 (b). It can be seen that the MTF computed from a step edge (solid blue curve) almost fits perfectly the ground truth MTF (solid black curve). Thus, it can be seen that Equation 3.8 provides a reasonably good approximation for an MTF computation. On the other hand, the green scatter points, which speak on behalf of Equation 3.10, seem to perform well at low frequencies but really poorly at higher frequencies. This could be attributed to the lack of data points when averaging over I_{max} and I_{min} in the contrast calculation. In fact, it should also be pointed out that calculating these contrast changes can be cumbersome unless an automated approach is developed. For example, in a real experiment there are often thousands of single ion images. Thus, if this method is to be applied routinely an automated approach ought to be used. Nevertheless, it is obvious that the edge approach (solid blue curve generated by Equation 3.8) performs much better than the traditional approach[67,69,137]. Notice that the MTF shown in Figure 3-8 (b) only approaches zero as the frequency approaches unity. In contrast, the MTF in Figure 3-8 (a) vanished at a certain critical frequency f_c. This means that an imaging system operating under the conditions of strong material removal is capable of detecting features finer than the width of the beam[130]. Therefore, image blur has been minimised and the use of the 86-14% criterion as a resolution metric is not appropriate as it will lead to distances that exceed the Nyquist limit (distances smaller than two pixels)[131,132]. The theoretical limit for resolution is placed by the Nyquist frequency (or twice the pixel size), although one should be aware of the fact that in the absence of blur aliasing might occur* - this was demonstrated in Chapter 2. The practical limit however will be placed by noise[69,137]. Thus, intuitively one would expect the resolution limit in the presence of noise to be sought in a similar way as that in the presence of blur – by finding a critical frequency f_c. Very soon a method for doing this will be developed.

To conclude this section, two methods for computing an MTF were compared using the image formation model outlined in Chapter 2. One method uses Equation 3.8 and a sharp step edge and the other, traditionally applied method uses a specially manufactured resolution device and Equation 3.10. It was demonstrated that in two different experimental conditions – weak and strong material removal, the edge approach performs better than the traditional approach. In addition, the traditional approach is costly, time consuming (both in terms of sample preparation and analysis), difficult to automate and can only output a limited number of data points. The proposed method on the other hand is cheaper, quicker (both in terms of sample preparation and analysis), easy to automate and the number

* The appearance of features smaller than the pixel size into features that are larger than the pixel size. These features are not accurate representations of the original features.

of data points is limited by the half the size of the image. All of this combined allows for a better estimate of the ESF. In addition, this method can also be applied on data sets where a sharp step edge feature is found, such as tissue imaging data sets. The limitations of the algorithm to be developed on its applications in tissue imaging will of course also be explored in this work. On the other hand, the resolution device has one particular advantage – it offers a visual explanation for the loss of resolution due to blur. It can also be used to demonstrate how the ability to distinguish between features deteriorates in the presence of noise.

3.2.4 Loss of resolution due to noise and blur

Every measurement contains an uncertainty. When a mass spectrometer measures the total number of particles that have been extracted from the surface between two times some uncertainty is introduced. In Chapter 2 it was shown that integrating a peak in the mass spectrum gives rise to image noise. Two main noise models were investigated – Poisson noise, arising from the uncertainty of the detector when counting particles, and combined noise. The combined noise model took into account the fluctuations in the peak height, which could be introduced due to a number of factors – in the case of MALDI craters have a slightly different shape, leading to a slightly different number of collected particles per crater and thus slightly different peak heights. In the case of DESI variations in the thin liquid layer could result in variations of the number of progeny droplets emitted. The mass spectrometer itself has a transmission coefficient, which itself could be thought of as a random variable. Ionisation reactions are also a stochastic process and there is a natural fluctuation in the number of ions produced. All of these mechanisms can lead to a fluctuation in the peak amplitudes. In terms of the image formation model, it was demonstrated in Chapter two that integrating corrupted peaks corrupted by Poisson and combined noise was equivalent using an additive signal dependant noise model. The noise function η was shown to be well approximated by a normal distribution centred at zero. In the case of Poisson noise η has linear variance and in the case of combined noise η has quadratic variance. This lead to SNR curves that had a drastically different shape. At high intensities images corrupted with Poisson noise had a very strong SNR, whereas images corrupted with combined noise had a substantially lower SNR. This of course means that the loss of resolution due to noise will be different for the two noise models. The images produced with the image formation model shown in the previous section were not corrupted by noise. However, they served a good purpose in demonstrating how resolution can be limited by blur. The image of the resolution device provided a clear visual proof for this, and all three systems were used for an MTF calculation to demonstrate the resolution performance quantitatively. Now, the images of the resolution device shall be corrupted by the two noise models. This will show how resolution deteriorates in the presence of noise. Moreover, the reader will be familiarised with the difference between the two noise models and will become convinced that this difference is striking and plays a crucial role for spatial resolution. The following table summarises the parameters used for the noise simulation.

	a	b	$Intensity$	SNR
Poisson noise, weak material removal	1	0	5×10^2	7.1
Poisson noise, weak material removal	1	0	1×10^3	31.6
Poisson noise, weak material removal	1	0	1×10^5	316.2
Combined noise, weak material removal	300	0.02	5×10^2	0.4
Combined noise, weak material removal	300	0.02	1×10^3	1.8
Combined noise, weak material removal	300	0.02	1×10^5	6.6
Poisson noise, strong material removal	1	0	5×10^2	7.1
Poisson noise, strong material removal	1	0	1×10^3	31.6
Poisson noise, strong material removal	1	0	1×10^5	316.2
Combined noise, strong material removal	300	0.02	5×10^2	0.4
Combined noise, strong material removal	300	0.02	1×10^3	1.8
Combined noise, strong material removal	300	0.02	1×10^5	6.6

Table 3-2. A summary of the parameters for the two noise models applied on the images of the resolution device.

The images of the resolution device obtained under weak and strong material consumption were corrupted with the two noise models at three different intensities. The intensities chosen were $I = 50, 10^3, 10^5$ counts per pixel. The final output was twelve different images – three per noise model, ranging from low to high intensity. The parameters for each noise model can be seen in Table 3-2. It should be noted that these parameters are close to real world experimental parameters obtained from different modalities. This will become apparent once some real data is analysed in the Chapters to follow. Thus, this simulation can be considered an accurate depiction of the interplay between blur and noise for different noise models and different burs and the consequence that these parameters have for spatial resolution. It should be noted that the bright pixels that appear when oversampling with material removal where removed so that the bars in the resolution device can be visible. The SNR for each image is also shown in Table 3-2. The values for the SNRs were computed with the aid of the equations derived in Chapter 2.4 (shown in Table 2-3). It is clear that Poisson noise dwarfs the combined noise model in terms of SNR. For example, at an average pixel intensity of 1×10^5, Poisson noise has an SNR of ≈ 316, while at the same intensity the combined noise model has an SNR of 6.6, which is almost fifty times lower. While such calculations can reveal information about the noise models, it is also useful to visually inspect the output images. The salient differences between the two noise models applied to different blurs and intensities become even more apparent when the images are examined. The twelve images are shown in the following figure:

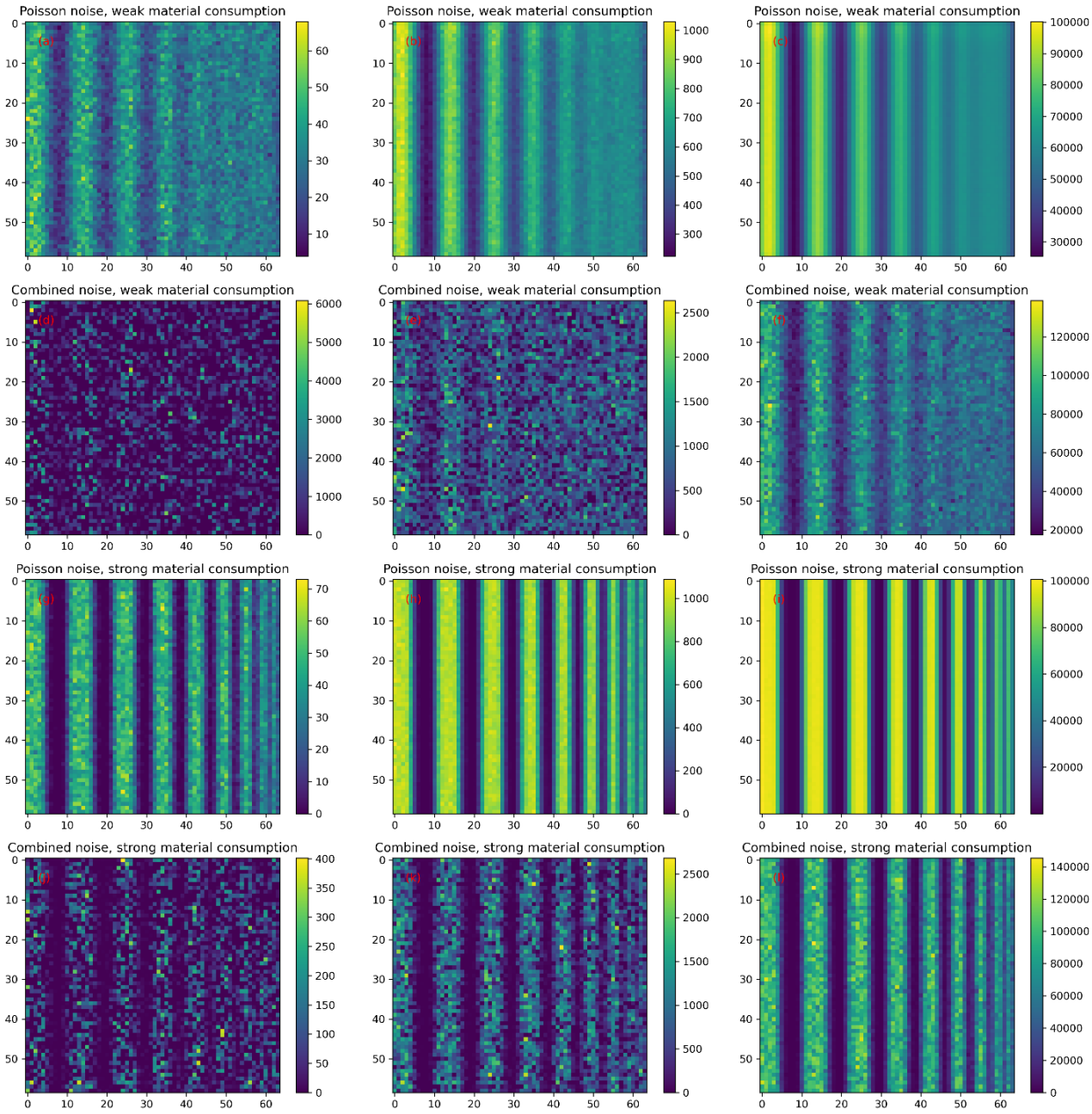


Figure 3-9 (a), (b), (c) – In increasing order of intensity – resolution device imaged under weak material consumption conditions and corrupted with Poisson noise. (d), (e), (f) – In increasing order of intensity – resolution device imaged under weak material consumption conditions and corrupted with combined noise. (g), (h), (i) – In increasing order of intensity – strong material consumption, Poisson noise. (j), (k), (l) – In increasing order of intensity – strong material consumption, combined noise.

The three images contained within the top row of Figure 3-9 correspond to the experimental conditions described in the first three rows of Table 3-2, the images contained in the second row correspond the rows four, five and six of the same table, etc. As mentioned previously, Poisson noise is negligible at high intensities. This can be easily verified upon reviewing Figure 3-9 (c) and Figure 3-9 (i), where the results for Poisson noise at high intensity ($I =$

10^5) at significant blur (weak material consumption) and minimised blur (strong material consumption) are shown respectively. Both images have an SNR of ≈ 316 and both almost perfectly resemble the original noiseless images shown in the previous subsection in Figure 3-6 (c) and Figure 3-6 (d). Thus, it can be concluded that in the presence of Poisson noise, at high intensities resolution is completely limited by blur. At low intensities however ($I = 50$), Poisson noise can lead to the loss of spatial information. This can be verified when Figure 3-9 (a) and Figure 3-9 (g), where low intensity Poisson noise images corresponding to significant blur and minimised blur are shown respectively. Both images have an SNR of 7.1. The ability to distinguish between the last four bars of the resolution device in the image shown in Figure 3-9 (a) has been lost. This is an example of how resolution can be lost both due to noise and blur. On the other hand, when blur is minimised only the last two or three bars cannot be distinguished in the image shown in Figure 3-9 (g). This is as example of loss of resolution due to noise only, as blur has been minimised due to effects of material removal (see the MTFs shown in Figure 3-8).

As for the effects of the combined noise model on the loss of spatial resolution, in the high intensity regime ($I = 10^5$), the predicted SNR is much lower than that of Poisson noise. This can be verified in the images shown in Figure 3-9 (f) and Figure 3-9 (i), which correspond to significant and minimised blur respectively. According to table 3-2, the SNR of those images is 6.8. Indeed, the ability to differentiate between the last three or four bars in Figure 3-9 (f) has been lost due to the effects of blur and noise. On the other hand, only the last couple of bars appear to be unresolved in Figure 3-9 (i), since blur has been minimised and only noise leads to the loss of spatial information. Notice that at an average intensity of $I = 10^5$ both images have very similar SNR metrics to their low intensity ($I = 50$) Poissonian counterparts shown in Figure 3-9 (a) and Figure 3-9 (g). Not only that, but the images look strikingly similar and appear to have a similar loss of resolution due to noise and blur. The fact that the two sets of images exhibit a similar loss of resolution when several orders of magnitude apart in terms of average pixel intensity strongly suggests that the combined noise model is much more detrimental for spatial resolution than Poisson noise. In fact, in the case of Poisson noise, even the images in the middle intensity regime with $I = 10^3$, shown in Figure 3-9 (b) and Figure 3-9 (h), seem to outperform the high intensity ($I = 10^5$) combined noise images seen in Figure 3-9 (f) and Figure 3-9 (i). In terms of SNR, the middle intensity regime ($I = 10^3$) have an SNR of 31.6, which is almost five times higher than the combined noise images at high intensity ($I = 10^5$). It gets even worse when the lower intensity combined noise images are examined. Notice that is impossible to distinguish between any of the bars in the image of the resolution device with maximised blur (imaged under the conditions of weak material consumption) at low intensities ($I = 50$), shown in Figure 3-9 (d). At medium intensities ($I = 10^3$), it may be said that some of the bars become distinguishable again. As for the low and middle intensity regimes of combined noise in the case of strong material removal, since blur has been minimised it is possible to distinguish between the bars. This can be seen in Figure 3-9 (j) and Figure 3-9 (k). It should be pointed out that the SNR of the low intensity image in Figure 3-9 (j) is 0.8. This implies that the average signal intensity is weaker than the noise

standard deviation – the signal is buried beneath noise at this point. However, the bars can still be distinguished as the noise is signal dependant and vanishes entirely when the signal also vanishes. Thus, although the bars appear to be distinguishable, what appears in the non-zero pixel is technically only noise. Thus, in a very peculiar way, the bars become distinguishable only because the noise vanishes when the signal vanishes. Because the same structure is repeated vertically for roughly sixty pixels it becomes very easy for the human eye to see the pattern of the bars. To convince the reader that the nonzero pixels are pure noise, a horizontal linescan is superimposed on the ground truth intensity signal in the following figure:

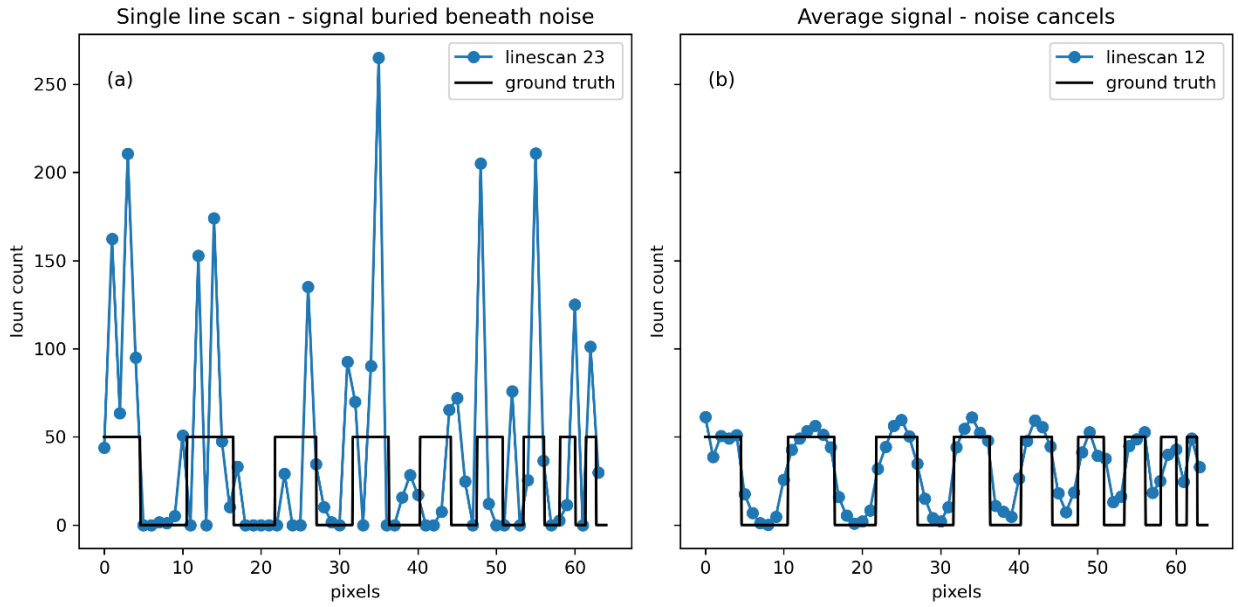


Figure 3-10 (a) – the 23^{rth} horizontal linescan of image Figure 3-9 (j). (b) – average profile cancels noise out and signal is recovered.

In Figure 3-10 the black line represents the ground truth signal. As the signal vanishes the noise also vanishes, making it possible to distinguish between the bars. Notice that in Figure 3-10 (a) when the black line reaches a constant value of 50, the signal (represented by blue dotted line) begins to fluctuate really strongly and the constant surface of the bars cannot be recovered. This is because the signal is weaker than the noise function. On the other hand, if an average profile is produced, shown in Figure 3-10 (b), the fluctuations from the noise will cancel out and the real signal can be recovered. Thus, in a single linescan taken from that image, the non-zero pixels are dominated by noise. The only reason why it is possible to distinguish the bars is because noise vanishes with the signal. Had the ground truth value of the density not been zero between the bars, the signal and therefore the noise would not vanish. And had the ground truth density not consisted of long vertical bars, but smaller features instead, the human eye would not be able to pick up the structure of the bars.

This study of the interplay between noise and blur allowed for the examination of the loss of resolution under different amounts of blur and different noise models. This examination was not quantitative, but the loss of resolution is certainly different when the blur and noise levels differ. The nature of noise corrupting the images also plays a very important role. It could be claimed, that the best resolution is achieved in the presence of Poisson noise and strong material removal (blur is minimised), followed by Poisson noise and weak material removal (blur is strong), combined noise with minimised blur and finally combined noise with strong blur. In the next section a method for computing resolution based on the interplay between noise and blur is provided.

3.3 Calculating spatial resolution

It could be said that all of the work done so far in this thesis was for the sake of this section. The development of an image formation model and the study of different noise models showed visually that resolution can be limited by blur and SNR. The image formation model also explained why using the blur in an edge can be useful for some modalities, but fail as resolution metric in modalities with strong material removal. This meant that a new resolution metric must be established. With all of the tools acquired so far it is time to develop a method for computing what the minimum distance between features is such that they can be distinguished. This distance is spatial resolution and this section is the heart of this thesis. For the construction of this algorithm, the use of a sharp step edge is chosen, as it approximates the ground truth MTF quite well in scenarios with weak and strong material consumption.

A particularly useful way of computing resolution as a function of blur was the MTF. As a reminder, the MTF characterises how much signal per frequency can the imaging system transmit from the object to the image. More precisely, the MTF describes the number of hits a mass spectrometer will register per unit spatial frequency. The idea of a critical frequency f_c was laid down when it was seen that the MTF can vanish, which meant that all frequencies above f_c are not transmitted. This means that no change in signal above f_c will be registered. Thus, those frequencies are blurred out in the image. One could ask if a similar notion of a critical frequency f_c can be established in the presence of noise. This would require in a similar way to look at the amount of noise per frequency. If so, then the noise spectral decomposition could be used in conjunction with the MTF to find a resolution frequency that depends on both blur and noise.

3.3.1 The noise spectral density (NSD)

A method for characterising the properties of noise in real space was already shown in Chapter 2. This involved simply using empirical statistics to find the mean, variance and standard deviation. It is critical that these calculations are performed on an area where the signal is uniform/homogeneous.

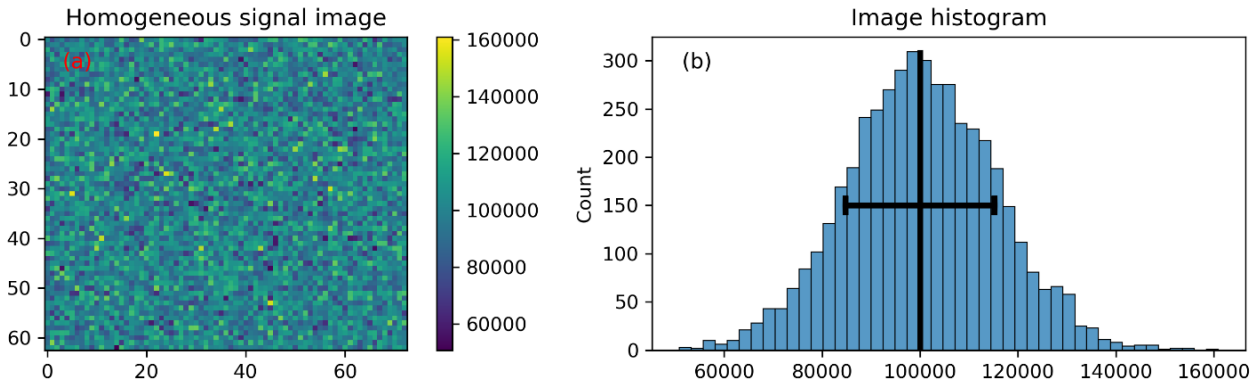


Figure 3-11. (a) – image of a homogeneous area. (b) – histogram of the image, black horizontal line shows the standard deviation and black vertical line is the average.

An intuitive explanation of the statistics behind these calculations can be developed with the aid of Figure 3-11. A noisy image generated with the aid of the combined noise model with the parameters used previously can be seen in Figure 3-11 (a). The histogram of the image is presented in Figure 3-11 (b), where the black horizontal and vertical lines depict the standard deviation and the average signal intensity respectively. The SNR is simply the ratio of the two. Since the noise is signal dependent, as the mean intensity increases so does the standard deviation. Thus, the histogram widens as its mean increases. This was described in Chapter 2.4. Therefore, it is imperative that a homogeneous area is picked when estimating the noise statistics. It should also be pointed out that a sufficient amount of pixels need to be used in order to obtain an accurate estimate of the mean, variance and/or standard deviation.

An alternative approach to describing the realisations of a random variable can be envisioned in frequency space. The object that allows for the description of noise in frequency space is called the noise spectral density (NSD). For a two dimensional image, the NSD is defined as:

$$S(\nu_x, \nu_y) = \lim_{\Delta x, \Delta y \to \infty} \frac{1}{\Delta x \Delta y} \langle |\mathcal{F}[I(x,y)]|^2 \rangle \qquad \text{Eq. (3.11)}$$

Where $I(x,y)$ is the noisy image, $\Delta x, \Delta y$ are the dimensions of the image, ν_x, ν_y are the spatial frequencies and the angle brackets denote an ensemble average. The NSD is a great way of characterising noise which is zero centred and stationary – meaning its variance does not depend on the spatial positions x, y. It is obvious that this is not the case for a general MSI image. However, if a homogeneous image, such as the one shown in Figure 3-11 (a) is studied, since the intensity is fixed the NSD may be used. It is also evident from Equation 3.11 that an ensemble average of many such images needs to be obtained, with the dimensions of the images being as large as possible. This places some practical limitations and computing the two dimensional NSD can be a difficult task. Fortunately, the two dimensional NSD would be needed in the case of a two dimensional MTF. As a point source is difficult to

produce experimentally, an edge source is used to obtain an MTF in this thesis. Depending on the direction of the orientation of the edge, an approximation of a one dimensional MTF can be obtained. If the edge is aligned horizontally, an approximation of the MTF in the x direction is obtained. Thus, a two dimensional NSD is not required for the purpose of this work and the one dimensional equivalent can be used:

$$S(\nu_x) = \lim_{\Delta x \to \infty} \frac{1}{\Delta x} \langle |\mathcal{F}[I(x)]|^2 \rangle \qquad \text{Eq. (3.12)}$$

Where now $|\mathcal{F}[I(x)]|^2$ denotes the magnitude of the one dimensional Fourier transform of a given linescan and the angle brackets is the ensemble average over all linescans. Thus, instead of averaging over many homogeneous areas, now only an average over all linescans is required. The fact that for this averaging procedure only the pixels that contain a homogeneous area must be used is now repeated again; there exist noise estimates in literature that do not follow this rule[108]. Defined as such, the NSD has units of counts squared per frequency (or counts squared times pixel). This mathematical object tells us the power of the noise carried per unit frequency. The procedure for computing the NSD is shown in the following figure.

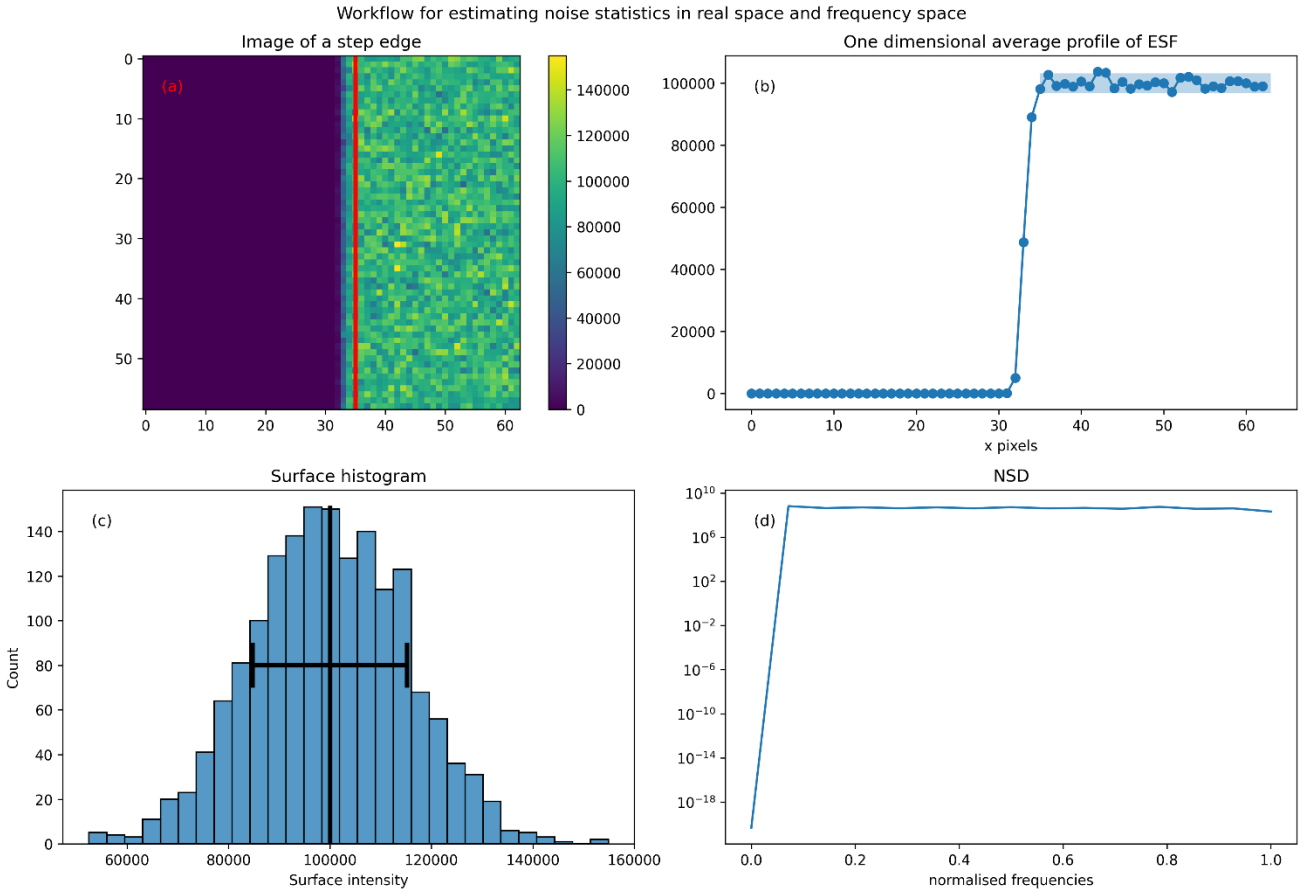


Figure 3-12 (a) – image of a sharp step edge with a homogeneous surface. (b) – an average profile resulting in a 1D ESF. (c) – histogram acquired from the edge surface. (d) – NSD computed from all the linescans of the edge surface.

Figure 3-12 (a) shows a two dimensional ESF generated via the image formation model and Figure 3-12 (b) shows the one dimensional ESF average. The sharp jump from zero to a signal is what helps us compute an MTF (the sharper the jump, the sharper the MTF). However, this jump introduces extra variance when estimating the noise statistics and only the homogeneous edge surface area should be selected. The beginning of the homogeneous edge surface considered for these calculations is at the right hand side of the vertical red line in Figure 3-12 (a). Alternatively, the shaded blue area in Figure 3-12 (b) also marks the homogeneous edge area considered in the statistical calculations, but this time in one dimension. It should be emphasised that Figure 3-12 (b) depicts an average 1D ESF. During the process of averaging the negative and positive noise contributions tend to cancel out – individual linescans are much more noisier (see Figure 3-10). Thus, care needs to be shown when computing the variance/standard deviation and NSD. If the averaged 1D ESF is used the computed SNR would be much higher as one is computing the noise of the average. Instead, the average of the noise should be computed. Thus, the image histogram shown in Figure 3-12 (c) is produced over individual linescans containing the edge surface. As for the NSD shown in Figure 3-12 (d), as per Equation 3.12 an ensemble average over all surface linescans containing the edge surface was used. The NSD can help study the nature of the noise. Notice that at a frequency of zero the NSD is also zero, indicating that the noise is zero centred. At high frequencies the NSD becomes constant, indicating that the noise function behaves like an additive Gaussian noise. Of course, this was already known as the intensity of the edge surface was fixed and at a fixed intensity the noise can be thought of as being stationary. An alternative explanation is that the standard deviation of the histogram shown in the histogram in Figure 3-12 (c) does not change and this is simply because the mean is fixed. Thus, when measuring resolution it is vital that a homogeneous area is selected so that both real space and frequency space estimates of the noise behaviour are punctual.

Since the noise from the edge surface can be thought of as a realisation of a random variable, each linescan can be thought of as a repetition of the same experiment[*] and therefore it would look differently. This of course is the main idea behind the empirical statistics shown in the histogram. It is interesting to point out that the empirical estimates can be obtained also from a frequency space approach. In particular, the variance and the NSD are related in the following way:

$$\sigma^2 = \int_{-\infty}^{\infty} \frac{N_0}{2} |H(\nu)|^2 d\nu \qquad \text{Eq. (3.13)}$$

Where $H(\nu)$ is the bandpass filter of the sampling system and $N^{\dagger}_0$ is the value of the NSD (see Figure 3-12. (d)). Since one is dealing with a digital system and it was already mentioned that a normalised frequency space is used,

[*] This is another reason why the system needs to be as homogeneous as possible.
[†] The factor of two comes from the folding around zero in frequency space.

where $f_N = 1$, then $H(\nu)$ is an ideal low pass filter and the limits of the integral in Equation 3.13 change from negative infinity to infinity to negative unity to unity. Then, the variance can be written as:

$$\sigma^2 = \frac{N_0}{2} \qquad \text{Eq. (3.14)}$$

And the standard deviation then becomes

$$\sigma = \sqrt{\frac{NSD}{2}} = \sqrt{\frac{N_0}{2}} \qquad \text{Eq. (3.15)}$$

Let us consider the physical meaning of the square root of the noise spectral density. The spectral density itself characterises the amount of power the noise carries per unit frequency. In terms of units, this can be thought of as counts squared per unit frequency (or counts squared times distance). Thus, it characterises the variance of the noise per unit frequency. On the other hand, the MTF has units of counts per unit frequency. If one wishes to compare the effects of signal transfer with the effects of noise transfer, the NSD ought to be expressed in terms of counts instead of counts squared. Therefore, $\sqrt{NSD/2}$ has units of counts per square root frequency and it is comparable to the MTF. The mathematical object in Equation 3.15 also has a rather nice physical interpretation – it describes the amount of noise standard deviation per unit root frequency. Alternatively, it is the root mean square (RMS) amount of noise carried per root frequency.

3.3.2 Calculating spatial resolution.

In the previous subsection it was shown that by imaging a sharp step edge various metrics related to resolution can be obtained. From the surface of the step edge real space estimates of the noise behaviour, such as mean, variance and/or standard deviation can be obtained. An image SNR can be also computed from the ratio of the signal mean and noise standard deviation. On the other hand, the surface of the sharp step edge allowed us to compute a noise spectral density. This was done by averaging of the square of the magnitude of the Fourier transform of all surface linescans. For an accurate estimate of those parameters it is imperative that the edge surface is as homogeneous as possible and that the jump in the edge transition is omitted. However, the jump in the edge transition is what is used to obtain an MTF. Calculating an MTF from a step edge was discussed in detail in the previous section. However, for the sake of completion, the workflow is presented in the following set of graphs.

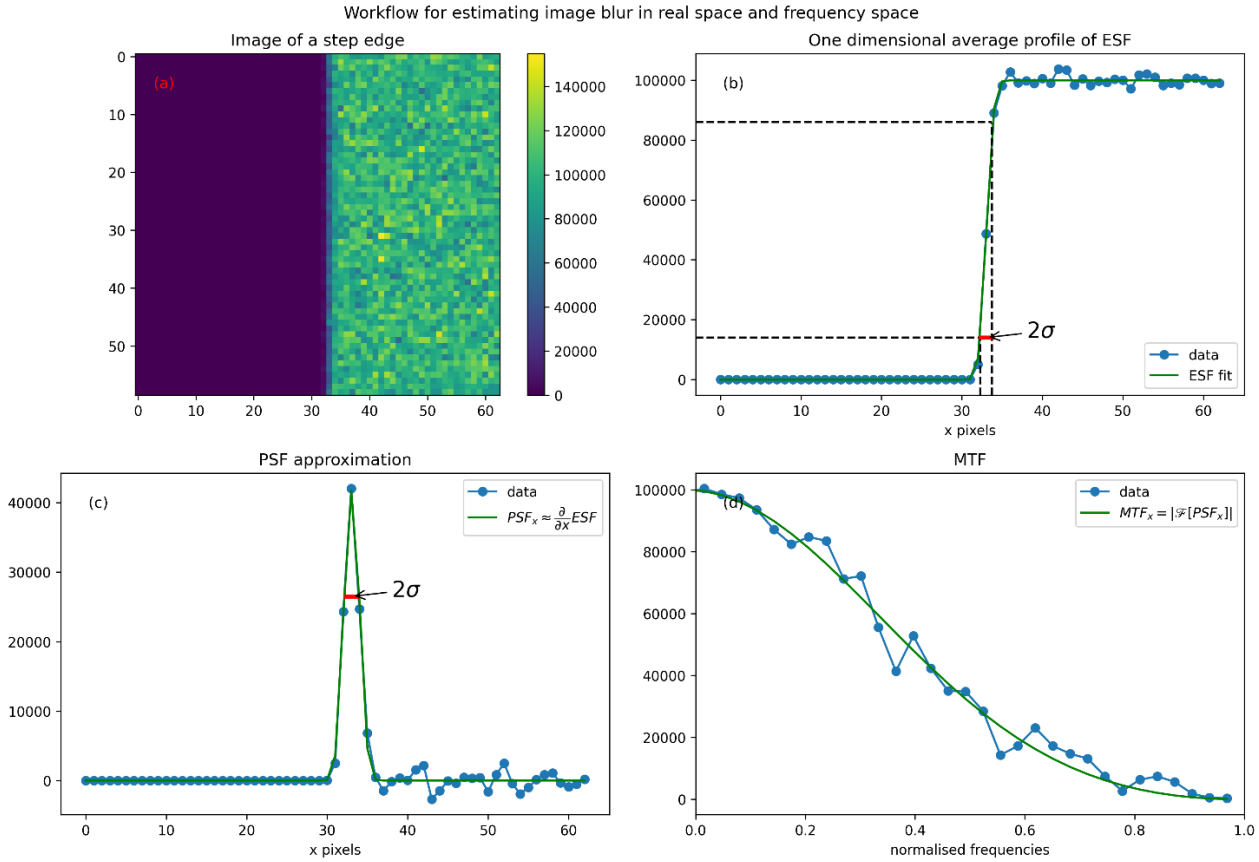


Figure 3-13 (a) – image of a sharp step edge with a homogeneous surface. (b) – average profile resulting in a 1D ESF. (c) – PSF approximation obtained after numerical differentiation. (d) – MTF obtained after computing the magnitude of the Fourier transform of the PSF.

Again, starting with an image of a sharp step edge, shown in Figure 3-13 (a), an average one dimensional profile of an ESF is produced, shown in Figure 3-13 (b). The black horizontal dashed lines in Figure 3-13 (b) correspond to the 86% and 14% of the average surface intensity intensity and the black vertical dashed lines correspond to the spatial positions at which the $86-14\%$ intensity change takes place. The thick red horizontal corresponds to the distance over which this intensity change takes place (the difference between the two dashed black horizontal lines). Theoretically, assuming that the edge profile is described by a Gaussian cumulative distribution function (CDF), the distance corresponding to the $86-14\%$ of the intensity change corresponds to 2σ (twice the standard deviation) of the Gaussian function[68]. To emphasise this, a text label $'2\sigma'$ with a black arrow pointing at this distance (thick red line) was added. The blue scatter points are connected with a line and represent the data, while the continuous green curve was generated after curve fitting. The equation used to fit the data is given by the following formula:

$$ESF = \frac{(I_1 - I_0)}{2}\left(1 + \mathrm{erf}\left(\frac{x-\mu}{\sqrt{2}\,\sigma}\right)\right) \qquad \text{Eq. (3.16)}$$

Where $I_1,\ I_0$ are the average edge surface intensity and average intensity of the area at the left hand side of the edge. In this case $I_0 = 0$, but in general there may a signal there, thus one allows for this term in Equation 3.16 so that curve fitting may produce good results in those scenarios. The positions of pixels are given by x and the parameter μ indicates the position at which 50% of the average surface intensity occurs. Finally, σ corresponds to half the distance depicted by the thick red line in Figure 3-13 (b). Thus, with the aid of curve fitting, the traditional $86 - 14\%$ can be obtained. In this particular case $2\sigma = 1.4$, which is smaller than two pixels and hence blur cannot be used as a resolution metric. The next step is to compute the numerical derivative of the average ESF. This is shown in Figure 3-13 (c), where the PSF is depicted. Again, the blue dots connected by a blue line represent the data and the continuous green curve represents the numerical derivative of Equation 3.16 after the parameters I_1, I_0, σ, μ have been extracted. The thick red line in Figure 3-13 (c) marks the 2σ distance and to signify this a text label has also been added. Note that this is the same distance as the one shown in Figure 3-13 (b). Finally, the MTF is computed by obtaining the absolute value of the fast Fourier transform (FFT) of the approximated PSF. The blue data points connected with a line are the data and the continuous green curve is the magnitude of the FFT of the numerical derivative of Equation 3.16. Notice that the measured image blur $2\sigma = 1.4$ falls outside of the normalised frequency range. As a reminder, unity on the frequency axis corresponds to the Nyquist frequency f_N, which corresponds to a distance of two pixels. Because the MTF describes the amount of signal transmitted per unit frequency and blur is minimised the MTF appears sharp. It is therefore expected that resolution is limited by noise.

But what can be done in order to quantify this? It was discussed that $\sqrt{NSD/2}$ can be interpreted as amount of RMS noise carried per root frequency, while the MTF is the amount of signal carried per frequency. Let us now consider the spectral decomposition of signal and noise into frequencies at the same time. To do this, let us investigate a low intensity and a high intensity image generated with a strong material consumption condition and corrupted with an additive noise model. Intensities of $I_1 = 10^5, 10^3$ are used (refer to Table 3-2). Then, the MTFs and squared NSDs of each image is plotted on the same graph:

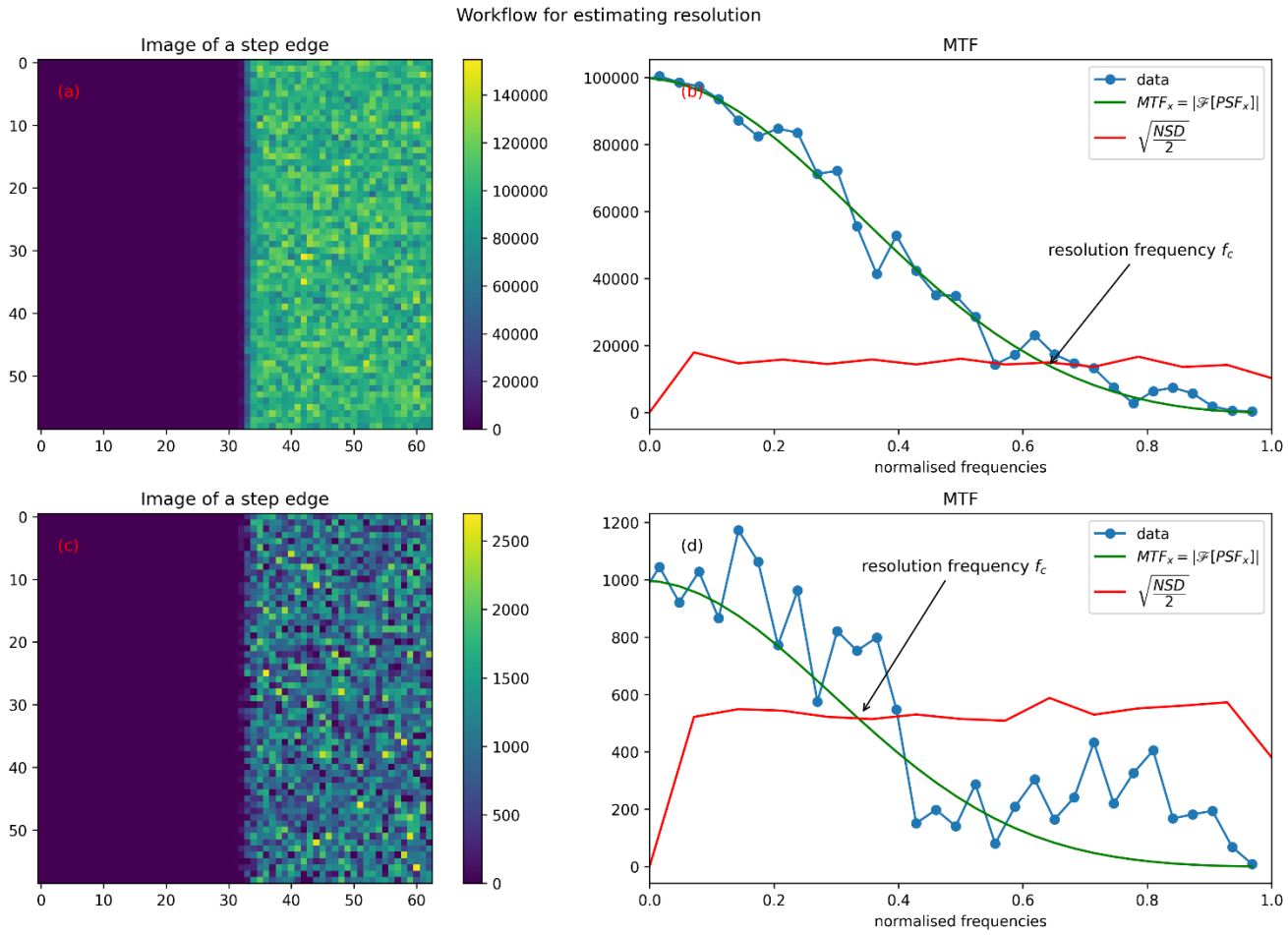


Figure 3-14 (a) – high intensity edge image. (b) – MTF and $\sqrt{NSD/2}$ at a high intensity. (c) – low intensity edge image. (c) – MTF and $\sqrt{NSD/2}$ at a low intensity.

The high and low intensity edge images are depicted in Figure 3-14 (a) and (b), while the superposition of the respective MTFs and $\sqrt{\mathrm{NSD}/2}$ are shown in Figure 3-14 (c) and Figure 3-14 (d). Notice that the square root of the NSD (solid red line) intersects the theoretical MTF (solid green curve) at a particular critical frequency f_c. Since the red line describes the amount of noise caried per square root frequency and the green curve shows the amount of signal carried per unit frequency, it follows that all frequencies above f_c will be dominated by noise, while frequencies below f_c contain meaningful signal. Thus, f_c is the resolution frequency. It describes the loss of spatial resolution due to blur and noise. To convert to distance from the frequency domain, the following formula can be used:

$$d = \Delta p \frac{2}{f_c} \qquad \text{Eq. (3.17)}$$

Where d stands for the resolution distance, Δp is the pixel spacing (typically in microns for MSI), f_c is the resolution frequency and the factor of 2 comes from the Sampling theorem. Notice that the low intensity image, which also

has a lower SNR appears to have a lower resolution frequency. Thus, according to Equation 3.17 a larger distance is required to resolve between features, as frequency is reciprocal to distance. For the high intensity image the intersection happens $f_c = 0.64$, while the low intensity image has a resolution frequency of $f_c = 0.34$. Since the pixel spacing used in this simulation is $\Delta p = 3\mu m$ (see Table 3-1), the resolution distance for the high intensity image is $d \approx 9.4\ \mu m$, while the low intensity image has a resolution distance of $d \approx 17.7\ \mu m$. Thus, the resolution of an MSI image has been successfully characterised as a function of blur and noise. Moreover, the mechanisms which cause blur and noise were thoroughly investigated. Not only that, but the intersection point is computed adaptively, without making any assumptions on the nature of the noise. The two methods in the entire field that propose an adaptive resolution estimate make specific assumptions about the nature of the noise[69,137]. Here no such assumptions are made as the nature of the noise will naturally lead to a different NSD and therefore a different resolution frequency.

Now, the pseudocode for the resolution measurement algorithms is provided.

Algorithm 1: Real space analysis of blur and noise

Input: *Two dimensional image of an edge*
Output: *Blur parameter in real space, image SNR, average surface intensity,*

Compute 1D ESF: *obtain average profile of ESF*
Compute 1D PSF: *numerical differentiation of 1D ESF*
Curve fitting: *fit Equation 3.16 to extract relevant parameters -* I_1, I_0, μ, σ
Find edge surface: *do a simple calculation that finds the index corresponding to the start of the edge surface*
    find the maximum argument of 1D PSF: *surface index 1 = argmax(PSF) + 3*
    use μ parameter to find edge surface: *surface index 2 = int(*μ*) + 3*
    if *surface index 1 > surface index 2 2:*
        surface index final = surface index 1
    else
        surface index final = surface index 2
Find surface mean intensity: *compute mean intensity* I_1 *using surface index final*
Find surface noise standard deviation: *compute noise standard deviation using surface index final*
Compute image SNR: *compute ratio of surface mean intensity and noise standard deviation - SNR*
Return output: *return* σ, SNR, I_1

Table 3-3 Pseudocode for real space estimates of blur and noise

Algorithm 2: Inverse space analysis of blur and noise and resolution calculation

Input: *Two dimensional image of an edge*

Output: *resolution frequency, error*

Compute 1D ESF: *obtain average profile of ESF*

Compute 1D PSF: *numerical differentiation of 1D ESF*

Curve fitting: *fit Equation 3.16 to extract relevant parameters -* I_1, I_0, μ, σ

Find edge surface: *do a simple calculation that finds the index corresponding to the start of the edge surface*

    find the maximum argument of 1D PSF: *Surface index 1 = argmax(PSF) + 3*

    use μ parameter to find edge surface: *surface index 2 = int(*μ*) + 3*

    if *surface index 1 > surface index 2 2:*

        surface index final = surface index 1

    else

        surface index final = surface index 2

Create theoretical ESF: *using the fit parameters from* ***3*** *create an array with values for a theoretical ESF.*

Find theoretical PSF: *use numerical differentiation on the theoretical ESF to obtain a theoretical PSF*

Find theoretical MTF: *use FFT on theoretical PSF and then compute the magnitude to obtain a theoretical MTF*

Compute NSD: *use surface final index to locate the start of the surface. Then, compute the NSD for each linescan and average all NSDs.*

Compute root of NSD: *compute* $\sqrt{NSD/2}$

Interpolate theoretical MTF: *create an interpolated function of theoretical MTF.*

Interpolate theoretical NSD: *create an interpolated function of* $\sqrt{NSD/2}$.

Find resolution frequency: *using the interpolated MTF and* $\sqrt{NSD/2}$ *find an intersection*

Compute error: *compute the error of the measurement*

Return outputs: *return resolution frequency, error*

Table 3-4. Pseudocode for inverse space estimates of blur and noise and a measurement of resolution

3.3.3 Resolution model

Finally, let us generalise these concepts to a resolution model. Since the ESF is modelled with the aid of Equation 3.16 and the PSF is generated by obtaining the derivative of Equation 3.16, the PSF can be modelled as a Gaussian function. And since the MTF is computed by Fourier transforming the PSF and the Fourier transform of a Gaussian function is also a Gaussian function, the MTF can also be modelled as a Gaussian function, centred at zero. The intersection of the MTF and the square of the NDS can be written as:

$$MTF = I_1 \exp\left(-\frac{f^2}{2\tilde{\sigma}^2}\right) = \sqrt{NDS/2} \qquad \text{Eq. (3.18)}$$

Where I_1 is the average surface intensity, f is the frequency and σ describes the width of the MTF and how quickly it decays. Note that this $\tilde{\sigma}$ is different than the one used in the ESF equation and it is reciprocal to its real space equivalent. Equation 3.18 can be solved easily:

$$f_c = \pm\tilde{\sigma}\sqrt{2\ln\left(\frac{I_1}{\sqrt{NSD/2}}\right)} \qquad \text{Eq. (3.19)}$$

Where f_c is the critical frequency, I_1 is the average surface intensity, and $\tilde{\sigma}$ is the blur parameter measured in inverse space (and not the real space one). Then, using Equation 3.15*, the term $\sqrt{NSD/2}$ is simply the noise standard deviation and therefore the ratio that appears inside the natural logarithm in Equation 3.18 is the ratio of the average signal intensity and the noise standard deviation. By definition, this is the SNR. Thus, after this simplification and after discarding the negative solution as it has no physical meaning, the resolution of an MSI image can be calculated according to:

$$f_c = \tilde{\sigma}\sqrt{2\ln(SNR(I))} \qquad \text{Eq. (3.20)}$$

An equation for calculation resolution based on image blur and image SNR has now been derived. If an appropriate noise model for an MSI imaging system is established and the blur parameter in frequency space is measured one can compute the resolution of an MSI image. The great thing about Equation 3.20 is that it does not require a PSF, ESF nor a resolution device in order to calculate resolution. Of course, in practice a sharp step feature is still needed in order to estimate the blur parameter. Equation 3.20 shows the direct link for loss of resolution due to blur and noise (SNR in particular). If one substitutes the value for the blur parameter in frequency space $\sigma \approx 0.32$ and the values for the SNR of the images (see Table 3-2) ,which are 6.6, 1.8 for $I_1 = 10^5, 10^3$ respectively, then one finds that the first image has a resolution frequency of $f_c = 0.62$ and the second image has a resolution frequency $f_c = 0.35$. It can be seen that the values from the resolution model are slightly different than those acquired by the experimental approach described by Algorithm 2. Thus, it would be useful to attach an uncertainty to the experimental approach.

3.3.4 Errors

The uncertainty in f_c can be estimated by examining Equation 3.20 closely. Let us label this uncertainty as δf_c.By definition δf_c is given by

$$\delta f_c = \sqrt{\left(\frac{\partial f_c}{\partial \tilde{\sigma}}\right)^2 \delta\tilde{\sigma}^2 + \left(\frac{\partial f_c}{\partial I_1}\right)^2 \delta I_1^2 + \left(\frac{\partial f_c}{\partial k}\right)^2 \delta k^2} \qquad \text{Eq. (3.21)}$$

* In that equation σ stands for noise standard deviation and not blur.

Where here $\delta\tilde{\sigma}$ is the uncertainty of the blur parameter obtained from the curve fitting process and δI_1 is the uncertainty of the average intensity. For the sake of beautiful notation, the value for $\sqrt{NDS/2}$ has been substituted by k. Note that this is simply the noise standard deviation, however the letter sigma is already used for blur. The term δk then just represents the standard error for $\sqrt{NDS/2}$. After computing all the partial derivatives, one obtains the following expression for the uncertainty in the resolution frequency:

$$\delta f_c = \sqrt{\frac{\delta k^2 \tilde{\sigma}^2}{2k^2 \ln(SNR)} + \frac{\delta A^2 \tilde{\sigma}^2}{2A^2 \ln(SNR)} + 2\delta\tilde{\sigma}^2 \ln(SNR)} \qquad \text{Eq. (3.22)}$$

Where the substitution $SNR = A/k$ has been made. Finally, this error can be propagated to real space. The error propagation happens through Equation 3.17:

$$\delta d = d\sqrt{\left(\frac{\delta f_c}{f_c}\right)^2} \qquad \text{Eq. (3.23)}$$

It should be noted that the uncertainty in the pixel spacing has been assumed to be zero hero. Now, the uncertainties of the experimental method can be compared. The following table provides the resolution frequencies for the two images investigated in this section. Two sets of resolution frequencies are provided – one computed from the resolution model and the other is obtained experimentally via Algorithm 2.

	$I_1 = 10^5$	$I_1 = 10^3$
Theoretical	0.62	0.35
Experimental	0.64 ± 0.02	0.34 ± 0.02

Table 3-5. Comparison of resolution frequencies calculated from the resolution model (Equation 3.20) and the experimental method outlined in Algorithm 2. Uncertainty calculated using Equation 3.22.

It can be seen that the slight discrepancies between the theoretical and experimental approach are within the uncertainty estimate. Moreover, the experimental approach seems to provide a very satisfactory result.

3.4 Resolution of a datacube

In a typical MSI experiment there could be up to several thousand unique images, each depicting the relative spatial distribution of different molecular species. The collection of all such images is referred to as a datacube. Therefore, MSI is a hyperspectral imaging technique. The images span a range of intensities. Low intensity images will exhibit a lower SNR and hence such images will suffer from a loss of resolution due to noise. It therefore may be expected that the resolution of an MSI data set will be characterised by a range of numbers, each of which is dictated by image blur and noise, as prescribed by Equation 3.20. Thus, a method for characterising the resolution of a datacube is now developed. By constructing this method, it will be possible to compare the resolution of different datacubes, which effectively means that it will be possible to compare the resolution performance of different modalities.

3.4.1 Data cube simulation

Previously some simple objects were simulated with the aid of the image formation model. Since a step edge was chosen as the primary method for measuring resolution, the step edge images will now be used. Once again, this will be done under conditions of strong material removal and weak material removal, and therefore simulating strong image blur and minimised image blur. Each of those scenarios is then corrupted by Poisson noise or combined noise. Thus, four datacubes will be simulated and a method for comparing the resolution performance of these data cubes will be developed. In **Section 3.2.4** upon visual inspection it was claimed that minimised blur with Poisson noise seemed to have the best resolution, whereas strong blur with combined noise had the weakest resolution performance. However, this was purely based on visual inspection. It shall be seen that the methods developed in this section can provide a quantitative answer.

In order to simulate a datacube a range of intensities was used. It can be established from empirical observations that the intensity distribution in an MSI datacube follows a log-skew normal distribution (this will be shown in the next Chapter). The following simulations was developed using the numpy, scipy, matplotlib and seaborn Python packages. A custom Python script was also written so that resolution can be measured (see Algorithm 1 and Algorithm 2). In order to mimic the intensity distribution of a real MSI data set, random variate samples were obtained from a log-skew normal probability density function (PDF). The parameters used to simulate to the range of intensities were very close to the parameters derived from real data sets using maximum likelihood estimation (see Chapter 4). In addition, several high intensities were appended. The values of the parameters used were $\alpha = 3.6, \mu_I = 4.3, \sigma_I = 1.5$, where α is the skew parameter of the skew-normal distribution, μ_I is the expected value and σ_I is the standard deviation of the skew-normal distribution. Since a log-skew-normal is used to approximate the distribution of intensities encountered in real data, $\exp(\mu_I)$ is the mean value of the intensities. The median can be computed by obtaining the cumulative distribution function (CDF) and obtaining the value for $CDF^{-1} = 0.5$, where CDF^{-1} is the inverse function of the CDF. The concept of flipping between the real PDF and the natural log of the PDF is shown on the following graph.

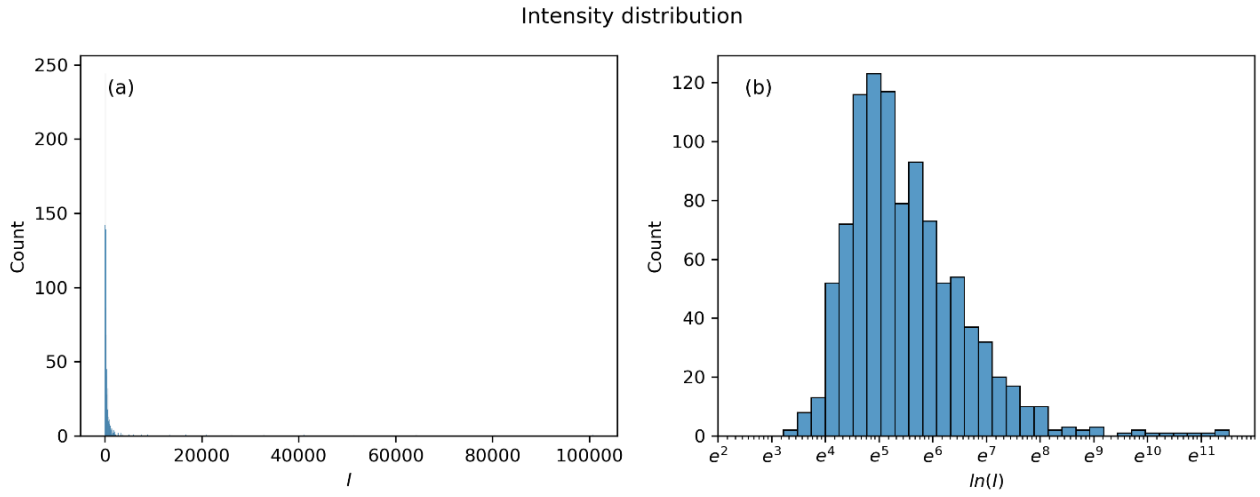


Figure 3-15 (a) – log-skew normal distribution of intensities. (b) – same but plotted after computing the logarithm of intensities – skew normal distribution.

The range of intensities are shown in Figure 3-15 (a). Presented as such not much information can be gathered apart from the majority of signals are low intensity and there are a few high intensity signals. However, computing the natural log of this can be useful. It can be seen that after computing the natural logarithm of the intensities a skew-normal distribution is obtained in Figure 3-15 (b). The following table summarises the parameters used in this simulation.

	Weak material removal	Strong material removal
Poisson noise	Data cube 1	
Combined noise	Data cube 2	
Poisson noise		Data cube 3
Combined noise		Data cube 4

Table 3-6. A summary of the noise and blur parameters used in the data cube simulation.

Four data cubes were simulated, each at 3 μm pixel size. The beam width, stage velocity, scan time and desorption coefficient for these can be found in Table 3-1 and the parameters for the noise model can be seen in

Table 3-2. Next, a high intensity and a low intensity image from each data cube is presented.

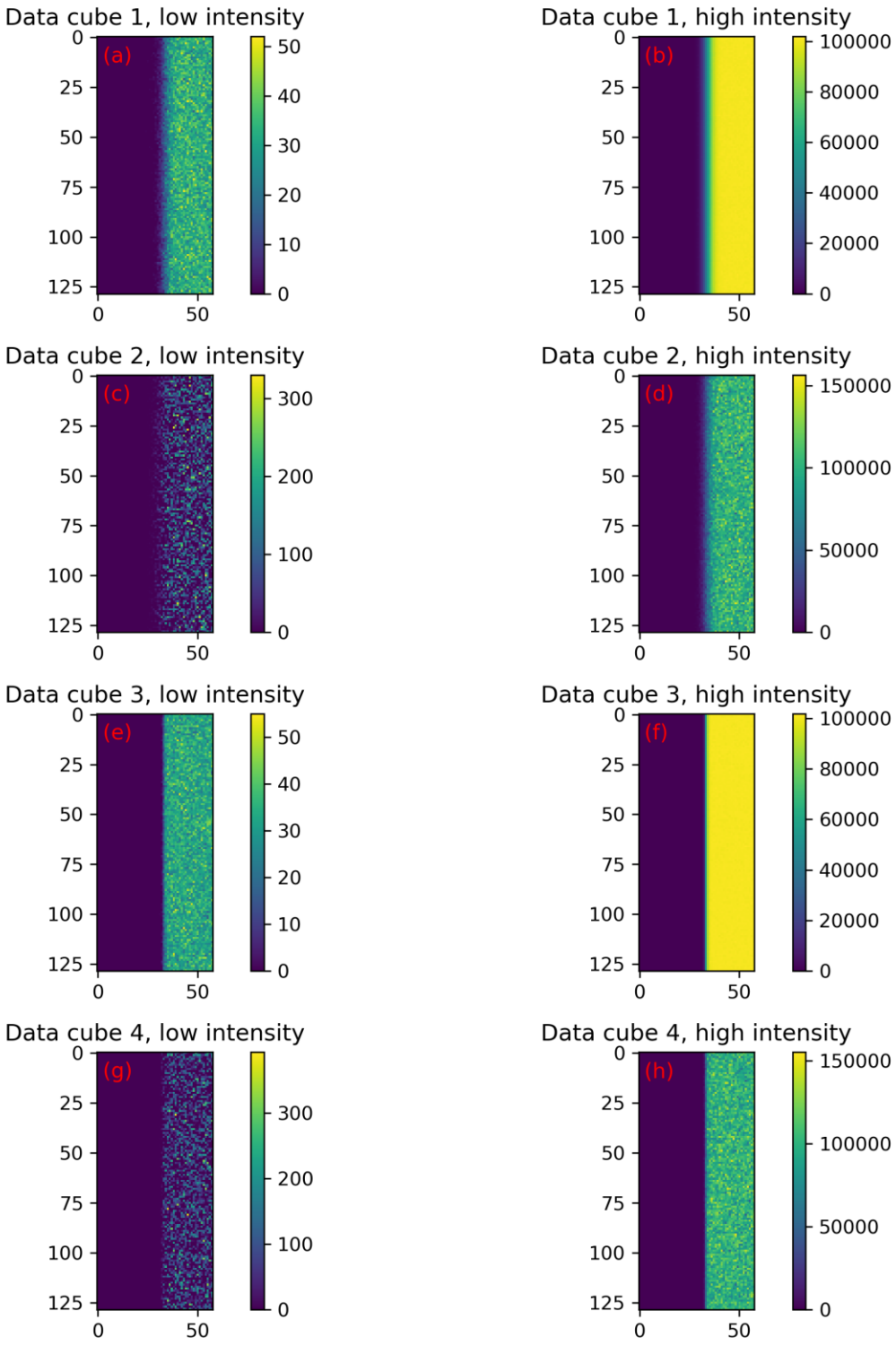


Figure 3-16 (a), (b) – Poisson noise, weak material consumption, low and high intensity ESFs. (c), (d) – Combined noise, weak material consumption, low and high ESFs. (e), (f) – Poisson noise, strong material removal, low and high intensity ESFs. (g), (h) – Combined noise, strong material removal, low and high intensity ESFs.

For each image in a given data cube Algorithm 1 and Algorithm 2 can be performed to obtain the average signal intensities, real space blur estimates ($86-14\%$ criterion), image SNRs, resolution frequencies and the error in the resolution frequency. The edge images generated have dimensions of $(58,129)$ pixels in terms of width and height. Since 58 pixels are used in the x direction, the retrieved MTFs would contain 29 data points. Instead of looking at a square region of interest, the height of the image was increase to 129 pixels so that the effects of a decreased number of linescans is investigated.

3.4.2 Data cube resolution

The retrieved parameters for each data cube allow us to investigate the image SNR as a function of intensity and the image resolution as a function of intensity. Other parameters, such as the real space blur estimate are also extracted. Using Equation 3.17 and Equation 3.20, the equation for the resolution distance may be written as:

$$d = \frac{2\Delta p}{\tilde{\sigma}\sqrt{2\ln\left(\mathrm{SNR(I)}\right)}} \qquad \text{Eq. (3.24)}$$

Where Δp is the pixel spacing, $\tilde{\sigma}$ is the blur parameter in inverse space and SNR(I) is the signal to noise ratio as a function of intensity. Since each image in a datacube has a different intensities, the resolution distances for each edge image can be computed and plotted as a function of intensity. Thus, this equation allows us to compute the resolution distance of an entire datacube, which spans a range of intensities. Notice that if the noise model and blur parameters are known, one could compute the resolution of a datacube without the need of any edge measurements. A generalised noise model can be used:

$$SNR(I) = \frac{I}{\sqrt{\mathrm{aI} + \mathrm{bI}^2}} \qquad \text{Eq. (3.25)}$$

Which is just the SNR of our combined noise model. However, in the case of $b = 0$ and $a = 1$ this reduces to perfect Poisson noise. The results from these measurements can be seen in the following log-log graph:

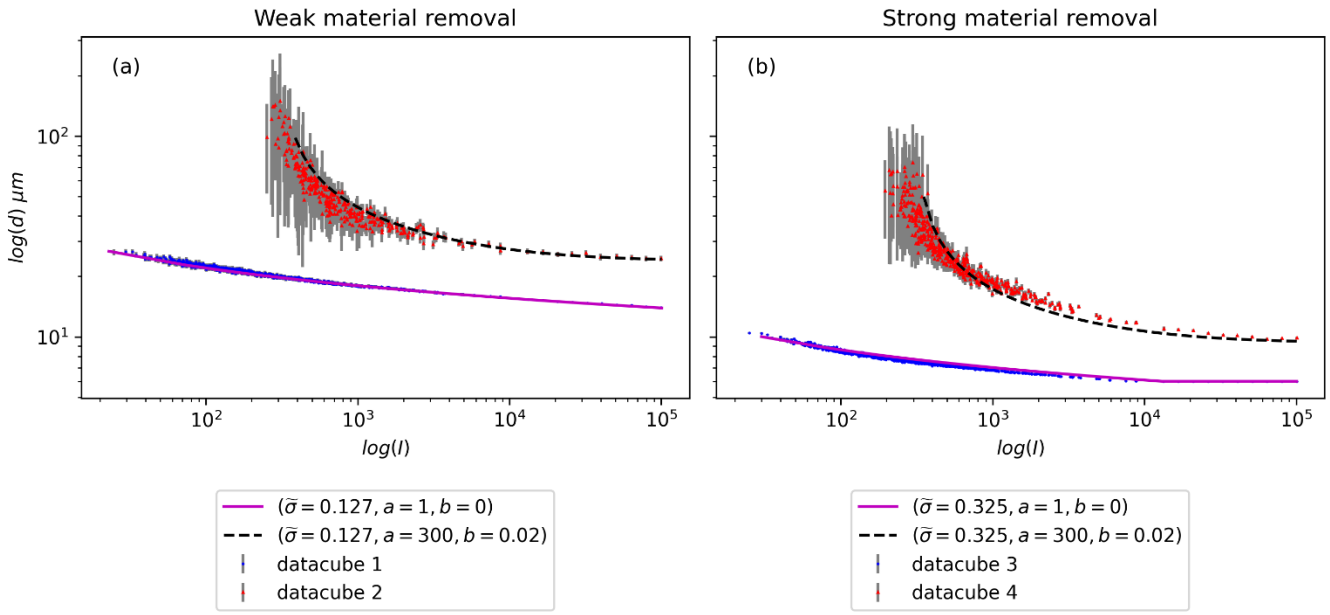


Figure 3-17(a) – Resolution distance in the case of weak material removal (maximised blur). The solid magenta and dashed black curves represent the theoretical prediction for Poisson noise and combined noise respectively. The blue circle and red triangle scatter points depict the experimentally measured resolution with the aid of Algorithm 2. The vertical grey lines are the errors in the resolution measurement. (b) – same but in the case of strong material removal (minimised blur).

The theoretical estimates for the resolution of a data cube were calculated by using Equation 3.24 They appear as a solid magenta or dashed black curve in Figure 3-17 (a) and (b), corresponding to either Poisson or combined noise. The blue circle and red triangle scatter points correspond to the experimentally measured resolution obtained with the aid of Algorithm 2. The vertical grey lines represent the error in that measurement. It can be seen that the error bars are almost invisible for the blue data points, indicating that uncertainty in resolution estimates is much lower for Poisson noise. On the other hand, the error bars at high intensities for the red scatter points are much smaller compared to the error bars for the low intensity data points. Error analysis was already performed so now one can understand that this happens due to the uncertainties in the image blur $\delta\tilde{\sigma}$, uncertainties in the standard deviation δk and uncertainties in the signal average δA. It is still reassuring to see that the black lines fall within the grey area in the low intensity regime. Notice that for datacube 2, shown in Figure 3-17 (a), the high intensity scatter points perfectly align with the theoretical prediction shown by the black curve. As for datacube 4 (Figure 3-17 (b)) some of the data points appear to deviate from the black curve and the error bars do not account for that. The effects of introducing blur to a data set have the effect of shifting the resolution curve up. For example, comparing the blue scatter points, or equivalently the magenta curves, in Figure 3-17 (a) and Figure 3.17 (b) it can be seen that the overall effect of introducing blur is to shift the resolution curve up. Both datacube 1 and datacube 3 have a resolution curve that exhibits the same shape but it has been moved up or down, depending on the amount of blur. The same thing could be said about the combined noise data cubes (data cube 2 and data cube 4), represented by the red

triangle scatter points and dashed black curves. However, comparing Poisson noise with the combined noise model it can be seen that the noise model affects the shape of the resolution curve, rather than its relative vertical position. It can be seen that combined noise has a much more detrimental effect on resolution, as the resolution curve seems to have its value increased much faster with decreasing intensities.

As for the uncertainties, since there are a sufficient amount of pixels in order to obtain a statistically accurate estimate of A and k, it may be speculated that the uncertainty in resolution is dominated by uncertainties in $\tilde{\sigma}$ that arise from the curve fitting process. The following figure reveals that indeed such is the case.

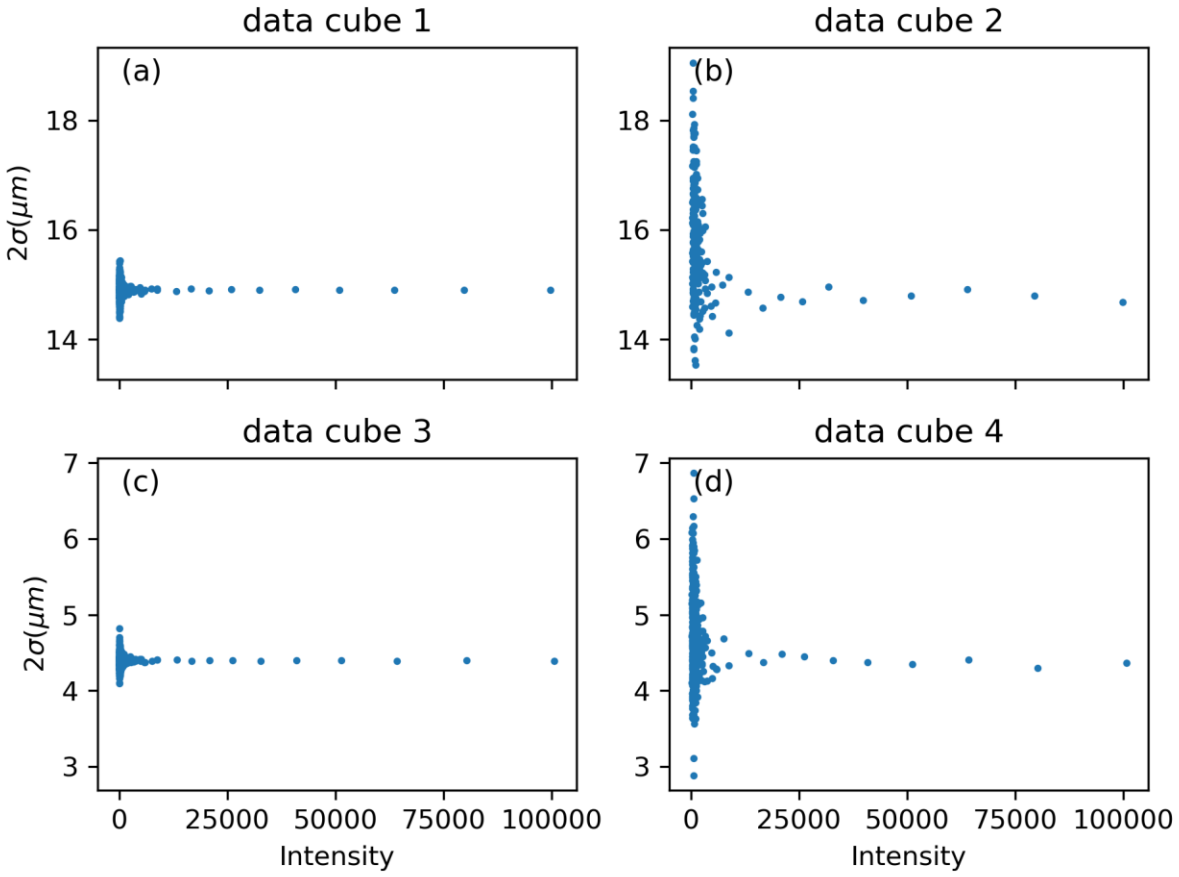


Figure 3-18 Image blur as a function of intensity for (a) – weak material removal and Poisson noise. (b) – weak material removal and combined noise. (c) – strong material removal and Poisson noise. (d) – strong material removal and combined noise.

It was already discussed in detail how and why weak material removal leads to image blur limited by the width of the beam, which was set to 15 μm in this simulation. It can be seen that this is the case in Figure 3-18 (a) and Figure 3-18 (b). It was also discussed why blur cannot be used as a resolution metric in the case strong material removal, as it will yield answers that violate the Sampling theorem – in this case the distance of two pixels corresponds to 6 μm. It can be seen that curve fitting produces a really stable estimate for the blurring parameter 2σ at high

intensities. In the case of Poisson noise (data cube 1 and data cube 3), at low intensities the curve fitting still yields a somewhat satisfactory estimate. However, for combined noise (data cube 2 and data cube 4), the blurring parameter cannot be estimated very well due the detrimental nature of this type of noise. Therefore, much more linescans are needed. And if less linescans had been used the blur estimates would be even worse, leading to an inaccurate estimate of resolution.

3.4.3 Dependence on number of number of linescans

A quick study on the dependence of the effects of a reduced number of linescans used in a resolution measurement now follows. Generally, it appears that the noisier the data set is, the more linescans are needed. Therefore, it seems pretty pointless to do a calculation on the minimum number of linescans needed for a good estimate as this would depend on the type of noise encountered. Thus, at the very least the noise should be characterised prior to a resolution measurement in order to have a rough idea of how many linescans should be used. For example, as combined noise is much more detrimental than Poisson noise, a lot more linescans should be used. Furthermore, the optimum number of linescans would depend on the a, b parameters, which could very well be different across different instruments, modalities and pixel sizes. Thus, as a general rule of thumb one should try to use as many linescans available.

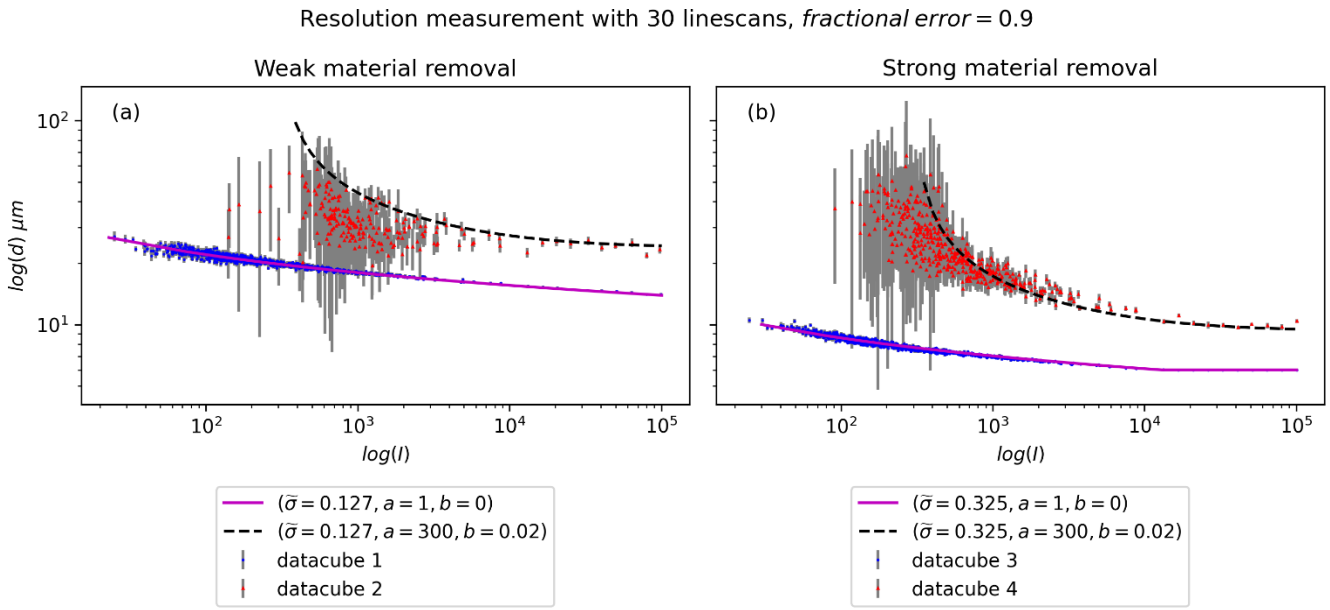


Figure 3-19 Resolution measurements with reduced number of linescans. (a) – resolution distance in the case of weak material removal (maximised blur). The solid magenta and dashed black curves represent the theoretical prediction for Poisson noise and combined noise respectively. The blue circle and red triangle scatter points depict the experimentally measured resolution with the aid of Algorithm 2. The vertical grey lines are the errors in the resolution measurement. (b) – same but in the case of strong material removal (minimised blur).

One can infer from the figure above that using 30 linescans as opposed to 129 has led to an increase of uncertainty. Notice the spread in the red triangle data points in both Figure 3-19 (a) and (b) at low intensities. For these plots, all red triangle scatter points displayed are those that had a fractional uncertainty less than 0.9. The Poisson noise model also appears to be affected by this, as there is some variation in the blue circle data points at low intensities. The resolution estimates appear to be particularly underestimated in the case of datacube 2 (weak material removal, combined noise). This could be attributed to an underestimated real space parameter (sharper blur was measured). This parameter gets propagated to its equivalent in Fourier space – $\tilde{\sigma}$, which in term determines the width of the MTF. Deviations from the ground truth value of $\tilde{\sigma}$ lead to deviations of the resolution frequency f_c, which then get propagated to real space.

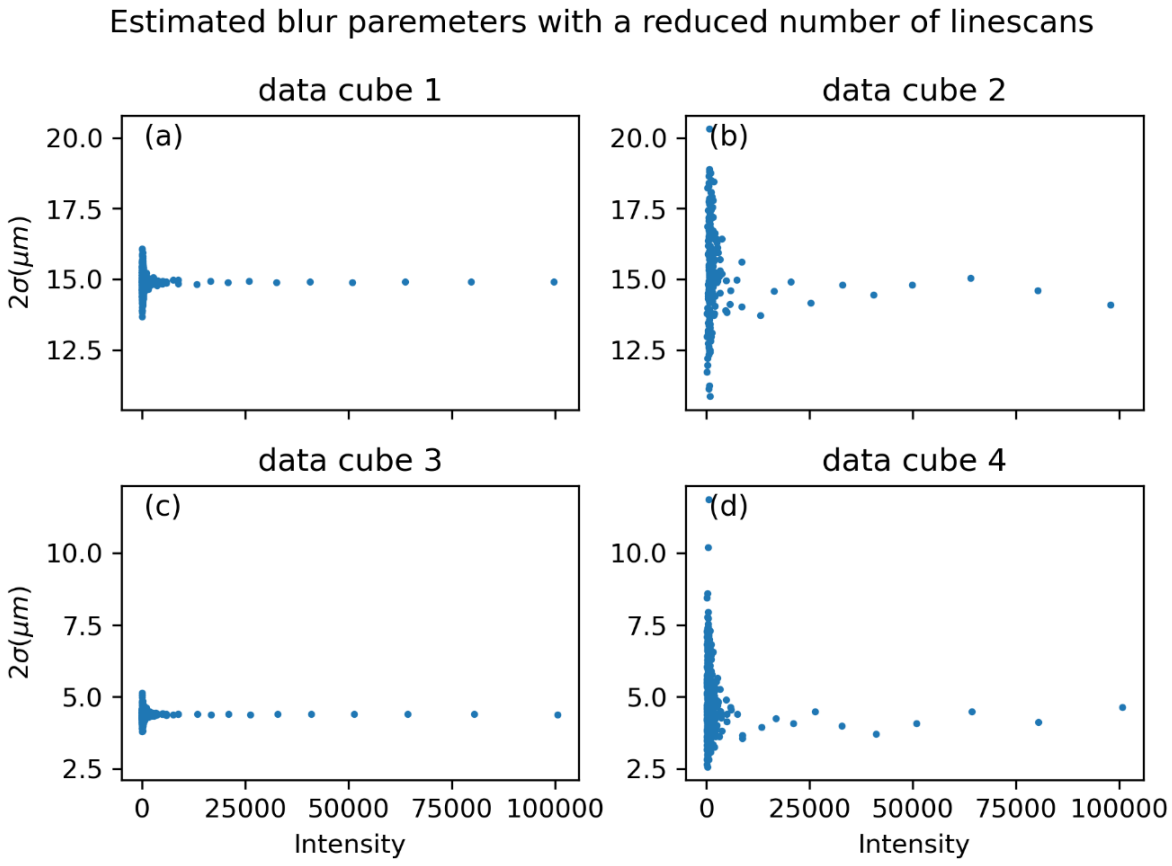


Figure 3-20. Blur parameter estimates when a reduced number of linescans is used. (a) – weak material removal and Poisson noise. (b) – weak material removal and combined noise. (c) – strong material removal and Poisson noise. (d) – strong material removal and combined noise.

Indeed, upon closer inspection, one finds that the spread in blurs at low intensities is now much larger. This increase in the variance in blur explains the increase in variance in the red data points in Figure 3-19. If one computes the mean value of blurs for intensities smaller than 1000 for data cube 2, one finds that the median blur value has

decreased, therefore explaining why the red data points in Figure 3-19 (a) underestimate resolution. The fact that the red scatter points underestimate resolution and deviate from the predicted model is problematic.

3.4.4 Recovering the resolution equation when reduced

It has been seen that using a decreased number of linescans leads to a greater uncertainty when estimating the resolution of a datacube, particularly in the low intensity regime. Unfortunately, when these algorithms are applied on tissue not very often one will be lucky enough to obtain even 30 linescans that can approximate an edge. Luckily, the noise model used in this simulations was a very severe model and depending on the values of the parameters a and b it may be the case that the uncertainties are not as bad as in this simulation. Furthermore, with the help of error analysis data points with a really large uncertainty can be disregarded. For example, in Figure 3-19 data points with a fractional error less than 90% are considered. This is not ideal, as the majority of the measurements are concentrated in that large fractional error zone. In contrast, the data points concentrated in the same intensity range and obtained from 129 linescans (Figure 3.17) exhibit a fractional error smaller than 0.2 One possible route to deal with this is to only consider data points beneath a certain threshold. By selecting only data points that exhibit a reasonable amount of fractional error and using curve fitting one can recover the parameters seen in Equation 3.24, which governs the resolution of a data cube. The following figure shows red scatter points that only exhibit a fractional error smaller than 0.23.

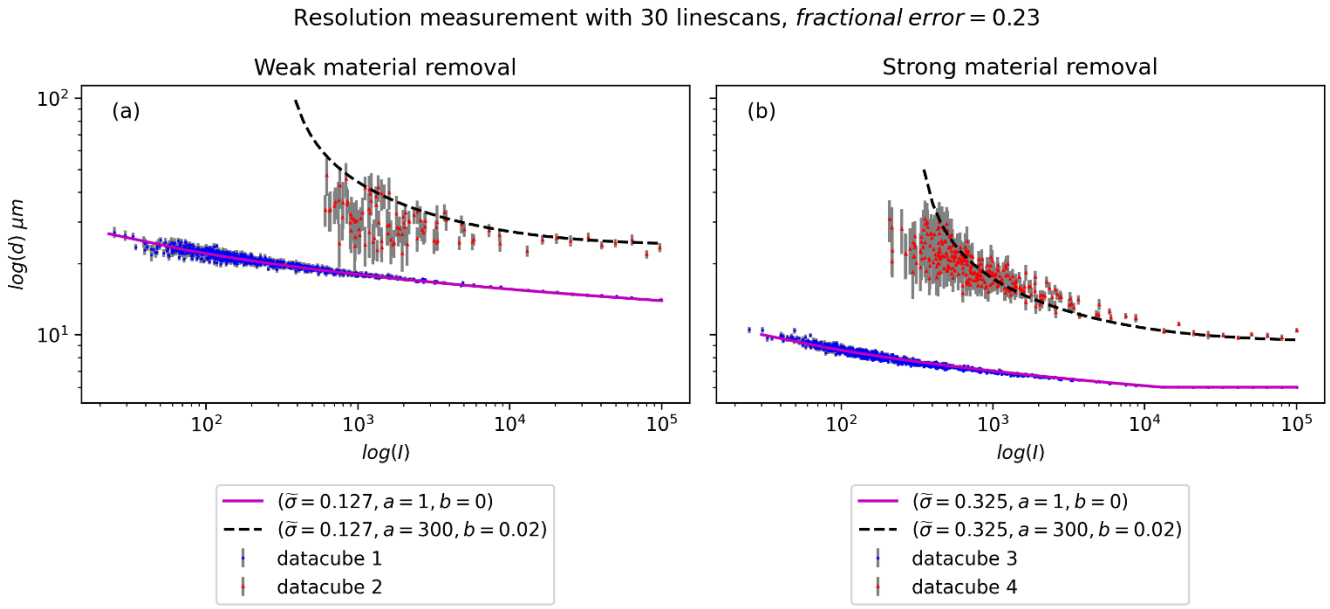


Figure 3-21 Resolution measurements with reduced number of linescans. Only red scatter points with a fractional error less than 0.23 are plotted. (a) – resolution distance in the case of weak material removal (maximised blur). The solid magenta and dashed black curves represent the theoretical prediction for Poisson noise and combined noise respectively. The blue circle and red triangle scatter points depict the experimentally measured resolution with the aid of Algorithm 2. The vertical grey lines are the errors in the resolution measurement. (b) – same but in the case of strong material removal (minimised blur).

However, even when considering these data points it seems that the deviation from the theoretical model can be significant. If the fractional error threshold gets reduced to only the data points that match the model, only very few data points will be left and curve fitting can fail in such a scenario. Another approach, which is employed in this work is to rely on a noise model calibration combined with a measurement of a few high intensity edge images so that the blur parameters may be obtained. The intuition is that the statistical estimates of mean, variance and standard deviation are not as sensitive to a reduced number of linescans as fitting a curve to a really noise edge. For example, from a (20,20) pixel region of interest a decent estimate of empirical statistics may be obtained, whereas fitting a curve to a noise edge fails (as seen in Figure 3-21, Figure 3-20, Figure 3-19, and Figure 3-18). Therefore, by relying on an estimate of the blurring parameter $\tilde{\sigma}$ obtained from high intensity images only, and empirical noise estimates acquired from the entire data set, Equation 3.24 may be recovered.

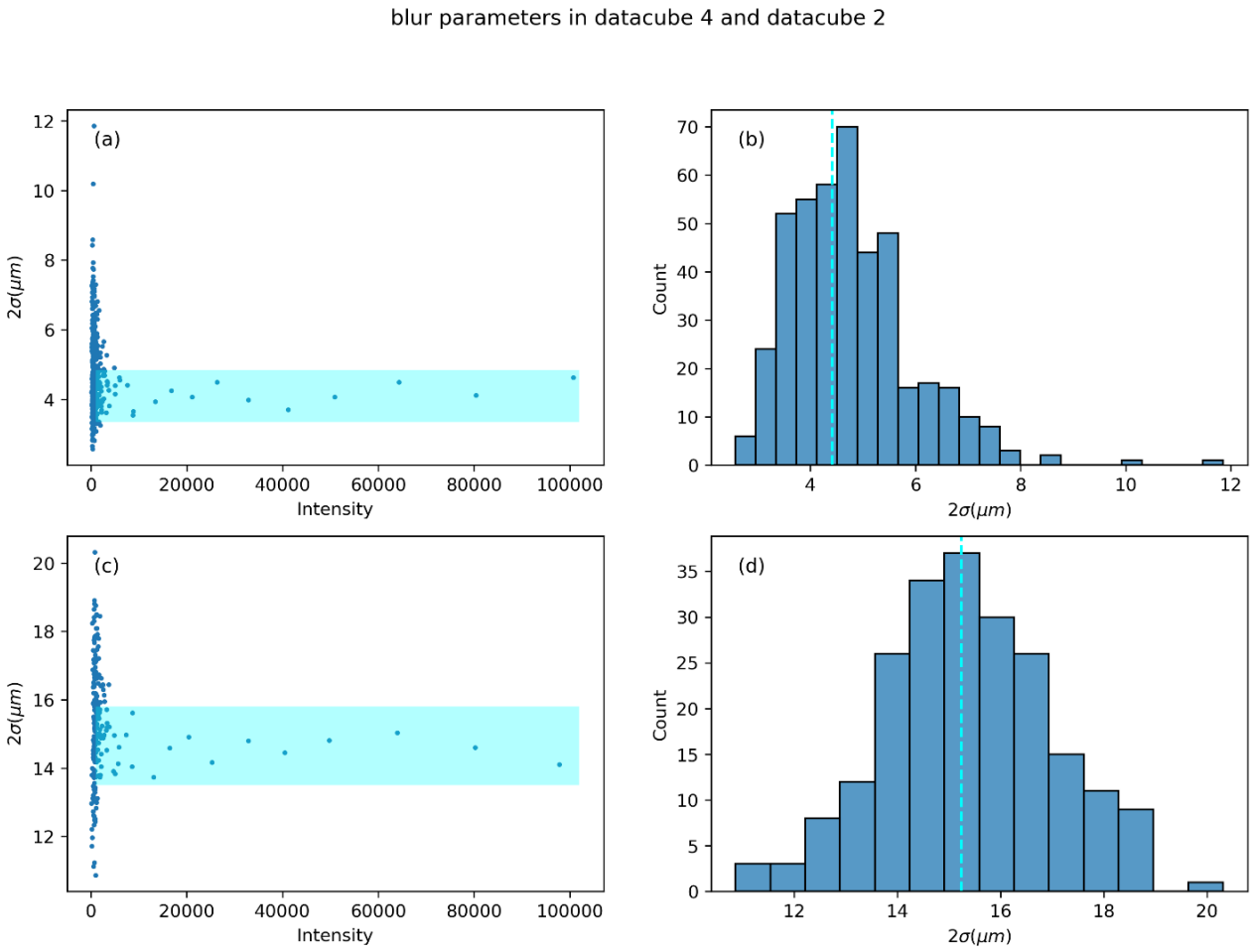


Figure 3-22 (a) – measured blur vs intensity for datacube 4. Shaded cyan region represents the high intensity region from which the blurring parameter is obtained. (b) – a histogram representing the distribution of blurs. Dashed cyan line is the median value obtained from the shaded cyan region in (a). (c) – same as (a) but for datacube 2. (d) – same as (b) but for datacube 2.

The caveat to this approach is now a global MTF has been imposed on every single image. It could be the case that different images exhibit a different amount of blur naturally; with this approach this information is lost. Once the median value for the high intensity blur estimates (dashed cyan line in Figure 3-22 (b) is the median value of the shaded cyan region in Figure-322 (a)) is obtained, its Fourier space counterpart $\tilde{\sigma}$ may be calculated and then plugged in Equation 3-21. The noise model parameters still need to be estimated. This was discussed in detail in Chapter 2 and some parts of this chapter. For the purpose of brevity, Equation 3-22 is fitted to the data so that the a, b parameters may be extracted. The results of the curve fitting are shown in the next figure.

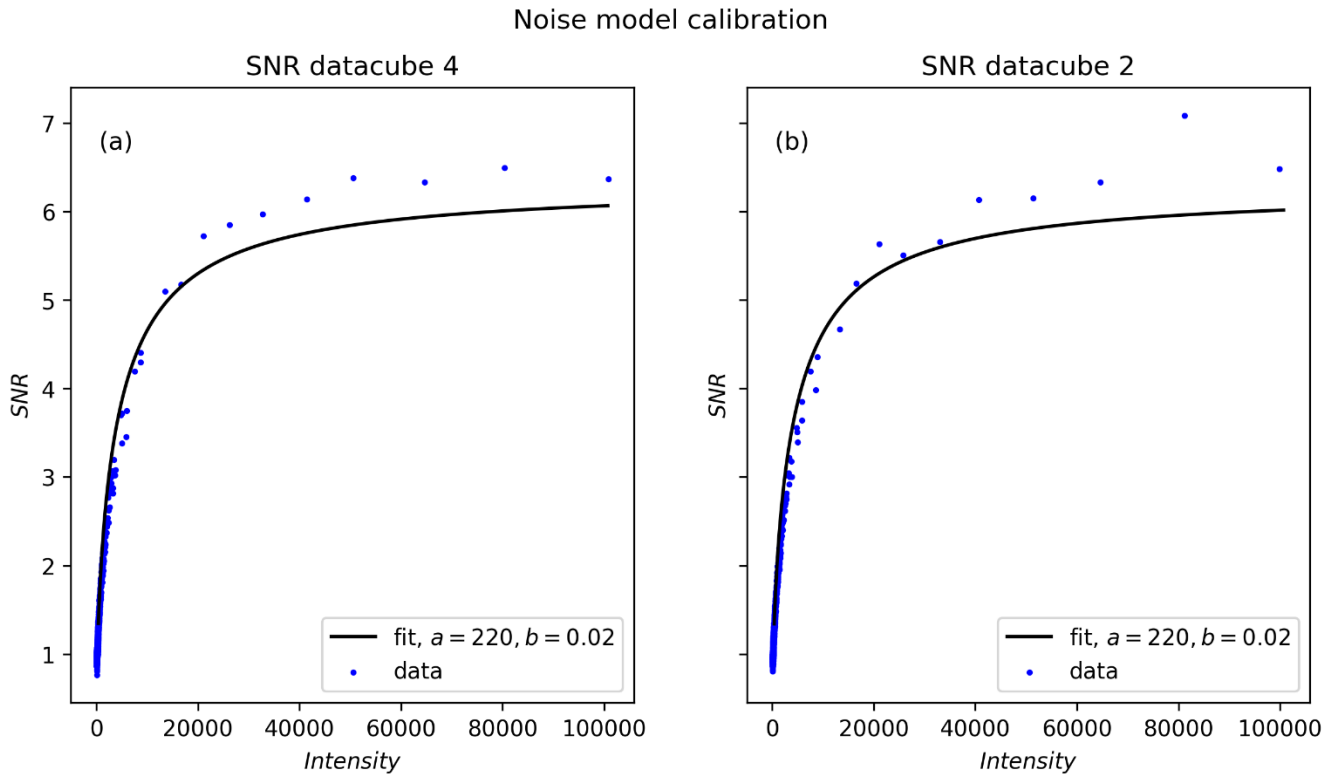


Figure 3-23 (a) – SNR for datacube 4. (b) – SNR for datacube 2.

Here the extracted parameters have values of $a = 220, b = 0.02$ and the ground truth parameters used are $a = 300, b = 0.02$. While the b parameter is estimated quite accurately, the estimation of the a parameter is less accurate. Thus, an error will be introduced in the recovered resolution. After extracting the a, b parameters, they may be simply plugged in Equation 3-21 together with $\tilde{\sigma}$ to recover the resolution model. This is shown in the following figure.

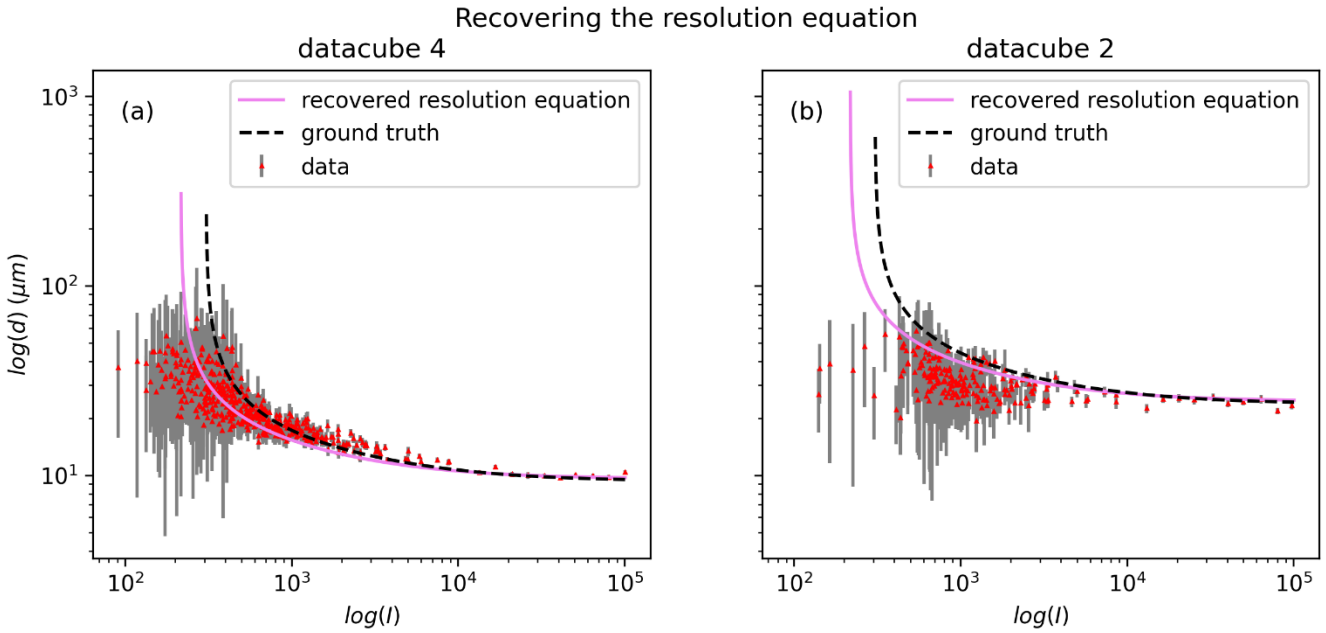


Figure 3-24. (a) – recovering the resolution equation for datacube 4. Red scatter points – measured with Algorithm 1 and 2. Dashed Black curve – ground truth. Violet solid curve – recovered using the procedure describe here. (b) – same but for datacube 2.

It can be seen that the process described for recovering the resolution equation works much better than simply using the noisy data points. This is because the uncertainties coming from the low intensity blur parameters estimates are minimised. The recovered resolution (violet solid curve) deviates from the ground truth (dashed black curve). This is because of the error in the estimation of the a parameter. Nevertheless, the solid violet curve appears to approximate the ground truth quite well. Thus, when not that many linescans are available, this strategy may be used in order to characterise the resolution of a data set. This is the advantage of having a resolution model – it is a very powerful approach that will be later applied to tissue imaging data sets. It will allow for the measurement of resolution of an entire data set by calibrating a noise model and extracting the relevant parameters; the MTF will be obtained from the average of a few high intensity edges and the critical frequency intersection point will be obtained from the relevant noise statistics and the globally imposed MTF. Furthermore, even the resolution of images that do not exhibit a step edge feature will be calculated. This will be investigated further in Chapter 5, but the foundations for this approach are laid out here.

3.4.5 Comparing the resolution of different datacubes

There are various metrics that can be considered when investigating the image quality of a data cube. Two were shown – resolution distance as a function of intensity and measured blur as a function of intensity. Image SNR as a function of intensity, noise variance as a function of intensity, and standard deviation as a function of intensity can also be plotted. This was not done here as it was already thoroughly investigated in Chapter 2 – the obtained curves

would look exactly the same. However, how can one compare the image quality of different data sets? In a sense this was already achieved; one approach would be to present in a table the noise parameters a and b. The variance/standard deviation/ SNR graphs are also an excellent way of comparing instrument performance. The resolution distance versus intensity graphs can also reveal valuable information. However, it would be nice if the four data sets can be compared on a single graph and a singular value be attached to the resolution of the entire data cube. A log-linear violin plot is chosen for accomplishing this task. The intensity distribution may also be plotted in this fashion. In fact, since resolution is a function of intensity, and one is seeking to compare the resolution of different datasets beginning our analysis with a plot of the intensity distributions is a convenient starting point.

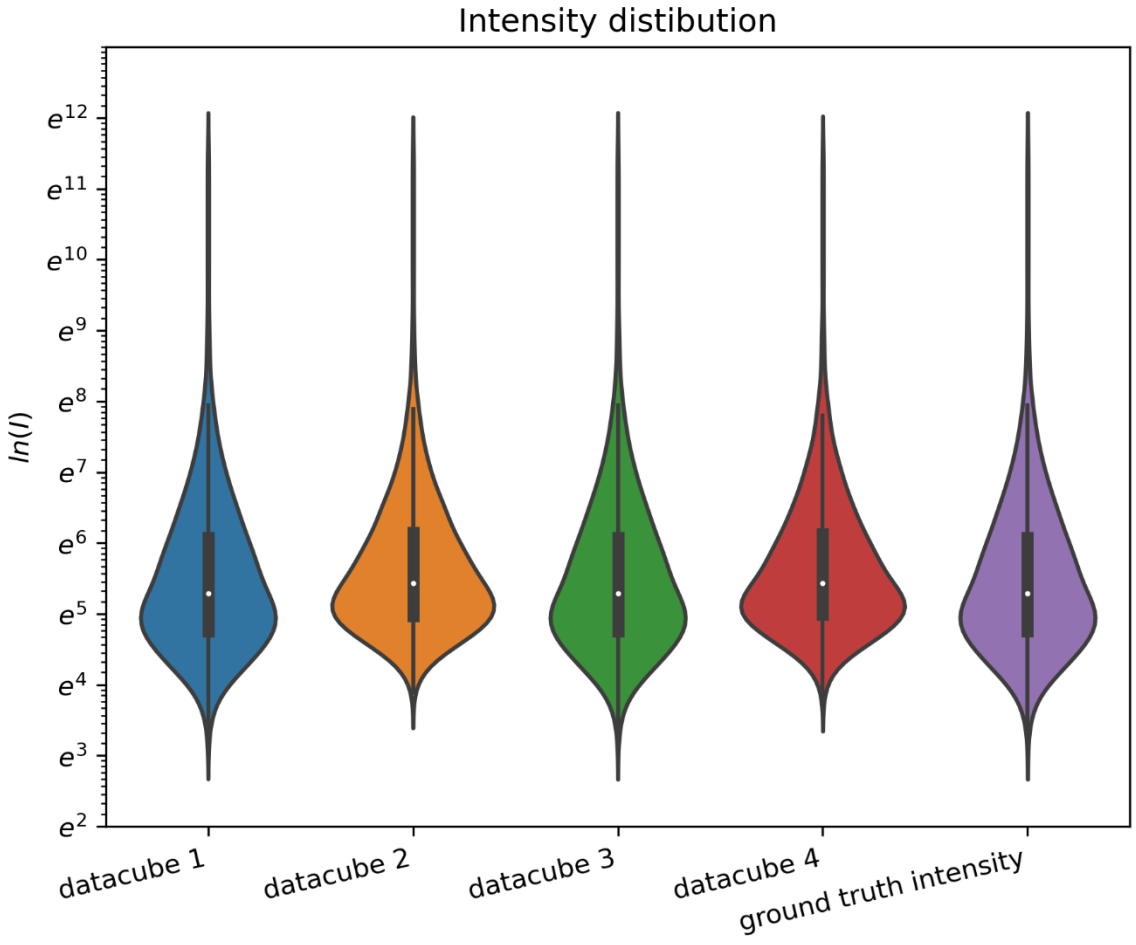


Figure 3-25 A violin plot of the intensity distributions of the four datacubes. The plot is presented on a semi-natural log scale.

The violin plots allow us to depict the distribution of intensities and some of the relevant statistics of those distributions at the same time. The black box within each violin is a miniature box plot depicting the first and third quartile of the distribution. The white dot in the middle is the median value (second quartile). The purple distribution at the far right is the ground truth intensity – it carries the same information as the histogram shown in Figure 3-15

(b). As mentioned, resolution is a function of intensity (and noise and blur too), which means that if there are a lot more low intensity images, the overall resolution of the datacube will be affected by this. This is why it was important to use a PDF that describes the distribution of intensities in real data sets (see Chapter 4). It is peculiar that the application of noise has had an effect on the intensity distributions for the different datacubes. The datacubes corrupted with Poisson noise (datacube1 and datacube2) retain the original shape of the ground truth density distribution and the median values are also the same. However, the application of combined noise (datacube 2 and datacube 4) seems to have an effect on the distribution of intensities – a slightly higher median value is observed. After reviewing the intensity distributions, the resolution distributions may be plotted.

3.4.5.1 Bootstrapping

Each image within a datacube can be described with a mean intensity value. For a homogeneous region, the noise variance is simply the variance around the mean intensity value. In particular, in the simulations discussed here, the noise strength increases quadratically with signal intensity. It therefore follows that images with unique intensity values will have unique resolution numbers. Thus, a resolution distribution associated with an MSI dataset arises. The resolution distribution will depend on the intensity distribution and the noise model. This begs the question how to compare two (or more) such distributions.

In this particular work, the median resolution is chosen as a statistic that represents the overall resolution trend in a dataset. However, in order to compare how close the calculated resolution median value is to the ground truth median resolution, a confidence interval is needed. Bootstrapping is a numerical technique that allows for confidence intervals on different statistics to be estimated. This is done by sampling the original data with replacement a number of times. Each resample can then be used to calculate a given statistic, for example the median value. When this is done for a sufficiently large number of resamples, the sampling distribution of the statistic of choice can be estimated. Here the scipy.stats package was used with a bias-corrected and accelerated (BCa) method [152].

3.4.5.2 Estimated resolution vs ground truth resolution

The ground truth resolution distribution for each datacube is presented on the following graph. Furthermore, the resolution distributions obtained via Algorithm 2 with different numbers of linescans, and the recovery method are depicted.

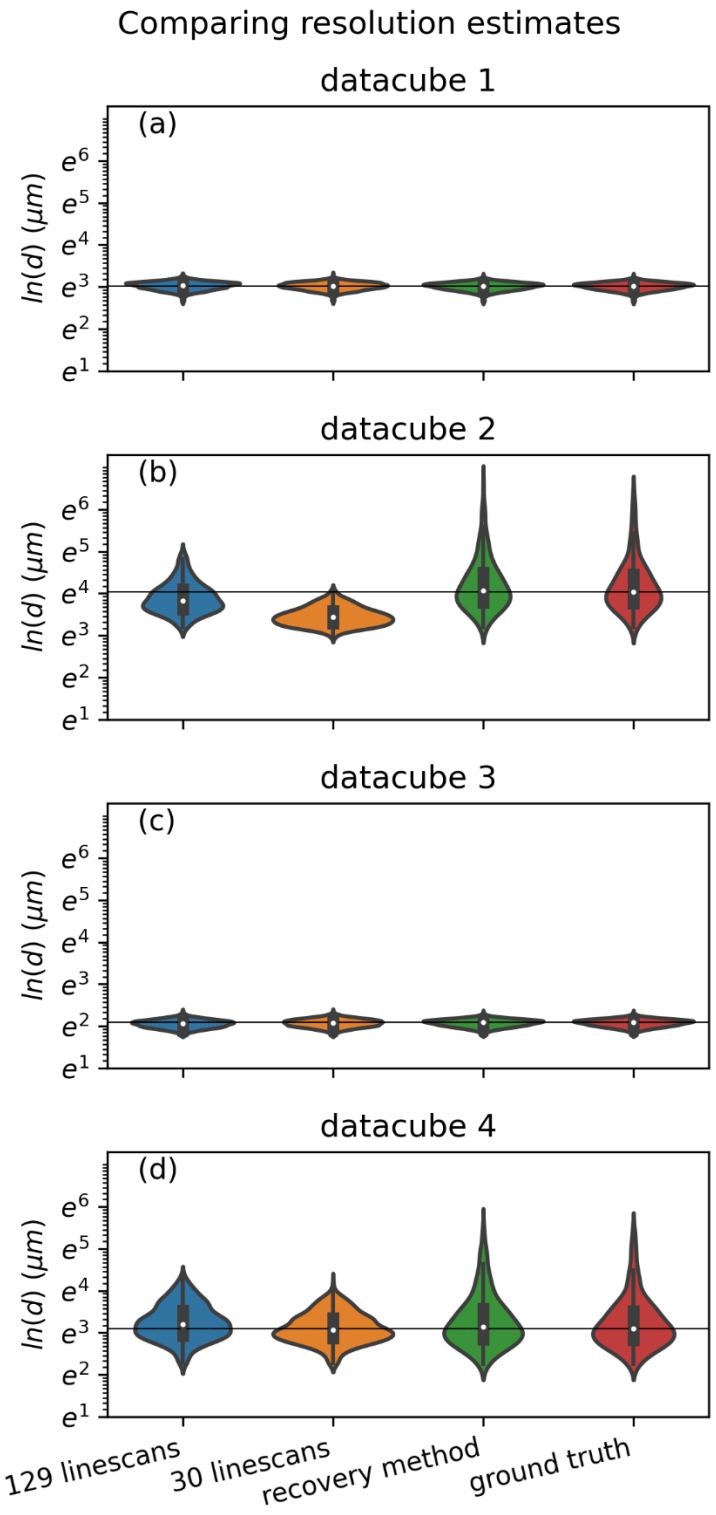


Figure 3-26 Comparing resolution estimates for each datacube obtained with the different methods. x-axis – Algorithm 2 with 129 linescans, Algorithm 2 with 30 linescans, recovery method and ground truth. Black vertical line in each plot is the ground truth median value. (a) – resolution estimates for datacube 1. (b) – resolution estimates for datacube2. (c) – resolution estimates for datacube 3. (d) – resolution estimates for datacube 4.

The violin plot allows for the resolution distribution of each of the four datacubes to be investigated and compared to that of the other datacubes. Since the resolution distributions are not symmetric, the statistic chosen for the purpose of characterising an entire data set is the median value. This is depicted by the white dot in the middle of each distribution; the black box is a miniature boxplot. For reasons of symmetry, so that the reader may compare the shape of the resolution distributions to the shape of the intensity distributions in Figure 3-25, the resolution distance d has been plotted on a natural log scale. The ground truth resolution for each datacube is shown in red. It was obtained from the ground truth intensity distribution (see Figure 3-25 and Figure 3-15) after using Equation 3.21 to compute the resolution distance d. This required knowledge on the ground truth values of the inverse space blur $\tilde{\sigma}$ and the ground truth noise model parameters a, b – those may be reviewed with the aid Table 3-6 (datacube description), Table 3-2 (noise parameters) and Table 3-1 (blur parameters). Note that the values in Table 3-1 are the real space equivalent of $\tilde{\sigma}$. The resolution distribution depicted in green are the ones computed with the recovery method (see Chapter 3.4.4). This involved imposing a global MTF and fitting a generalised noise model to the noise statistics. The global MTF was imposed by looking at the blur parameter $\tilde{\sigma}$ of high intensity images as the estimation of the same parameter for low intensity images suffers from large uncertainties. This was shown in Figure 3-22. Then, the parameters that govern the noise model are fitted, as shown in Figure 3-23. Finally, Equation 3-21 may be applied with the extracted blur and noise parameters to compute the resolution distance. As for the blue and orange resolution distributions, these were acquired through Algorithm 2 with 129 and 30 linescans respectively. The black vertical bar in each of the plots represents the median ground truth resolution value, computed from the ground truth (red) resolution distribution. For ease of comparing the median values the following table is provided; the standard error was derived from bootstrapping. The scipy.stats.bootstrap module was used, with BCa bootstrapping, two-sided alternative, 9999 resamples and a confidence interval of 0.95.

Method	Median datacube 1	Median datacube 2	Median datacube 3	Median datacube 4
129 linescans	$20.8 \pm 0.1\ \mu m$	$46 \pm 1\ \mu m$	$7.8 \pm 0.1\ \mu m$	$25 \pm 1\ \mu m$
30 linescans	$20.6 \pm 0.1\ \mu m$	$31 \pm 1\ \mu m$	$7.9 \pm 0.1\ \mu m$	$21 \pm 1\ \mu m$
Recovery	$20.6 \pm 0.1 \mu m$	$55 \pm 2\ \mu m$	$7.9 \pm 0.1\ \mu m$	$21 \pm 1\ \mu m$
Ground truth	$20.6\ \mu m$	$56.6\ \mu m$	$8.0\ \mu m$	$22.1 \mu m$

Table 3-7. Median values for the resolution of each datacube. Standard errors derived from bootstrapping.

Figure 3-26 (a) and Figure 3-26 (c) show how Algorithm 2 with 129 linescans, Algorithm 2 with 30 linescans, and the recovery method, perform compared to the ground truth resolution distribution (shown in red). These plots correspond to datacube 1 and datacube 3, which simulated strong blur with Poisson noise and minimised blur with Poisson noise. Therefore, since Poisson noise is not so aggressive, it can be seen that the three methods recover the ground truth resolution distribution quite well. This was already discussed when Figure 3-17 and Figure 3-19 were introduced. In terms of median values, they do not differ greatly from the ground truth either.

As for Figure 3-26 (b) and Figure 3-26 (d), which represent combined noise with strong and minimised blur respectively, it can be seen that the recovery method (shown in green) does the best job of approximating the ground

truth resolution distribution. Algorithm 2 with 129 linescans (blue distributions), appears to deviate from ground truth median by around 9 μm for datacube 2 and by around 3 μm for datacube 4. These correspond to strong and weak blur respectively. It can be seen that Algorithm 2 with 129 linescans produces a distribution with a truncated tail, compared to the recovery method (green) distribution and the ground truth (red) distribution. This is because a threshold for the fractional error was set – only measurements with a fractional error less than 90% were considered. This implies that the resolution of a portion of low intensity images is not included in the resolution measurement, as they are too noisy to be trusted. This loss of number of images estimated results in a truncated tail. The truncation of the tail of the distribution is even more severe in the case of Algorithm 2 with 30 linescans (orange distribution). Using less linescans in this case leads to an inaccurate estimate of the blurring parameter (see Figure 3-22), which is then propagated to a large uncertainty in the resolution distance. Therefore, a larger portion of low intensity images now have a resolution measurement with a fractional error greater than 90%. This is all simply because more linescans are needed to average out the noise and make it possible for curve fitting to extract the blurring parameter accurately. Disregarding those results in a greater loss of low intensity images and therefore the tail of the orange distribution shrinks even more. Thus, when computing the median resolution one needs to be careful as the uncertainties in the blur parameter have a twofold effect. Firstly, this can lead to a an artificial sharpening of the MTF and Algorithm 2 can therefore pick up a to an underestimated resolution distance (see Figure 3-19 (a) – red scatter points vs black curve). This can lead to an overall underestimation of the ground truth median resolution. Secondly, the loss of resolution measurements on low intensity images due to uncertainty in resolution measurement exceeding a pre-set threshold of 90% leads to a truncation of the tail of the distribution. This of course can lead to an overall lower median value. The combination of these effects explain why using a reduced number of linescans in the case of the really severe combined noise model (datacube 2 and datacube 4) leads to an underestimated median resolution. In particular, the median for datacube 2 is off by around 25 μm from the ground truth median and off by only 1 μm for datacube 4.

To conclude, a very simple approach was used to compare the means of all data sets is used in this work. Bootstrapping allows for computing the standard error of any statistic one chooses, in this case the median. By bootstrapping each data set and investigating the median one can obtain a median value with a 95% confidence interval and a standard error as well. It was found that Algorithm 2 may not perform well under sever noise and reduced number of linescans. Furthermore, it was shown that the recovery method can approximate the ground truth resolution distribution quite well. While Algorithm 2 can truncate the tail of the resolution distribution, the recovery method does not suffer from this issue. To test the robustness of the recovery method, the results shown here were performed on a reduced number of 30 linescans. The fact that the recovery method approximated the ground truth distribution involved no wizardry at all – it was simply noticed that Algorithm 2 cannot estimate the blurring parameter at harsh noise levels (or without a sufficient number of linescans to average out the noise) – curve fitting

simply fails. Thus, imposing a global MTF obtained from the high intensity images solved this issue. The only other information needed was obtained from the empirical noise estimates – mean, variance and standard deviation, which intuitively should be more robust to a decrease of linescans. The requirement of now having more than a hundred linescans for the accurate estimation of the blur parameter has shifted to having a sufficient number of pixels for the estimation of empirical statistics. Of course this approach comes at a price of assuming a global MTF – each image now exhibits the same blur.

Finally, now the question of which data has the best overall resolution can be answered. When the images of the resolution devices were inspected visually it was speculated that material removal with Poisson and strong material removal (blur is minimised) is best, followed by Poisson noise and weak material removal (blur is strong), combined noise with minimised blur and finally combined noise with strong blur (see Figure 3-9). In this simulation, these correspond to datacube 3, datacube 1, datacube 4 and datacube 2 (see Table 3-6). By using either Algorithm 2 (with some reservations) or the recovery method and computing the median values it can be seen that datacube 3 appears to have the best resolution, followed by datacube 1, datacube 4 and finally datacube 2. Thus, it has been numerically shown that crude visual estimates of resolution performance was correct. Generally, the recovery method provides a more accurate comparison. When the recovery method is used, the median resolution values for each datacube are within the uncertainty bound from the ground truth. This is a fantastic result and it implies that even when severe noise is present and a reduced number of linescans are available the ground truth median resolution of a datacube can be calculated. This will be essential for Chapter 5.

3.5 Conclusions

In this Chapter the ideas developed in Chapter 2 were built upon and used for a thorough investigation of resolution. In particular **Chapter 3.2** was concerned with the loss of resolution due to blur and noise. In order to investigate this in **Chapter 3.2.1** the image formation model was scaled to two dimensions. The possible beam paths were discussed and the simplest (and most commonly used one) was chosen for the 2D image formation model. It should be noted that more complex sampling patterns exist, such as the Bruker SmartBeam technology[153]. Modelling such sampling patterns remains a topic for future work. Then, possible strategies for obtain an MTF were discussed in **Chapter 3.2.2**. Three simple systems that can be used to measure an MTF were introduced – a point source, an edge source and a resolution device. The parameters for the image formation model that was applied on these systems were also shown there. The outputs of the image formation model were shown in **Chapter 3.2.3** where the loss of resolution due to blur was visually demonstrated. The resultant MTFs from each experiment were plotted and compared against each other. The MTF derived from the image of a point source server as a ground truth that allowed us to benchmark the other two methods. It was found that using an edge source allows for a really good approximation of the MTF. It produced more data points than the resolution device. From a practical perspective, an edge source is also much cheaper to produce. Finally, in **Chapter 3.2.4** the noise models discussed in **Chapter**

2.4 were applied to the data. It was shown that resolution can be lost due to blur and noise and a natural question arose – hoe does one measure resolution in the presence of both blur and noise?

This question was answered in **Chapter 3.3**. In order to answer this question another question was asked – is there a mathematical object that is equivalent to the MTF but instead of describing the signal carried per frequency it describes the amount of noise carried per frequency? A perfect candidate for this was introduced in **Chapter 3.3.1** – this was the noise spectral density (NSD), and the root of this object describes the amount of noise carried per root frequency. In this section it became apparent why an edge can be incredibly useful for analysing resolution – the transition from naught to signal can be used to compute an MTF, while the edge surface intensity can be used to characterise noise statistics in both real and frequency space. The relation between those was discussed. In **Chapter 3.3.2** some MTFs were plotted alongside the root of the NSD divided by two and the intersection between the two mathematical objects gave us a natural way of computing spatial resolution in the presence of noise and blur. Two algorithms were proposed. Algorithm 1 takes a two dimensional edge as an input and returns the real space blur parameter, the average surface intensity and the SNR. Algorithm 2 takes a two dimensional edge as an input and returns the resolution frequency and the uncertainty in the intersection point. In **Chapter 3.3.3** the act of measuring resolution was generalised to a single mathematical equation; this was called the resolution model. In **Chapter 3.3.4** error analysis was performed in order to understand the uncertainties associated with a resolution measurement. It was found that the estimate in real space blur σ and/or inverse space blur $\tilde{\sigma}$ (they are related reciprocally, up to a constant of proportionality that depends on how one computes a Fourier transform) can contribute to this uncertainty. Furthermore, the uncertainties from the average signal intensity and standard deviation get propagated to the resolution point.

In **Chapter 3.4** four data cubes were simulated. To simulated the range of intensities a log-skew normal distribution was used. The parameters for this distribution were obtained from real experiments, which will be shown in **Chapter 4.** In **Chapter 3.4.1** the properties of each datacube were described: strong blur and Poisson noise, strong blur and combined noise, minimised blur and Poisson noise, minimised blur and combined noise. The edges simulated here had dimensions of dimensions of $(58{,}129)$ pixels in terms of width and height. Then, in **Chapter 3.4.2** a ground truth equation derived from the resolution model in **Chapter 3.3** was proposed. The results were shown and plotted against the ground truth. It became apparent that uncertainties in the blurring parameter at low intensities can dominate the uncertainty in the measured resolution. This called for an investigation of how Algorithm 2 performs when a reduced number of linescans is used. The same measurement was repeated in **Chapter 3.4.3** but instead 129 linescans only 30 were used. As expected, the resolution estimates significantly deteriorated, especially in the case of combined noise with strong blur. Since the goal is to quantify the resolution of tissue imaging experiments in **Chapter 5** a strategy for dealing with this problem was proposed. **Chapter 3.4.4** outlined this strategy. The first step required a global MTF derived from the real space blur estimate of the high intensity

edges to be imposed on the entire data cube. The second step was a simple noise calibration, described in detail in **Chapter 2.4**. It was shown that this method for recovering the ground truth resolution approximated the ground truth quite well and even outperformed Algorithm 2, which turned out to be sensitive to reduced number of linescans in the presence of a strong blur and severe noise. However, the question of how to compare the data sets still remained. A simple approach for doing this was outlined in **Chapter 3.4.5**. A log-linear violin plot was used to show the resolution distributions. The statistic chosen to describe the general trend within each resolution distribution was the median value. In order to check if the medians are significantly different bootstrapping was used to compute the median within a 95% confidence interval and a standard error. The section was then concluded with a table that summarised the performance of the different resolution characterisations performed on the datacubes. In particular Algorithm 2 with 129 linescans, Algorithm 2 with 30 linescans and the recovery method used on the 30 linescans data. The recovery method was used on the 30 linescans data points to check if it would perform well under real world conditions. The results showed that the recover method performed quite well.

The process of measuring resolution was studied in depth in this chapter. A novel approach for measuring spatial resolution was proposed. While quantifying resolution as a function of blur and noise is not unique to this work[69,137], other methods rely on a resolution device to obtain an MTF. The method proposed here outperforms the current best methods[69,137] in two ways.

Firstly, the noise spectral density naturally encapsulates the noise behaviour of the image without making assumptions on the nature of the noise. The authors of one of the current best methods[137] did not verify that flicker noise is a dominant noise source and yet proceeded to constrain resolution based on flicker noise. The method proposed here computes resolution accurately without making any such assumptions (as long as the edge area is homogeneous). This is quite important as different modalities may be characterized by different noise models. If one modality exhibits Poisson noise, while another is dominated by the combined noise model, the method proposed here will be able to deal with this. Other methods[69,137] are not capable of taking this into account. Secondly, using a step edge to compute an MTF is much cheaper and less time consuming than producing a resolution device[67,69,137]. That is a significant advantage for any study that seeks to measure the spatial resolution across different pixel sizes and modalities. This method also has the potential to be applied to any data set that exhibits a sharp edge like feature, such as tissue imaging datasets.

Finally, a word on the general usefulness of the image formation model. The systems investigated here were very simple geometrical systems. However, it is also possible to simulate a whole tissue imaging experiment. For example, Voronoi tessellation may be used to discretise tissue into cells[154]. Each cell may be given a certain molecular distribution and overall different tissue features can be simulated in this way. Then, the image formation model could be applied to study the effects of noise and blur on a tissue imaging experiment. Moreover, this can be used as a ground truth for studying denoising algorithms and how accurately they can recover the ground truth

distribution of features. Furthermore, the effects of noise on multivariate analysis can be investigated with this method. Therefore, the image formation model is not only useful for the purpose of measuring resolution and it can be applied in the study of a range of different problems.

Chapter 4 Measuring spatial resolution experimentally using a step edge

4.1 Introduction

In Chapter 2 and Chapter 3 the theoretical ground work for measuring spatial resolution was laid down. In this Chapter spatial resolution is measured experimentally in real imaging experiments. An edge source was chosen a system for measuring spatial resolution because it allows for an accurate estimate of the MTF and the noise statistics of the imaging system. Furthermore, the use of the image formation model showed that features finer than the width of the beam can be detected. In the case of MALDI, which also uses strong material removal, this has been shown experimentally[151]. However, in Chapter 2 and Chapter 3 it was also shown that in the case of strong material removal applying the most commonly used resolution metric, which is based on blur and can be estimated from an edge profile ($86-14\%$ criterion), leads to resolution estimates smaller than two pixels, which violated the Sampling theorem. In this chapter this theoretical observation is confirmed experimentally. Not only that, but the workflow for measuring spatial resolution established in Chapter 3 is applied. It will become apparent that this method performs much better than the most common practice.

To do this, the resolution performance of a MALDI imaging system is tested, since MALDI experiments often involve strong material removal. This was done across a range of different pixel sizes, allowing for the change of resolution due to material removal to be quantified. In particular, once the pixel size is decreased a smaller area is then probed. This decrease in signal leads to a decrease in image SNR and therefore datasets acquired at a smaller pixel size will exhibit a worse resolution. Then, one might ask at what pixel size the effects of noise will triumph over the resolution gain due to strong material removal. The methods developed in Chapter 3 are excellent for answering this question. Furthermore, the change in noise levels across different pixel sizes is also characterised.

4.2 Methods

Methods can be divided in computational and experimental. The computational methods were already discussed in previous chapters. As for the experimental ones, various methods for creating a sharp step edge were tested. The best procedure found is presented in this work. Silver was chosen as a material to create a step edge. The reasons are several – it is easy to create a thin silver film of uniform thickness and silver is very reactive and can form various ions at a range of intensities.

4.2.1 Physical vapour deposition (PVD)

PVD is a method used for the production of thin films in vacuum conditions. The material that is to be deposited is in the solid state. It then transitions into a vapour state and once the vapours reach the desired substrate they transition back to the solid state. The initial transition from solid to vapour is most commonly achieved via

sputtering or evaporation. The experimental approach in this work used evaporation as means of growing a thin silver film. The following schematic depicts the PVD process:

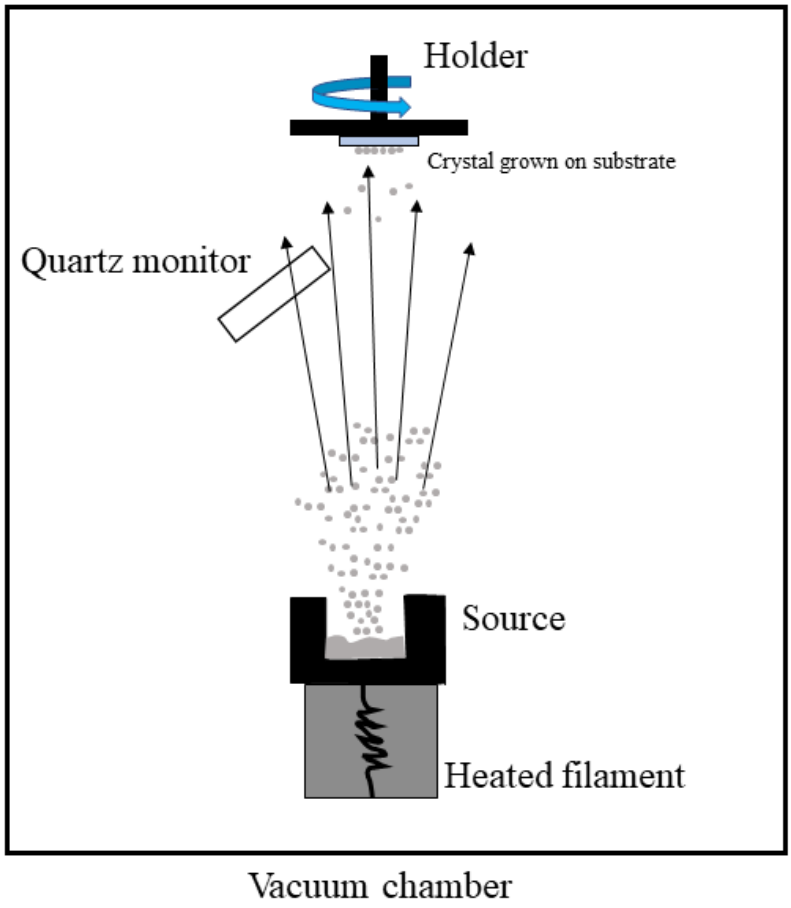


Figure 4-1 A schematic representation of the PVD process.

The material to be deposited is placed in a vacuum chamber. The material is then heated using a heated filament and the temperature is monitored. This allows for the vaporisation of the material. As particles leave the source the vapour expands towards the substrate, which is placed on a sample holder. The direction of movement of the particles is indicated by the black lines (particles are not to scale!). In order to monitor the number of particles arriving at the substrate a quartz monitor is used. This allows for the temperature to be adjusted in order to reach a steady stream of particles and ultimately control the thickness of the thin film that is being deposited. Once the particles reach the substrate they condense back into the solid state and a thin film is produced. The holder usually rotates – this avoids shadowing effects and helps produce an uniform thin film sample.

4.2.2 Sample preparation

A sharp silver step edge was deposited using a NEXDEP PVD platform (Angstrom Engineering, Canada). A silver pellet (Angstrom Engineering, Canada) was heated to its boiling point in vacuum conditions. Using the quartz monitor the estimated thickness of the thin film was 300nm. A Superfrost™ Plus microscope slide (Fisher Scientific, UK) was used as a substrate. The step edge feature was created with the aid of Polyimide (Hi-Bond HB830 Amber Polyimide Film Electrical Tape, 12mm x 33m) tape, which was used as a mask. Once the thin film was deposited and removed from vacuum, the mask was also removed allowing for a sharp step edge feature to be created. The step edge sample was then coated with alpha-Cyano-4-hydroxycinnamic acid (CHCA), (>98%, Sigma-Aldrich, UK) using a TM-Sprayer (HTX Technologies, USA). The matrix solution was prepared using 80% methanol (LC-MS grade) and 20% purified water (Water, Optima LC/MS Grade, Fisher Scientific UK); a 5 mg/mL solution was used.

4.2.3 Mass spectrometry imaging

Once the sample was prepared it was then ready to be imaged. A commercially available MALDI Synapt G2-Si (Waters, UK) was used for this purpose. The instrument was set in resolution mode and a positive polarity was chosen. Red phosphorus (>99%, Sigma-Aldrich, UK Merck) was used for the calibration of the mass spectrum. The datasets spanning 30 and 90 μm pixel sizes had the range of recorded mass to charge ratios calibrated for $50 - 1200$ Da. The 15 µm pixel size dataset was calibrated for a slightly different mass range – $50 - 1500$ Da and it was also acquired roughly a month and a half before the other five datasets. All datasets were acquired using spot mode. The scan time for each image was kept constant and set to $\Delta t_s = 0.2s$ while the stage velocity was adjusted in order to create different pixel spacings. A laser energy of 140 a.u (arbitrary units) was chosen. The laser repetition rate was set to $2.5kHz$. The following table summarises the imaging conditions for each experiment.

Pixel spacing (μm)	Stage velocity ($\mu m/s$)	Scan time (s)	Laser energy ($a.u$)	Laser repetition rate (kHz)
90	450	0.2	140	2.5
75	375	0.2	140	2.5
60	300	0.2	140	2.5
45	225	0.2	140	2.5
30	150	0.2	140	2.5
15	75	0.2	140	2.5

Table 4-1. A summary of the MSI parameters used in this MALDI experiment.

Before and after the imaging experiments were performed the sample was imaged with the aid of a bright field microscope. In total six different datasets of the sharp step edge were obtained. Both the rising and the falling edge were captured in those experiments, apart from the 15 μm pixel size one, for which only the rising edge profile was imaged. Therefore, to keep the analysis comparable, only the right hand side was used in the analysis. The range of

pixels sizes here allowed for an investigation of the resolution performance of the instrument when undersampling and oversampling (from the point of view of MSI). In particular, in Chapter 2 and Chapter 3 it was discussed in detail how material removal can allow for features finer than the width of the beam to be detected. This is the first study where the resolution of oversampling (from the point of view of MSI) with strong material removal is quantified!

4.2.4 Computational methods

4.2.4.1 Data handling and resolution analysis

The methods used to compute spatial resolution were discussed in detail in Chapter 3. Very briefly, with the aid of the numpy, scipy, seaborn and matplotlib packages, a custom Python script was crafted that was used for the analysis of resolution and noise statistics. How the script works was outlined in the pseudocode provided for Algorithm 1 and Algorithm 2 in Chapter 3. As for the actual data itself, the raw experimental data for pixel sizes between 30 and 90 μm was converted to an imzML using an imzML converter[155]. The data was then pre-processed using SpectralAnalysis[156]. This involved rebinning the m/z channel with linear interpolation using a $0.002 - Da$ bin width. After that, a mean spectrum was generated out of which the first 2000 most intense peaks were picked for each data set in order to generate a datacube. Unfortunately, the imzMLConverter script failed to convert the entire 15 μm dataset. Instead, the data was exported using the proprietary HDImaging (Waters, UK) software[157] and only the first 1000 most intense peaks were selected from the mean spectrum. The datacubes were parsed into a .csv or .txt format which allowed for the Python script to be used in order to perform the analysis outlined in Chapter 3. It should be noted that the 15 μm dataset is still comparable to the other five datasets despite the difference in the pre-processing workflow. This is because both software use (almost) identical pre-processing steps. If anything, the fact that the 15 μm dataset was acquired at an earlier time point with a different mass range could introduce a greater difference between the datasets than the pre-processing workflows used.

4.2.4.2 Maximum likelihood estimation (MLE)

While the scripts used to measure spatial resolution were described in detail in Chapter 3, some previously undiscussed methods are used in this chapter. Namely, characterising the distribution of intensities was done using Maximum Likelihood Estimation (MLE).Very briefly, for the purpose of this discussion, a quick overview of how MLE works is now provided. Suppose one has a set of n observations $(x_1, x_2, \dots, x_n)$, corresponding to a random sample $X_1, X_2, \dots X_N$. The assumed probability density function of X_i depends on some unknown parameter (or set of parameters) θ, which one wishes to estimate. Let the probability density function for each X_i be $f_i(x_i; \theta)$. Since there are many observations, the joint probability density function of observing the collection of all observations is simply the product of all $f_i(x_i; \theta)$:

$$L(\theta) = P(X_1 = x_1, X_2 = x_2, \dots, X_N = x_n) = f(x_1, ; \theta) f(x_2, ; \theta) \dots f(x_n, ; \theta) = \prod_{i=1}^{n} f(x_i, ; \theta) \quad \text{Eq. (4.1)}$$

Where here $L(\theta)$ is the *likelihood* of observing these data given a particular value of the parameter θ. The maximum likelihood estimator $\hat{\theta}$ is the one that maximisies the above likelihood.

$$\hat{\theta} = \arg\max L(\theta; X) \quad \text{Eq. (4.2)}$$

Equation 4.1 and Equation 4.2 can be simplified by considering the natural logarithm of $L(\theta)$:

$$l(\theta) = \ln(L(\theta)\,) = \sum_{i=1}^{n} f(x_i; \theta) \quad \text{Eq. (4.3)}$$

Where the beauty of the simplification is that the product has now turned into a summation; the term $l(\theta)$ is the *log-likelihood* function. Therefore, the estimator $\hat{\theta}$ may be computed as:

$$\hat{\theta} = \arg\max l(\theta; X) \quad \text{Eq. (4.4)}$$

The optimisation can be done computationally or analytically. This may be done by solving:

$$\frac{\partial}{\partial \theta} l(\theta; X) = 0 \quad \text{Eq. (4.5)}$$

In this thesis, the MLE estimates were performed numerically using the scipy.stats Python module.

4.2.4.3 Mann-Kendall hypothesis testing (MK test)

In some of the investigations relating to the noise statistics, in particular the functional dependence of the a, b parameters on pixel size, the MK test shall be used in order to detect the presence of a trend or to confirm if there is no trend at all. It is based on a null hypothesis (H_0) and an alternative hypothesis (H_1). H_0 states that there is no trend at all and H_1 is true if there is a significant monotonic (either decreasing or increasing) trend in the data. The test is usually applied on a time series but here it shall be used to check if the a, b parameters to examine the validity of H_0 or H_1 across pixel sizes. The statistic chosen to interrogate the null/alternative hypothesis is the rank correlation between the original series and all possible shifted versions of the original series:

$$S = \sum_{i=1}^{n-1} \sum_{j=i+1}^{n} sgn(x_j - x_i) \quad \text{Eq. (4.6)}$$

Where S is the rank correlation and sgn is the sign function. If the rank correlation is zero that suggests that H_0 is true; if S is positive or negative then H_1 is true and the data exhibits a monotonic trend – increasing if $S > 0$ and decreasing if $S < 0$. The variance in S is given by:

$$Var(s) = \frac{1}{18}\left[n(n-1)(2n+5) - \sum_{p-1}^{g} t_p(t_p-1)(2t_p+5)\right] \quad \text{Eq. (4.7)}$$

With g being the number of tied groups and t_p is the number of observations in the group p. From here an associated MK test statistic can be computed:

$$Z_{MK} = \begin{cases} \frac{S-1}{\sqrt{Var(S)}} & if\ S > 0 \\ 0 & if\ S = 0 \\ \frac{S+1}{\sqrt{Var(S)}} & if\ S < 0 \end{cases} \quad \text{Eq. (4.8)}$$

And the corresponding p-value is then obtained from a z-table. In this work the 5% significance level is used, which corresponds to $p = 0.05$. If the p-value exceeds this threshold then H_0 is accepted and there is no trend in the data. If the p-value is smaller than the threshold, then H_1 is accepted and the data exhibits a monotonic trend. In this work the MK test was performed using the pymannkendall Python package. The specific function used to compute the relevant statistics was the pymannkendall.original_test.

4.3 Results and discussion

4.3.1 Edge characteristics

The following figure shows an image of the obtained with bright field microscopy sample after one of the imaging experiments was performed.

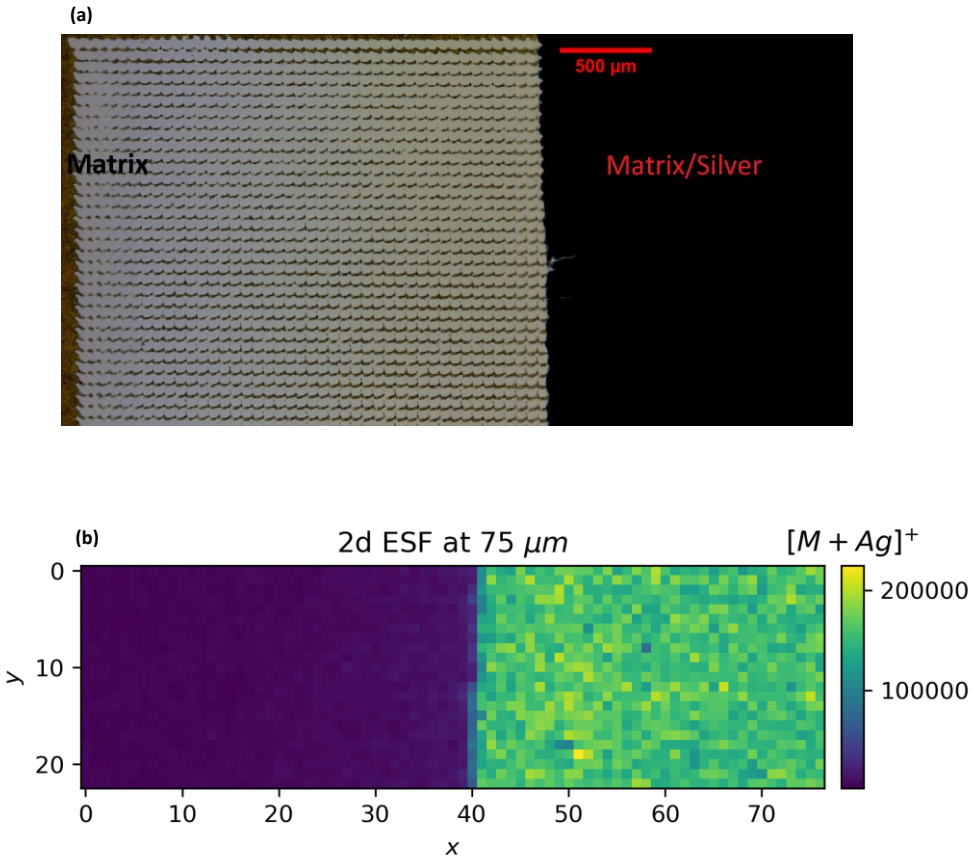


Figure 4-2 (a) – A bright field microscopy image of the matrix/step edge obtained via bright field microscopy after an MSI experiment. The MSI experiment was set to 75 µm *pixel size. (b) – A two dimensional ESF of the most intense ion image acquired at* 75 µm *pixel size. Here M denotes the matrix molecule – the ion signal displayed is a matrix/silver adduct.*

The dark region in Figure 4-2 (a) is the silver region. Because a bright field microscope was used to characterise the matrix/silver edge system and the silver step edge had a thickness of 300 nm, the light was blocked and the silver surface appeared as a dark region. The matrix region can be seen in the left hand side of Figure 4-2 (a). The white elliptical regions are the craters left after complete material removal. The pixel spacing here is 75 µm. Therefore, the pixel sizes selected for this experiment ($90 - 15$ μm, in 15 µm increments, see Table 4-1) span the range of undersampling to oversampling with strong material removal. Upon closer inspection of the craters it is evident that they all have a slightly different area.

Crater	Semi-major (μm)	Semi-minor (μm)	Area(μm^2)
1	38	31	3641
2	38	34	4059
3	35	34	3784
4	35	31	3421
5	36	34	3850
6	31	33	3170
7	38	31	3669
8	38	36	4221
9	38	37	4450

Table 4-2. Variations in crater area for nine randomly selected craters.

This is one of the processes that were hypothesised to lead to fluctuations of the peak heights discussed in Chapter 2.4. This becomes more evident when the semi-major and semi-minor of ten randomly selected craters were measured. The average area measured was $3800\ \mu m^2$ with a standard deviation of $400\ \mu m^2$. Thus, it can be seen that the fluctuations around the average are not insignificant. The differences in the semi-major and semi-minor axis of the craters can be attributed to fluctuations of the laser energy and uncertainties in the lase repetition rate. Therefore, it should not be surprising once the noise statistics are presented that there is a deviation from the Poisson noise model, as discussed in Chapter 2. As for Figure 4-2 (b), the most intense single ion image is shown.

4.3.2 Mean spectra

The mean spectra for all pixel sizes is depicted in the following figure.

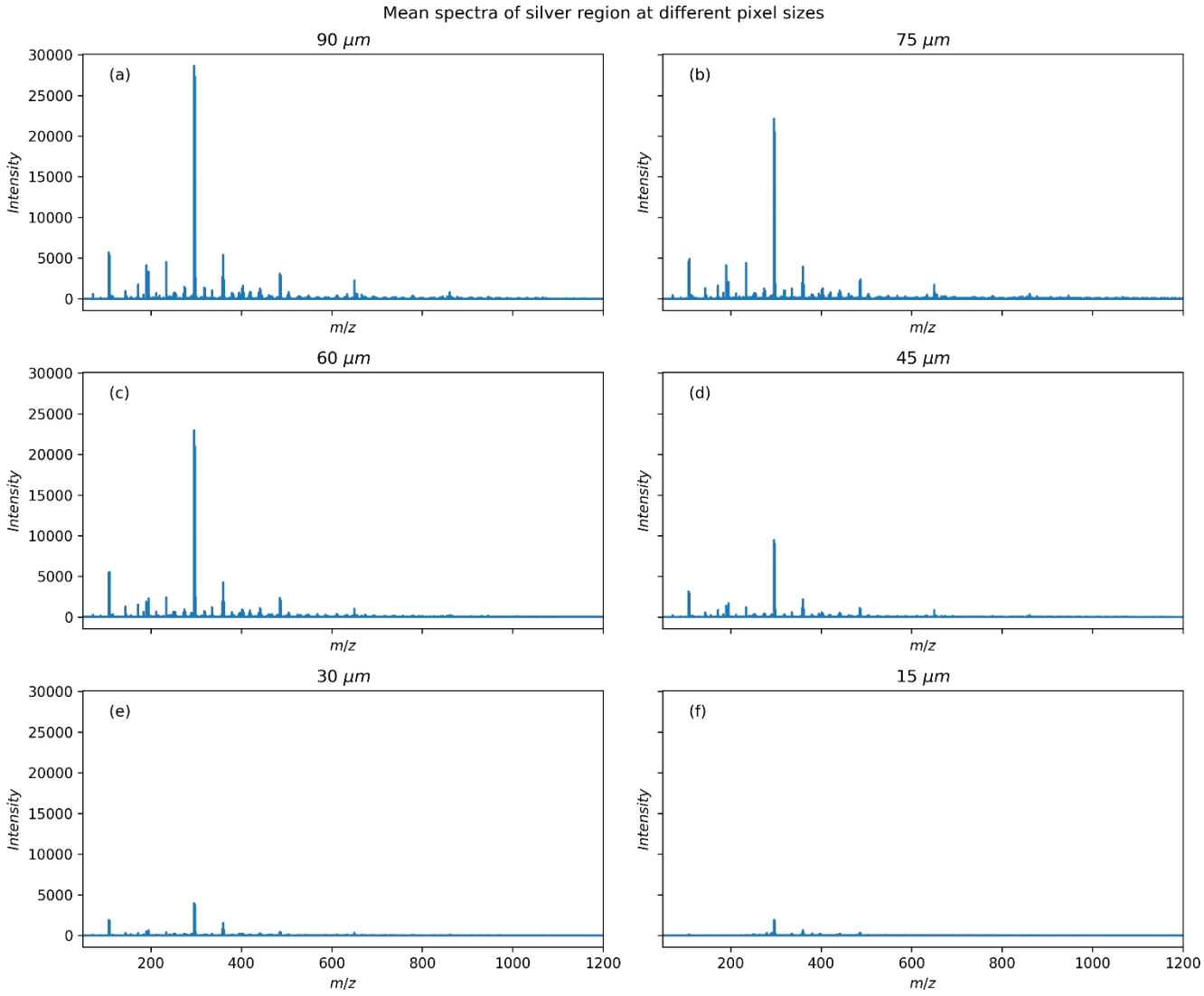


Figure 4-3. Mean spectra from silver region acquired at different pixel sizes. (a) – 90 μm pixel size. (b) – 75 μm pixel size. (c) – 60 μm pixel size. (d) – 45 μm pixel size. (e) – 30 μm pixel size. (f) – 15 μm pixel size.

The most intense peak in each of the mean spectra shown in Figure 4-3 is the $[M + Ag]^+$ ion, where M denotes the matrix molecule. This corresponds to a predicted *m/z* value of 295.9477 Da. All experimentally observed values exhibited a fractional error smaller than 10ppm. The mean spectral intensities are presented on the same scale. It is apparent that a decrease in pixel size leads to a loss of signal intensities. This will affect the spatial resolution. Next, a zoomed in version of the mean spectra is shown.

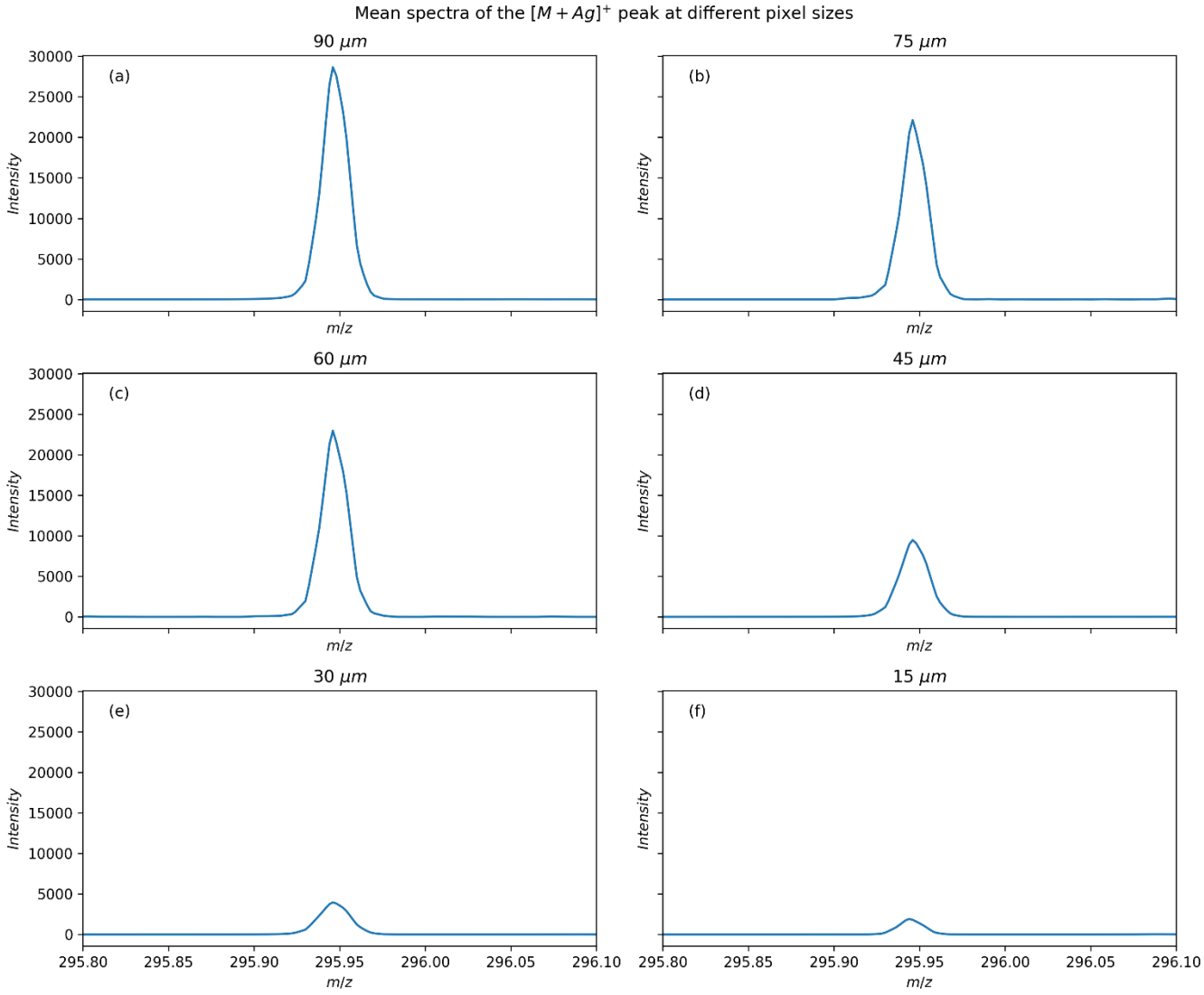


Figure 4-4. Base silver peak at different pixel sizes. (a) – 90 *µm pixel size. (b) –* 75 *µm pixel size. (c) –* 60 *µm pixel size. (d) –* 45 *µm pixel size. (e) –* 30 *µm pixel size. (f) –* 15 *µm pixel size.*

The intensity scale is kept the same. Similarly, finer pixel sizes lead to a loss of intensity. The peak height diminishes more than an order of magnitude when comparing the 90 *µm* measurement to the 15 *µm* one. The single ion images of this signal are showed in Figure 4-5.

4.3.3 Characterising the distribution of intensities across pixel sizes using maximum likelihood estimation (MLE).

Across all datacubes, the most intense ion image originating from the silver/matrix region was the same and it was identified as a CHCA silver adduct. This is symbolically represented as $[M + Ag]^+$. It can be concluded from this figure that the experimental method proposed for producing a step edge has been successful. Next, the most intense signal for each of the datacubes is shown.

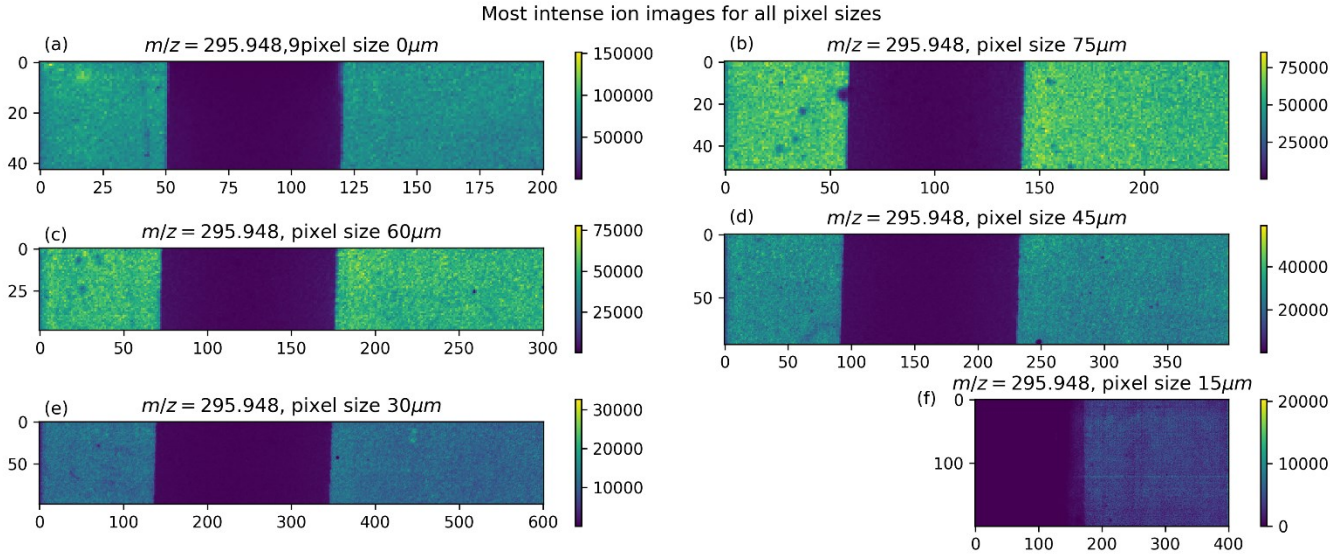


Figure 4-5. The most intense ion images across the six datacubes. (a) – 90 μm pixel size. (b) – 75 μm pixel size. (c) – 60 μm pixel size. (d) – 45 μm pixel size. (e) – 30 μm pixel size. (f) – 15 μm pixel size.

Several things should be pointed out here. Firstly, when this experiment was being designed there was no notion of what the minimum number of linescans is needed so that the blurring parameter can be fitted – the theoretical investigations shown in Chapter 3.4.4 were simply not performed at this point in time. Thus, as a rule of thumb each region of interest (ROI) was designed to have as many linescans as possible. However, since the noise model parameters were not known either, there is no way of knowing what the optimum number of linescans would be regardless. Secondly, while it would be tempting to use all of the available linescans, care must be exercised. It can be noticed in the lower pixel size images (Figure 4-5 (c), (d), (e)) that the edge appears to be slightly tilted. When Algorithm 1 and Algorithm 2 are applied, since in the first and in the last linescan the edge is centred at different positions, averaging over a tilted edge would exaggerate the blurring parameter. A greater tilt in the edge will result in a greater overestimation of the blurring parameter. Similarly, the more linescans are used the greater this overestimation becomes. Thus, it is imperative to select a ROI for which this tilt is minimised. Furthermore, some of the edges exhibit imperfections in the edge surface. This will affect the estimates of the noise statistics and therefore a ROI that avoids such imperfections must be selected. As for the actual images themselves, it is evident that as the pixel size decreases so does the intensity of the edge surface. This is because of the effects of material

removal – as the craters begin to overlap a smaller area is being effectively sampled, leading to a decrease in intensity. Since resolution is a function of intensity, blur and noise, it would be interesting to consider what the intensity distribution across all pixel sizes. Namely, if a lot of images appear to be concentrated in the low intensity regime, the tools and considerations laid out in Chapter 3.4.3, Chapter 3.4.4 and Chapter 3.4.5 can be quite useful. The following graph depicts the distribution of intensities for all six pixel sizes used in this study:

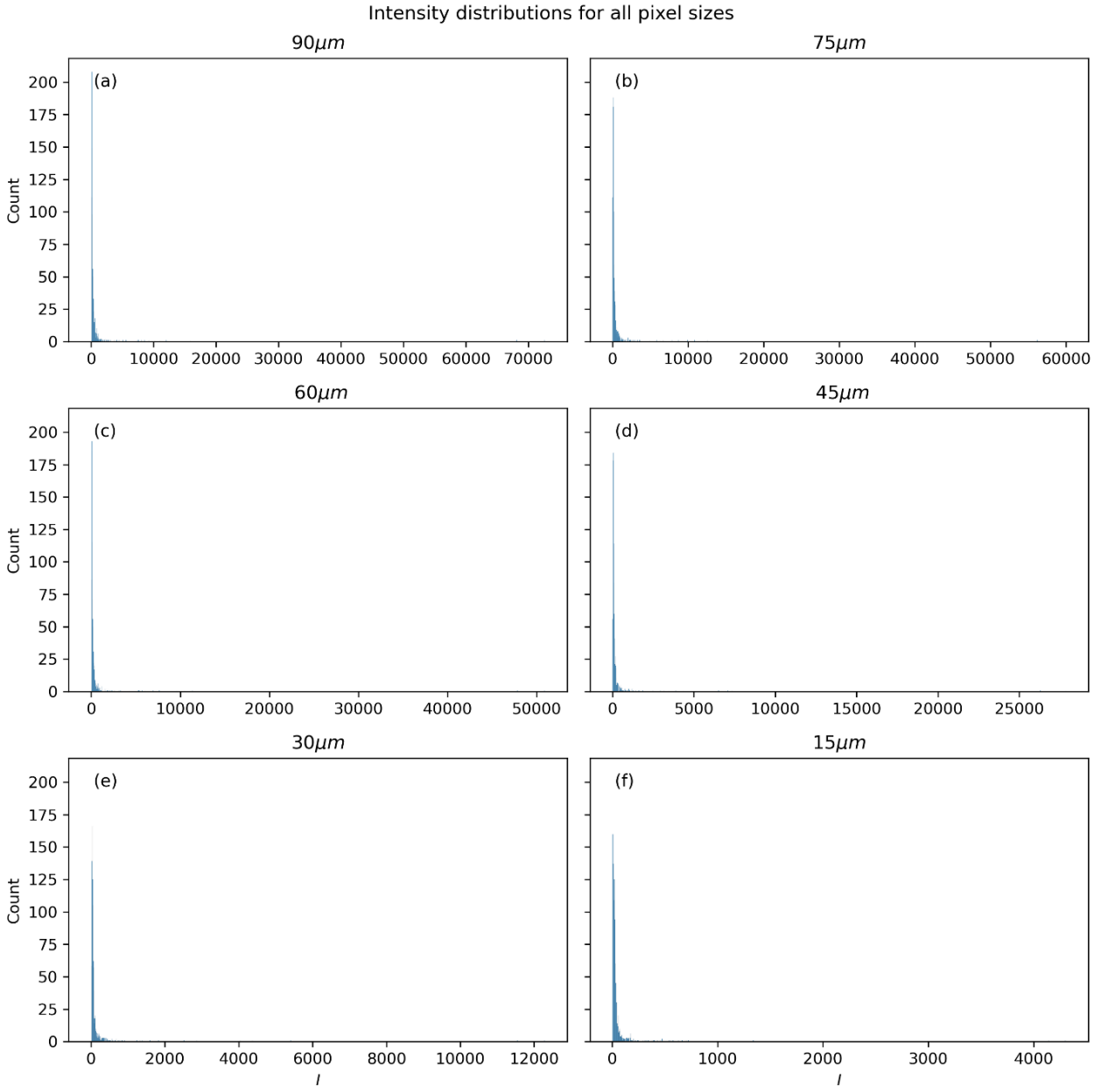


Figure 4-6 The distribution of intensities across all pixel sizes. (a) – intensity distribution at 90 μm *pixel size. (b) – intensity distribution at* 75 μm *pixel size. (c) – intensity distribution at* 60 μm *pixel size. (d) – intensity distribution at* 45 μm *pixel size. (e) – intensity distribution at* 30 μm *pixel size. (f) – intensity distribution at* 15 μm *pixel size.*

It can be seen that the majority of the images are concentrated in the low intensity regime, with only very few images spanning the high intensity region. This is observation is generally true for most MSI experiments. Therefore, the median resolution of a datacube will mostly be affected by the images in the low intensity regime. Unfortunately, presented as such these plots do not allow for a thorough investigation of the distribution of intensities. Consider for a moment taking the natural logarithm of each of the intensity distributions. The results are shown in the following graph.

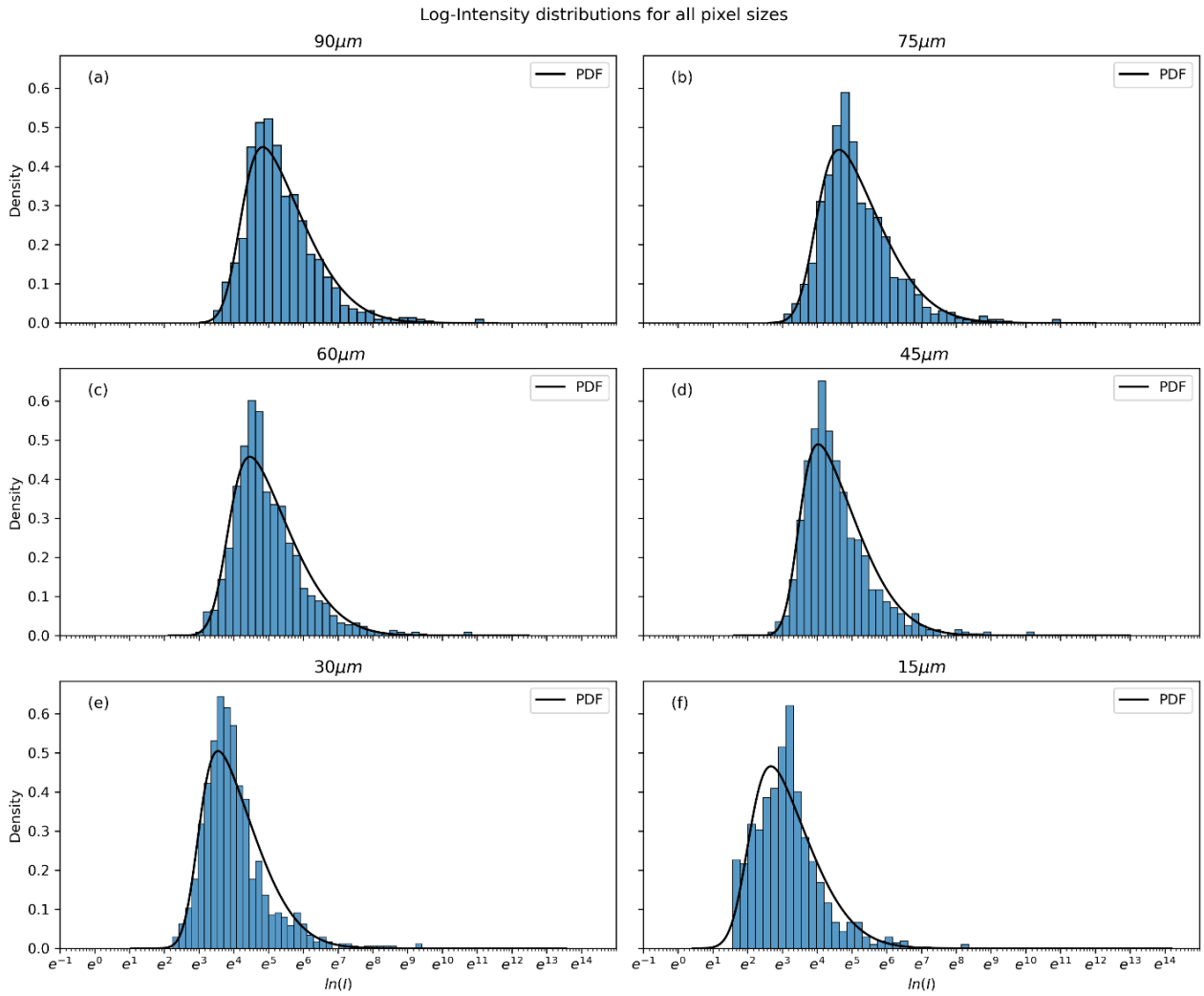


Figure 4-7 The natural logarithm of the intensity distributions across various pixel sizes. (a) – natural log of the intensity distribution at 90 *μm pixel size. (b) – natural log of the intensity distribution at* 75 *μm pixel size. (c) – natural log of the intensity distribution at* 60 *μm pixel size. (d) – natural log of the intensity distribution at* 45 *μm pixel size. (e) – natural log of the intensity distribution at* 30 *μm pixel size. (f) – natural log of the intensity distribution at* 15 *μm pixel size.*

The intensity distributions in Figure 4-7 are derived from the mean spectra shown in Figure 4-3. In particular, the top 2000 most intense peaks were selected when producing those histograms. For the 15 μm dataset, the top 1000

peaks were used. These distributions are derived by computing the logarithm of the mean spectra shown in Figure 4-3 and then histogramming. It can be deduced from Figure 4-7 that the natural logarithm of the intensity distributions reveals valuable information about the nature of those distributions. Each of the histograms appears to exhibit some amount of skewness. While it would be tempting to model the natural log of the intensity as a log-normal distribution, this skewness calls for a slightly different approach. For example, since the natural log of the intensity distribution appears to resemble a skew-normal distribution, it could be that a log-skew normal distribution is a more appropriate choice. The skew-normal probability density function (PDF) is defined as:

$$f(I) = \frac{2}{\sigma_I\sqrt{2\pi}}\exp\left(-\frac{(I-\mu_I)^2}{2\sigma_I}\right)\int_{-\infty}^{\alpha\left(\frac{I-\mu_I}{\sigma_I}\right)}\frac{1}{\sqrt{2\pi}}\exp\left(-\frac{t^2}{2}\right)dt \qquad \text{Eq. (4.9)}$$

Where here $f(I)$ is the PDF and it describes the probability of observing a given intensity, given the parameters α, μ_I, σ_I, which describe the shape, location and scale respectively. The shape parameter α determines the skewness (right-skewed if $\alpha > 0$, left-skewed otherwise), the location parameter μ_I is the expected value and the scale parameter σ_I determines the variance. Alternatively, recognising the leading term as the standard probability density function of normal distribution $\phi\left(\frac{I-\mu_I}{\sigma}\right)$ and the integral term as a the cumulative distribution function (CDF) of a normal distribution $\Phi\left(\alpha\left(\frac{x-\mu_I}{\sigma}\right)\right)$, the PDF may be written as:

$$f(I) = \frac{2}{\sigma_I}\phi\left(\frac{I-\mu_I}{\sigma}\right)\Phi\left(\alpha\left(\frac{x-\mu_I}{\sigma}\right)\right) \qquad \text{Eq. (4.10)}$$

The CDF of the skew-normal distribution is given by:

$$CDF = \Phi\left(\frac{I-\mu_I}{\sigma_I}\right) - 2T\left(\frac{I-\mu_I}{\sigma_I}, \alpha\right) \qquad \text{Eq. (4.11)}$$

Where $T\left(\frac{I-\mu_I}{\sigma_I}, \alpha\right)$ is Owen's T function:

$$T\left(\frac{I-\mu_I}{\sigma_I}, \alpha\right) = \frac{1}{2\pi}\int_0^{\alpha}\frac{e^{-\frac{(I-\mu_I)^2}{2\sigma_I^2}(1+x^2)}}{1+x^2}dx \qquad \text{Eq. (4.12)}$$

At this point one might ask how can it be known if a log-skew normal distribution is good candidate for modelling the intensity distribution. The natural log of the data seems to have some skew, but what parameters of the skew-normal distribution best describe this? In order to provide an answer for this question, the right mathematical tool needs to be selected. Maximum likelihood estimation (MLE) is a great candidate for this task. For the current problem it is much more convenient to do this computationally. The MLE estimates of the parameters α, μ_I, σ_I were

obtained using the Python scipy.stats package. The black curves in each of the plots shown in Figure 4-7 is a skew-normal distribution fitted to the data using MLE. It can be seen that the proposed PDFs model the data well. The values of the α, μ_I, σ_I parameters are shown in the following table:

pixel size (μm)	α	μ_I	σ_I
90	3.92	4.18	1.54
75	3.74	3.96	1.55
60	3.92	3.82	1.52
45	4.45	3.45	1.44
30	4.06	2.98	1.38
15	3.52	2.02	1.46

Table 4-3. A summary of the α, μ_I, σ_I parameters obtained from MLE for each of the six data sets.

After obtaining the α, μ_I, σ_I parameters, the PDFs and CDFs for each pixel size were plotted using Equation 4.7 and Equation 4.8 respectively:

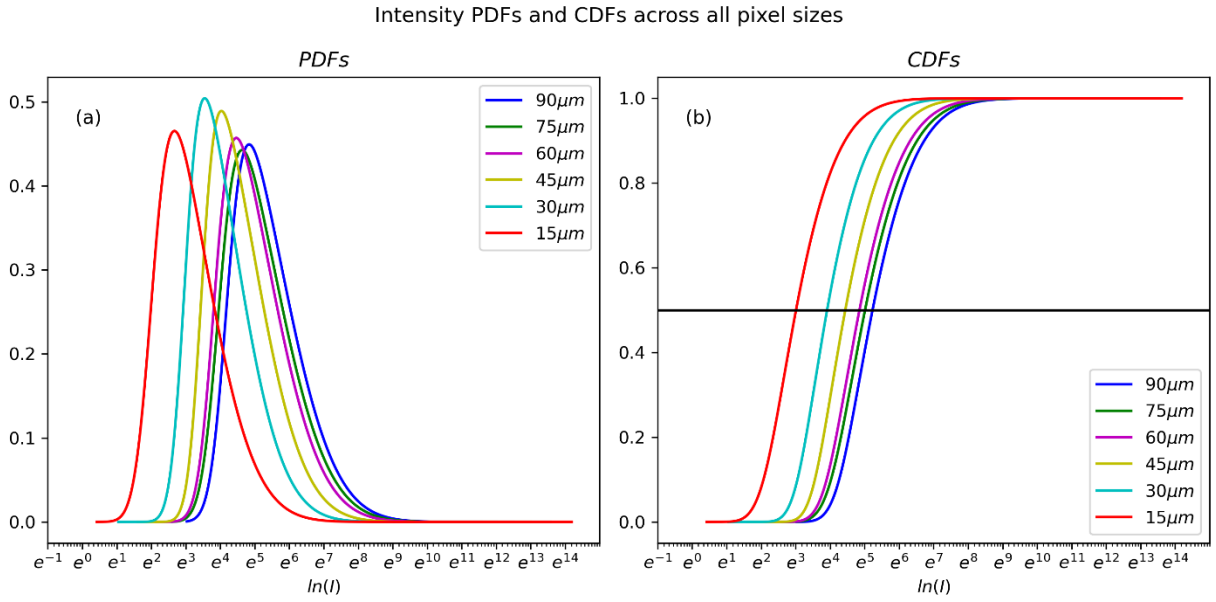


Figure 4-8 (a) – the skew-norm PDFs describing the intensity distributions. Plotted on a natural semi-log scale. (b) – the skew-norm CDFs describing the intensity distributions. Plotted on a natural semi-log scale. The black line represents the 0.5 threshold.

Both Figure 4-8 (a) and Figure 4-8 (b) are incredibly informative when it comes to gaining new insights about the intensity distributions across different pixel sizes. It can be seen that as the pixel size is decreased the location of each PDF shifts towards unity. The scale parameter also decreases steadily with decreasing pixel size, indicating that higher pixel sizes exhibit a larger spread of intensity. The median values for each data set can be obtained from the CDF shown in Figure 4-8 (b). The black horizontal line is placed at 0.5 and value of intensity at which a given CDF intersects the black line is the median. For example, for the 90 μm data set (blue curve) this intersection happens at around $exp(5) \approx 148$. Therefore, half of the intensities will have a value less than 148. The other half

will fall between $exp(5)$ and $exp(11.9)$ or roughly between 148 and $\approx 1.5 \times 10^5$. This can be done for any quantile one is interested in. For example, less than 1% of the data will have an intensity greater than $exp(8.15) \approx 3463$. Therefore, it may be concluded that only very few high intensity images will be available and the resolution of a datacube will be affected by the majority of the images, which are in the low intensity region. An alternative depiction of this can be presented in the following violin plot.

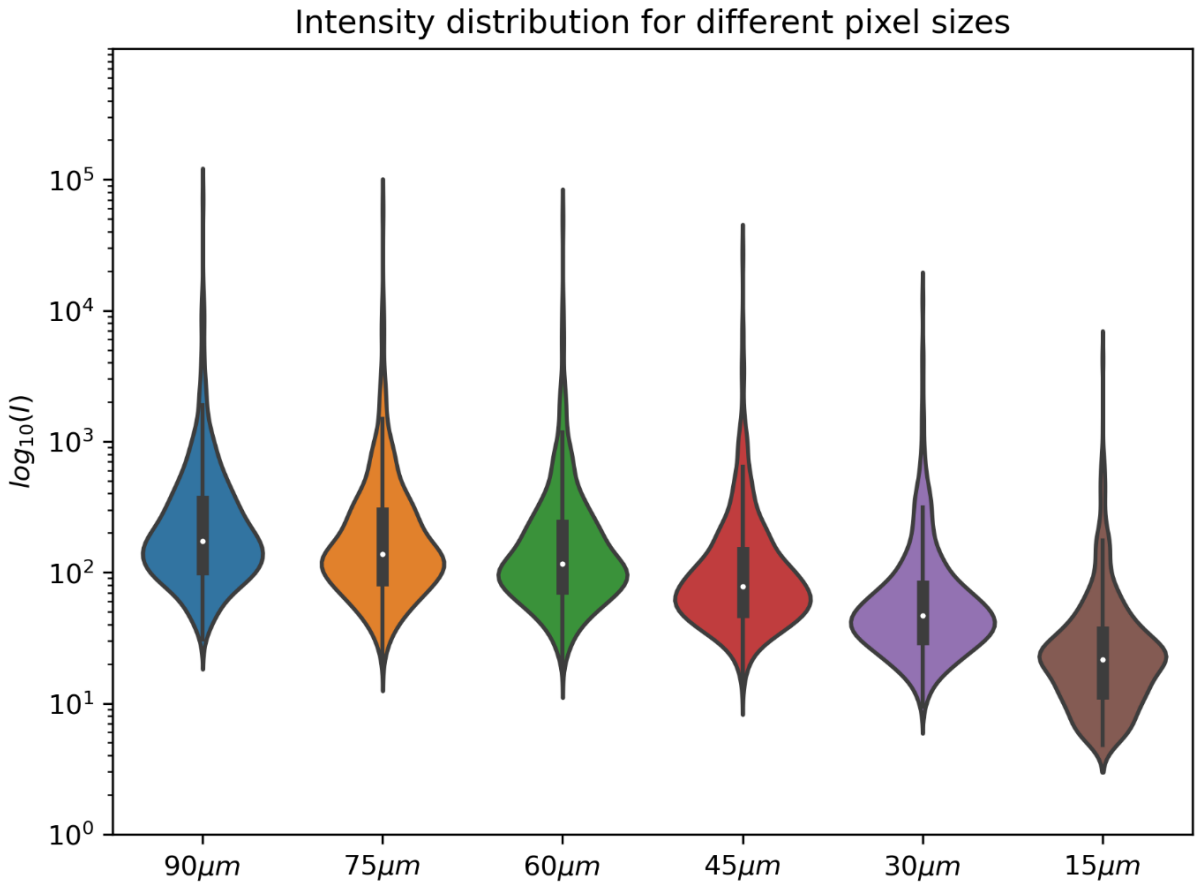


Figure 4-9 A violin plot of the intensity distributions at different pixel sizes. The plot is presented on a log scale.

Each violin plot has a miniature boxplot shown within it; the white dot in the middle is median value. It can be seen that only very few images span the high intensity regime. When the pixel size is reduced from 90 μm to 15 μm there is more than an order of magnitude drop in the highest measured intensities – from $I \approx 10^5$ to $I \approx 10^4$. The same thing could be said for the median values – from $I_{\mu_{1_{1/2}}} \approx 180$ to $I_{\mu_{1_{1/2}}} \approx 20$. Therefore, just by looking at these plots and considering the fact that 50% of images in the 15 μm pixel size will have an average intensity between 0 and 20, it could be hypothesised that the median spatial resolution of the 15 μm datacube is significantly worse due to noise. Indeed, it will be shown that this is true later in this Chapter.

It should be noted that the median values extracted from the CDF, shown in Figure 4-8 (b), are quite close to the empirically estimated medians (white dots within each distribution in Figure 4-9). For example, the CDF obtained with the MLE parameters at $90\,\mu m$ pixel size yields a median of 187, while the empirically estimated median intensity is ≈ 174. Therefore, it may be concluded that the intensity distribution is well described by a log-skew normal distribution. This is incredibly useful for several reasons. Firstly, this may be used when simulating a dataset to test the performance of different computational algorithms. In fact, this was already done in this thesis – the main goal of Chapter 3.4 was to develop a method for measuring the resolution of a datacube. Using the methodology developed here it was possible to simulate the intensity distribution of a datacube in order to test the performance of Algorithm 2 across various noise and blur conditions. Secondly, it was shown in Chapter 3 that an insufficient number of linescans can lead to the low intensity portion of the datacube not having its resolution estimated, due to the fractional uncertainty exceeding a pre-set threshold. Using a percentiles obtained from the CDFs the number of images that will not have their resolution estimated can be computed. Thirdly, the information revealed from the modelling is quite insightful and tells us that the majority of images in a datacube will be low resolution images. Only very few images will exhibit a high resolution. Therefore, by estimating the median intensity of a datacube one can also find the median resolution. Of course, this would still require knowledge on the Fourier space blur parameter $\tilde{\sigma}$ and the noise parameters a, b. As discussed in Chapter 3, $\tilde{\sigma}$ is obtained from the edge transition and a, b are obtained from the empirical statistics of the edge surface.

4.3.4 Noise statistics

4.3.4.1 The noise model – observed variances and SNRs

Now the reader will be convinced that the noise statistics observed in MALDI deviate from Poisson noise. The work done in Chapter 2.4 established a noise model that exhibits a quadratic variance. This is referred to as the combined noise model. This model can be broken down in two parts – a parameter a that is related to the detection process and the overall observed variance is proportional to the product of this parameter and the intensity, namely $Var(I) \propto aI$ [*]. The other part of the model has a quadratic intensity term with a proportionality constant b; $Var(I) \propto bI^2$ [†]. This term arises due to fluctuations in the peak heights, which themselves can be attributed to fluctuations in the ion flux. One possible reason provided for this was that craters can exhibit a slightly different area, therefore a slightly different amount of material is collected, leading to a fluctuation in the peak amplitudes. Other reasons may be the variance of the ion transmission coefficient, natural fluctuations of the chemical reactions that lead to ion formation, or perhaps a combination of all things listed here. A numerical simulation of peaks spanning a range of

[*] In Chapter 2.4 the symbol σ^2 was used to represent variance. Here $Var(I)$ is used instead in order to avoid a clash of notation with the blurring parameter.
[†] Same here.

intensities corrupted with Poisson noise and a height that was allowed to fluctuate, where the fluctuations in the peak amplitude were normally distributed and the spread of the normal distribution was directly related to the b parameter. The b parameter therefore is a measure of how much the peak amplitudes fluctuate and this is a property of the 'front end' (ion source part of the instrument) of the imaging set up rather than the 'back end' (detection part of the instrument). If then in the following experiments a quadratic variance were to be observed, one would be prepared to describe it mathematically. Furthermore, a specific physical interpretation may be given to the two noise model parameters. Since these experiments span a range of pixel sizes and the a parameter is only related to the 'back end' of the instrument it better be the case that the a parameter remains independent of the pixel size used. On the other hand, the b parameter is related to fluctuations arising from the 'front end'. Therefore, one can expect the that the b parameter exhibits a specific functional relationship to the pixel size.

The process of characterising noise statistics was already outlined in Chapter 2.4. There it was mentioned that it is of vital importance to use a region of interest that is as homogeneous as possible. As some of the edge surfaces exhibit defects (see Figure 4-5), only ROIs that appear homogeneous were used. In the next figure the noise variance as a function of intensity is presented across all pixel sizes. As discussed in Chapter 2.4, the origins of the noise variance may be traced back to detector counting uncertainties, which gives rise to a linear variance term, and fluctuations in the peak heights, which can manifest as a quadratic term. While there are other sources of noise, such as quantisation error introduced by the analogue-to-digital converter (ADC) [100,101], modelling these remains beyond the scope of the current work.

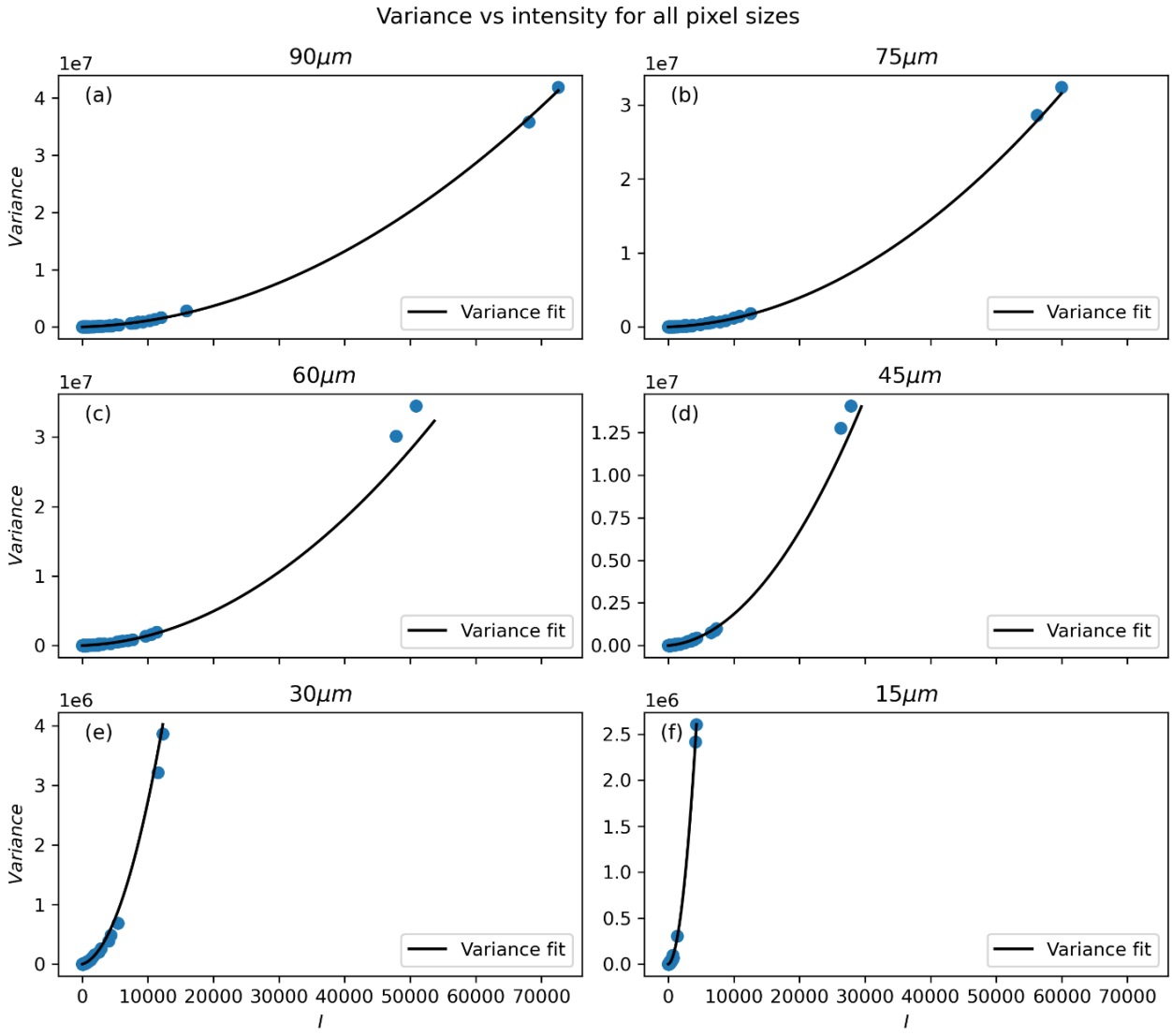


Figure 4-10 Noise variance as a function of intensity plotted across all pixel sizes. (a) – 90 μm pixel size datacube. (b) – 75 μm pixel size datacube. (c) – 60 μm pixel size datacube. (d) – 45 μm pixel size datacube. (e) – 30 μm pixel size datacube. (f) – 15 μm pixel size datacube.

The plots in Figure 4-10 depict the empirically estimated variance as a function of intensity. In order to show the change of the variance across pixel sizes the same x-axis, which represents intensity range of the 90 μm datacube, was used. While the plots would be more aesthetically pleasing presented on a log-log scale, they are deliberately presented on a linear scale. Indeed it has been experimentally shown that the noise in MALDI deviates from Poisson noise and appears to exhibit a quadratic response. This behaviour is consistent across all pixel sizes. The black curve in each of the subplots was plotted after curve fitting was performed with the combined noise model equation (see Chapter 2.4, Table 2-3). Unfortunately, the fits for the 60 μm and 45 μm datacubes miss out on the two high intensity datapoints (this would be barely noticeable if the data were presented on a log-log scale) but seem to

perform very well on the other data sets. Each curve fit allowed for the extraction of the a, b parameters across pixel sizes. These are summarised in the following table.

Data set	a	b
90 μm	37 ± 1	0.00734 ± 0.00001
75 μm	32.5 ± 0.4	0.0082 ± 0.0001
60 μm	36.2 ± 0.5	0.0106 ± 0.0001
45 μm	34.1 ± 0.2	0.0150 ± 0.0001
30 μm	33.3 ± 0.1	0.0240 ± 0.0001
15 μm	24.8 ± 0.4	0.1348 ± 0.0001

Table 4-4. Parameters of the combined noise model extracted from curve fitting the variance as a function of intensity for each datacube.

The errors here were obtained from the covariance matrix provided from scipy.curve_fit module. In particular, the errors represent the standard deviation error of the parameters. This same method was used in Chapter 2 and the extracted parameters showed good agreement with the ground truth parameters used to produce the noise simulation. The a, b parameters may also be estimated from the SNR equation (see Chapter 2.4. Table 2-3). In particular, the SNR equation may be better suited for curve fitting – the variance exhibits a sharp jump along the y axis that can be more than an order of magnitude for the two high intensity data points. The SNR on the other hand, as explained previously approaches a constant as the intensity tends to infinity. Thus, curve fitting may perform better in this situation. The following figure shows the empirically measured SNRs as a function of intensity across all six datasets.

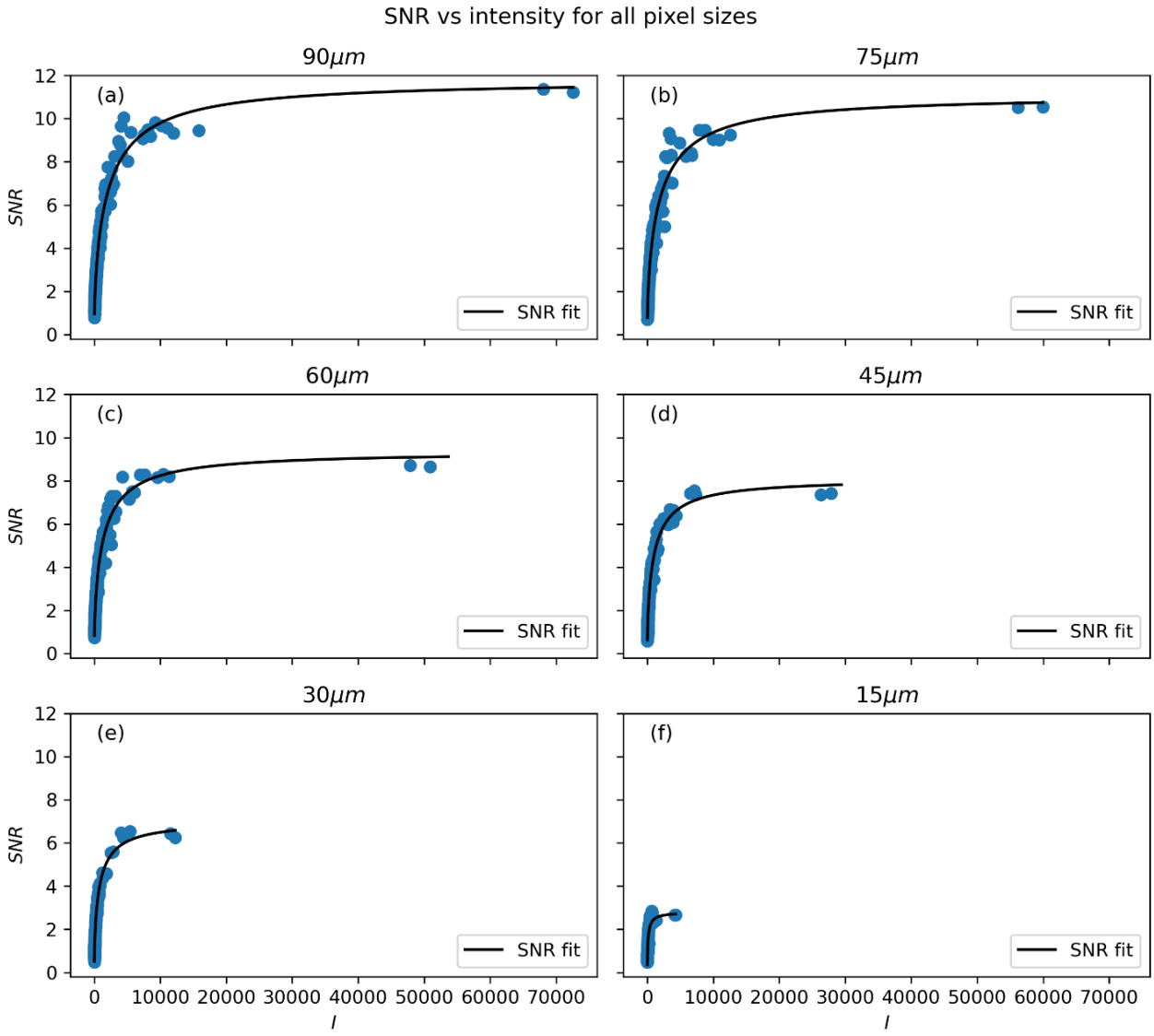


Figure 4-11 SNR as a function of intensity plotted across all pixel sizes. (a) – 90 μm pixel size datacube. (b) – 75 μm pixel size datacube. (c) – 60 μm pixel size datacube. (d) – 45 μm pixel size datacube. (e) – 30 μm pixel size datacube. (f) – 15 μm pixel size datacube.

In order to show the change between SNR values across all pixel sizes the x and y axis have been kept the same for all subplots – the intensity/SNR ranges are the same across all plots and correspond to the ones shown in the 90 μm datacube. It can be seen that as the pixel size is decreased the SNR becomes weaker as well. Unsurprisingly, the highest achievable SNR is exhibited by the 90 μm data set. This is because this datacube represents undersampling (from the point of view of MSI) – as the craters do not overlap a greater area is probed and therefore a higher signal intensity is detected. As the craters begin to overlap, the effectively sampled area diminishes and features finer than the beam width may be resolved. On the other hand, sampling a smaller area implies a decrease in signal intensity and SNR. Therefore, one might ask what the interplay between resolution gain due to strong

material removal and resolution loss due to decrease in SNR is. While this question cannot be answered yet, one begins to gather evidence that indeed as the pixel size is being decreased the effects of noise strengthen. As for the black solid curves in each of the subplots, those were plotted after performing a curve fitting step using the SNR equation. The optimised values for the a, b parameters are presented in the following table.

Data set	a	b
90 μm	32.3 ± 0.2	0.0072 ± 0.0001
75 μm	33.0 ± 0.2	0.0081 ± 0.0001
60 μm	33.1 ± 0.2	0.0114 ± 0.0002
45 μm	33.5 ± 0.2	0.0152 ± 0.0002
30 μm	34.1 ± 0.1	0.0203 ± 0.0003
15 μm	24.7 ± 0.1	0.127 ± 0.002

Table 4-5. Parameters of the combined noise model extracted from curve fitting the SNR as a function of intensity for each datacube.

Upon inspecting the values of the a, b parameters presented in Table 4-5 and Table 4-4 it is evident that they are quite close to each other. Unfortunately the measurement shown in each table are not within the error bounds. Therefore, a closer estimate of the ground truth values for the a, b parameters can be obtained by averaging the values presented in Table 4-5 and Table 4-4.

4.3.4.2 Dependence of the noise model parameters on pixel size

Now, let us consider the functional relation between the a, b parameters and the pixel sizes. This relationship is encapsulated in the following figure; the values of the plotted parameters were obtained after averaging the SNR and variance fits.

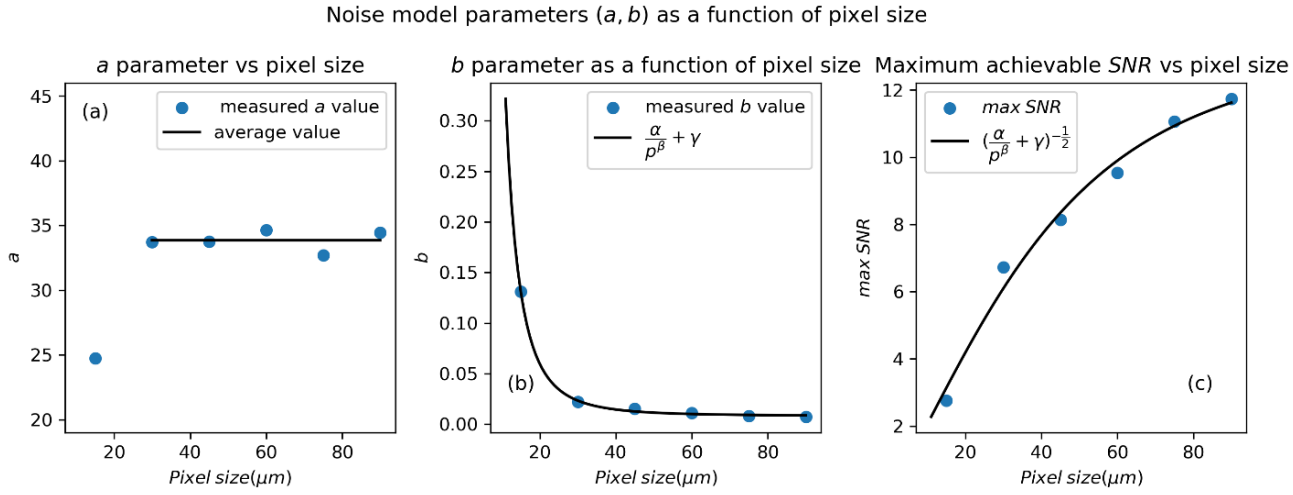


Figure 4-12 The functional relationship between the combined noise model parameters and pixel size. (a) – a parameter plotted against pixel size. (b) – b parameter plotted against pixel size. (c) – maximum achievable SNR as a function of pixel size.

In the beginning of this section the noise model derived in Chapter 2.4 was summarised. It was mentioned that the a parameter should be a property of the detector and the b parameter is related to fluctuations induced by the 'front end' (ion source). Therefore, the a parameter should be functionally independent from the pixel size but could however vary over time and different instrument parameters, such as the mass range used. This claim is asserted by Figure 4-12 (a), where the values of the a parameter are plotted across all pixel sizes. As mentioned in the methods section (Chapter 4.2), the $15\ \mu m$ dataset was acquired roughly a month and a half before the other five datasets. The mass range used was also different – $50 - 1500\ Da$ as opposed to the $50 - 1200\ Da$ mass range used for the other five data sets. To indicate that the five datasets belonging to the same experimental run exhibit a constant behaviour with respect to pixel size a black solid line representing their mean value is plotted among them. This is strong evidence that the physical interpretation of the noise model is correct. In order to supplement this statement a Mann-Kendall test was performed on the five data points belonging to the same experimental run. The calculated p-value was $p = 0.81$ and therefore the null hypothesis can be accepted – the data exhibits no monotonic trend. If the $15\ \mu m$ data point is included, then $p = 0.26$ and the null hypothesis can still be accepted. It should be pointed out that the minimum number of data points required for a successful MK test is four; here five and six were used. Despite this, the MK test strongly suggests that the a parameter exhibits no trend with respect to the pixel sizes and confirms the physical interpretation of the combined noise model derived in Chapter 2.4. Therefore, the fact that the a parameter takes a smaller value for the $15\ \mu m$ data set, which was acquired at a different point in time and with a different mass range, and remains constant for the other five, is encouraging and should be considered as evidence that the a parameter can successfully describe detection noise. The use of the methods outlined in this thesis could add immense value when it comes to characterising the noise statistics of MSI instruments. For example, it would be interesting if the time series of the a parameter is recorded as means of characterising the detector performance.

It was also mentioned that the b parameter could very well be dependent on the pixel size. This is because the b parameter determines the fluctuations in the peak heights and those fluctuations are caused by processes arising in the ion source rather than the instrument detector. It is therefore really pleasing to present the plot in Figure 4-12 (b), where a clear functional dependence on pixel size can be seen. To model this the following formula is proposed:

$$b = \frac{\alpha}{p^{\beta}} + \gamma \qquad \text{Eq. (4.13)}$$

Where p is the pixel size and α, β, γ are free parameters that are extracted from the data. The best fit is drawn with a black solid curve. An MK test was also performed on the b parameter. The test was done twice – once on the five data points belonging to the same experimental run and once on the full data set. The first MK test yielded $p = 0.027$ and $S = -10$. Therefore the alternative hypothesis is accepted and the b parameter exhibits a decreasing trend. When the test was performed with all data points, a p-value of $p = 0.009$ and MK statistic of $S = -15$ were

obtained. Therefore, the alternative hypothesis is accepted again the b parameter exhibits a decreasing trend. The fact that the MK test performs well here with five and six data points, where the decreasing trend of the b parameter is apparent from Figure 4-12 (b), only reinforces the interpretation of the results on the a parameter discussed in the previous paragraph. The b parameter also limits the maximum achievable SNR – this was one of the main differences between the combined noise and Poisson noise models. While Poisson noise has no limit for the highest achievable SNR, the combined noise model limits SNR; as the intensity tends to infinity the SNR equation tends to $b^{-\frac{1}{2}}$. Therefore, Equation 4.13 can also be used to predict the maximum achievable SNR.

$$\max SNR = \left(\frac{\alpha}{p^{\beta}} + \gamma\right)^{-\frac{1}{2}} \qquad \text{Eq. (4.14)}$$

The best fit for Equation 4.14 is depicted in Figure 4-12 (c). This also has a really nice application – if the α, β, γ parameters are known the maximum achievable SNR at *any* given pixel size can be predicted. For example, using the fit depicted in Figure 4-12 (c) one can attempt to estimate the maximum achievable SNR for the MALDI Synapt G2-Si instrument at 5 μm pixel size, which could be considered a sufficient pixel spacing required for obtaining a tissue image that resolves between single cells. Unfortunately, the predicted maximum achievable SNR predicted is 0.98 – the noise and signal have roughly the same strength. Therefore, one could argue that single cell imaging cannot be achieved using this instrument. Of course, this calculation is to be taken with a pinch of salt – ideally more data points can be used for a better fit and an actual dataset imaged at 5 μm can be obtained in order to confirm this prediction.

As for the statement that an image with an SNR smaller than unity cannot have spatial resolution, there are two ways of showing that this is the case. The algebraic approach involves looking at the resolution equation (see Chapter 3.4.2, Equation 3.24) – in there the SNR term appears within the square root of a natural logarithm. If the SNR is less than unity, the natural logarithm takes a negative value and the square root becomes an imaginary number. Of course imaginary distance is unphysical and therefore the resolution of an image with an SNR less than unity is has no physical meaning. There is also a geometrical way of demonstrating this. This is depicted in the following figure.

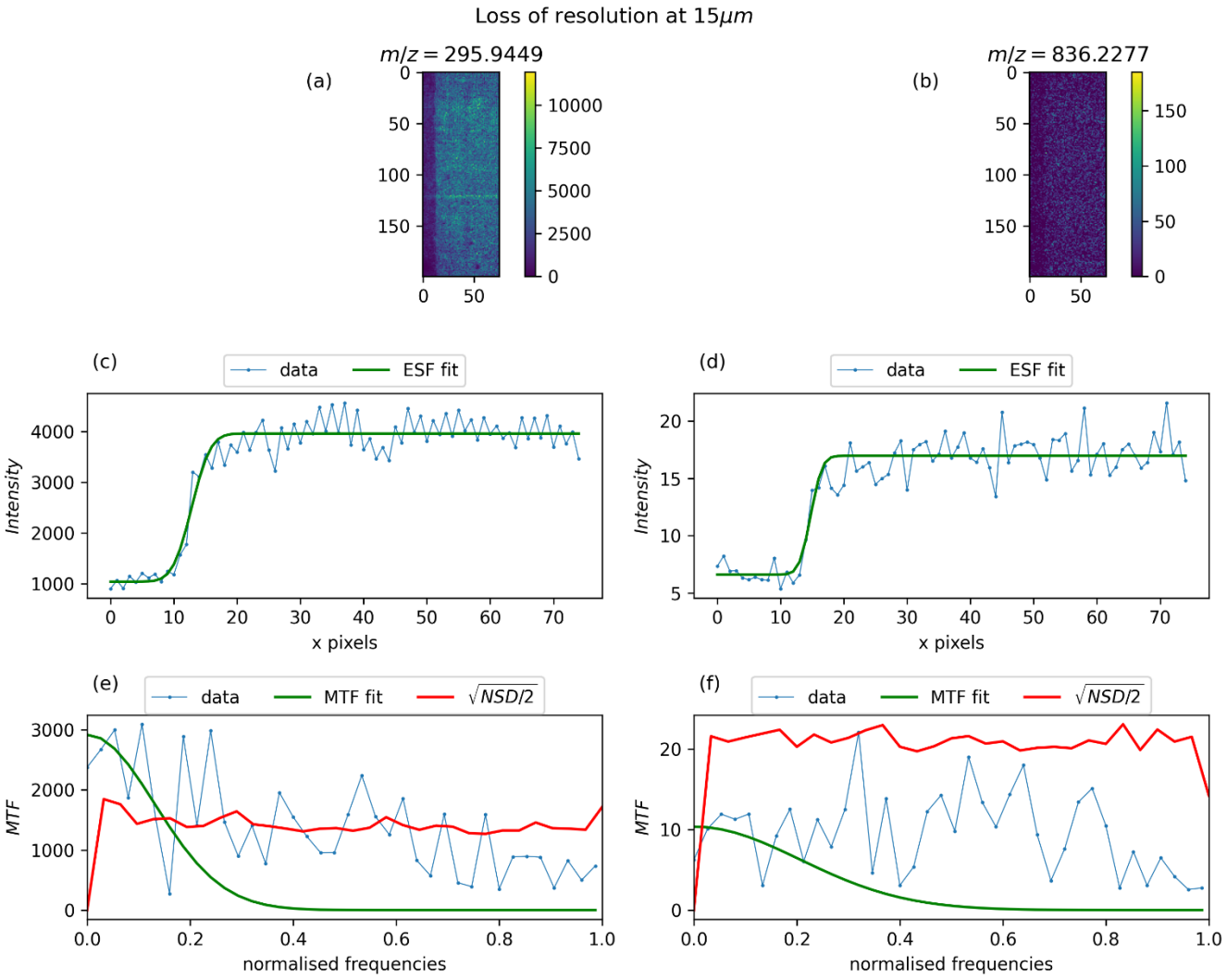


Figure 4-13 Loss of resolution for two signals at 15 μm *pixel size. (a) – high intensity signal. (b) – low intensity signal. (c) – ESF fit on high intensity signal; SNR=2.5. (d) – ESF fit on low intensity signal ; SNR = 0.7. (e) – the MTF and scaled NSD intersect at a critical frequency of 0.18. (f) – the MTF and scaled NSD never intersect.*

The resolution frequency is the intersection between the MTF and root of the noise spectral density divided by two. The latter is also equal to the noise standard deviation, namely $\sqrt{NSD/2} = std(\eta)$, where η is the noise function. Since SNR is the ratio of the average signal intensity and the noise standard deviation $std(\eta)$, namely $SNR = MTF(0)/std(\eta)$, if the SNR is less than unity then the quantity $\sqrt{NSD/2}$ always exceeds the MTF value at any given frequency. In other words, the noise strength exceeds the signal strength for all frequencies. Therefore, no intersection between the two ever happens and such an image cannot have a resolution frequency.

4.3.4.3 Calculating the number of images that do not have a spatial resolution

The overall SNR distribution for different pixel sizes will depend on the intensity distributions for those pixel sizes (shown in Figure 4-6, Figure 4-7, Figure 4-8 and Figure 4-9 ; the mass spectra are shown in Figure 4-3) and the values that the combined noise model parameters a, b manifest as those pixel sizes. The following figure shows the distribution of SNRs for different pixel sizes; the distributions are displayed with the aid of a violin plot.

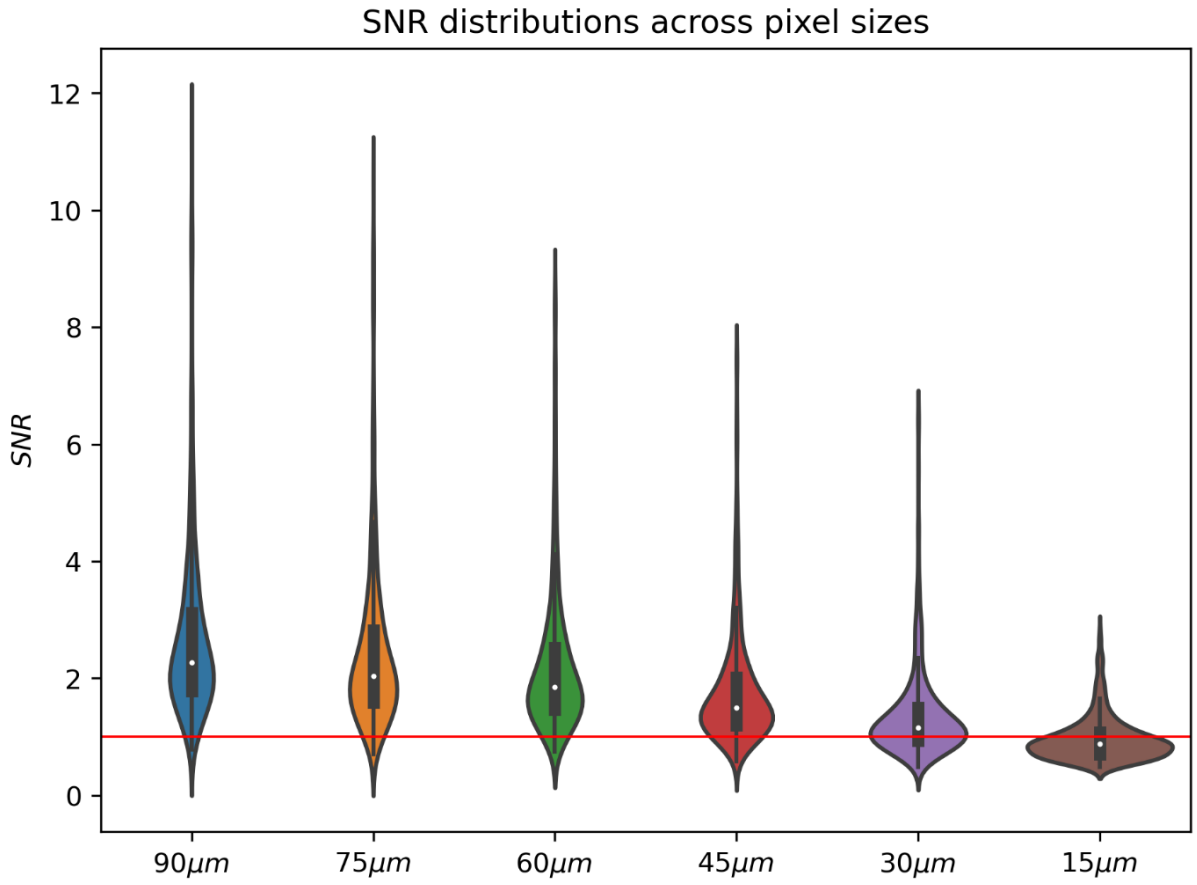


Figure 4-14 The SNR distributions for all pixel sizes. The red horizontal line cutting through all distributions shows an SNR value of unity.

It can be seen from Figure 4-14 that the highest achievable SNR belongs to the 90 μm datacube and the smallest one belongs to the 15 μm datacube. The SNR value in those cases is around 11 and 2.9 respectively. Overall, as the pixel sizes is decreased the maximum achievable SNR also decreases. The experimentally measured maximum SNRs are very close to those predicted by the maximum achievable SNR derived from the b parameter.

Datacube	Experimental SNR	$b^{-1/2}$
90 μm	11.4	11.7
75 μm	10.5	11.1
60 μm	8.7	9.5
45 μm	7.5	8.1
30 μm	6.5	6.7
15 μm	2.9	2.7

Table 4-6. Comparison between the empirically estimated SNRs and those predicted from the noise model curve fitting.

In general, it can be seen that the noise model does a decent job of predicting the SNR. All SNR values, apart from that for the 15 μm datacube, seem to be slightly overestimated. As for the median values, it can be seen from the violin plot that those have much more lower values. This of course reflects the fact that the majority of signals are distributed in the low intensity region. The red horizontal line cutting through each of the distributions represents an SNR value of unity. Signals below this line do not have a well-defined spatial resolution. It is apparent that as the pixel size decreases, more and more signals begin to have an SNR lower than unity. This is particularly bad in the case of the 15 μm dataset as the median falls below unity. Therefore, more than half of the images in this dataset will not have a well-defined resolution as whatever signal they exhibit will be completely obscured by noise. At this point one might ask again what the interplay between gain in spatial resolution due to material removal and loss of spatial resolution due to SNR weakening is? It appears that at 15 μm the gain of spatial resolution due to oversampling with material removal will be shadowed by the fact that the majority of the images are pure noise. The exact percentage of images that have an SNR lower than unity can be calculated with the aid of the CDFs shown in Figure 4-8. The parameters for those were obtained using MLE and discussed previously. Note that the critical SNR value here is unity as the MTF and scaled NSD never intersect.

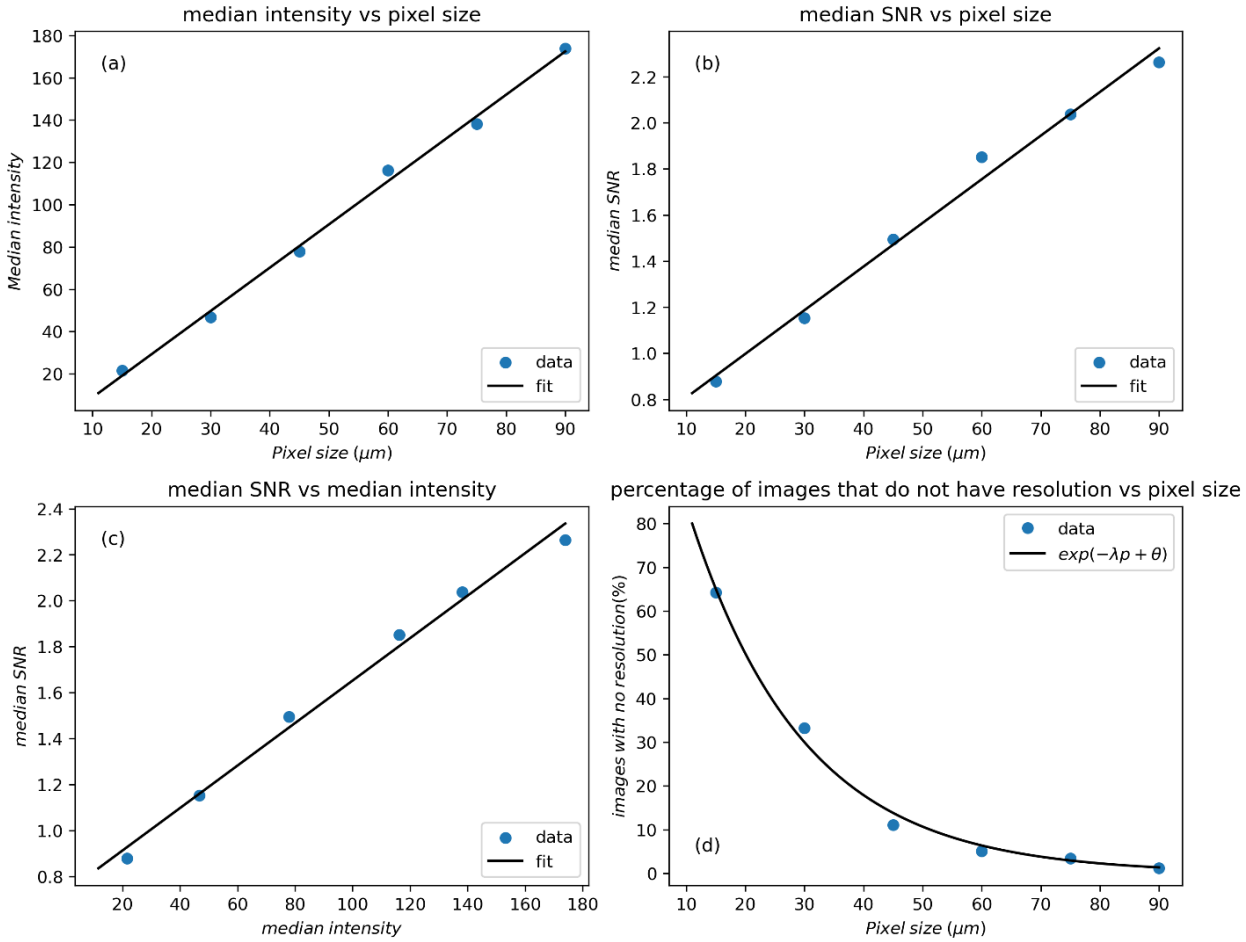


Figure 4-15 (a) – median intensity as a function of pixel size. (b) – median SNR as a function of pixel size. (c) – median SNR as a function of median intensity. (d) – the percentage of images with SNR less than unity.

Figure 4-15 (a) shows the calculated median intensity as a function of pixel size. The black line is a linear equation fit to the data ($R^2 = 0.996$); it is interesting to point out that the slope has a value of 2.04, indicating that the median intensity at a given pixel size is approximately twice the value of the pixel size. Next, the median SNR for each of the datasets is plotted as a function of pixel size in Figure 4-15 (b). Unsurprisingly the linear relation is preserved. It is also interesting to consider the median SNR of a datacube as a function of its median intensity. This is shown in Figure 4-15 (c) where a linear relation is also observed. Finally, by referring to Figure 4-14 and where the red line (indicating a critical SNR of unity) intersects each of the SNR distributions and finding the corresponding intensity, the CDFs shown in Figure 4-8 can be used to calculate the number of images with SNR below unity. In other words these are the images that do not have a spatial resolution as the noise is dominating the signal at all frequencies. This is shown in Figure 4-15 (d), where the percentage of images that do not have a spatial resolution are plotted against the pixel size. It can be seen that at high pixel sizes, corresponding to higher intensities and therefore higher SNRs only a small percentage of all images will be dominated by noise. In particular, at 90 μm

pixel size around 1% of all images will be pure noise and at 45 μm pixel size this number grows to around 11 %. At 30μm pixel size roughly one third of all images will be pure noise and at 15 μm this number grows to ≈ 66%. Therefore, the amount of useful spatial information contained within a dataset decreases as the pixel size is decreased. This indicates that as the pixel size is decreased one would expect the gain in spatial resolution due to material removal to stop improving due to the weakening of the SNR. To model the observed functional dependance a simple exponential decay model is used:

$$\%\ of\ images\ with\ no\ resolution = \exp(-\lambda p + \theta) \qquad \text{Eq. (4.15)}$$

Where here λ, θ are free parameters that are optimised so that Equation 4.15 can fit the data and p is the pixel size. The black curve in Figure 4-15 (d) was plotted after optimising the values of those parameters ($\lambda = 0.052, \theta = 4.95$). Similar to the calculation performed that predicted the maximum achievable SNR at 5 μm, this can allow us to predict the pixel size at which all images will have an SNR less than unity. This happens at a pixel spacing of ≈ 6.667 μm where nearly 100% of all images will be useless as the signal strength will be weaker than the noise fluctuations. While this prediction agrees with that made by Equation 4.14 (which predicted $\max SNR = 0.98$ at 5 μm) in order to really validate this another experiment should be performed. Nevertheless, those two calculations do not take away from the potential value that these calculations have and they only merely seek to demonstrate the possible applications that they could have.

4.3.5 Spatial resolution

4.3.5.1 The blurring parameter and the failure of the $86-14\%$ criterion

Now the properties of image blur across all pixel sizes is studied. The process of obtaining the blur parameter σ was described in Chapter 3. Algorithm 1 is used to obtain an experimental value for σ. Note that 2σ is simply the $86-14\%$ criterion[68]. In Chapter 2 and Chapter 3 it was proved using theoretical considerations (applying the image formation model) that under the conditions of strong material removal the blurring parameter σ is minimised, while if weak material removal is used to obtain an image, 2σ gets mapped back to the width of the beam. In MSI modalities such as SIMS, where weak material removal is present it has been known and experimentally verified that the $86-14\%$ criterion successfully recovers the width of the beam [67–69]. Therefore, resolution is limited by blur. This was also recovered by the image formation model presented in this thesis – in Chapter 3 it was demonstrated that the MTF of a system that uses weak material removal will decay at a frequency corresponding to the width of the beam. However, in Chapter 2 and Chapter 3 it was shown that the MTF of a system utilizing strong material removal decays at the Nyquist frequency, which corresponds to a distance of two pixels. Therefore, applying the blurring parameter, which is minimised due to the effects of material removal, as a resolution metric yielded resolution numbers that violated the Sampling theorem. Therefore, the $86-14\%$ criterion cannot be used

as a resolution metric in such imaging systems. Such failures have been reported previously in systems that utilise strong material removal. One study reported a subpixel value for the $86-14\%$ criterion[131], while another study measured a value of unity[132]. This is why this thesis exists – the main purpose of this work is to clarify why the $86-14\%$ criterion works in some cases and fails in others and to therefore provide a procedure for measuring spatial resolution that can be applied in all MSI modalities. While the explanation was already provided by the image formation model one has yet to demonstrate experimentally that the blurring parameter violates the Sampling theorem minimum. Therefore, the results from the application of Algorithm 1 on the six datasets is now presented.

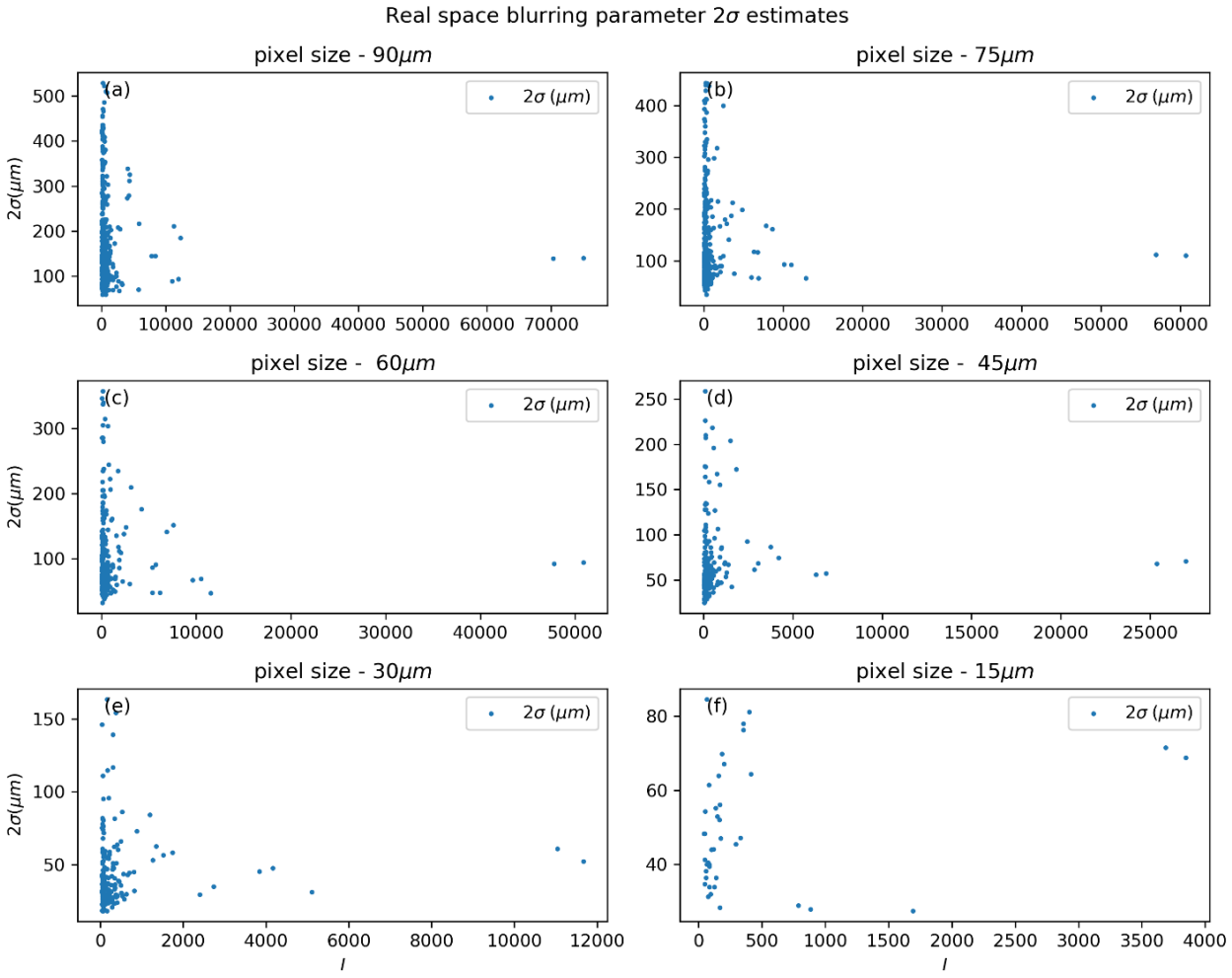


Figure 4-16 The 86-14% criterion plotted as a function of intensity across all pixel sizes. (a) – effective image blur vs intensity for the $90\ \mu m$ *datacube. (b) – effective image blur vs intensity for the* $75\ \mu m$ *datacube. (c) – effective image blur vs intensity for the* $60\ \mu m$ *datacube. (d) – effective image blur vs intensity for the* $45\ \mu m$ *datacube. (e) – effective image blur vs intensity for the* $30\ \mu m$ *datacube. (f) – effective image blur vs intensity for the* $15\ \mu m$ *datacube.*

The effectiveness of this method was already tested in four synthetic datacubes in Chapter 3.4. The results there suggested that at low intensities the combined noise model required a large number of linescans in order to recover

the ground truth blurring parameter. Unfortunately, it was shown in the previous section that MALDI exhibits this combined noise and the number of linescans available is not sufficient to estimate the ground truth blur in the low intensity images. This also leads to the failure of Algorithm 2, which produced an unnaturally sharp MTF since the blurring parameter in Fourier space $\tilde{\sigma}$ is inversely proportion to the real space blurring parameter σ. Therefore, the resolution estimates of the datacubes were not accurate in the case of the combined noise model because of this but Algorithm 1 and Algorithm 2 still performed well in the case of Poisson noise. The method proposed to deal with this was the recovery method, which only utilized the blurring parameter estimates from the high intensity images and combined that with the noise statistic estimates from the edge surface region. This allowed for the accurate recovery of the ground truth resolution. Figure 4-16 shows the estimated effective blur 2σ, also known as the $86-14\%$ criterion as a function of intensity for all six datacubes. Similar to the simulation in Chapter 3.4 where the low intensity images suffering from a severe combined noise could not have their ground truth blurring parameters estimated, the low intensity images in all six data sets exhibit a large variance. Unfortunately, this is just the curve fitting process failing due to how severe noise is; adding more linescans will certainly help to deal with this but there is also a practical limit to this such as the dimensions of the edge sample and the time required to obtain large images. Therefore, the recovery method will be useful in estimating the ground truth resolution, especially in the smaller pixel sizes where SNR weakens dramatically. The first step is to threshold the blurring parameters and compute the median blur values of only the high intensity images.

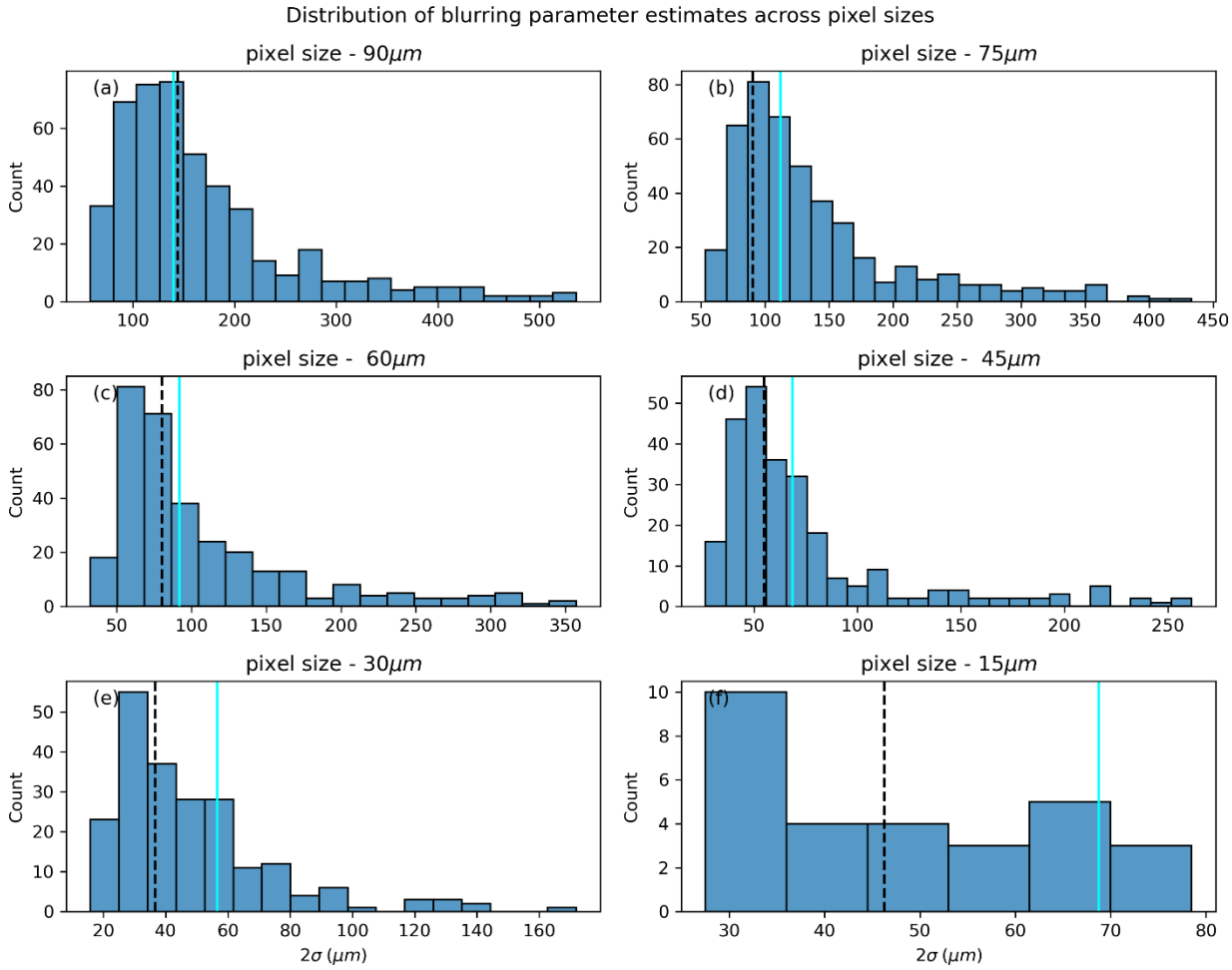


Figure 4-17. Distribution of the effective blur parameter for all pixel sizes. The cyan vertical line represents the median blur obtained from high intensity images and the black vertical dashed line is the median of the entire distribution. (a) – distribution of the measured blurring parameter for the 90 μm *datacube. (b) – distribution of the measured blurring parameter for the* 75 μm *datacube. (c) – distribution of the measured blurring parameter for the* 60 μm *datacube. (d) – distribution of the measured blurring parameter for the* 45 μm *datacube. (e) distribution of the measured blurring parameter for the* 30 μm *datacube. (f) – distribution of the measured blurring parameter for the* 15 μm *datacube.*

The histograms shown in Figure 4-17 depict the variance of the measured blurring parameter. As discussed, this spread is not due to natural differences in image blur but instead arise because of the noise nature of the data combined with the requirement of a large number of linescans necessary to cancel out the noise so that curve fitting may extract an accurate value for the blurring parameter. The black vertical dashed line in each of the subplots shows the median value of the entire blurring parameter distribution while the continuous vertical cyan line is the median value for the high intensity images. The higher SNR datasets, namely the 90 μm one, exhibits a median value for the high intensity images that is really close to that of the entire dataset. This is not surprising as the effects of noise are not so detrimental here. However, as the pixel size decreases, a sharper blurring parameter is estimated for the low intensity images. Unfortunately, this sharpness does not depict the truth about the natural image blur in

those low intensity images but simply reflects the fact that if more linescans were available curve fitting would have extracted the natural blur more accurately. Therefore, as the pixel size is decreased and the SNR weakens, the dashed black line (median of entire dataset) decreases further from the cyan line (median of high intensity images). It was shown in Chapter 3.4 that the same thing happened in synthetic datasets where the ground truth blur was known. The blurring parameter was accurately measured in high intensity images but it was underestimated for low intensity images. Therefore, with these data the cyan line (median of high intensity) should also be closer to the ground truth rather than the median of the entire dataset (dashed black line). The analysis of the blur distributions also reveals that when Algorithm 2 is applied to measure resolution, since the blurring parameter is underestimated the MTF would be sharpened and a higher resolution frequency will be measured. Therefore, the resolution of datacubes (especially the ones with weak SNR) will be underestimated. Nevertheless the recovery method will allow for an accurate estimation of the ground truth resolution. The drawback, as discussed in Chapter 3.4, is that this imposes a global MTF on all images – if, for whatever reason, different images exhibit a different natural blur, the recovery method would not be able to take that into account. Now, let us check if the blurring parameter can be used as a resolution metric in MALDI, where strong material removal was used.

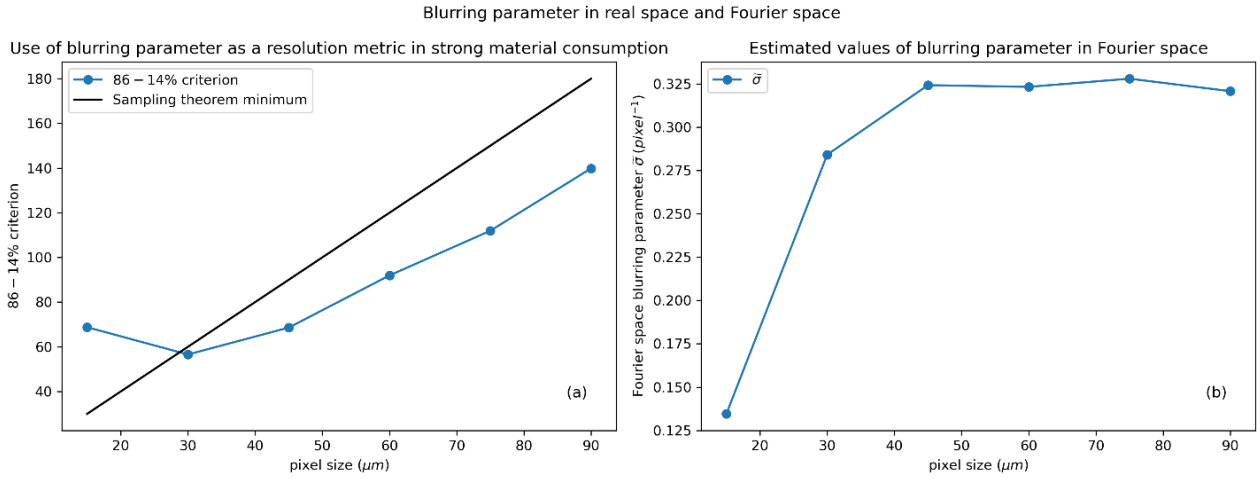


Figure 4-18. (a) – The blurring parameter used as a resolution metric across all pixel sizes. The black diagonal line depicts the Sampling theorem minimum and the blue dots are the measured blur. (b) – the estimated blurring parameter in Fourier space $\tilde{\sigma}$.

Since in the datacube simulations in Chapter 3.4 the high intensity images accurately recovered the ground truth blur, the median value of the blurring parameter of the high intensity images was used to produce Figure 4-18. These were depicted as a cyan vertical line in Figure 4-147. The usefulness of the $86-14\%$ criterion as a resolution metric is shown in Figure 4-18 (a) – the blurring parameter is plotted as blue dots and the Sampling theorem minimum is represented as a black line. For all cases above $15\ \mu m$, the measured image blur cannot be used as a resolution metric as it is beneath the Sampling theorem minimum, which stated that no change in signal less than two pixels can ever be recorded by a digital system. As for the lowest pixel size, the blurring parameter can be used

as resolution measurement as it does not violate the Sampling theorem. It should be pointed out that this increase in image blur, when oversampling with material removal is somewhat consistent with the simple 1D PSF simulation in Chapter 2. As for how accurately can blur describe the loss of resolution in the case of the $15\ \mu m$, it should be pointed out that the SNR is also incredibly weak there. In Chapter 3 it was demonstrated that resolution can also be lost due to noise. Therefore, the effects of noise on resolution should be considered and it shall be shown that these are far more worse than the loss of resolution due to blur. Therefore, while the $86-14\%$ criterion has been an excellent tool for modalities such as SIMS, where weak material removal is used, it fails to estimate spatial resolution accurately in MALDI. The theoretical justifications for this were already provided and now this has also been shown experimentally.

As mentioned, the recovery method proposed in Chapter 3.4 for estimating the resolution of a datacube shall be used. For this an estimated of the inverse space equivalent $\tilde{\sigma}$ of the blurring parameter σ is needed. In general, depending on how one defines the Fourier transform, $\tilde{\sigma}$ will be inversely proportional to σ with a scaling factor (usually something like $\sqrt{2\pi}$). Unfortunately, the scaling factor could not be derived analytically but simple numerical computations allowed for the conversion of σ to $\tilde{\sigma}$. This is shown in Figure 4-18 (b), where $\tilde{\sigma}$ is plotted against the pixel size. Note that $\tilde{\sigma}$ controls the width of the MTF and since it was chosen to present the MTFs on a normalized scale of zero to unity, the units of $\tilde{\sigma}$ here correspond to reciprocal pixels instead of reciprocal metres. Roughly the same value of the blurring parameter is mention in terms of pixels for the $45, 60, 75, 90\ \mu m$ datacubes – when converted to microns this explains the linear decrease of the blurring parameter in Figure 4-18 (a). However, since $\tilde{\sigma}$ is depicted in units of inverse pixels this manifests as a constant line. Since σ and $\tilde{\sigma}$ are inversely related, the increase in σ for the $15\mu m$ dataset corresponds to a decrease in $\tilde{\sigma}$ in Figure 4-18 (b). Note that if the median values of the entire datacube (black dashed vertical lines in Figure 4-17) were used to calculate σ, the Fourier space blurring parameter $\tilde{\sigma}$ would have higher values. This would lead to a sharper MTF and an overestimated resolution frequency, which when converted back to real space would mean that resolution has been underestimated (see Chapter 3.4).

4.3.5.2 Measuring the spatial resolution of all six datacubes

The intensity distributions and noise statistics were thoroughly reviewed, followed by an investigation on the blurring parameter and the applicability of the $86-14\%$ criterion as a resolution metric for images acquired under the conditions of strong material removal. Now it is time to apply Algorithm 2 and the recovery method in order to measure the resolution of the datasets. The answer of what the interplay between resolution gain due to oversampling with material removal and resolution loss due to increase of noise will also be provided. The following figure shows the results acquired from Algorithm 2 and the recovery method on each of the six datasets.

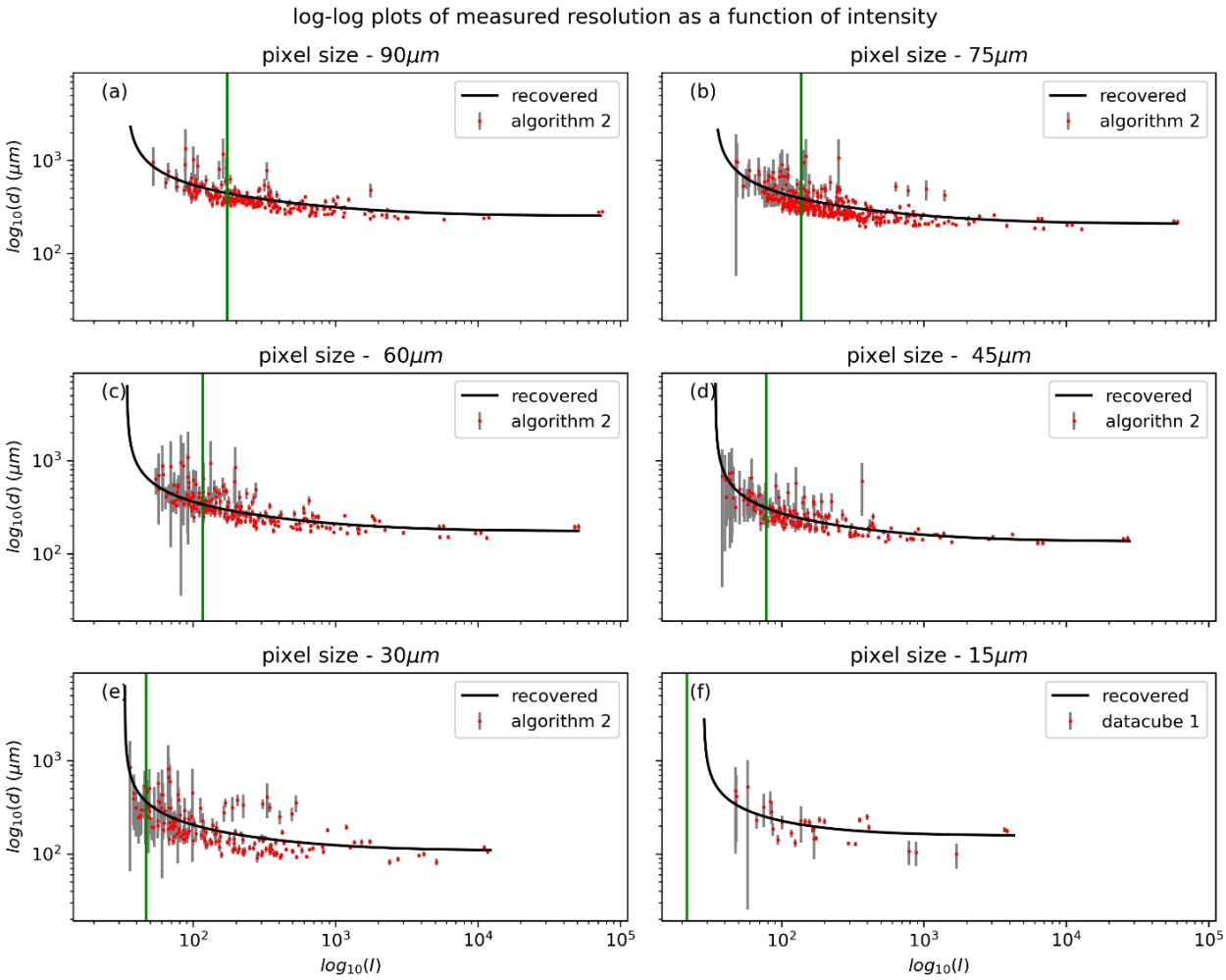


Figure 4-19 log-log plots of measured resolution using Algorithm 2 (red scatter points) and the recovery method (continuous black curve). The vertical grey bars are the errors. The green vertical line is the median intensity. (a) – resolution measurement for 90 μm datacube. (b) – resolution measurement for 75 μm datacube. (c) – resolution measurement for 60 μm datacube. (d) – resolution measurement for 45 μm datacube. (e) – resolution measurement for 30 μm datacube. (f) – resolution measurement for 15 μm datacube.

The red scatter points in each of the subplots are the measured resolutions acquired from Algorithm 2, the vertical grey bars are the associated errors in the measurement and the continuous black curve is the recovery method. The recovery method was discussed in Chapter 3.4 – the first step is to acquire the inverse space blurring parameter $\tilde{\sigma}$ and the second step is to fit a noise model to the data in order to extract the noise model parameters. Then, Equation 3.24 is used to obtain the resolution distance. The process for obtaining the noise model parameters were discussed thoroughly in Chapter 2.4 and the values used here can be seen in Chapter 4.3.3. The estimation of $\tilde{\sigma}$ was discussed

in Chapter 4.3.4.1. As for Algorithm 2, datapoints with fractional errors larger than 99%* were excluded. As discussed in Chapter 3.4, this means that a large portion of low intensity images may not have their resolution estimated. The major contribution of those errors was the error in the blurring parameter. The effects of this were twofold – firstly, since the blurring parameter gets underestimated (see dashed vertical black lines in Figure 4-17), the MTF is sharpened and the resolution distance also becomes underestimated. Secondly, since a portion of the low intensity images suffer from large errors and cannot be considered an accurate resolution estimate, the median will get shifted which would lead to an underestimated spatial resolution (see Chapter 3.4). The recovery method deals with both those issues but at the cost of imposing a global MTF. Note that while the black curves representing the recovery method in each of the subplots are truncated at the limit of spatial resolution, corresponding to SNR values less than unity, the red scatter points are truncated at a higher intensity due to the fractional errors exceeding a preset threshold. The resolution measurements acquired by Algorithm 1 for the $90{,}75\ \mu m$ datacubes, shown in Figure 4-19 (a) and (b) respectively, show that the red scatter points extend to almost to the end of the black solid curve, generated by the recovery method. Since the recovery method truncates at intensities corresponding to images with SNR values less than unity, Algorithm 2 has not generated that many datapoints that exceed the preset fractional error threshold of 0.99 for those two datasets. Algorithm 2, which is susceptible to the underestimation of the blurring parameter, will also not experience the sharpening of the MTF – the median blurs for the high intensity images are very similar to those of the entire median blur for those two datasets (see Figure 4-17), indicating that the blurring parameter is not significantly underestimated at the low intensity regime. Using the PDFs derived in Figure 4-8 and the smallest intensity estimated by Algorithm 2 for each of the six datasets, the percentage of measurements that exceed the preset error threshold can be estimated. In particular, the PDFs are integrated from the theoretical value for which there is no resolution (SNR less than unity) to the smallest intensity below the fractional error threshold. Note that this is completely different from the calculation performed to estimate the number of images that did not have a resolution. The results are summarised in the following table:

* This is still a terrible fractional error threshold to pick but MALDI data is also incredibly noisy. If one picked 0.1 then only very few high intensity images would survive this purge. The alternative is to design experiments with a great number of linescans.

Dataset	Percentage of images that exceeded fraction error threshold	Number of linescans used in the dataset
$90\ \mu m$	2.2%	43
$75\ \mu m$	2.6%	22
$60\ \mu m$	10.0%	24
$45\ \mu m$	38.1%	30
$30\ \mu m$	22.2%	21
$15\ \mu m$	31.6%	180

Table 4-7 The percentage of unsuccessfully estimation of Algorithm 2 due to pre-set fractional error threshold for each datacube. The number of linescans is also listed.

The linescans were selected in such a manner to avoid the tilt in the edge. If the whole edge region is included, the blurring parameter is overestimated and the resolution distance increases. Therefore, one needs to be incredibly careful when selecting an edge ROI. The downside is that the reduced number of linescans lead to an increase in the percentage of images that will have a fractional error exceeding the pre-set threshold of 0.99. It can be seen that Algorithm 2 performs well on the $90{,}75\ \mu m$ data sets and only less than 3% of all images cannot be estimated due to errors. This can be verified when Figure 4-19 (a) and Figure 4-19 (b) are inspected – the red scatter points almost reach the theoretical minimum indicated by the end of the solid black curves. As for the three datasets with pixel sizes smaller and including $45\ \mu m$, this number exceeds 20% and since these will have a much lower resolution than the images from the high intensity portion, omitting those from a resolution study can result in an underestimated spatial resolution. This was discussed in Chapter 3.4 where the violin plots of Algorithm 2 and the recovery method were plotted against the ground truth resolution. It was seen that the effect of the fractional error thresholding truncated the tail of the resolution distributions. A similar comparison now follows.

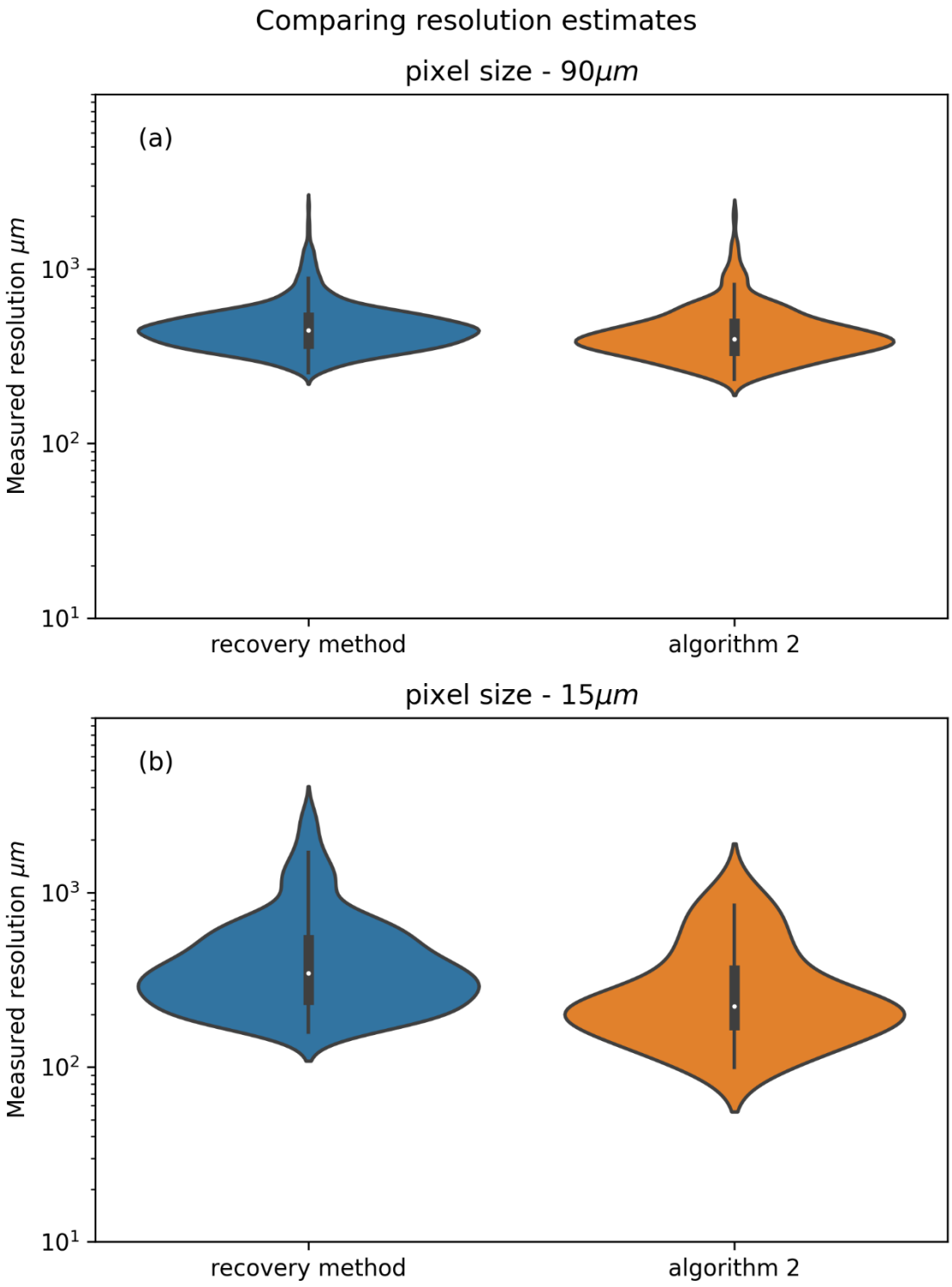


Figure 4-20. Distributions of resolution estimates using the recovery method and Algorithm 2 for (a) – the 90 μm datacube. (b) – the 15 μm datacube.

The distributions for the highest and lowest SNR datasets, corresponding to pixel sizes of $90\ \mu m$ and $15\ \mu m$ respectively is shown in Figure 4-20. The results for the high intensity dataset are shown in Figure 4-20 (a). It is evident that both distributions are very similar to each other. The reasons are two – as shown in Figure 4-17 (a), the median blur of the high intensity images was very close to the median blur of the entire blur distribution. Therefore, the errors in the blur estimates at low intensities were not as severe and the MTF was not sharpened at lower intensities, which would have led to an underestimated resolution distance. Furthermore, only around 2% of images could not have their resolution estimated due to fractional errors exceeding the pre-set threshold. Thus, the truncation of the tail of the distribution is not as severe and the two median values are quite close to each other. Unfortunately, not the same could be said about the low SNR $15\ \mu m$ dataset. The results from this measurement are depicted in Figure 4-20 (b). Referring to Figure 4-17 (f) this time shows that the median blur for the high intensities is much larger than the median blur of the entire dataset. This means that the low intensity images have had their blurring parameter underestimated; this then to sharper MTF and an underestimated resolution distance. Hence, the entire distribution has been shifted down. Furthermore, due to the noise nature of the dataset, even with the aid of 180 linescans, 31.6% of images did not have a successfully measured resolution as their fractional errors exceeded the pre-set threshold. Thus, the tail has been truncated and the median has been pushed down. Precisely this type of behaviour was investigated in Chapter 3.4. It was found that the recovery method did a much better job at approximating the ground truth resolution estimates. Therefore, the recovery method should be used to calculate the median resolution of a datacube. It should also be apparent from Figure 4-20 that the resolution estimates for the datacubes with a higher SNR are similar for the two methods. As the pixel size decreases, the SNR weakens and Algorithm 2 starts to misperform.

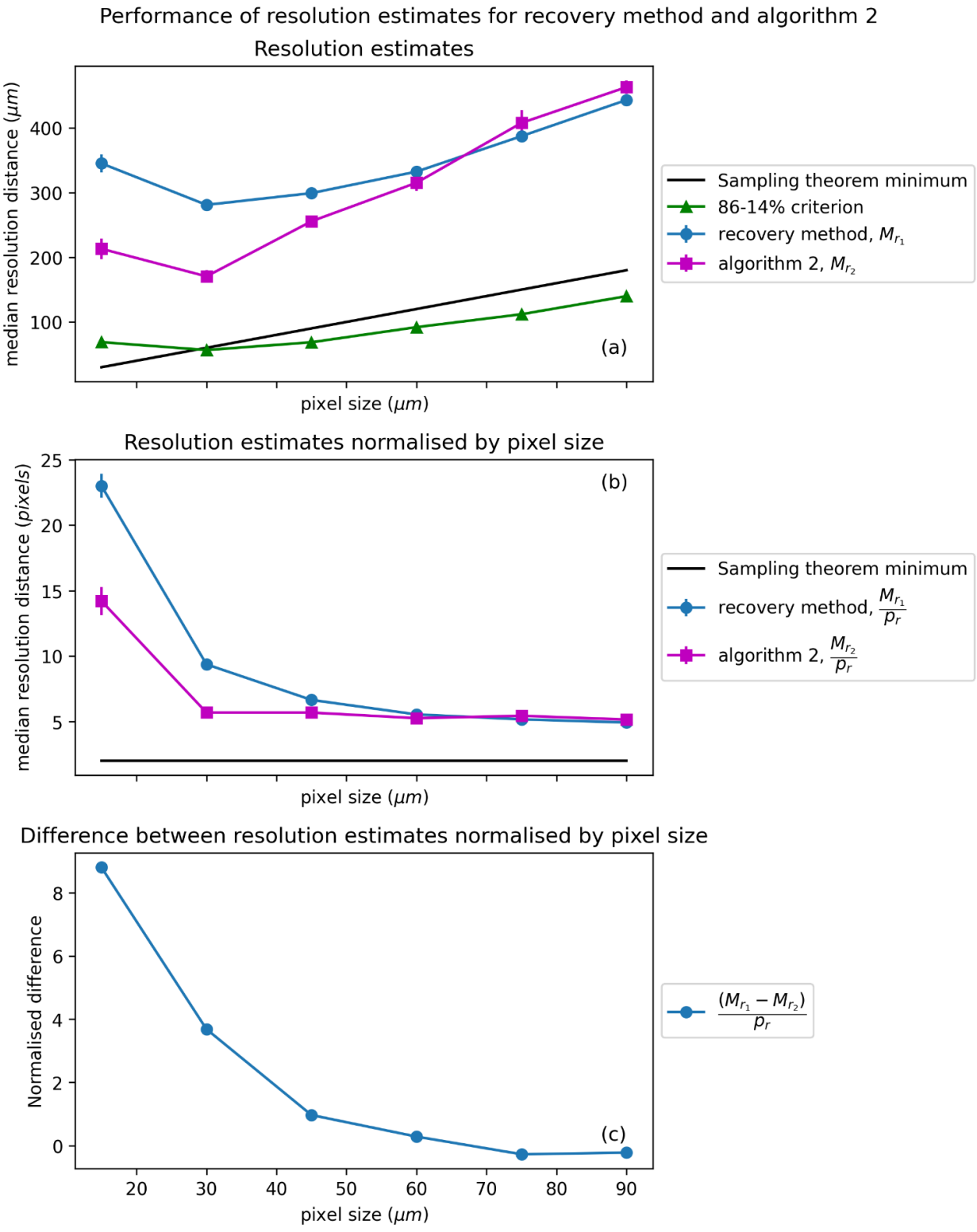


Figure 4-21. (a) – median resolutions acquired from both methods and computed in microns plotted as a function of pixel sizes. (b) – median resolutions acquired from both methods and computed in pixels plotted as a function of pixel sizes (c) – Difference between resolution estimates normalised to the pixel size of each estimate.

This is confirmed by Figure 4-21 (a), where at pixel sizes above $45\ \mu m$ the calculated median resolutions fall quite close to each other. The resolution estimates acquired with the recovery method are represented by the blue dots; the dots are connected by lines for ease of visualising the trend. Each median resolution can be labelled as M_{r_1}, where r is a dummy variable for the pixel size. The resolution estimates acquired via Algorithm 2 are depicted with the magenta dots; these have also been connected by lines to aid visualising the trend. These data points can be labelled as M_{r_2}, where r indexes the pixel size. The error bars for both M_{r_1} and M_{r_2} were acquired via bootstrapping. The scipy.stats module was used with the bootstrapping set to the BCa method, number of resamples to 9999 and the confidence interval was set to 0.95. The black line represents the minimum resolution estimate required by the Sampling theorem and the green data points (also connected by a line) depict the resolution estimates acquired from the $86-14\%$ criterion. The fact that the majority of them fall beneath the Sampling theorem minimum was discussed in Chapter 2, Chapter 3 and earlier in Chapter 4.3.4.1. It can be seen that the methods developed here outperform the current best practice as both noise and blur have been taken into account.

Unfortunately, at pixel sizes below $45\ \mu m$ Algorithm 2 underestimates resolution. This was also demonstrated in Chapter 3.4, however the dangers of not being prepared to take this into account become evident here. In Chapter 3.4 it was also shown that the recovery method outperformed Algorithm 2 and obtained resolution estimates that were much closer to the ground truth (within the error derived from bootstrapping). It should be noted that below $45\ \mu m$ Algorithm 2 exhibits the same trend but there has been a systematic error introduced to the resolution measurement. Therefore, the recovery method is used here as an estimate of resolution. The question about the interplay between resolution gain due to material removal and resolution loss due to SNR weaking can now be answered. It is clear that the optimum median resolution falls at $30\ \mu m$. However, the median resolution at $30\ \mu m$ is around $280\ \mu m$, while the median resolution at $45\ \mu m$ is around $300\ \mu m$. Therefore, the median gain in resolution is only $20\ \mu m$, which is ultimately a subpixel difference for both datasets. Therefore, it may be concluded that the true resolution optimum lies somewhere between 30 and $45\ \mu m$. At a pixel size of $15\ \mu m$ the median resolution deteriorates. While the $15\ \mu m$ datacube exhibited a significantly higher blurring parameter, the loss of resolution is predominantly due to the effects of noise. As a reminder, approximately 66% of all images in that datacube scored an SNR lower the unity and the maximum achievable SNR was around 2.8. The resolution measurements shown here also have an important application. The acquisition time for microprobe imaging techniques increases rapidly as the pixel size is made smaller. If the same field of view is kept constant between two images acquired at two different pixel sizes, one at higher pixel size and one at a lower, the number of pixels in the image with the smaller pixel spacing would increase by a factor of the square of the ratio of the two pixel sizes. Thus, if the same field of view is kept constant between the $60, 30$ and $15\ \mu m$ datasets, the $30\ \mu m$ dataset would have four times as many pixels as the $60\ \mu m$ one and the$15\ \mu m$ dataset would contain 16 times as many pixels as the $60\ \mu m$ datacube and four times as many as the $30\ \mu m$ dataset. If then the scan time is kept constant it

becomes apparent that the $15\mu m$ dataset would require 16 times the amount of time to acquire a $60\mu m$ dataset while maintaining a median resolution that is worse than that of the $60\ \mu m$ one. On the other hand, it is worth decreasing the pixel size from $60\mu m$ to $30\mu m$ – this would result in an increase of acquisition time by a factor of four but also, a gain in spatial resolution of $50\mu m$. If therefore there is a particular feature of interest that is the decrease in pixel size may be worth it, depending on the size of the feature. Finally, switching from $30\mu m$ to $15\mu m$ would also increase the acquisition time by another factor of four, but almost $70\mu m$ of median spatial resolution would be lost.

It is also interesting to consider the normalised median resolution, namely the median resolution distance expressed in pixel size instead of distance. This is shown in Figure 4-21 (b), where the recovery method and Algorithm 2 are plotted or in other words M_{r_1}/p_{r_1} and M_{r_2}/p_{r_2}, where r is an index for the pixel size and the numbers 1 and 2 represent each of the both methods respectively. The black horizontal line represents the Sampling theorem minimum of two pixels. The three coarsest pixel sizes maintain a constant resolution median of around five pixels. At $45\mu m$ pixel sizes the median resolution distance starts to increase; as the pixel size is lowered the median resolution keeps growing. When multiplied by the appropriate pixel spacing the minimum exhibited in Figure 4-18 (a) can be recovered but it is not apparent here as the median resolutions are plotted in a normalised scale. This graph has a very similar application to the one subplot shown in Figure 4-21 (a): when devising an imaging experiment one can infer to it in order to select the right pixel spacing for the purpose of resolving a certain feature. Finally, it would be insightful to compare the difference between the two methods on a normalised scale, namely $(M_{r_1} - M_{r_2})/p_{r_1}$. It is evident that at the coarser pixel sizes the difference is around zero. As the pixel size is decreased Algorithm 2 becomes more sensitive to the increased noise and lack of linescans and it therefore underestimates resolution. For the noisiest dataset, this underestimation is about 8 pixels.

The gain and loss of resolution can also be investigated by computing the derivative of the median resolution with respect to pixel size. This is shown in the following figure:

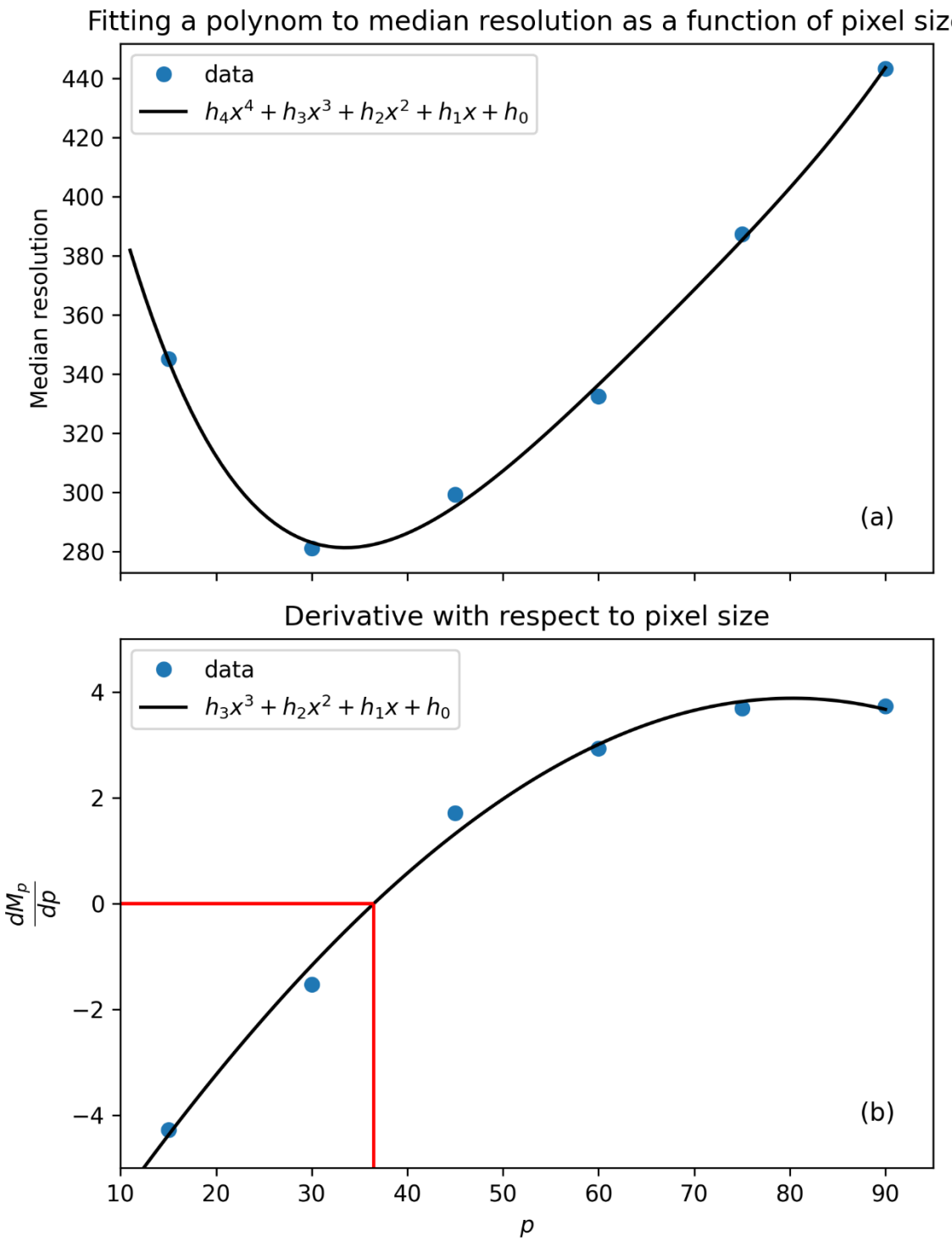


Figure 4-22 (a) – median resolution acquired through the recovery method as a function of pixel size. Blue scatter points is the data and the continuous black curve is a fourth degree polynomial fit to the data. (b) – derivative of median resolution with respect to the pixel size as a function of pixel size. Blue scatter points is the data and the continuous black curve is a third degree polynomial fit to the data.

In order to model the functional dependence of median resolution on pixel size a fourth degree polynomial was used. The black curve in Figure 4-22 (a) was obtained after optimising the polynomial coefficients through curve fitting and the blue scatter points are the actual data. The coefficients are shown in the following table.

h_4	h_3	h_2	h_1	h_0
1.92×10^{-5}	-5.09×10^{-3}	5.15×10^{-1}	-2.02×10^{1}	549

Table 4-8. Polynomial coefficients describing the median resolution as a function of pixel size.

While numerical differentiation with a low number of datapoints may be unstable, using a polynomial to model the data allows for the derivative to be computed in a more stable manner. This is represented in Figure 4-22 (b), where the black continuous curve is the derivative of the median resolution as a function of pixel size, modelled as a third degree polynomial, and the blue scatter points are the numerical derivative of the median resolutions. This is another useful way of studying the loss/gain of resolution. Starting from $90\mu m$ and up to a pixel size corresponding to roughly $37\ \mu m$, resolution is gained as the pixel size is decreased. This is indicated by the positive sign of the derivative; below the zero point resolution is lost as indicated by the negative sign of the derivative. Therefore, the minimised median resolution falls at around $37\mu m$ pixel size.

To finalise this study, a final violin plot showing the resolution distributions across all six pixel sizes is shown. Since the recovery method performed better only this method is displayed here.

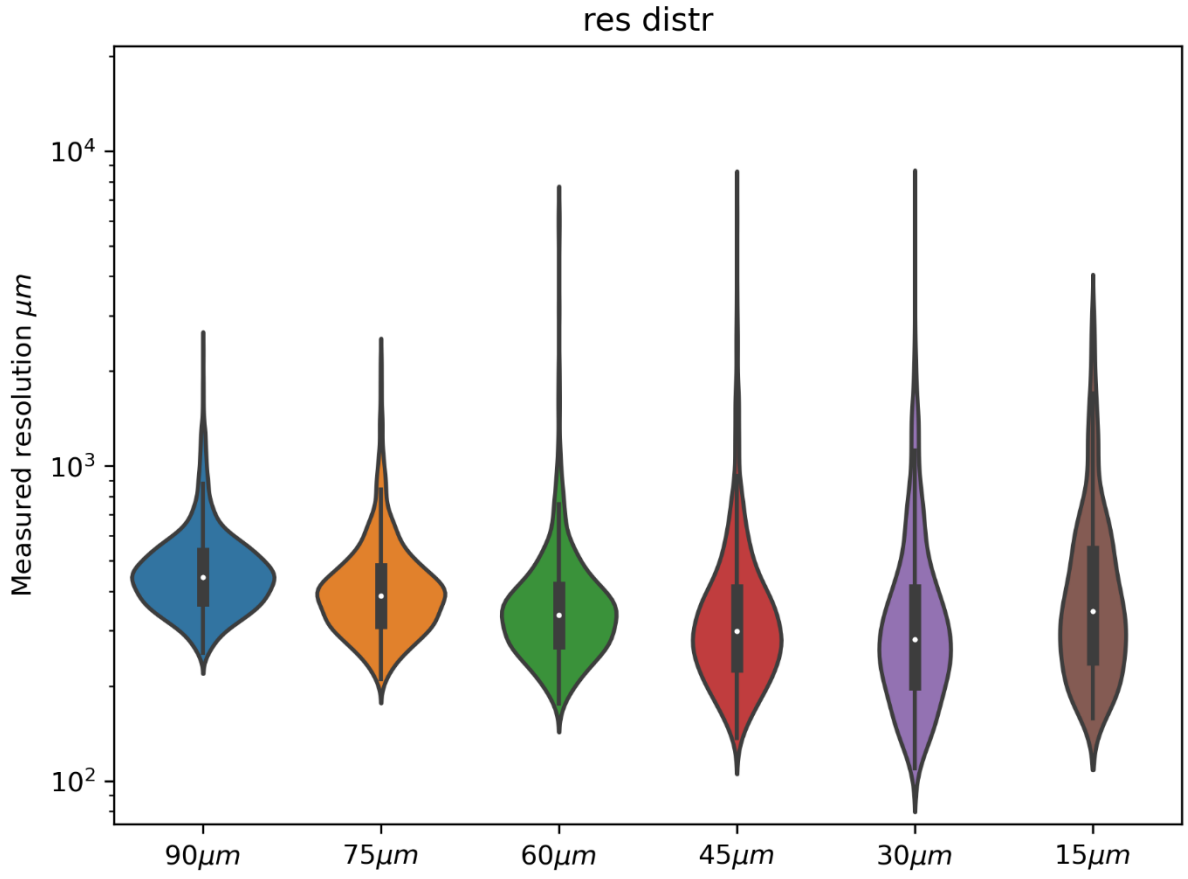


Figure 4-23. Resolution distributions across all pixel sizes.

As per usual within each violin plot a miniature boxplot is presented. The white dot in the middle is the median. The highest achievable resolution is at the bottom tail of each distribution and the worst resolutions are at the top tail. The distributions have been plotted using a log10 base; it is evident that these can also be modelled as a skew-log normal distribution. As the pixel size is decreased it appears that the scale parameter of each distribution increases. It would be interesting to use MLE in order to extract the relevant parameters that define each distribution. In a spirit similar to that of the PDF/CDF models for the intensity distributions, such a calculation can be used when one has an interest in computing the expected resolution between two distances or even two intensities. No such example is provided in this work, however this could be quite useful when comparing different modalities operating at different pixel spacings.

4.4 Conclusions.

The purpose of Chapter 2 was to introduce an image formation model and Chapter 3 was concerned with establishing a methodology for a resolution measurement based on the image formation model. Chapter 4 allowed for the experimental application of all of the ideas developed in Chapter 2 and Chapter 3. An experiment was performed – a silver step edge deposited and coated with a CHCA matrix. It was then imaged at various pixel sizes with strong material removal. This is the first experiment where the interplay between resolution gain due to strong material removal (minimised blur) and resolution loss due to SNR weakening is investigated *quantitatively*. In **Chapter 4.3.2** it was discovered that the distributions of intensities can be modelled as a log-skew normal distribution. The relevant parameters for the PDFs and CDFs were obtained via MLE. This showed us that the majority of images occupy the low intensity region with only very few images spanning the high intensity region. It also had three important applications: one was in the simulation of an intensity distribution for the four datacubes tested in **Chapter 3.4.** This was very important as it allowed us to accurately compare the performance of Algorithm 2 and the recovery method to a ground truth resolution estimate. The second was to estimate the number of images that have an SNR below unity – those can be discarded as pure noise and do not have spatial resolution. The third was to calculate the number of images that exceeded the pre-set threshold of 0.99 fractional error.

In **Chapter 4.3.3** the noise statistics were investigated. This is where the importance of **Chapter 2.4** becomes evident. The combined noise model, which has been reported previously[105,106], was outlined there. Unfortunately, the $1/f$ noise (flicker noise) was not observed[102]. That could be attributed to the fact that the original report performed the noise spectral density analysis by collecting an 'empty' spectrum. The detector noise and peak fluctuations could therefore obscure whatever electronic noise hides within an 'empty' spectrum. The physical significance of the noise model parameters was also explained – the a parameter is related to the uncertainty of counting discrete particles introduced by the detector and the b parameter is related to fluctuations in the ion flux which give rise to fluctuations in the peak amplitudes. The combination of the two parameters gave rise to a quadratic variance as shown in a numerical simulation in **Chapter 2.4**. In **Chapter 4.3.3** it was experimentally

demonstrated that the observed variance grows quadratically with intensity! It should be pointed out that it is also precisely the use of a noise model that allowed us to use the recovery method. This method was shown to perform better than Algorithm 2 in the presence of reduced linescans and severe noise. Therefore, had the quadratic noise model not be considered, Algorithm 2 would be systematically underestimating resolution. This is also very important for what follows in **Chapter 5** where several tissue imaging data sets acquired from different modalities are compared. There are only linescans that can be used to approximate a step edge and one will rely solely on the recover method to compare the resolutions of those modalities. Finally, the physical interpretation of the noise model parameters a, b could also be tested. It was shown that the a parameter appears to remain independent from the pixel size for the five datapoints that belonged to the same experimental run. This was also confirmed with an MK test. As for the sudden drop in the $15\ \mu m$ data point, this could be attributed to a difference in detector performance due to that particular dataset being acquired at a different time point; the mass range can also affect the detector performance. This is all strong evidence that the physical interpretation of the noise model is correct. However, measurements acquired at different time points can be used in order to cement this statement as a truth. The b parameter on the other hand was expected to be dependent on pixel size; the MK test confirmed this and an equation that modelled this dependence was proposed. The b parameter also limits the maximum achievable SNR. The theoretical computation, which assumed that the intensity tended towards infinity, was compared to the highest empirically measured SNRs and the two showed a plausible agreement.

Finally, in **Chapter 4.3.4** the spatial resolution of all six datacubes was estimated. The process for doing this was started with a review of the blurring parameters. The failure of the 86-14% criterion, which was explained theoretically in Chapter 2 and Chapter 3, was experimentally observed. Then, the spread in the blurring parameter for each individual datacube was shown. In **Chapter 3.4** the lower intensity images (which comprise the majority of each datacube) where found to have a significantly underestimated blurring parameter. This was also observed here. This meant that resolution would be underestimated when applying Algorithm 2, as the MTF would be artificially sharpened. The other thing that would lead to an underestimated resolution is the fractional error of measurements exceeding a pre-set threshold when an insufficient number of linescans are used. The results from the recovery method and Algorithm 2 were presented and the interplay between resolution gain due to material removal and resolution loss due to SNR weakening was discussed. The loss and gain of resolution was also briefly investigated through the lens of the first derivative of the median resolution with respect to pixel size. It was demonstrated that a clear minimum is exhibited at around $37\ \mu m$. It is clear that performing this study by using the current best methods[69,137] would have been a lot more time consuming as a special resolution devices would need to be prepared for each pixel size; neither method would also be equipped with the tools to deal with quadratic variance.

Overall, all of the theoretical considerations laid out in Chapter 2 and Chapter 3 came to fruition in Chapter 4.

Chapter 5 Applications for tissue imaging

5.1 Introduction

MSI finds the majority of its applications in biological and pharmaceutical studies and as such a large portion of MSI datasets are tissue imaging datasets. Therefore, it would be useful to extend some of the methodologies developed in this work to tissue imaging. In this Chapter the resolution performance of several imaging setups that also span a range of modalities is investigated. Unfortunately, the presence of a well-defined step edge is a requirement. As shown in Chapter 3, this edge needs to be aligned either vertically or horizontally in order to recover the y or x component of the MTF respectively. In Chapter 3 it was also shown that in the presence of sever noise and a reduced number of linescans Algorithm 2 tends to underestimate resolution. As it shall be seen there are not that many linescans that can approximate a step edge and thus one would expect a systematic error introduced in the median resolution if Algorithm 2 is to be used. Even more problems arise when considering the fact that tissue images will naturally depict a spatially heterogeneous signal. Situations may arise where the intensity of a step edge can be present at a particular ROI for one signal while the same ROI exhibits a low intensity step edge for another signal. If the latter signal happens to exhibit higher intensity elsewhere, the resolution would be overestimated as the selected ROI would have a lower SNR, whereas the image itself might contain regions with higher SNR elsewhere. An excellent example of this is signal derived from white matter and grey matter when imaging brain tissue. Such signals tend to be anticorrelated with each other – images depicting the distribution of molecules related to white matter will exhibit a higher intensity at some ROIs while those that depict the distribution of molecules related to grey matter will have a much lower intensity at the same ROIs. Therefore, if a high intensity ROI that exhibits a step edge feature is selected for a white matter signal, one would expect the same ROI to exhibit a low intensity edge for a grey matter signal; this would mean the SNR is low and the resolution distance is high; if the grey matter image contains higher SNR regions the overall resolution of the image will then be overestimated. Therefore, when estimating the resolution of a datacube, this could skew the resolution estimates towards white matter signals and falsely measure that all grey matter signals have a low resolution. A final caveat to relying on sharp step edge features in tissue images is that some images may have a high intensity and therefore exhibit a good resolution but there may simply be not edge-like features within the image.

Luckily, a noise model was established and by relying on the estimates of the noise model parameters combined with the blurring parameter obtained from a few high intensity images that do exhibit a step edge feature, the resolution equation may be recovered. The recovery method was shown to approximate the ground truth resolution quite well and therefore this will be the preferred method for analysing resolution in the context of tissue imaging. The downside of this method is the imposition of a global MTF – if images exhibit a different natural blur then this information will be missed out on. The upsides are several. Firstly, one can deal with the reduced number of

linescans as long as a decent estimate of the noise statistics can be obtained. Unfortunately, the fact that tissue images are spatially inhomogeneous can prevent us from doing this accurately. The ROI selected for computing the empirical estimates of the noise must be homogeneous. This was thoroughly explained in Chapter 3 and it should be obvious that any natural variation in the signal can be interpreted as noise variance. There exists a beautiful piece of work that allows for the detection of homogeneous regions within an image[158] and the method proposed in that work shall be used for the accurate estimation of the noise model parameters. This will then allow us to use the recovery method for estimating resolution in an automated fashion.

The noise model will also allow for the comparison of the different modalities simply by comparing the relevant noise model parameters. Information such as the maximum achievable SNR can be acquired from those. More interestingly, the noise models that govern different modalities will be compared. The modalities that will be investigated are SIMS, in particular NanoSIMS and OrbiSIMS, MALDI and DESI. The resolution estimates will allow for the construction of a 'resolution ruler' that depicts the possible resolutions that each modality can achieve. Ideally, in order to cover the range of all possible resolution distributions, just like the experiments in Chapter 4, several pixel sizes should be used. Sadly this is not the case in this study as only a limited amount of data is available – some of the data analysed here is part of the CRUK Grand Challenge study and as such they have a limited availability. Nevertheless, the 'resolution ruler' will still reveal valuable information. The experiments conducted here will also allow us to demonstrate the modality agnostic nature of the resolution metrics proposed in this thesis. For example, in Chapter 3 and Chapter 4 the 86-14% criterion was shown to fail in modalities with strong material consumption such as MALDI. This metric, however, has been known to recover the width of the beam in modalities with weak material consumption such as SIMS [67,68]. In Chapter 3 it was demonstrated that when weak material consumption is used resolution is indeed limited by the width of the beam, especially in the case of Poisson noise at high intensities. When the NanoSIMS datacube is analysed it will indeed be demonstrated that the method proposed in this thesis predicts the blurring parameter (86-14%) to be the limit to spatial resolution at high intensities. This has also been reported previously[67–69]. At low intensities however, resolution is lost due to noise[69,137].

5.2 Methods

5.2.1 Experimental

For the modality comparison study performed three of the most commonly used modalities are interrogated. These are SIMS, MALDI and DESI.

5.2.1.1 SIMS

In the case of SIMS the resolution performance of two different datasets is tested. The first one was acquired with an instrument that can be considered to achieve the highest spatial resolution in MSI in general, namely NanoSIMS (CAMECA, Société par Actions Simplifiée). A thin tissue section of a mouse breast tissue was imaged at a pixel size of $117\ nm$. For this experiment a Cs^+ primary ion beam was used with an impact energy of 16 keV per ion. The beam was shaped using the D1-3 aperture. Since NanoSIMS corresponds to an MSI modality with weak material consumption and it would be therefore be expected that the blurring parameter should be equal to the width of the beam, it would be useful to know what the probe size is. Using the NanoSIMS manual[159] one can roughly estimate that the beamwidth is between $100 - 400nm$; this fact will allow to test if our method can recover the 86-14%, especially when considering high intensity images with high SNR. This data was kindly provided by Dr. Greg McMahon.

The second SIMS data set investigated here was acquired with a SIMS instrument coupled to an Q Exactive HF Orbitrap (Thermo Fisher Scientific, Germany). A thin pork liver tissue section was imaged at a pixel size of $3\ \mu m$. The instrument was operated at a positive polarity, with a cycle time of $200\ \mu s$ and default options. A $20\ keV\ Ar3000^+$ ion beam was used at a field of view of $200 \times 200\ \mu m^2$. The mass range was set to $80 - 1200\ m/z$, with an injection time of $200\ ms$. Unfortunately, the beam width is not known in advance here like it is for NanoSIMS. However, it is possible to estimate this value using a sharp step edge feature.

5.2.1.2 uMALDI

Next, the resolution of a prototype MALDI source (also known as 'uMALDI') coupled with a Synapt G2-Si mass spectrometer (Waters, UK) is measured. It should be noted that the spatial resolution of the same mass spectrometer was measured in the previous chapter; the only difference here is the ion source. For this experiment a CryoStar MX70 cryo-microtome (ThermoFisher Scientific, USA) was used to obtain a thin tissue section ($10\ \mu m$). The biological sample used was mouse brain and the sectioning was performed in the sagittal plane. Thaw mounting was used to attach the section to a glass slide. The imaging experiment itself was conducted at a pixel spacing of $20\ \mu m$ using continuous raster mode.

5.2.1.3 DESI

Finally, three DESI datasets are investigated. These belonged to a larger study that was part of the CRUK Grand Challenge and the original aim was to estimate the molecular coverage in an interlaboratory study. Three MSI laboratories participated in this study (Lab A, Lab B, Lab C). The first lab, referred to as DESI Lab A, used a Q128

Exactive Orbitrap mass analyser (Thermo Scientific, Bremen, Germany). A home-built sprayer was used as an ion source; this was combined with a commercially available 2D DESI stage (Prosolia Inc, Indianapolis, IN, USA). Then, Lab B used an automated 2D DESI source (Waters, UK) coupled with a Xevo G2-XS Q-ToF (Waters, UK) mass analyser. The DESI sprayer was also commercially available. Finally, Lab C also used a Xevo G2-XS Q-ToF (Waters, UK) mass analyser. However, a prototype DESI sprayer was used by Lab C. This set up is known as Desorption Electro-flow focusing (DEFFI)[160]. Since all three labs used a different DESI sprayer it would be interesting to investigate the blurring parameter and how that affects resolution. All three labs used a 95:5 (v:v) methanol:water solution as means of generating the DESI beam. The pixel spacing used by Lab A was $80\ \mu m$, while Lab B and Lab C used a pixel spacing of $100\mu m$. Consecutive thin tissue sections of pancreatic mouse tissue were used to acquire the imaging datasets.

The following table summarises the modalities used in this study and the pixel sizes used for acquiring those datasets:

Modality	Pixel size
NanoSIMS	$117nm$
OrbiSIMS	$3\mu m$
uMALDI	$20\mu m$
Orbitrap DESI LAB A	$80\ \mu m$
XevoToF DESI LAB B	$100\mu m$
XevoToF DESI LAB C	$100\mu m$

Table 5-1. Summary of the modalities investigated in this chapter in their relative pixel sizes.

5.2.2 Computational methods

5.2.2.1 Pre-processing

All data was already pre-processed by other parties before resolution analysis was performed. The DESI datasets contained a needless amount of signals (5200 for lab B, 5830 for Lab C and 22978 for Lab A). Presented as such these signals were either background solvent peaks or meaningful tissue images; in the case of Lab C a really large amount of those signals were also pure noise (average signal intensity much smaller than unity). Therefore, some amount of extra pre-processing was much needed in order to separate the background signals from the useful tissue signals. This was done with the aid of watershed segmentation; a tissue mask was generated which was then used to compute the average intensity within and without the mask. Signals with a higher mean intensity outside the tissue mask were considered as background signals and were discarded. In the case of Lab A dataset a further minimum intensity threshold was applied in order to weed out the useless signals (which unfortunately were a large part of the pre-processed data). After these steps, the dataset from Lab A had 3193 images left, Lab B was left with 2278 signals and the dataset from Lab C was reduced to a datacube with 3704 images. As for the uMALDI data set, the data was neatly pre-processed and all background matrix signals were removed prior to the analysis performed

by the author. As for the OrbiSIMS and NanoSIMS datacubes, they contained 200 and 8 images respectively and no need for tissue/background separation was needed due to the nature the modality used.

5.2.2.2 Watershed segmentation

As described in the previous section the watershed segmentation algorithm was used to as a mask to delineate between tissue signals and background signals. However, it will also be particularly useful when the median intensity of the tissue signal needs to be calculated. Since the background would often contain pixels with a value of zero, if the intensity of the entire image is computed the median will be dragged towards zero as there are a lot of background pixels with a value of naught. Therefore, the watershed segmentation algorithm will allow for a tissue mask to be produced and the true median of the tissue only region can be computed; an accurate image histogram may be obtained as well in this manner.

The watershed algorithm is a wonderful tool for segmenting two regions that are close to each other and are separated by a sharp transition[161,162]. This is perfect for the purpose of segmenting tissue from background. The algorithm is inspired by how water flows; the pixel intensities of a grayscale image may be thought of as a topographical map. A higher intensity would indicate a higher elevation and a lower intensity would correspond to a lower height. Naturally, water would flow from high to low elevations. User defined markers are selected and those are referred to as basins. The basins are then flooded until different basins meet at the watershed lines. In this work the basins are defined with the aid of Sobel filter[163]. The watershed algorithm and the Sobel filter are readily available in the scikit-image (skimage) Python library and were used in this thesis.

5.2.2.3 Goodness of Fit (GoF) – the reduced χ^2

It was demonstrated in Chapter 3 and Chapter 4 that curve fitting fails when not many linescans are used. This is because when averaging over many linescans the noise cancels out and the ground truth edge profile is recovered. Should an insufficient amount of linescans be used then overfitting to noise occurs. This typically leads to an underestimated blurring parameter, which in terms leads to a sharper MTF and consequently the resolution distance is underestimated. When dealing with tissue images the number of available linescans that approximate a step edge are very limited. Unfortunately, in this scenario the art of measuring spatial resolution devolves to staring at ROIs that resemble a step edge for hours. Adding an extra linescan could dramatically change the blurring parameter estimate; taking away or adding a few rows of pixels can also produce vastly different results.

While in principle an edge detection algorithm can be used to find edges, such an algorithm would also need to know how many rows of pixels from the edge surface to include. The surface of a tissue image edge ROI is not necessarily a constant as biological features may be present. These can also cause curve fitting to underperform as the model used assumes a homogeneous surface. Even worse, Algorithm 1, which measures the blurring parameter,

also measures the SNR. If the edge surface is not homogeneous because of the presence of biological features, the SNR estimate will be affected by this – a larger noise standard deviation will be picked up as the signal that describes the biological feature will be misinterpreted as noise. Algorithm 2 on the other hand computes spatial resolution via a Fourier transform; if an edge ROI with ten data points is used, then only five datapoints would be available in the final MTF. Therefore, human intervention is still needed in order to check that the selected edge ROI somehow satisfies those two criteria – a sufficient number of linescans and a sufficiently homogeneous surface region. This is not surprising as the method devised to measure spatial resolution assumes a ground truth step edge with many number of linescans available; the surface of the step edge should be as homogeneous as possible. Tissue images may or may not exhibit a small ROI that approximates those requirements. In order to aid anyone attempting to deal with such a task the reduced chi-squared goodness of fit estimate is proposed. The chi-squared statistic is defined as:

$$\chi^2 = \sum_i^{\square} \frac{(y_i^{mean} - y_i^{model})}{\epsilon_i} \qquad \text{Eq. (5.9)}$$

Where here y_i^{mean} is the i^{th} datapoint acquired from averaging all linescans available, y_i^{model} is the model prediction for i^{th} data point and ϵ_i is a term representing the data uncertainty. The reduced chi-squared statistic is then defined as chi-squared per degree of freedom:

$$\chi_\nu^2 = \frac{\chi^2}{\nu} \qquad \text{Eq. (5.2)}$$

Where ν denotes the degrees of freedom and is equal to the number of datapoints minus the model parameters. Curve-fitting is performed on Equation 3.16 in both Algorithm 1 and Algorithm 2; this equation has four free parameters – σ, μ, I_1, I_0. These correspond to image blur, edge position, average surface intensity and average background intensity. The reduced chi-squared statistic is used as a measure of goodness of fit. If $\chi_\nu^2 \gg 1$ this indicates that the model fits the data poorly. In the cases studied here this may happen if actual biological features are appearing among the edge surface (which is meant to be homogeneous.). Therefore, if a ROI is selected but the model fits the data poorly due to biological features appearing on the surface and an inaccurate blurring parameter is measured as a consequence, one would be able to discard this measurement if $\chi_\nu^2 \gg 1$. On the other hand, if $\chi_\nu^2 \ll 1$, then the model is overfitting the data to noise. The consequence is either an overestimated or an underestimated blurring parameter. It was seen in Chapter 3 that the majority of low intensity measurements suffered from an underestimated blurring parameter. Some measurements will also overestimate it. Therefore, if a measurement exhibits a $\chi_\nu^2 \ll 1$, one may reject it as the model has overfit the data due to noise. Finally, if $\chi_\nu^2 \approx 1$ the model captures the data well and blurring parameter may be accepted. Generally, finding an appropriate scaling parameter ϵ_i is a tricky task; in this study the data uncertainty is taken as the standard deviation of the data. This is a good

starting point and yields acceptable results. For the purpose of estimating the GoF statistics the Python package lmfit was used.

5.2.2.4 Estimating noise - detecting homogeneous blocks

The reader should be convinced by now that estimating the noise levels as a function of intensity is vital for a resolution measurement. It should also be obvious by now that Algorithm 2 will not perform well due to the lack of a sufficient number of linescans. Therefore, resolution will be measured using the recovery method. There are several steps required to achieve this. The first one is an accurate blurring parameter measurement. This was discussed in the previous section. The second step is to an accurate intensity measurement. Ideally, the median of intensity of a tissue image should be used. The means of accomplishing this were outlined in **Chapter 5.2.2.2** where the watershed segmentation algorithm was described. Finally, an accurate noise model is a must. Then, Equation 3.24 may be used in order to compute resolution. Unfortunately, tissue images are naturally inhomogeneous and empirically estimating the noise model can become tricky as biological features may appear among the edge surface. Even worse, for the same ROI, some images may exhibit a homogeneous edge surface while others can have a change in signal due to the presence of said features. Then, the variance/noise standard deviation will be overestimated for those images, which can cause the false believe that the noise model is not stationary. This would also mean that the resolution distance for those images will be overestimated. That is problematic. Fortunately, there exists a beautiful approach for the punctual empirical estimation of the noise level function (NLF)[158]. The NLF is simply the noise variance as a function of signal intensity (see Chapter 2.4). This is based on an non-parametric hypothesis test using Kendall's τ as a measure of correlation. The idea is simple: divide an image into multiple small blocks of equal size. If the block is homogeneous (meaning the only change in signal is due to noise and not biological features), then the rank correlation will be zero. If there is a signal, the rank correlation will be different from zero. The authors establish a non-parametric statistical test based on two hypothesis - H_0 is the null hypothesis and it assumes that the block is homogeneous and H_1 is the alternative hypothesis and assumes that the block contains a stepwise jump in signal. It is well known that if the rank correlation is zero (null hypothesis is true) then the z scores are $\sim\mathcal{N}(0,1)$. The authors that discovered this method proved that if the alternative hypothesis holds (there is a signal in the block), then the expected value of the z scores will be of the order of $\sqrt{n}$, where n is the number of pixels in the block. Thus, based on the measure of Kendall's τ within a block and its associated z, a p-value may be computed that will accept/reject the alternative hypothesis. The result is that all homogeneous blocks within an image have been detected and punctual empirical estimates of the noise variance and noise standard deviation may be performed. This will allow us to calibrate the noise model for each modality and estimate resolution using the recovery method (Equation 3.24). Furthermore, this will allow us to investigate the noise models exhibited by different modalities. It was shown in Chapter 4 that MALDI exhibits a quadratic variance and this was explained with the aid of computational simulations in Chapter 2. However, there is an opportunity to test

DESI and SIMS and across a range of different mass analysers and observe if the quadratic variance model appears again. Quadratic variance has been reported in ESI previously[105] and it can therefore be expected that the noise statistics in DESI are described by the combined noise model. While the scripts for estimating the NLF in natural images were provided in the original paper[158], those scripts were written in MATLAB. Due to a genuine dislike for the MATLAB programming language, this algorithm was reimplemented in a custom Python script. The original MATLAB script invokes a custom C program that does all the heavy lifting and computes Kendall's τ and its associated z values; attempts were made to write a wrapper for Python but alas those were unsuccessful. Thus, the Python script used for this work is much slower than the original but provides good results nonetheless.

5.3 Results and discussion

5.3.1 Intensity distributions across different modalities.

The first step for the accurate estimation of spatial resolution using the recovery method is to compute the intensity of the signals. Ideally, only the tissue intensity should be measured and the background neglected. Watershed segmentation was used to achieve this. For each image in each datacube, a custom tissue mask was produced and

the median intensity for the tissue only region was computed. The following figure demonstrates this process for one of the DESI datasets.

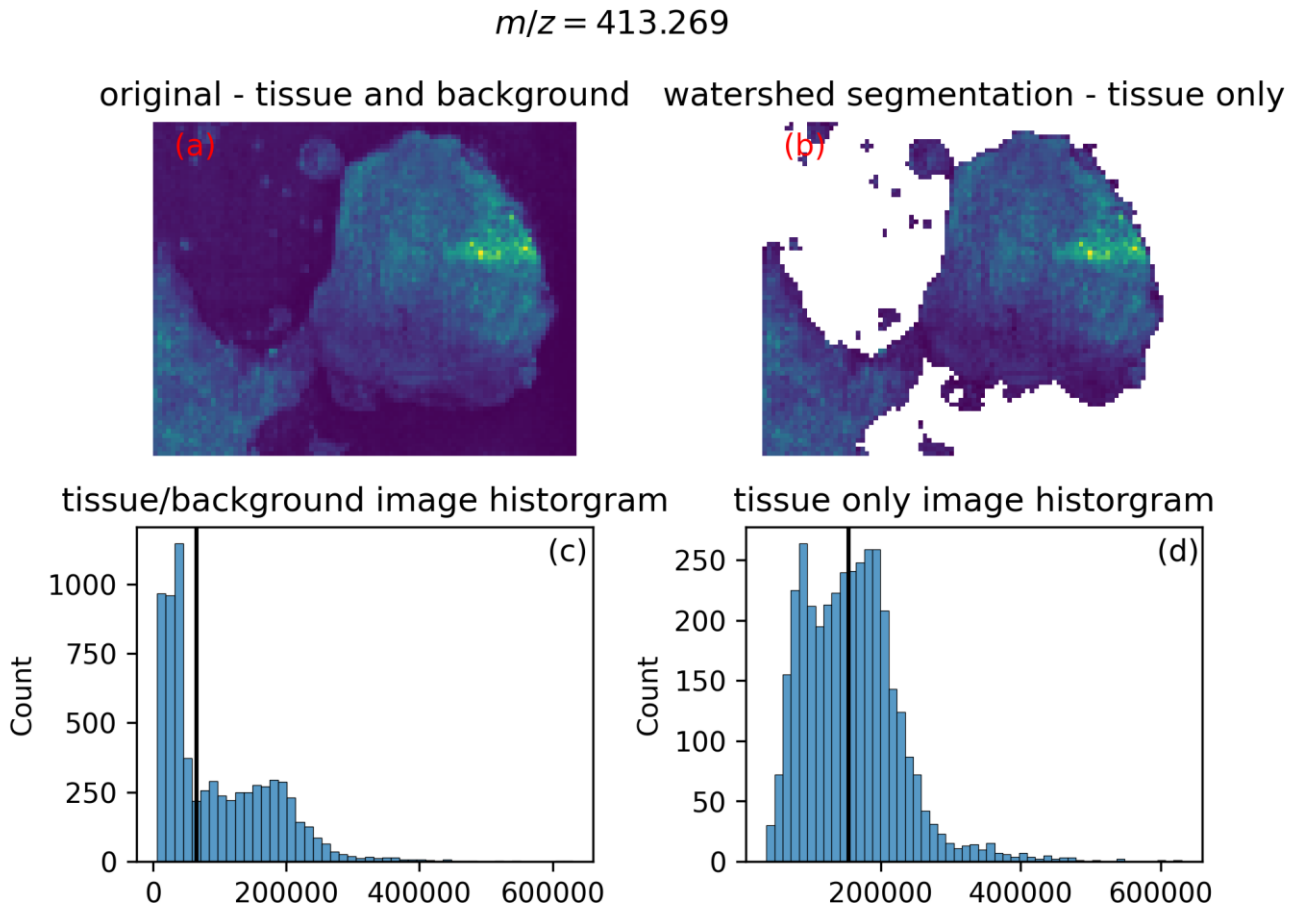


Figure 5-1 The use of watershed segmentation to separate tissue from background. (a) – original image. (b) – tissue segmentation and separation from background. (c) – image histogram of the original image. (d) – image histogram of the tissue only region.

The original image is displayed in Figure 5-1 (a) and the segmented image in Figure 5-1 (b). In general the parameters used for segmentation varied from dataset to dataset and the optimal parameters were found with trial and error. The original image, shown in Figure 5-1 (a), contains intensities from the background that are not relevant for the tissue only region. These manifest as a high number of counts in the low intensity region of the histogram of the original image, shown in Figure 5-1 (c). The median value of the entire image intensity is drawn with a black vertical line and it can be seen that it lies near the intensity of the background pixels (which have a low intensity). However, the histogram of the segmented image, shown in Figure 5-1 (d), is representative of the tissue region only. The black vertical line here represents the median tissue intensity. Unfortunately, due to the heterogeneity of tissue images the spread around the median is not due to noise only, but instead is a combination of noise and actual tissue features. Thus, one cannot use the histogram of the entire tissue image to estimate the noise variance.

This process was repeated for every single image in each of the six datasets. The following figure shows the distribution of the median tissue intensities across those datasets.

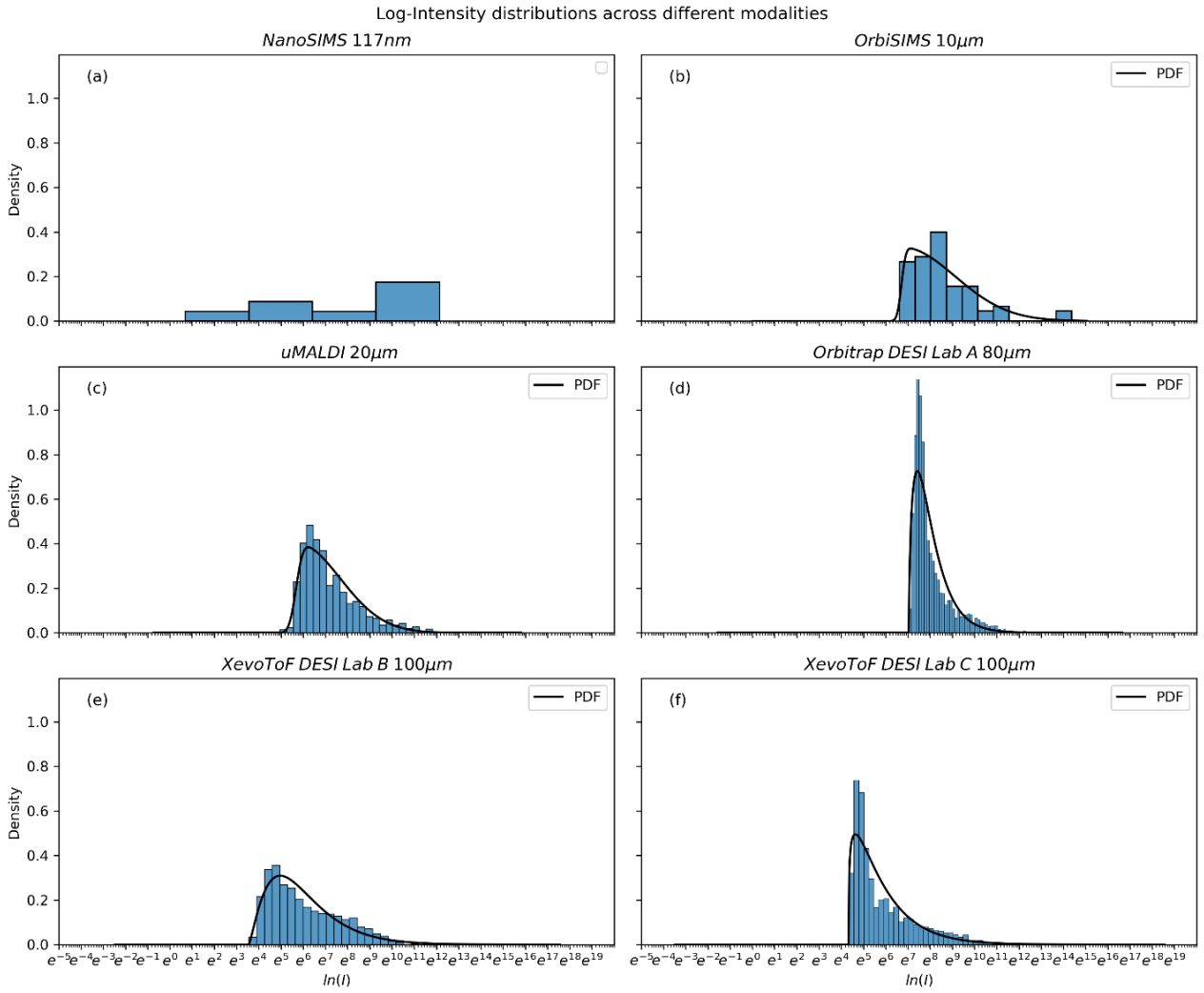


Figure 5-2 Natural logarithm of the median tissue intensities for each datacube. The black curve is a probability density function estimated with MLE. (a) – natural log median tissue intensity in NanoSIMS. (b) – natural log median tissue intensity in OrbiSIMS. (c) – natural log median tissue intensity in uMALDI. (d) – natural log median tissue intensity in DESI Lab A. (e) – natural log median tissue intensity in DESI Lab B. (f) – natural log median tissue intensity in DESI LAB C.

As in Chapter 4, the intensity distributions are plotted on a natural log scale. The only difference is that the intensities in Chapter 4 were the average intensity acquired from a homogeneous surface and here the median intensity acquired from a heterogeneous tissue image is shown. However, there are several similarities. Firstly, it seems that the majority of intensities are concentrated in the low intensity region. Secondly, MLE can also be used to estimate the PDF that underpins the distribution of the median tissue intensity. Those are plotted with a black curve on each of the subplots. The PDF for NanoSIMS was not estimated as only eight images are present in the dataset. The

NanoSIMS dataset also exhibits the opposite trend – it appears that it has more high intensity tissue signals than low intensity. It is peculiar to mention that the log-skew normal distribution was used to estimate the median tissue intensity in OrbiSIMS and uMALDI. The parameters were obtained with MLE and the corresponding PDFs are shown with black solid curves in Figure 5-2 (b) and Figure 5-2 (c) respectively. The log-skew-normal distribution however did not perform well on the three DESI datasets. It was empirically found that the gamma distribution does a better job at modelling the median tissue intensity distribution of DESI Lab A, DESI Lab B and DESI Lab C. MLE was used to find the optimal parameters for each datacube and the PDFs are plotted with a black solid curve in Figure 5-2 (d), Figure 5-2 (e) and Figure 5-2 (f). The extracted PDFs (apart from NanoSIMS) are shown in the following figure.

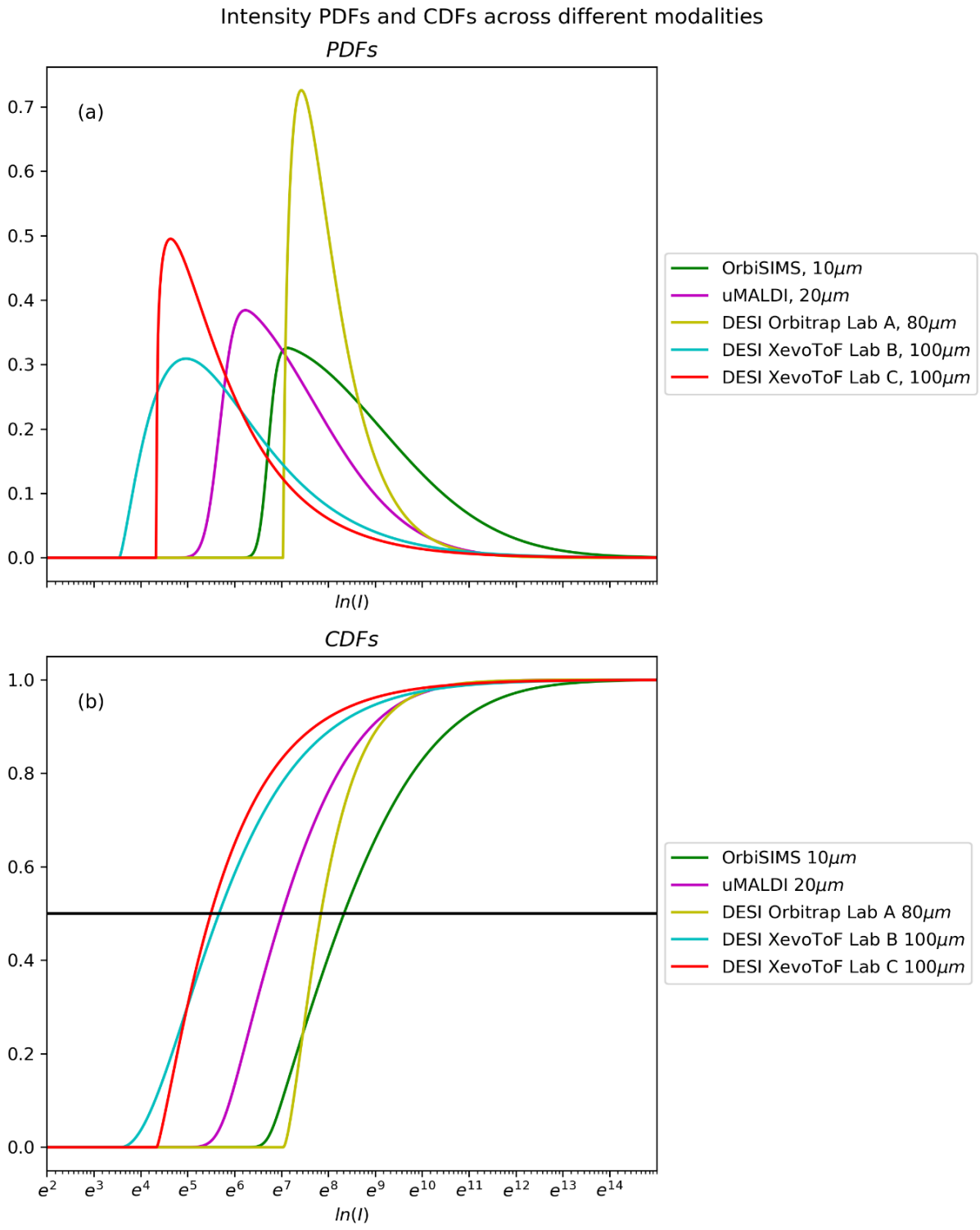


Figure 5-3. (a) – PDFs describing the distribution of the median tissue signals for different modalities. (c) – the corresponding CDFs; black vertical line is the 50th percentile.

Generally, the PDFs and CDFs, shown in Figure 5-3 (a) and Figure 5-3 (b) respectively, can be incredibly useful when comparing different modalities. For example, if one is interested in computing how good a given modality is

in detecting a certain set of molecules that belong to a given molecular class, one can use the PDFs in Figure 5-3 (a) to compute the expected median intensity. One can then use a noise model and a blurring parameter to compute the expected resolutions of that group of molecular signals. For example, one could compare the resolution distributions for lipid molecules and metabolites. While this is a nice idea, no such calculation is performed here. Implementing such a calculation would require an automated approach to edge detection, as step edge regions for different molecules are not guaranteed to occupy the same ROI.

The CDFs in Figure 5-3 (b) reveals which of the modalities has the highest median tissue signal intensity. Note that the NanoSIMS dataset is not shown in the figure above, however an empirical calculation shows that it has the highest median tissue intensity. Next is OrbiSIMS (green curve), followed by DESI Lab A, uMALDI, DESI Lab B and finally DESI Lab C. Of course, this would have an impact on the median datacube resolution. To obtain a median resolution, as prescribed by Equation 3.24, a noise model and a blurring parameter are still required. Next, the noise statistics observed in different modalities is studied.

5.3.2 Noise statistics

The introduction section already discussed why Algorithm 1 would struggle to recover an accurate blurring parameter and a trustworthy SNR. To put it simply, the method for measuring spatial resolution assumes an input of a sharp step edge (that has as many linescans as possible and a homogeneous surface). This assumption is simply not true for edge ROIs in tissue images. The fact that biological features may appear on the edge surface will upset the estimates of the noise variance, noise standard deviation and image SNR. This in turn will affect the estimated resolution. One could attempt to manually find a homogeneous region in a tissue image but one would run into problems – for example what is a homogeneous area for one image may not be for another image. Generally, estimating the noise statistics in a tissue imaging data set is a difficult task which others have failed at[108]. To achieve this, a custom script based on[158] was used. The following figure shows the process of detecting homogeneous blocks.

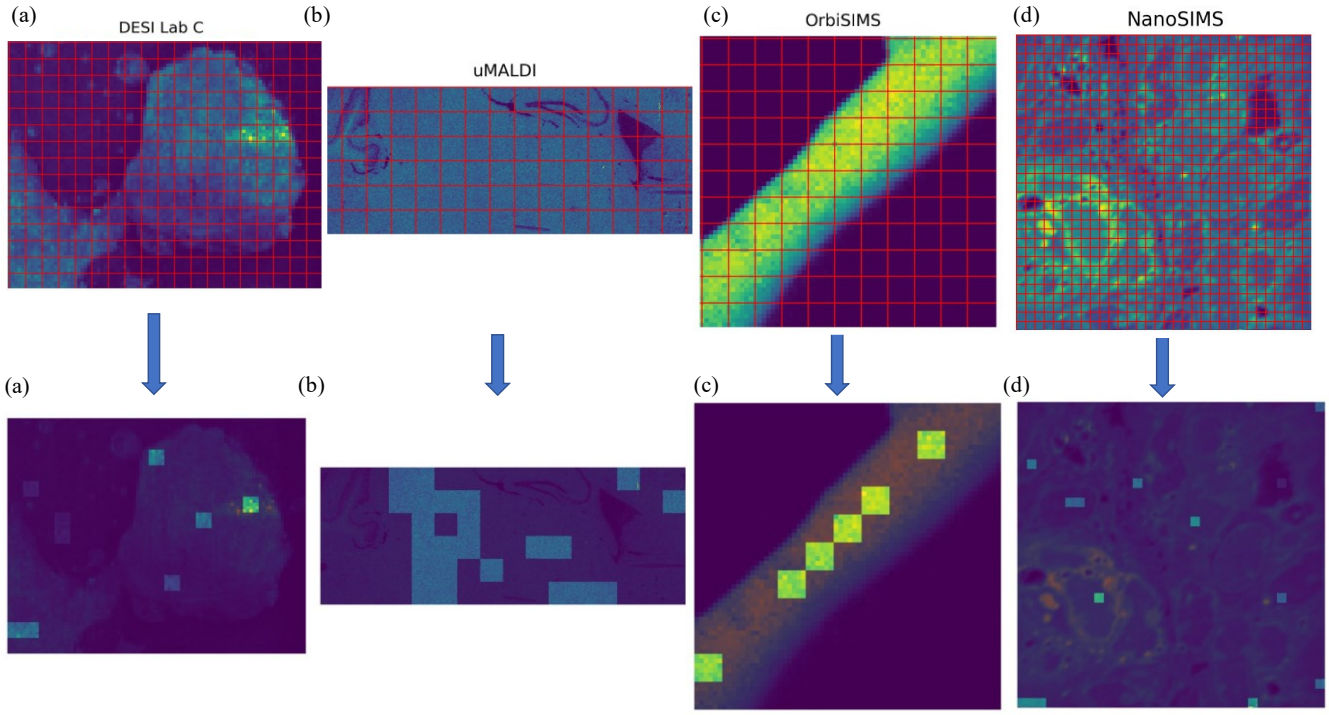


Figure 5-4. Detection of homogeneous blocks for different modalities. (a) – a single ion image from the DESI Lab C datacube. (b) – a single ion image from the uMALDI datacube. (d) – a single ion image from the OrbiSIMS datacube. (c) – a single ion image from the NanoSIMS datacube. (e), (f), (g), (h) – the detected homogeneous blocks for (a), (b), (c), (d) respectively.

The results from this algorithm are shown in the figure above. Briefly, each image is divided into little blocks (represented by the red squares in Figure 5-4 (a), (b), (c) and (d)). Kendall's τ and an associated z score is computed for each block. Based on those the null hypothesis can be accepted and the block can be identified as homogeneous. The blocks that qualify as homogeneous are highlighted in Figure 5-4 (e), (f), (g), (h). It can be seen that the performance of the algorithm is very satisfactory. The local noise variance, local noise standard deviation and local SNR can be then accurately estimated from each of the homogeneous blocks. Sometimes a false alarm will occur and an actual change in signal due to a biological feature will be contained withing a block. Therefore, the noise statistics acquired from such blocks will not be a truthful estimate. For example, this can lead to an overestimation of the noise variance. To deal with this the median local intensity and median local noise standard deviation/ median local variance and median local SNR are computed. This is done for every single image in all six datacubes. The obtained variance as a function of intensity is presented in the following graph.

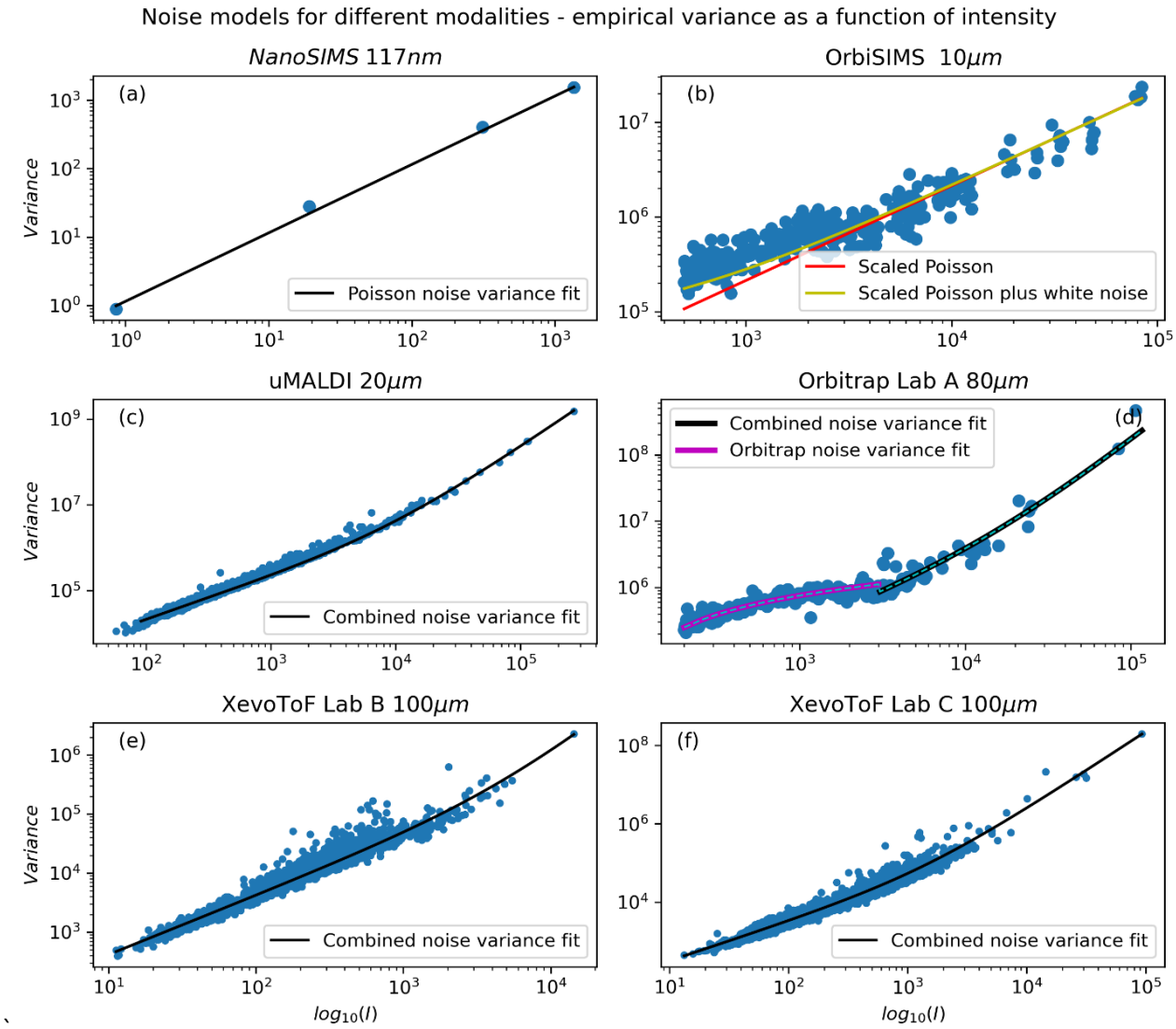


Figure 5-5. Noise variance as a function of intensity measured across different modalities. The black/coloured curves are different noise models fitted to the data (a) – NanoSIMS. (b) – OrbiSIMS. (c) – uMALDI. (d) – Orbitrap DESI Lab A. (e) – XevoToF DESI Lab B. (f) – XevoToF DESI Lab C.

Note that the noise level estimates for NanoSIMS, shown in Figure 5-5 (a), contain only four out of eight data points. This is because for half the images in the dataset no homogeneous areas were detected. The most amazing thing about this estimate of noise is the beautiful straight line with a slope coefficient of $a \approx 1.1$. This line indicates (almost) perfect Poisson noise. This is perfectly in line with the detailed NanoSIMS manual, which describes the noise statistics of the instrument[159]. This is already quite informative, as the simulations in Chapter 3 revealed that in the presence of Poisson noise at high intensities, resolution is completely limited by blur; this has also been shown previously[68,69]. The same thing is observed in this Chapter when the blurring parameter for NanoSIMS is measured.

Next, the NLF for the OrbiSIMS is displayed on Figure 5-5 (b). Unfortunately, no methods for modelling this theoretically have been discussed in this thesis. The red straight line is a scaled Poisson noise model with a scaling parameter $a \approx 210$. This model was described in detail in Chapter 2.4. It is evident that the red line models the noise variance well at high intensities. Therefore, the SNRs of OrbiSIMS and NanoSIMS are not limited like the SNRs of images plagued by combined noise. The scaling parameter of $a \approx 210$ indicates that at a given intensity level NanoSIMS will exhibit an SNR that is $\sqrt{210} \approx 14.5$ times higher than for an OrbiSIMS image with the same intensity. At low intensities, however, it is clear that the scaled Poisson model does not capture the NLF behaviour. This is problematic for resolution estimates, because one will overestimate the spatial resolution at low intensities. To deal with this a mixed Poisson-white noise model is used. This model is described by the following equation:

$$Var(I) = aI + c \qquad \text{Eq. (5.3)}$$

Where a is the scaling parameter for the Poisson noise component, I is the intensity and c is a constant that describes the white noise variance. This model is represented by the yellow line and it can be seen that it performs better than the scaled Poisson model in that regime. Of course, it is obvious that a better model can be used as the yellow line also does not capture the low intensity region well. However, for the purpose of this work, this model will be employed so that a more accurate estimate of the resolutions of low intensity images may be obtained. A physical explanation of the deviation from the scaled Poisson model remains well outside of the scope of this work. The mixed model (yellow line) recovers the scaled Poisson model at high intensities. Curve fitting reveals that $a \approx 210$ and $c \approx 7 \times 10^4$. The linear growth of the noise variance at high intensities implies a square-root growth in the standard deviation and therefore a monotonic growth in SNR.

This is not the case for images corrupted with combined noise as their SNR becomes limited to a constant as the intensity increases. The uMALDI dataset shown in Figure 5-5 (c) is an excellent example for this. The combined noise model was derived in Chapter 2.4 and experimentally verified in Chapter 4. Here it is observed again. The black solid curve is a parabola that was fit to the data and the noise model parameters a, b were extracted. The reader is reminded that the proposed interpretation of the a parameter is that it is a property of the detector (scaled Poisson noise), while the b parameters determines the fluctuations of the peaks in the mass spectrum. The b parameter also limits the SNR; $\max SNR = b^{-\frac{1}{2}}$. The reader is reminded that in Chapter 4 this theoretical prediction was compared to the experimentally measured max SNRs and a good agreement was found. For uMALDI $b \approx 0.02$ and therefore $\max SNR \approx 7$. Thus, at a signal intensity of $I = 10^6$, NanoSIMS would have an image SNR of 1000, OrbiSIMS would have an image SNR of ≈ 70 and the uMALDI would have an image SNR of ≈ 7. This simple calculation is quite insightful and reveals information about the image quality and the achievable resolution of different modalities.

While the combined noise model was derived in Chapter 2.4 and a physical meaning can be attached to the noise model parameters, the mixed Poisson/white noise model used to describe the OrbiSIMS data was invoked without much justification (in particular the white noise part). Even more peculiar is the case in Orbitrap DESI Lab A, shown in Figure 5-5 (d). While the lower part of the variance curve shares a similarity with the other Orbitrap instrument, namely OrbiSIMS – Figure 5-5 (b), the use of a mixed Poisson/white model completely failed to model the data. In fact, at higher intensities ($I > 3 \times 10^3$) Orbitrap DESI Lab A exhibits a quadratic variance (combined noise model). This can easily be justified for DESI as one would expect the combined noise to arise when the number of collected ions is fluctuating. That can happen in DESI – in Chapter 1 studies conducted on the distributions of sizes and velocities of the primary droplets were reviewed. These natural fluctuations in the primary droplets would imply fluctuations in the secondary droplets and therefore fluctuations in the peak height. The quadratic noise model was fit to the data at those intensities; it is represented by the black continuous curve.

At lower intensities ($I < 3 \times 10^3$), the combined noise model ended up underestimating the variance. This will cause the resolution distance of those images to be overestimated and that is a problem for us. Unfortunately, as mentioned before the mixed Poisson/white noise model also failed to fit the data well. Therefore, the following monstrosity is proposed to model the empirically calculated NLF:

$$Var(I) = \begin{cases} \alpha I^{\beta} + \gamma, & I < 3 \times 10^3 \\ aI + bI^2, & I \geq 3 \times 10^3 \end{cases} \quad \text{Eq. (5.4)}$$

Unfortunately, due to a lack of knowledge for the type of noise seen in Orbitrap systems, a piecewise function had to be used. At intensities greater than 3×10^3 the combined noise model is used (continuous black curve); at intensities smaller than this threshold the function $\alpha I^{\beta} + \gamma$ is used (continuous magenta curve). It should be pointed out that the $\alpha I^{\beta} + \gamma$ reduces to the mixed Poisson/white noise noise model when $\beta = 1$. There is no physical justification for using this function to describe the lower end of the intensity but the practical need of calculating the spatial resolution for the lower intensities somewhat rationalises this. The observant reader will notice that at an intensity of $I \approx 10^3$ the measured noise variance is $Var(I) \approx 10^6$. Recalling the definition of SNR one quickly finds that the SNR for images in that region will be around unity. Therefore, all tissue images with median tissue intensity less than 10^3 will not have a resolution and will be pure noise. Thus, the mysterious magenta curve will only be responsible for the resolution of images between the range of 10^3 and 3×10^3. Using the PDF derived in the previous section and integrating between $\ln(10^3)$ and $\ln(3 \times 10^3)$, one finds that roughly 58% of all median tissue intensities will be contained in the interval 10^3 and 3×10^3. Had this not been done, one would risk to underestimate the real resolution as the combined noise model underestimates the variance in that portion. The other 42% of images will have their resolution estimated with the aid of the familiar combined noise model. The b parameter in this case is approximately equal to 1.5×10^{-2} implying a $\max SNR \approx 8$. This is very different from the OrbiSIMS noise estimate, where the SNR was not limited. Last but not least there is a discontinuity between

the two models. The dashed cyan curve represents Equation 5.4; this discontinuity is there because the piecewise function used here is only an approximation. Understanding the real behaviour of the NLF and deriving a realistic noise model for Orbitrap DESI lies outside of the scope of this work.

Finally, the estimates of the two XevoToF DESI NLFs are shown in Figure 5-5 (e) and Figure 5-5 (f). These correspond to Lab B and Lab C respectively. Both of these are described well by the combined noise model. The a parameters are $a \approx 430$ for Lab B and $a \approx 310$ for Lab C. More interestingly, the measured b parameters are $b \approx 6 \times 10^{-3}$ for Lab B and $b \approx 1.8 \times 10^{-2}$ for lab C. This implies a $\max SNR \approx 12.8$ for Lab B and $\max SNR \approx 7.5$. Based on this information alone one may conclude that DESI Lab B would exhibit a better median spatial resolution than DESI Lab C as the median intensity (see Figure 5-3 (b)) and max SNR values are higher. However, the blurring parameters for both labs still need to be estimated – the reader is reminded that Lab B used a commercial DESI sprayer while Lab C used a prototype DEFFI sprayer. In the next figure the SNR estimates for different modalities is shown. Generally, it is really pleasing to report that at high intensities all three DESI set ups exhibit a quadratic variance as the same behaviour was reported in ESI previously[105]. Despite the fact that no appropriate noise model is provided here, it is also pleasing to report the fact that both Orbitrap setups exhibit the same behaviour at low intensities, as shown in Figure 5-5 (b) and Figure 5-5 (d).

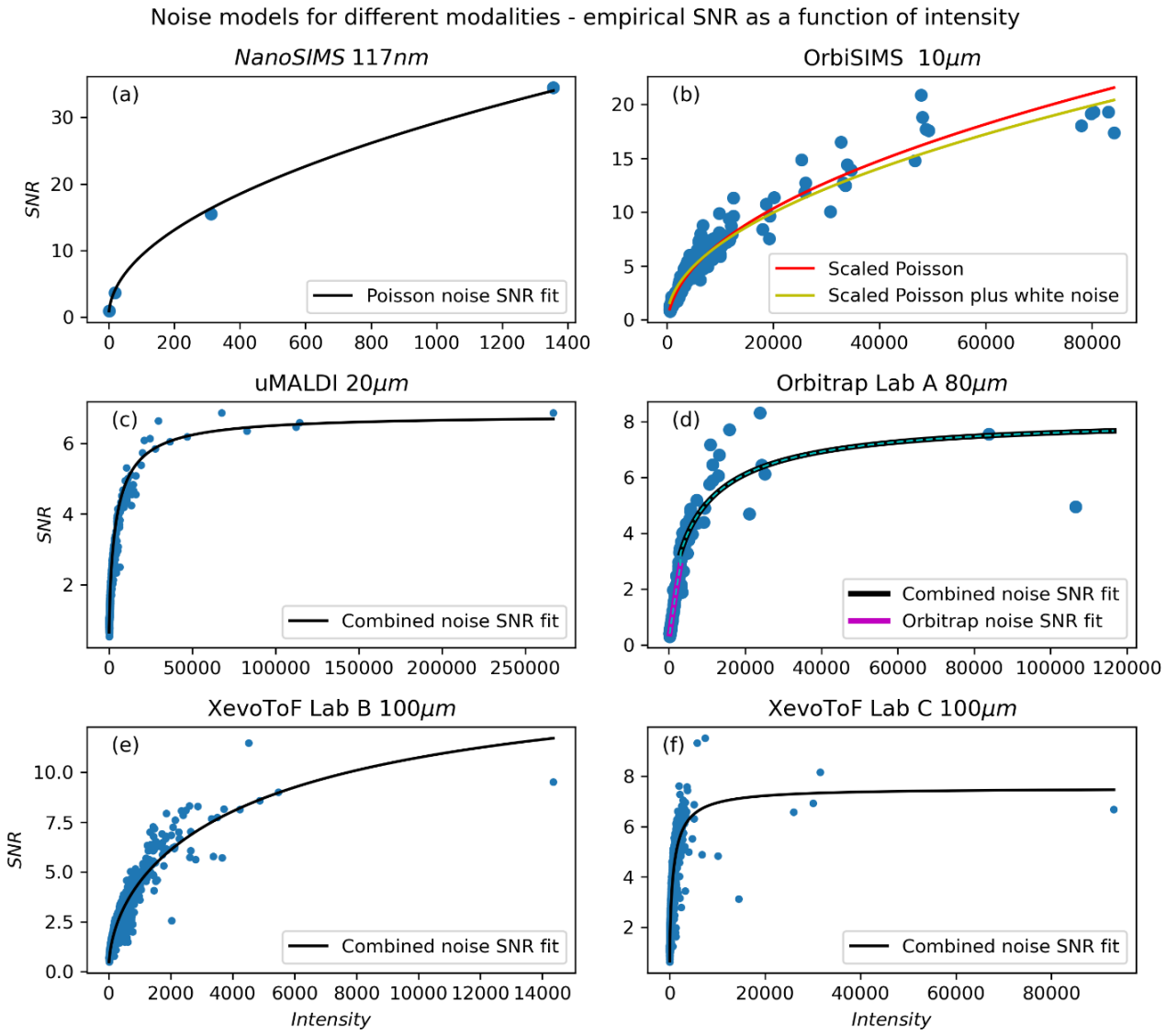


Figure 5-6 Local image SNR as a function of intensity measured across different modalities. The black/coloured curves are different noise models fitted to the data (a) – NanoSIMS. (b) – OrbiSIMS. (c) – uMALDI. (d) – Orbitrap DESI Lab A. (e) – XevoToF DESI Lab B. (f) – XevoToF DESI Lab C.

Much of the information shown in the figure above is the same as that in Figure 5-5 and the paragraphs that followed after. Therefore not much time will be spend explaining each of the panels in Figure 5-6. The purpose of this figure is to serve as a transition to what the main goal of the noise calibration step is. The algorithm used to obtain the noise model parameters for each of the modalities (detection of homogeneous blocks) only shows the *local* variance/SNR as a function of intensity (see Figure 5-4). Instead, one would wish to compute a global SNR number that is representative of the entire tissue region.

This could be achieved by plugging in the median tissue intensity in each of the noise models presented above. The purpose for doing this is of course to compute the median spatial resolution of a tissue image as a function of the

median (global) tissue SNR. The median tissue intensities were already calculated (see Figure 5-1, Figure 5-2 and Figure 5-3). Using the curves generated with the noise model parameters and plugging in the median tissue signal intensities one can estimate the global SNRs for each single ion image within each datacube. The results are presented in the following graph:

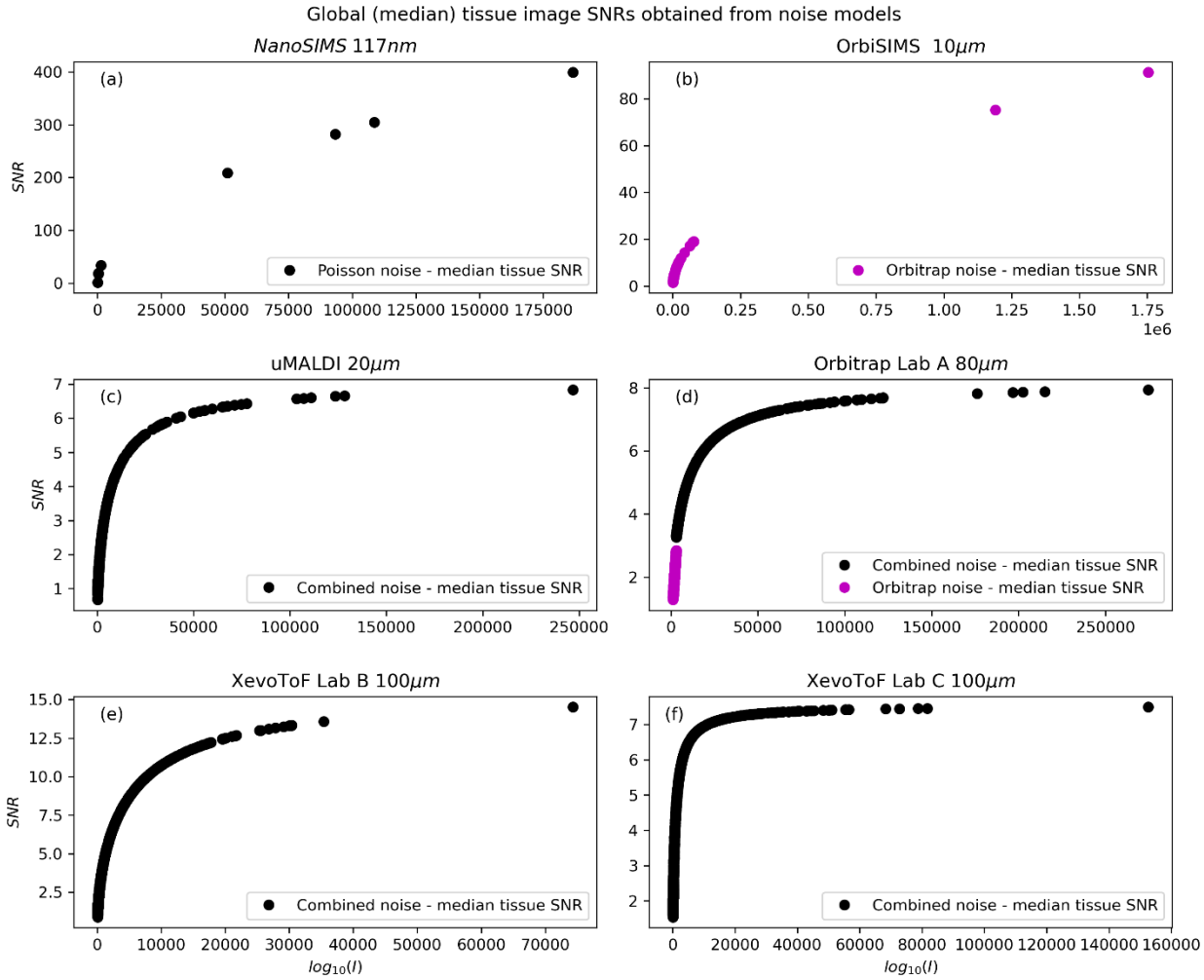


Figure 5-7 Global (median) image SNR as a function of intensity measured across different modalities. The black/coloured curves are different noise models fitted to the data (a) – NanoSIMS. (b) – OrbiSIMS. (c) – uMALDI. (d) – Orbitrap DESI Lab A. (e) – XevoToF DESI Lab B. (f) – XevoToF DESI Lab C.

As expected, the NanoSIMS modality, whose noise statistics are governed by the Poisson distribution, casts a shadow over the SNR estimates of all other modalities (Figure 5-7 (a)). The next highest SNR is achieved by OrbiSIMS (Figure 5-7 (b)). Despite the fact that OrbiSIMS has the highest median tissue signal intensity – roughly 1.75×10^6 – and that this intensity is an order of magnitude higher than the highest global intensity of the NanoSIMS datacube (roughly 1.75×10^5), OrbiSIMS still measures a lower SNR than NanoSIMS. The noise statistics of all other modalities are governed by the combined noise model (at the high intensity regime at least).

Therefore, their SNRs are limited at high intensities and are much lower than those of NanoSIMS and OrbiSIMS. The highest SNR among these datasets is measured in Figure 5-7 (e), which corresponds to DESI Lab B.

Finally, let us reflect on what the whole point of calibrating the different noise models and computing the global tissue image SNR is. If one were to meditate on Equation 3.24 and the symbols that appear therein, one would realise that spatial resolution can be computed as a function of SNR. Computing the global SNR for each tissue image allows us to then compute the global resolution distance of the various tissues images within a datacube. As the global (median) tissue SNR encapsulates the local SNR in both high intensity and low intensity regions of a tissue image, so does the global resolution distance encapsulate the local resolution of low and high intensity regions of a tissue image. Thus, the whole point of calibrating the noise models exhibited in different modalities is to measure spatial resolution using the resolution model (recovery method) outlined in Chapter 3. Thus, each of datapoints shown in Figure 5-7 will be plugged in Equation 3.24 in order to estimate the global (median) spatial resolution of different tissue images; the final goal has almost been reached. The other crucial parameter needed for doing this is the blurring parameter.

5.3.3 The blurring parameter

In order to estimate the blurring parameter Equation 3.16 is fit to the data. This is how Algorithm 1 estimates blur. However, it was shown in Chapter 3 that when not enough linescans are used and the edges are noisy, the blur estimates become unreliable. To deal with this the reduced chi squared statistic is used as a goodness of fit measure. There are several things that one should be aware of before one dives into this section. Only vertical or horizontal edges are considered. Edges that are tilted shall be ignored. This is because averaging over a tilted edge will exaggerate the blurring parameter. In principle, it is possible to rotate the tilted edge ROI by an appropriate amount so that edge becomes aligned. However, most image rotation algorithm employ an interpolation step and this would affect the measured SNR from Algorithm 1. This is not much of a problem, as a method that can estimate the noise statistics has been utlisied[158]. The interpolation step could however affect the ground truth value of the blurring parameter. More importantly, if a naturally different blur is exhibited in different directions, then this information would be lost. Suppose a given modality exhibits a larger natural blur in the x direction but one only has an edge in the y direction. One proceeds to compute the resolution distance and a number is obtained. One then acquires a different dataset with the same modality but this time only an edge oriented in the x direction is available. Since this modality was assumed to have a larger blurring parameter one would now estimate a larger resolution distance. Therefore, one would conclude that this modality has a worse resolution than itself. It is therefore imperative to select edges that are oriented in the same direction when comparing the resolution of different modalities; otherwise a systematic error may be introduced in our comparison. With this in mind only edges oriented in the x direction were selected for NanoSIMS, OrbiSIMS and uMALDI. The three DESI data sets did not exhibit such a step edge but had *somewhat* well-defined edge ROIs in the y direction. Therefore, one cannot compare the DESI data sets

with the other modalities but one can compare them between each other. For the purpose of symmetry, the DESI images were rotated by an appropriate amount so that the vertical edge ROIs appear horizontal. This was done for the ease of applying Algorithm 1 and rotations by multiples of 90° do not require an interpolation step.

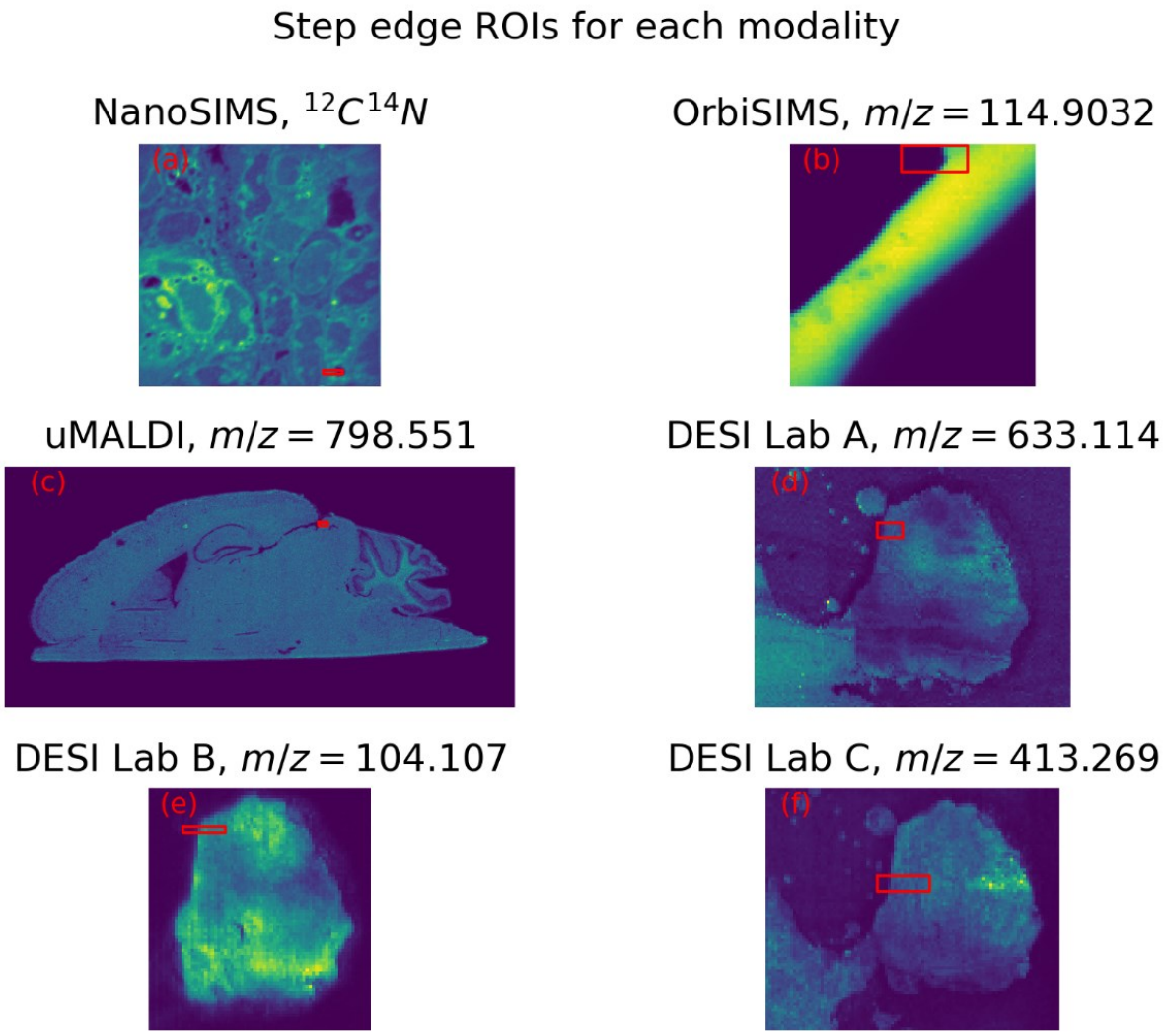


Figure 5-8. A high intensity single ion image from each of the modalities. The red square in each subplots represents the selected 'edge' ROI. (a) – NanoSIMS. (b) – OrbiSIMS. (c) – uMALDI. (d) – Orbitrap DESI Lab A. (e) – XevoToF DESI Lab B. (f) – XevoToF DESI Lab C.

The figure presented above shows a high intensity single ion image from each modality. It serves two purposes. The first one is to demonstrate how small the edge ROI is compared to the entire tissue image. Some of the images shown above are approximately 100×100 pixels; one might as well be trying to measure the spatial resolution of 1970s pixel art corrupted with severe amounts of noise. The datacube simulations of step edges in Chapter 3 had dimension of 129×60 pixels. Here there are 2×13 pixels available for the smallest ROI and 7×18 pixels for the largest one. Recall that Algorithm 2 fails to estimate resolution accurately when an insufficient number of

linescans are used and the noise is sever (combined noise); however, it still performed well when Poisson noise was used. Therefore, one may expect that it does a good job for NanoSIMS and OrbiSIMS but it will perform terribly for the other modalities. Of course it will fail as it was designed for a perfect step edge as input and not tissue imaging. The other rather unpleasant thing is the number of data points available in the x direction. For the 7×18 ROI there are only 9 data points available to fit an MTF… luckily, with the aid of the noise models combined with the median tissue intensity estimates (SNR term), the reduced chi-squared goodness of fit metric (blur) and Equation 3.24 (resolution model), one is be able to calculate spatial resolution without relying on Algorithm 2. It was mentioned that Figure 5-8 has two purposes. The second is to simply show some tissue images as then the MSI community may consider this work relevant. The ROIs shown here are quite small. The next figure remedies this and shows a zoomed in version of the red boxes.

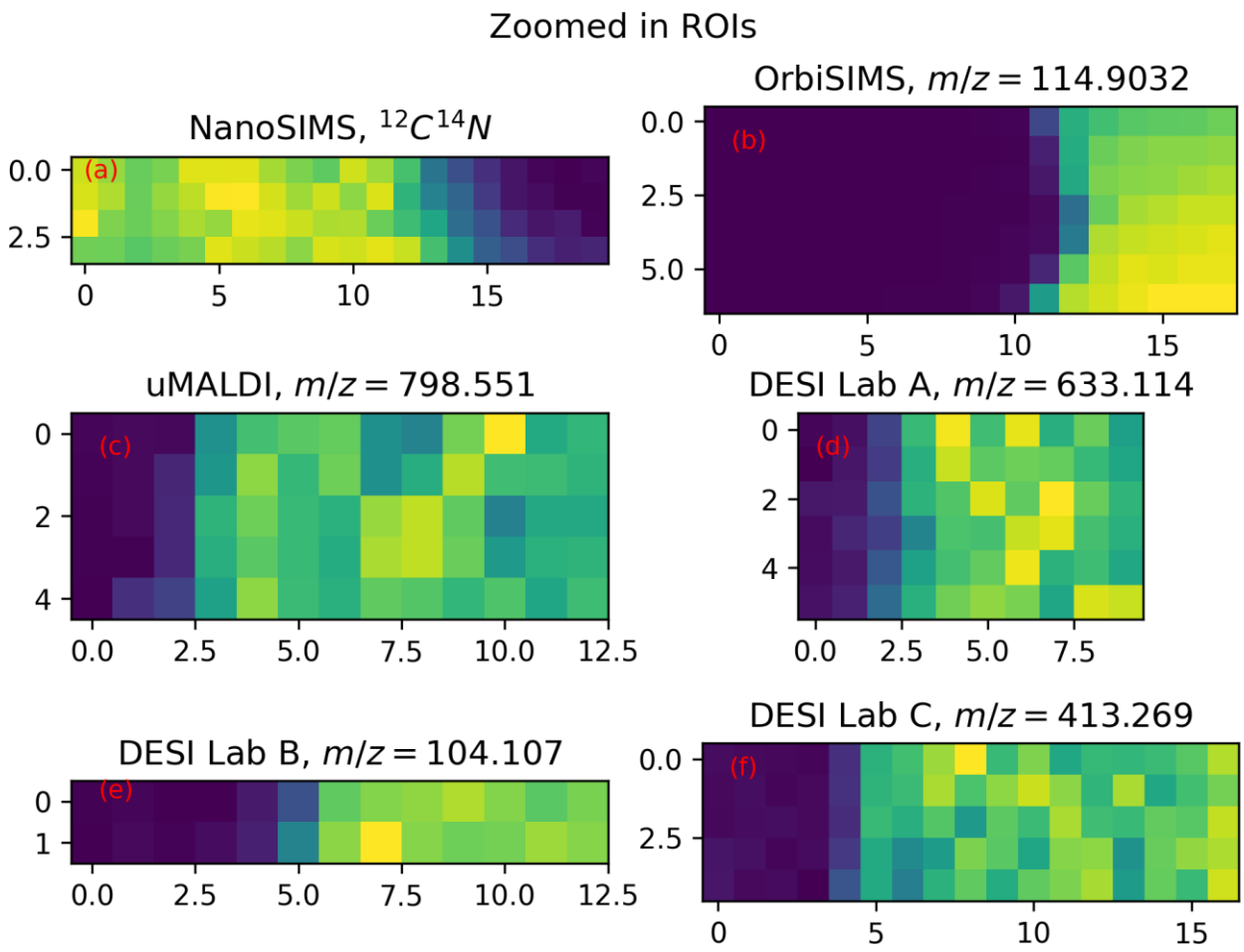


Figure 5-9. Zoomed in 'edge' ROIs. (a) – NanoSIMS. (b) – OrbiSIMS. (c) – uMALDI. (d) – Orbitrap DESI Lab A. (e) – XevoToF DESI Lab B. (f) – XevoToF DESI Lab C.

It is obvious that some of the ROIs are not pure step edges. Each ROI was *manually* selected with the assumptions behind Algorithm 1 and Algorithm 2 in mind – the tilt in the edge is minimised and no biological features should be present on the edge surface. In general, this is a really annoying thing to do but such is the natura of the data. Things become much more pleasant when the reduced chi-squared metric is invoked. To keep things simple the general workflow is explained by using the Orbitrap DESI Lab A dataset as an example. Then, the final estimates of the blurring parameter for each data set will be shown. The next graph shows three results from the reduced χ^2 statistic obtained from the Lab A datacube.

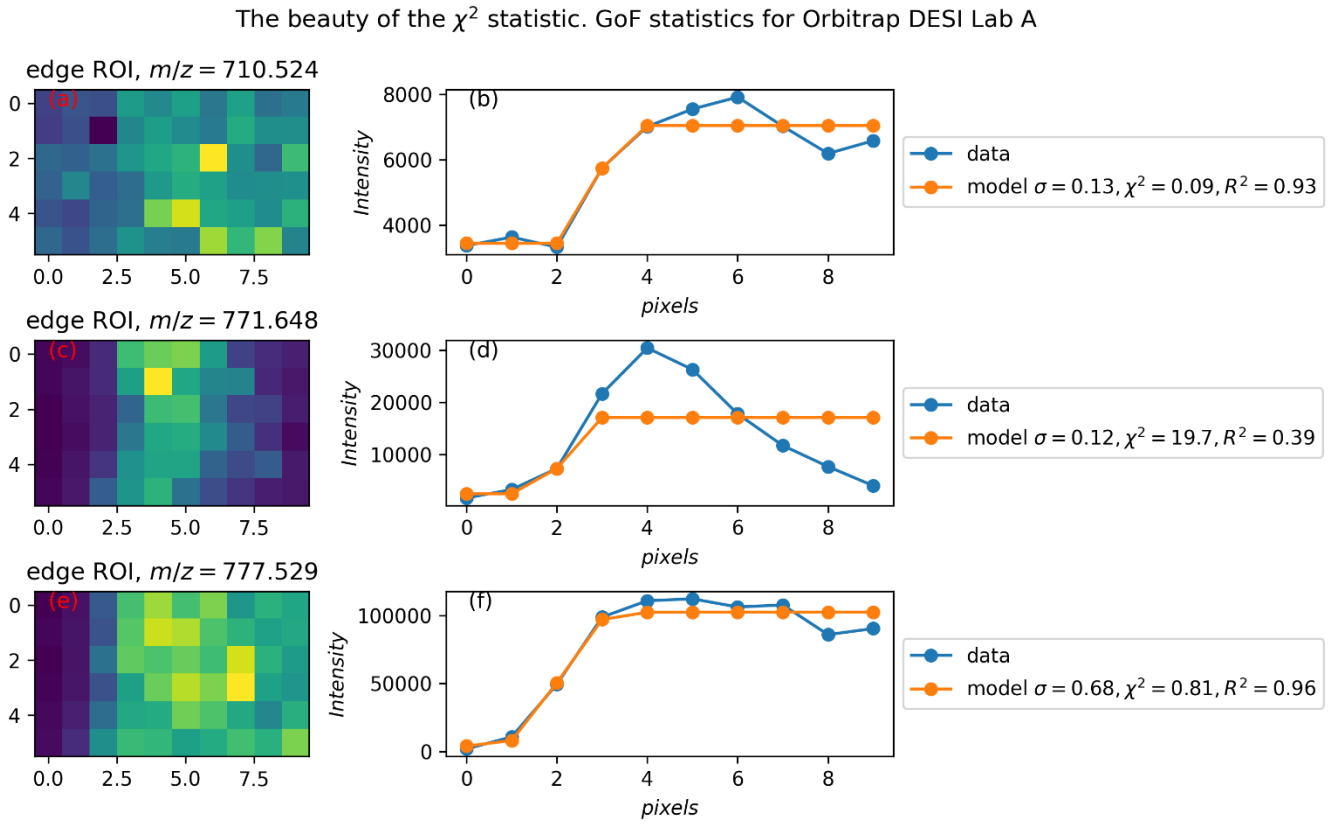


Figure 5-10. Performance of Algorithm 1 on three ROIs. Goodness of fit estimates for Orbitrap DESI Lab A. (a) – ROI 1 - overfitting to noise: reduced $\chi^2 \ll 1$. *(b) – ROI 2 - fit not capturing data:* $\text{reduced } \chi^2 \gg 1$. *(c) – ROI 3 - good fit: reduced* $\chi^2 \approx 1$.

An example of a overfitting to noise is shown in ROI 1, presented in Figure 5-10 (a) and Figure 5-10 (b). The panel outside shows that the measured blur is $\sigma = 0.13$ and $\chi^2 = 0.09$. This low blurring parameter will cause the MTF to be sharpened an the resolution distance will be overestimated. The R^2 metric is also shown; in this case the R^2 metric estimates this as a good fit and cannot detect the overfitting to noise. Next, ROI 2 is shown in Figure 5-10 (c) and Figure 5-10 (d) an example of the model not capturing the data well. This is because the presence of a biological feature in Figure 5-10 (c). The averaged edge profile picks this up as evident in Figure 5-10 (d). The measured blurring parameter has a value of $\sigma = 0.12$ with $\chi^2 = 19.7$; this would also sharpen the MTF. It can be seen that this is relatively high intensity signal. The presence of the biological feature will be interpreted as noise and the resolution frequency will be pushed down due to a lower SNR. The R^2 metric detects that this is a not good fit indicated by the fact that only 39% of variance is explained. Finally, an example of a good edge fit is shown in Figure 5-10 (e) and Figure 5-10 (f), ROI 3. The ROI seems to approximate an edge at least visually. The performance of Algorithm 1 on measuring the blurring parameter is supported by a $\chi^2 = 0.81$. The measured blurring parameter is $\sigma = 0.68$. This is around six times higher than the overfitted to noise case (Figure 5-10 (a) and (b)) and the upset due to biological feature case (Figure 5-10 (c) and (d)). Therefore, one may expect that the

resolution estimates acquired with this blurring parameter to be closer to the truth than the other two cases. Next, the performance of Algorithm 2 is shown on the same ROIs.

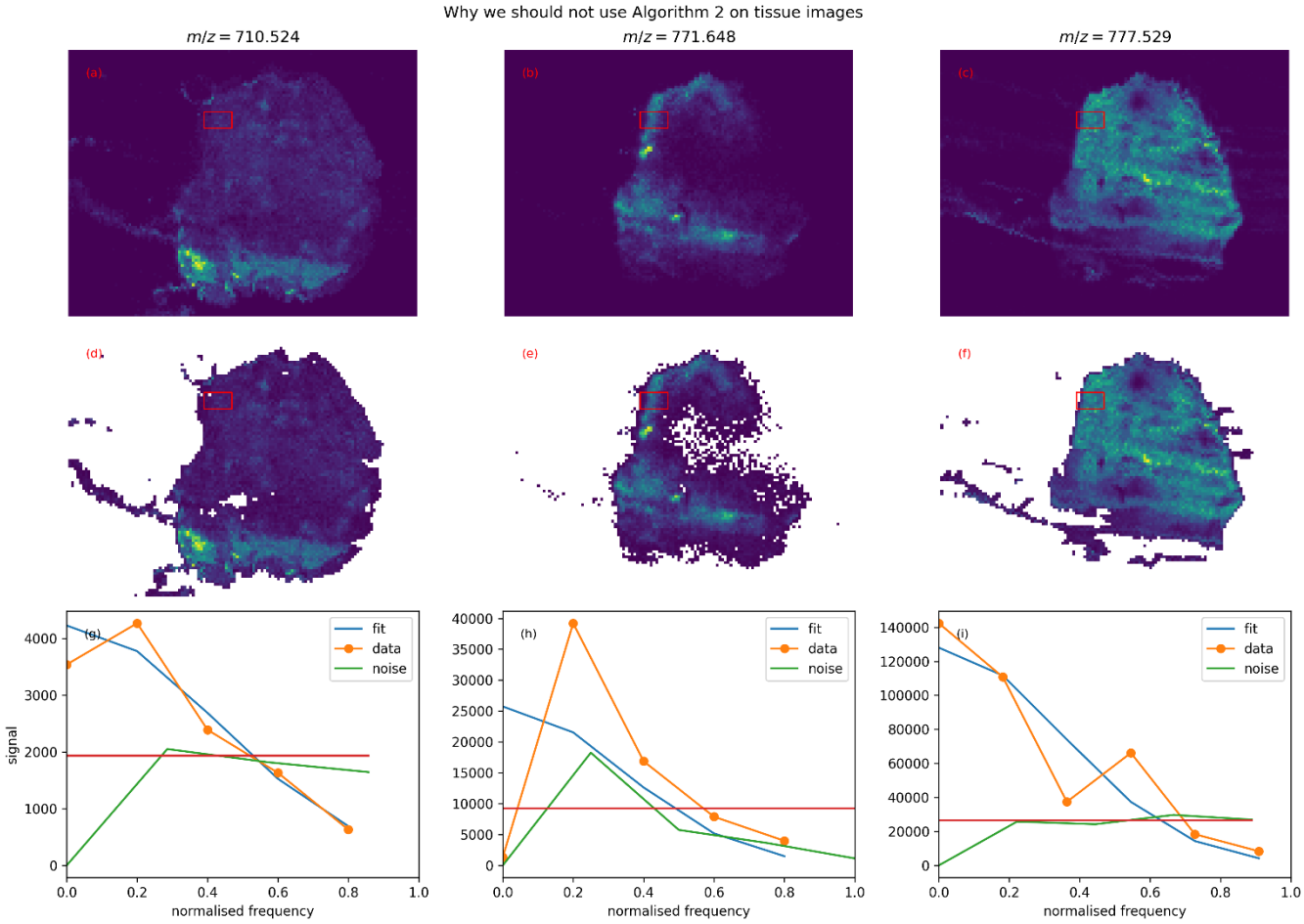


Figure 5-11 Performance of Algorithm 2 on ROI 1, ROI 2 and ROI 3. (a), (b), (c) – tissue images; red boxes are the edge ROI. (d), (e), (f) – masked tissue images. (g), (h), (i) – the MTF/NSD intersections computed with Algorithm 2.

ROI 1, ROI 2 and ROI 3 represent the same spatial location but were acquired from different images. The failure of Algorithm 1 was quantified with the aid of the reduced chi-squared statistic for two of those ROIs. Let us now investigate the failure of Algorithm 2 for these ROIs and see if it picks up the right resolution for ROI 3 which had $\chi^2 \approx 1$. To do this the resolution model (Equation 3.16) with the calibrated noise parameters is used. The subplots in Figure 5-11 (a), (b) and (c) show the different tissue signals used to generate ROI 1, ROI 2 and ROI 3 respectively; the red box is the actual ROI. One can see what the zoomed in version looks like in Figure 5-10 (a), (c) and (e); these are important and will be discussed shortly. Next, the tissue masks generated via watershed segmentation are displayed in subplots Figure 5-11 (d), (e) and (f). Finally, the outputs of Algorithm 2 for each of the edge ROIs are shown in the subplots Figure 5-11 (g), (h) and (i). Firstly, notice that the edge ROI contains 10 data points in the x direction. As a consequence the MTF has only 5 data points. This is not ideal. Secondly, the sharpening of the MTF

was discussed as the measured blurring parameter was $\sigma = 0.13$. Therefore the root NSD/2 average (red line) meets the MTF (blue line) at a higher frequency. The resolution frequency here is about $f_c = 0.6$, which corresponds to a resolution distance of $d \approx 330\mu m$. The measured SNR is around 3 and the measured blurring parameter is $\sigma = 0.13$, which was also severely overfit to noise and is far away from the ground truth value of the real blurring parameter. If one uses the resolution model (Equation 3.24) with the calibrated noise parameters (see Figure 5-5, Figure 5-6 and Figure 5-7 from previous section) and the value of $\sigma = 0.13$, the computed resolution frequency is $f_c = 0.59$, which is in a good agreement with the experimental measurement. The problem here is that the experimental measurement has been plagued with an artificially sharpened MTF; the reduced chi-squared of the blurring parameter is $\ll 1$ indicating that $\sigma = 0.13$ is not a good estimate. However, the blurring parameter from ROI 3 had a value of $\sigma \approx 0.7$ and a reduced chi-squared statistic of $\chi_v^2 \approx 1$. Assuming a global blur across all single ion images and using that a blurring parameter value of $\sigma \approx 0.7$ is more reliable due to the reduced chi-squared statistic, then one finds that the estimated resolution from the resolution model is $f_c \approx 0.5$, which corresponds to a distance of $d \approx 400\ \mu m$. While a difference of $70\mu m$ may not seem like much, in the previous section it was estimated that around 58% of images have a median intensity between 1000 and 2000. If the blurring parameters is not estimated accurately due to the noise levels and insufficient linescans, then more than half of our resolution estimates will be underestimated. Thus, relying on the recovery method (which was already proven to recover the ground truth resolution in Chapter 3) is the right approach here. This is why one also needs to go through a noise calibration step.

The MTF in Figure 5-11 (h) shows what happens when a biological feature is present in the edge ROI (ROI 2). Note that the data (orange connected points) and the scaled root NSD (green line) exhibit a peak at roughly the same frequency. This is because some of the signal has been interpreted as noise. As a consequence the resolution frequency here is also not estimated correctly. Going back to the zoomed in ROIs in Figure 5-10 (c) and (d) one may see how the average edge profile is affected by the presence of a biological feature. This feature is clearly visible in the red rectangle ROI in Figure 5-11 (e). Notice that the signal intensity is around an order of magnitude higher from that seen in ROI 1 and yet the measured SNR is still around 3. The experimentally measured resolution here is $f_c \approx 0.4$, which is lower than that for ROI 1, despite the fact that ROI 1 has a signal intensity that is an order of magnitude lower. Computing the resolution frequencies with the resolution model (with the calibrated noise parameters and a blurring parameter of $\sigma \approx 0.7$) one finds that $f_c = 0.67$. This is higher than the resolution frequency for ROI 1, as it should be given that ROI 1 sits at a much lower intensity.

Finally, ROI 3, which had $\chi_v^2 \approx 1$, is discussed. The experimentally measured resolution frequency is $f_c = 0.65$. This is incredibly close to the one obtained from the artificially sharpened MTF (ROI 1, Figure 5-11 (g)). ROI 1 has an measured edge surface intensity that is two orders of magnitude lower than the surface intensity of ROI 3. And yet the measured resolution for ROI 1 with Algorithm 2 was $f_c \approx 0.6$, while ROI 1 is two orders of magnitude

lower than ROI 3. However, the recovery method predicts a lower resolution frequency of $f_c \approx 0.5$. The discrepancy between Algorithm 2 and the recovery method are summarised in the following table.

	Intensity	Algorithm 2	Recovery method
ROI 1	2000	$f_c \approx 0.6$	$f_c = 0.5$
ROI 2	10000	$f_c \approx 0.4$	$f_c = 0.67$
ROI 3	100000	$f_c \approx 0.65$	$f_c = 0.7$

Table 5-2. A quick comparison between the performance of Algorithm 2 and the recovery method with the right blurring parameter.

It is clear that the recovery method performs much better than the Algorithm 2. This is because it relies on an accurate estimate of the noise statistics, which was achieved using a beautiful algorithm[158], and an accurate estimate of the blurring parameter, which was also achieved with the aid of the reduced chi-squared statistic. Unfortunately, Algorithm 2 does not perform well here precisely because the scaled root NSD and the Fourier space blurring parameter are not estimated well. This was a theme in Chapter 3, when it was shown what happens in the case of combined noise and reduced linescans and in Chapter 4 where one could not estimate the resolution of a portion of images due to the fractional error exceeding a pre-set threshold. The same problem is manifesting here again. As for the subplots in the middle row of Figure 5-11 ((d), (e), (f)), these show the masked single ion tissue images. It is obvious that Algorithm 2 measures the resolution locally – a quick glance at Figure 5-11 (a) reveals that the resolution estimated at ROI 1 will be not representative of the global resolution as the ROI captures a low intensity region and there is a high intensity region towards the bottom of the tissue region. Similar information can be retrieved from Figure 5-11 (e) and (f). Thus, the recovery method will outperform Algorithm 2 in this respect as well. The final ingredient needed for the application of the recovery method is imposing a global MTF, for which one needs an appropriate blurring parameter estimate. The following figure proposes a method for doing this.

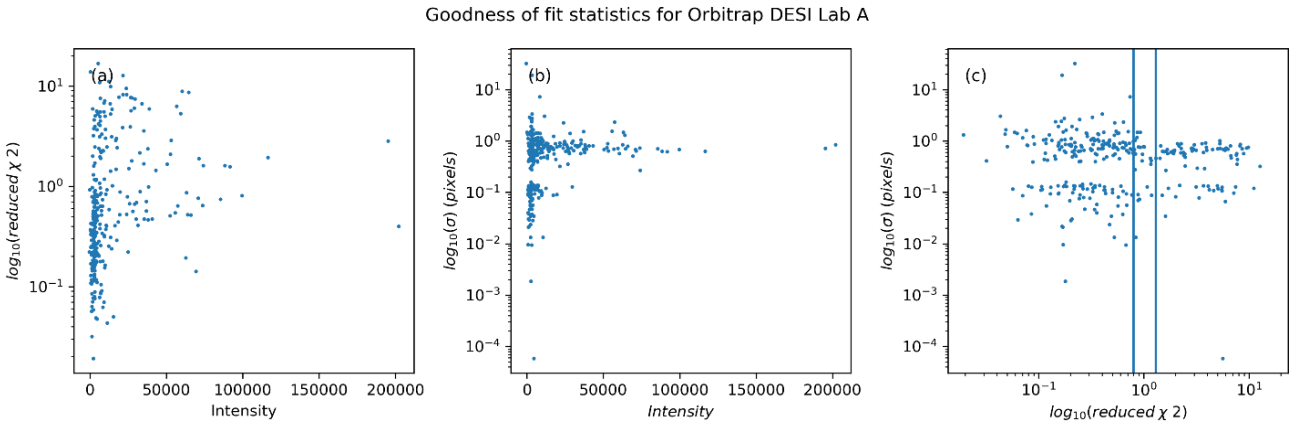


Figure 5-12 (a) – log base 10 reduced chi squared plotted against intensity. (b) – log base 10 blurring parameter plotted against intensity. (c) – log base 10 blurring parameter plotted against log base 10 the reduced chi squared statistic.

Figure 5-12 (a) shows that as the intensity is lowered the reduced chi-squared either overfits the data due to noise ($\chi_\nu^2 \ll 1$) or does not capture the data well due to the interference of biological features ($\chi_\nu^2 \gg 1$). The latter also happens at moderately high intensities. Figure 5-12 (b) shows the estimated blurring parameters as a function of intensity. It can be seen that at lower intensities the blurring parameter is severely underestimated due to model overfitting to noise. These will drag the resolution measured by Algorithm 2 down (see Chapter 3.4). There are also some blur estimates that go up to almost 30 pixels. These are obviously poor fits. Finally, Figure 5-12 (c) shows the thresholding method used to selected an appropriate value for the globally imposed MTF. The two vertical blue lines indicate $\chi_\nu^2 = 0.8$ and $\chi_\nu^2 = 1.2$. All blurring parameters within this window were selected for the purpose of measuring the spatial resolution of this particular datacube. The next figure shows the result obtained after repeating this step for the other five datacubes.

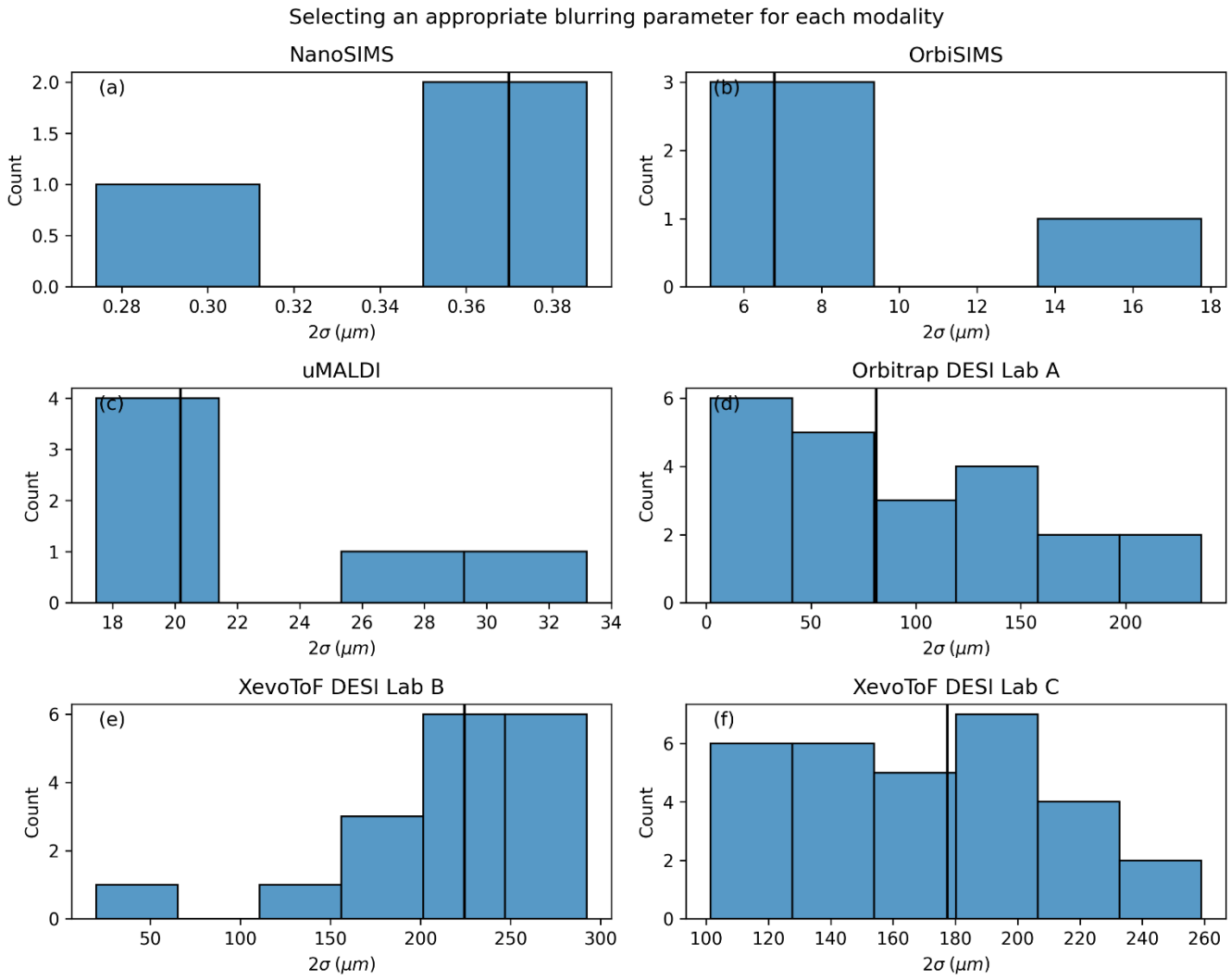


Figure 5-13. The distribution of blurring parameters acquired from different modalities after thresholding the reduced chi squared values. Median vertical line is the median. (a) – Nano SIMS. (b) – OrbiSIMS. (c) – uMALDI. (d) – Orbitrap DESI Lab A. (e) – XevoToF DESI Lab B. (f) – XevoToF DESI Lab C.

It should be mentioned that slightly different thresholding limits were used for each dataset. Very pleasingly, the NanoSIMS blurring parameter has a median of around $370nm$; while it is difficult to calculate the probe size the NanoSIMS manual suggests that this value is in the right range[159]. Of course, quantifying this rigorously remains outside the scope of this work. As for OrbiSIMS, the thresholded reduced chi squared values suggest a median blurring parameter of 7 μm. If the material removal was weak, then this could be used as an estimate of the beam size. Then, uMALDI, Orbitrap DESI Lab A, and XevoToF DESI Lab C (Figure 5-13 (b), (c), (d) and (f)) appear to exhibit a median blurring parameter smaller than twice the pixel size. This indicates that either strong material removal was used (certainly the case for uMALDI) or that the probe size was smaller or around the size than the pixel spacing distance. Finally, the blurring parameter of DESI XevoToF Lab B shows a significant blur. One should bear in mind that in the case of the DESI comparison, this is the blurring parameter in the y direction; it would be

interesting to see how the three instruments perform in the x direction. Sadly, the nature of the data does not allow for this comparison.

5.3.4 Spatial resolution

After calibrating the noise models of the different modalities, calculating the median tissue SNRs and imposing a global blurring parameter on each image one may finally use Equation 3.24 to calculate the spatial resolution as a function of intensity for each dataset. The results are displayed in the following figure.

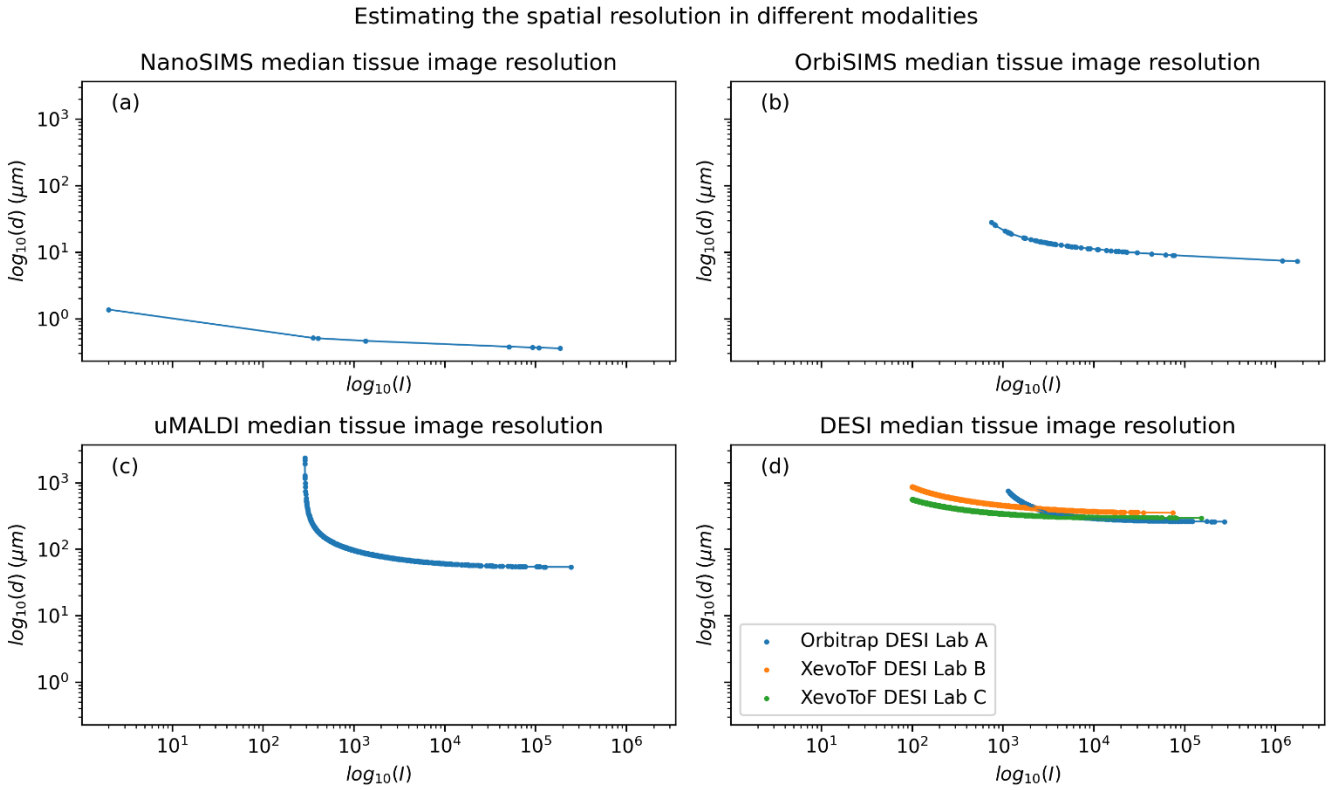


Figure 5-14. Resolution as a function of intensity for different modalities. (a) – NanoSIMS. (b) – OrbiSIMS. (c) – uMALDI. (d) – DESI Lab A, DESI Lab B and DESI Lab C.

The median tissue resolution is represented by a dot in each of the scatter plots; the dots have been connected by lines to indicate to remind the reader that these have been obtained from Equation 3.24. It is pleasing to observe the results for NanoSIMS shown in Figure 5-14 (a). At high intensities resolution is limited by the blurring parameter. This is because Poisson noise is negligible at high intensities. This was shown in the simulations in Chapter 3 and it is fantastic to see an agreement between theory and experiment. At lower intensities resolution loss due to noise occurs as shown in previous SIMS resolution studies[69]. The resolution of the OrbiSIMS datacube is shown in Figure 5-14 (b). The other three datasets, which exhibited a quadratic variance (at high intensities at least) begin to lose resolution at a faster rate as the intensity decreases. Those are uMALDI, shown in Figure 5-14 (c), and the three

DESI datasets shown in Figure 5-14 (d). This behaviour was also predicted in the simulations done in Chapter 3. As for the discontinuity in DESI Lab A, this comes from the use of a piecewise function. However, had this not been done, the variance would have been underestimated and a better resolution would be measured for images in that range. The resolution curve for DESI Lab A vanishes at around $I = 10^3$ as expected from the noise calibration curve (this is where SNR is less than unity for this data set. It is worth mentioning that while DESI Lab B exhibited the highest SNR out of the three DESI datasets it also exhibited a higher blurring parameter. Therefore, the resolution curve for this dataset is shifted upwards. Let us now consider the resolution distributions for each intensity.

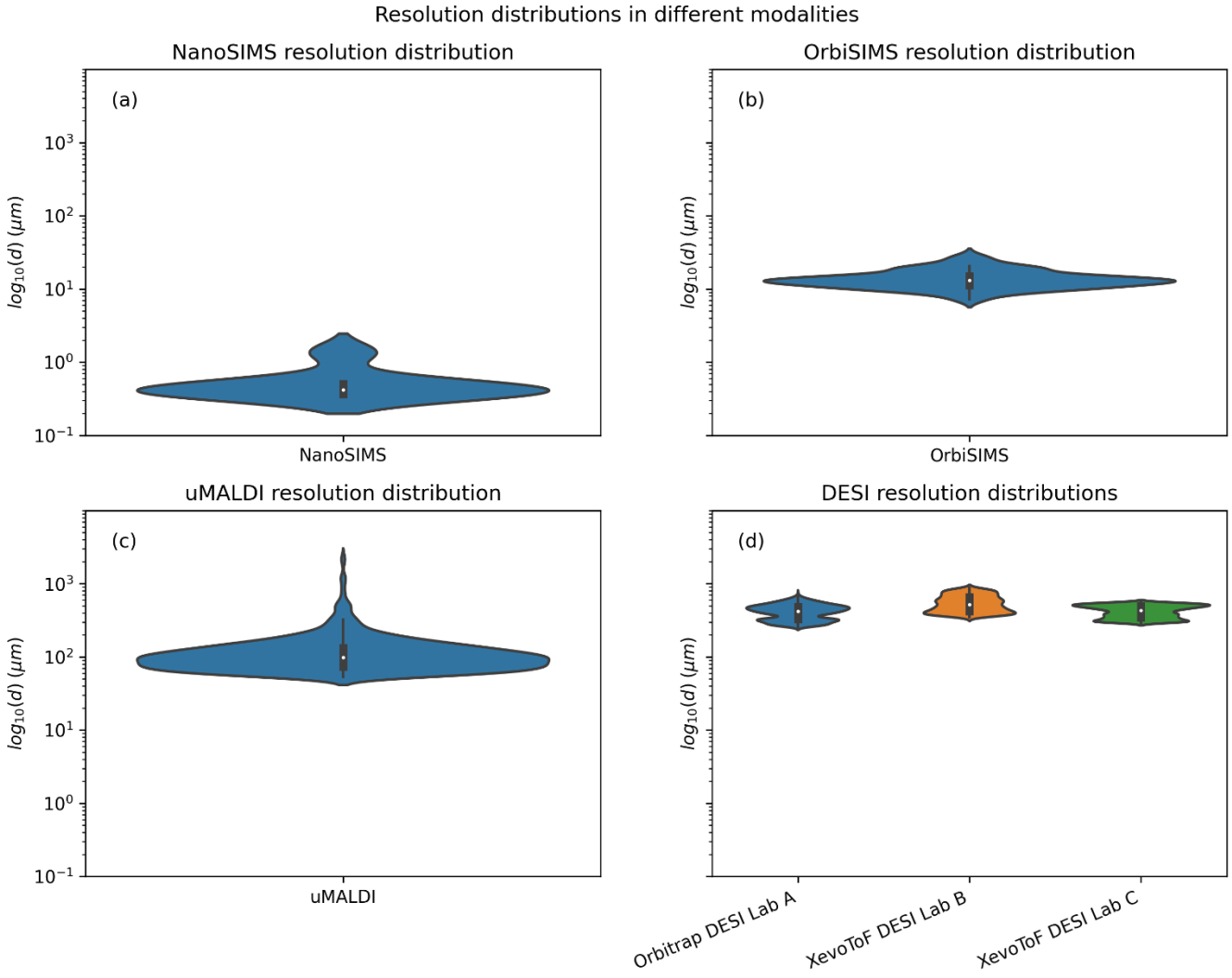


Figure 5-15. Violin plots depicting the resolution distributions of the different modalities. (a) – NanoSIMS. (b) – OrbiSIMS. (c) – uMALDI. (d) – the three DESIs.

As per usual, the resolution distributions are plotted on a log scale; the white dot in the middle is median. The following table summarizes the median resolution distributions for each modality. The violin plots for the median

tissue resolution distributions of NanoSIMS and uMALDI, shown in Figure 5-15 (a) and (c) respectively, indicate that the majority of tissue signals have their median resolution concentrated around $400\,nm$ and $100\,\mu m$ respectively; both exhibit a tail indicating that the datasets contain a portion of really low resolution images. This is not the case for OrbiSIMS (Figure 5-15 (b)), which exhibits no apparent tail. As for the DESI estimates, shown in Figure 5-15 (d), the bimodal appearance in DESI Lab A is due to the discontinuity in the SNR function, although it is completely possible that the bimodal natural is real. The bimodal distribution of median tissue resolutons in DESI Lab C however, appears to be a genuine one. In contrast to NanoSIMS, OrbiSIMS and uMALDI, both DESI Lab A and DESI Lab C show that the majority of the tissue images have a higher resolution distance (lower resolution). DESI Lab B however has its distribution waist at the lower distances (better resolution). The median resolutions for each dataset are presented in the following table.

Modality	Pixel spacing	Median resolution	Blurring parameter $(86-14\%)$ criterion
NanoSIMS	$117nm$	$420\ nm$	$370\ nm$
OrbiSIMS	$3\mu m$	$13\ \mu m$	$7\ \mu m$
uMALDI	$20\mu m$	$100\ \mu m$	$20\ \mu m$
Orbitrap DESI Lab A	$80\mu m$	$420\ \mu m$	$80\ \mu m$
XevoToF DESI Lab B	$100\ \mu m$	$520\ \mu m$	$220\ \mu m$
XevoToF DESI Lab C	$100\mu m$	$430\ \mu m$	$180\ \mu m$

Table 5-3. Median tissue image spatial resolution from different modalities.

High intensity NanoSIMS and OrbiSIMS images have the same resolution as the blurring parameter listed in the table above. If weak material removal is employed during the process of image acquisition, then this may be equated to the beam size.

For the sake of fairness, it would be interesting to compare the median tissue resolution for the three DESI labs at intensities $I > 10^3$. This is because Lab A loses its spatial resolution at intensities below that, while Lab B and Lab C can keep resolving features. The measured median resolution then become $\approx 400, 310\ \mu m$ for Lab B and C respectively. Despite the fact that Lab A used a lower pixel spacing its spatial resolution is matched by Lab B and outperformed by Lab C for images with median tissue signal $I > 10^3$. In the beginning of this Chapter the construction of a resolution ruler was mentioned. Let us now conclude this Chapter with such a figure, which demonstrates the spread of resolutions that different modalities exhibit.

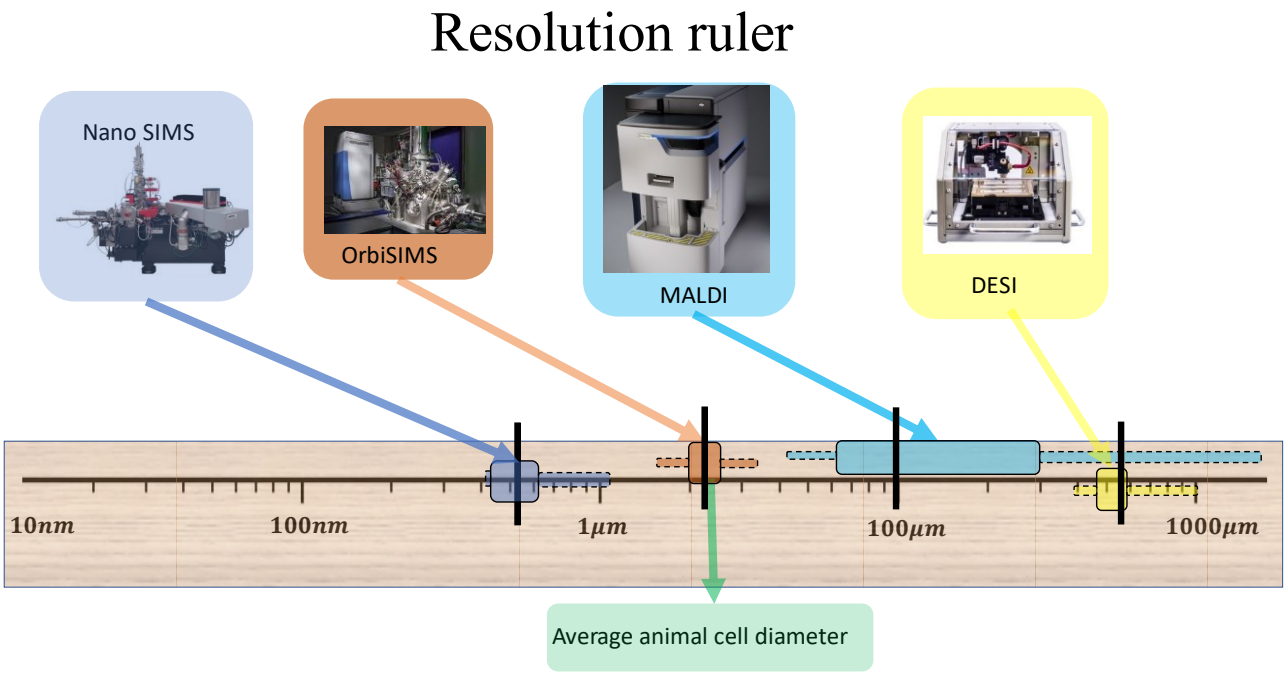


Figure 5-16. The MSI resolution ruler.

The resolution estimates are presented on a logarithmic ruler using an improvised box-and-whisker plot; the statistics for the box plots were derived from the previous data depicted in the previous two graphs. The bulky region in the middle of each distribution represents the median tissue image resolution between the first and third quartile. The black vertical line crossing each distribution vertically is the second quartile (median). The small dashed rectangular regions are the whiskers and in this case they represent the smallest and greatest resolutions respectively. The average animal cell diameter is indicated with a green arrow on the resolution ruler. It is obvious that NanoSIMS is the only modality capable of single cell imaging. OrbiSIMS is right at the border. MALDI and DESI have a far way to go. In principle, this kind of study can be very informative in the optimisation of large scale biological studies. The following table is provided as a proof of concept.

Cell feature	Typical size (nm)	Can NanoSIMS resolve it?
Ribosomes	≈ 30	No
Golgi Apparatus	$\approx 500 - 5000$	Yes
Mitochondria	$\approx 500 - 1000$	Yes

Table 5-4. A table showing the ability of NanoSIMS to resolve different cell organelles.

The typical size of several different cellular organelles are listed in the table above. Using the median NanoSIMS resolution one can ask whether or not certain features can be expected to be resolved. Things like ribosomes remain too small for NanoSIMS. However, it is completely possible to image the Golgi apparatus and mitochondria according to our resolution estimates. Such a table could be constructed for all kinds of different tissues, depending

on the study that is being performed. Unfortunately, the size of possible tissue features can vary depending on the biological specimen (age, sex, genetic factors), the nature of the section (sagittal, coronal, transversal) and other parameters. Thus, this thesis will not provide any tissue features and their sizes and shall remain content with the proof of concept table shown above.

5.4 Conclusions

Estimating the spatial resolution of tissue images is a challenging task. The heterogeneous nature of tissue images is what makes them valuable in biological studies but it is also makes it difficult to estimate the spatial resolution. To deal with the fact that a tissue may exhibit low and high intensity regions, the median intensity of the watershed segmented tissue only region was calculated. The estimates of the noise statistics made it possible to compute the global tissue SNR, taking into account the low and high intensity regions. This then meant that the calculated resolution distance for each tissue image could be considered a good representative of the resolution of the entire tissue image. As a comparison, Algorithm 2 would only measure the local spatial resolution. While using a global tissue image SNR is an advantage, the disadvantage here is that a global MTF was imposed. Nevertheless, Algorithm 1 and Algorithm 2 would still struggle to recover the ground truth blur when a limited number of linescans are available. Therefore, the individual blurring parameters will still not be estimated. Future work may involve providing a confidence interval for the resolution estimates acquired by the recovery method. Needles to say, the current best methods for estimating spatial resolution have been outperformed again – it is impossible to apply those to a tissue imaging data set[69,137]. Even it were possible to apply those somehow one of them would only accurately estimate the resolution capabilities of the NanoSIMS data set as it restricts resolution based on Poisson noise[69]. The other one would not perform well on any of the datacubes as it assumes flicker noise[137].

The final paragraph of this chapter is directed at anyone who wishes to measure the spatial resolution of a tissue imaging data set. Whoever may be interested in achieving this has to make sure that they do not misuse Algorithm 2. Algorithm 2 was designed for a step edge image with many linescans available and a homogeneous edge surface. If a tissue imaging dataset that satisfies these conditions is available then Algorithm 2 may be used. However, if this is not the case, the steps outlined in this Chapter should be followed by anyone interested in estimating the spatial resolution of a tissue imaging dataset. The first step is to obtain a median tissue intensity with a watershed segmentation algorithm. The second step involves calibrating the noise model. The third step requires the median tissue SNR to be computed. This can be done by combining the median tissue intensity (acquired in step one) with the calibrated noise model (acquired in step two). The final step requires a punctual estimation of the blurring parameter. This must be backed by some kind of goodness of fit statistic. Whoever attempts to do this calculation should avoid tilted edges; if no other option is available rotation should be done without interpolating the rotated image. The estimated blurring parameters should then be filtered based on the goodness of fit statistic. Finally, use

the estimated blurring parameter in combination with the median tissue SNR and with the aid of Equation 3.24 compute the resolution distance. Good luck and have fun!

Chapter 6 Conclusions and future work

6.1 Summary

In this thesis an image formation model was described for the purpose of measuring spatial resolution. Spatial resolution itself was defined as the smallest distance between two features that belong to an object such that features can be distinguished in an image of the object. This distance is limited by two main factors: blur and noise. A brief summary of this thesis now follows. The blur part was covered by the image formation model, which was introduced in Chapter 2. In fact, the image formation model allowed us to describe why the current best practice used to measure spatial resolution (86-14% criterion) works well in some modalities but fails in other modalities. This discrepancy was explained by the rate of material consumption. When material consumption is weak blur is maximised. The opposite happens in the case of weak material consumption. The other limiting factor to spatial resolution is noise. Noise was thoroughly investigated and two different noise models were provided. The first noise model is Poisson noise, which is expected to arise from the detector due to its inability to count particles without an uncertainty. The second noise model was a combination of the Poisson noise model and a term that took into account the fluctuations of the peak amplitudes. Such fluctuations can arise due to many different factors. In MALDI this most likely happens because of the fluctuations in crater sizes, which themselves can be caused in fluctuations of the laser beam energy. In DESI this can happen due to fluctuations in the primary droplets inducing variations in the emission of secondary droplets. Various other parameters can be hypothesised to lead to fluctuations in the peak amplitudes. This was the primary goal of Chapter 2, where digitisation was also explained and the Sampling theorem was introduced. A special emphasis on the fact that pixels are not squares was made and the smallest resolvable distance of two pixels was derived. The oversampling and undersampling clash of terminology was also explained and an example of the dangers that it can cause was shown. A union of the noise models and the image formation model was then presented in Chapter 3. Based on this, a new method for measuring spatial resolution was proposed. Then, the performance of Algorithm 2 and the recovery method was tested on edge data sets prepared with the image formation model and corrupted with the two noise models using numerical simulations. The performance of those was tested against the ground truth resolution, which was computed with a resolution model. It was shown that Algorithm 2 does not perform well when the noise is strong and a small number of linescans. This was particularly important for Chapter 5. Then, in Chapter 4 the methods for measuring spatial resolution were tested on a real imaging data set. The resolution of a commercially available MSI set up was investigated across a range of pixel sizes and an optimal pixel spacing was found based on these parameters. More importantly, Chapter 4 allowed us to experimentally verify that the combined noise exists; to the best of the author's knowledge similar behaviour has only been reported twice before[105,106]. One study clearly demonstrated this behaviour[105] but did not consider the physical origin of it. The other study admitted that a Gamma distribution, which exhibits a quadratic variance, could model the data better[106]. In Chapter 5 some applications for tissue imaging were shown. A methodology for dealing

with tissue images was provided. This involved using the recovery method, which was shown to outperform Algorithm 2 when not many linescans are available in Chapter 3 and Chapter 4. The recovery method also has the advantage of calculating the global spatial resolution of a tissue image, while Algorithm 2 would only be able to calculate the local spatial resolution. This of course is because Algorithm 2 was designed for an image of a step edge and not a highly heterogeneous tissue image. To use the recovery method the median tissue intensities were calculated for each modality. Then, the noise models for those modalities are calibrated and the median tissue SNRs can be predicted. Finally, a blurring parameter is estimated based on a goodness of fit threshold. Then, the resolution of those modalities was finally calculated. Despite the efforts made in this work, it will probably take a lot of time for the MSI community to get rid of the thought forms that plague the concepts related to spatial resolution. Those include referring to the pixel size as spatial resolution[110,111,120–124,112–119], thinking that pixels are squares, calling undersampled imagery oversampled and incorrectly assuming that Poisson noise is the only type of noise that exists[108,109].

6.2 Future work

6.2.1 Image formation model – ion flux generation

The image formation model presented here is only a toy model used to explain how to measure spatial resolution. It is a qualitative model but has the potential to become a quantitative one, at least in simple systems. Extending it to a quantitative model would be very difficult in tissue imaging experiments and while it is certainly a possibility there are currently no obvious routes for doing this yet. At the very least the MSI community needs to agree on a well-established ionisation mechanism for each of its modalities. The image formation model assumes thermal desorption as a primary mechanism. While this has been shown experimentally to be the case in MALDI (see Chapter 1), at higher laser energies the primary material removal mechanism is a mixture of desorption and ablation. It would therefore be nice to be able to incorporate ablation into the picture. While the flow of ions from a surface induced by an analytical beam (dubbed as ion flux in Chapter 2) can be considered an universal commonality between all MSI modalities, each modality can exhibit a different form of ion flux. It is interesting to think about DESI and how an image formation model can be further improved to pick on some of the features that are characteristic to DESI. Those are namely washing effects and analyte relocalisation*.

* Analyte relocalisation can also occur in MALDI during a ‘wet’ matrix application step.

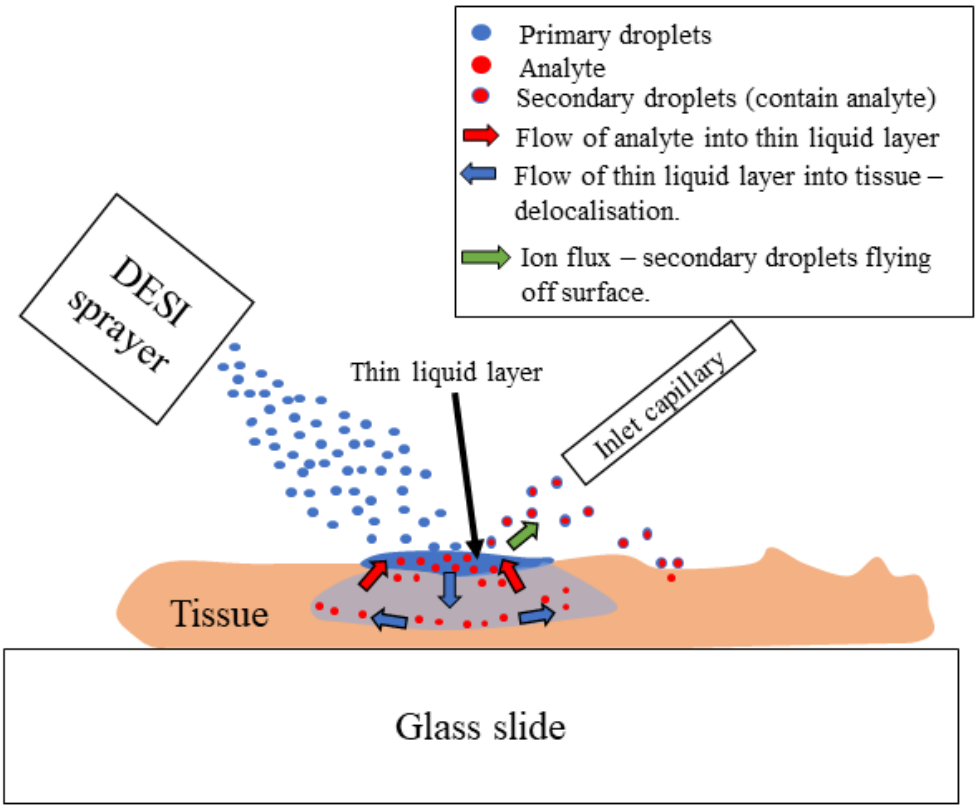


Figure 6-1. Image formation model that incorporates DESI.

To demonstrate some of those peculiarities the figure above is provided. The primary droplets originating from the sprayer bombard the surface to create a thin liquid layer. Analyte (red circles) is then desorbed into the liquid layer; this process is indicated by the red arrows. However, it is also possible that the thin liquid layer diffuses into the tissue section. This is indicated by the vertical blue arrow and the transparent blue region penetrating the tissue section. This can then lead to analyte relocalisation, as indicated by the two horizontal vertical lines and the spread of the analyte (red circle) into the tissue region. In an image this will manifest as an enhanced blurring parameter. As the primary droplets bombard the thin liquid layer, secondary droplets are emitted. The secondary droplets, which carry the extracted analyte, are represented with red circles enclosed by a blue circle. The green arrow shows the ion flux – the flow of analyte from the surface as a function of time. Some of the secondary droplets enter the inlet capillary, while others may splash back on the tissue, resulting in a greater amount of analyte delocalisation. It is clear that our image formation model only encapsulates one part of this complicated picture – the green arrow indicating the ion flux. The analyte relocalisation effects have not been considered and more importantly, the effective cross-section between the inlet capillary and the ion flux has not been taken into account. Incorporating this cross-section area can be of great importance, especially in atmospheric pressure MSI. Nevertheless, the image formation model developed here can be used as a stepping stone for the discovery of a mathematical model that describe the processes described above. This might take years and most certainly could be classified as ‘future

work'. Other things that can be thoroughly investigated are other atmospheric pressure modalities that involve the interaction between a laser light source and a tissue material.

Some other extensions that can be made is a study of different mathematical functions that can describe the analytical probe. Currently a Gaussian function is used. Sadly, the mathematical idealisations behind this can lead to some unrealistic simulations. The Gaussian function has infinite support; it only vanishes at negative and positive infinity. When used in the image formation model, this means that the extreme tails of the Gaussian function can also consume material far from the centre of the beam. In fact, in simulations where the time is large this mathematical abstraction causes the extreme tails of the beam to remove a somewhat significant amount of material. Thus, investigating probe function that have a finite support is certainly a possible thing to do in the future. Some good candidates would be a truncated Gaussian function, a top-hat function and perhaps even a beta-PERT distribution. The same problem arises when the MTF is modelled as a Gaussian and Poisson noise is considered. The resolution frequency is the intersection between the MTF and the noise standard deviation. In Chapter 3 it was shown that if a Gaussian MTF is assumed, the intersection point happens at $f_c = \tilde{\sigma}\sqrt{2\ln\left(SNR(I)\right)}$. For Poisson noise the signal to noise ratio is a monotonically increasing function and thus the scaled root NSD and MTF intersect at infinity. This problem should certainly be fixed but that will have to happen in the future. Possible solutions include using a truncated Gaussian (truncated at the Nyquist frequency) or using a beta-PERT function. The latter may not yield a nice analytical solution.

6.2.2 Image formation model – noise models

Future work could also involve further investigation of the noise models seen in this thesis. If somehow MALDI and DESI could switch to pure Poisson noise, this will greatly improve spatial resolution and could be an essential thing to do for accomplishing single cell imaging. Investigating the sources of the peak amplitude fluctuations are one possible way of achieving this. It was also shown that Orbitrap instruments exhibit a peculiar behaviour at the low intensity region. Using an appropriate noise model for this can help quantify resolution in tissue imaging experiments; this was outlined in Chapter 5. Generally, selecting an appropriate noise model is a really crucial part of the overall image formation model. While one cannot claim that the ion flux generation part of the image formation model is quantitative, the combined noise model proposed in this thesis was justified using computational simulations in Chapter 2 and experimentally verified in Chapter 4 and Chapter 5. Chapter 4 also allowed us to test if the physical interpretation of the noise model is correct. Therefore, one may claim that this noise model may be used to accurately simulate the noise statistics in synthetic data. Nevertheless, a rigorous theoretical investigation still needs to be performed and the distribution function of the combined noise should be derived analytically.

6.2.3 Possible applications for the image formation model in its current state

While there are more things to be done on both the ion flux generation and the noise parts of the image formation model, that does not mean that one cannot use it in its current state for some extra applications. In fact, it was already used it to derive a resolution metric but there are other things that can be done. An interesting application would be to simulate imaging of more complex systems such as thin tissue section. First, one needs to define a tissue. A generalised Voronoi tessellation has already been proposed to model tissue structures[154]. Voronoi tessellations have been applied in the study and description of cancer cells[164,165] and even plant cells[166]. There are plenty of other examples that are not listed here.

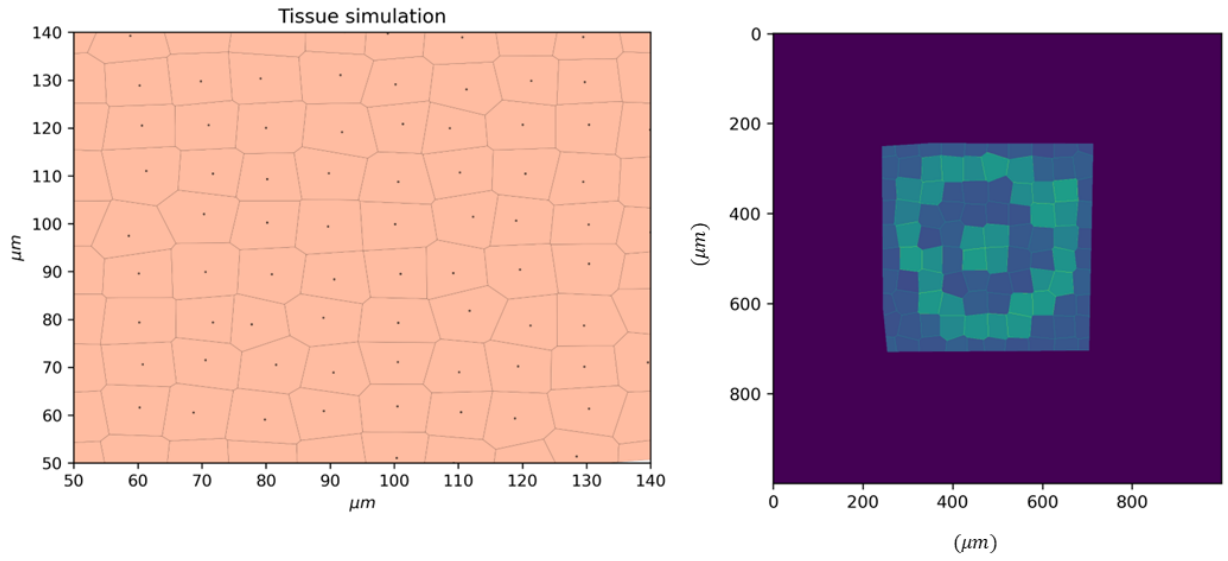


Figure 6-2. A Voronoi tessellation simulating a tissue structure.

One possible way of utilising Voronoi tessellations is shown in Figure 6-2. On the left some cells were created and on the right these cells were given an average molecular density. For the purpose of this demonstration let us imagine it's the commonly encountered lipid PC 38:6. Its isotopes will also follow the same spatial distribution. Using some computational sleight of hand a ring-like structure with a smaller circle within it was drawn. Then, using image formation model and an instrument response function (see Chapter 2), the following two images were obtained. The mass spectra for each pixel were corrupted with the combined noise model.

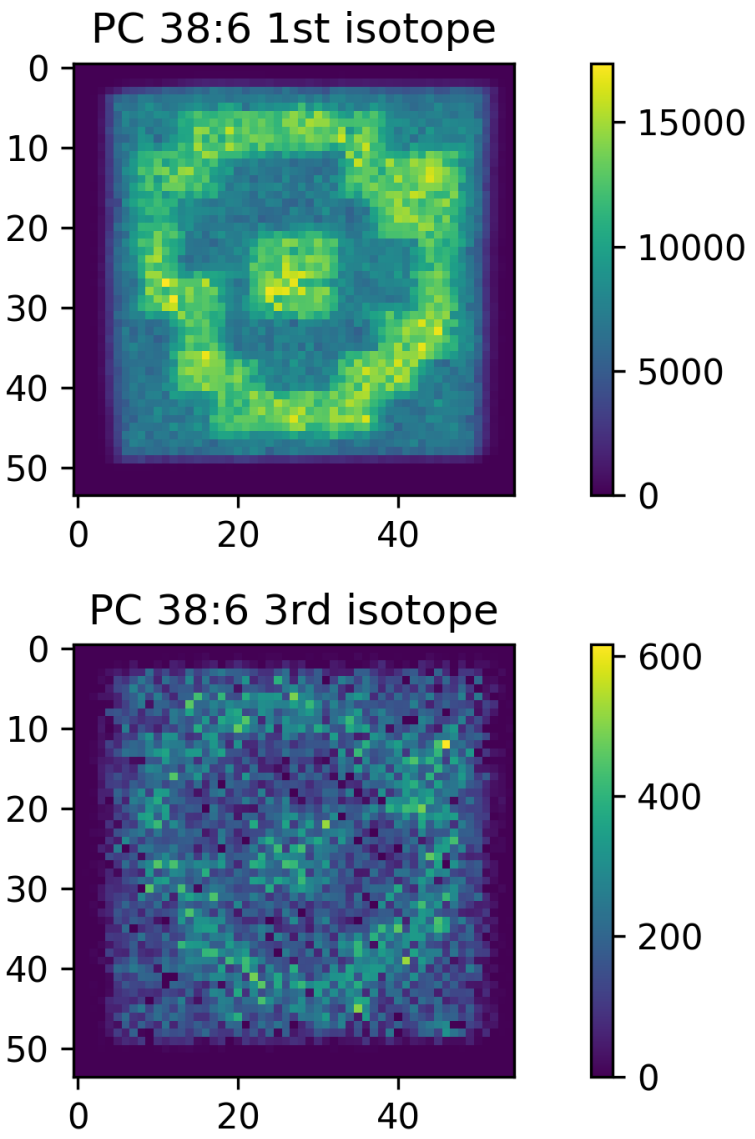


Figure 6-3 The image formation model in action. Top – first isotope. Bottom – third isotope.

It is obvious that such simulations could have immense applications for tissue imaging. Firstly, the ability of commonly used multivariate tools, such as k-means clustering and principal component analysis (PCA)can be put to the test because a ground truth structure can be used. One could study how k-means performs in the presence of a noise model that has been derived from real instruments and investigate if the ground truth number of clusters is recovered. As for PCA, MSI data suffers from heteroskedasticity. It is of vital importance to scale the data before doing any kind of PCA as the importance of components would be underestimate/overestimated, depending on the type of noise exhibited. The methods proposed in this work can help deal with this issue in a novel way; this will be incredibly valuable for the accurate interpretation of biological data.

Other possible applications include the study of denoising, deconvolutions and super resolution. Furthermore, with the kinds of simulations shown here, one can figure out what the optimal conditions for single cell imaging are (or if they are even possible given the noise levels) before wasting a ton of money on developing a new instrument. Out of everything so far two possible applications are shown as a proof of concept.

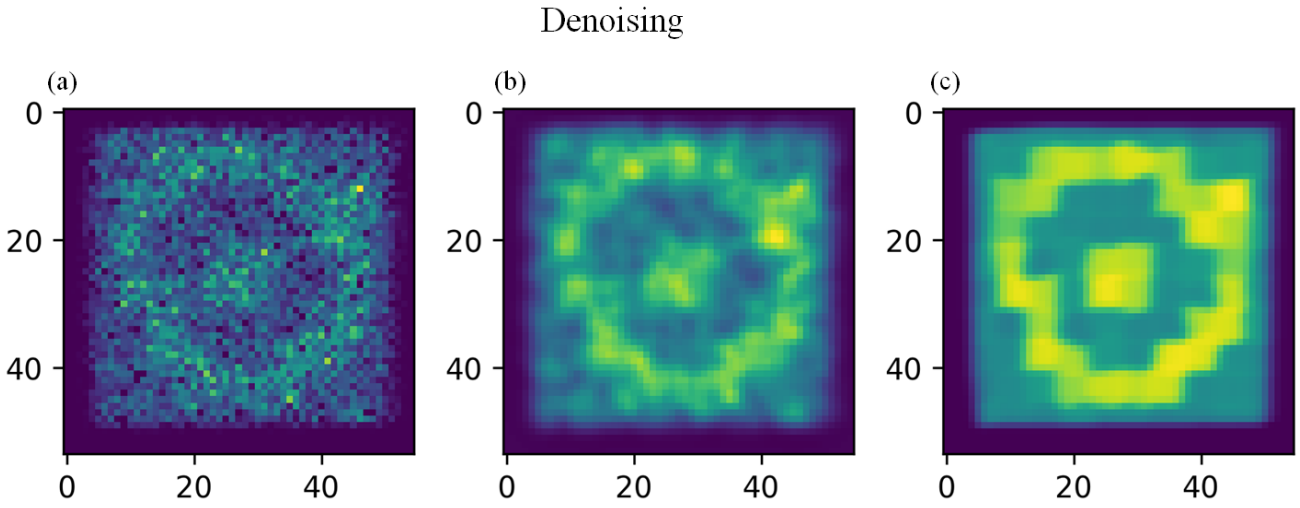


Figure 6-4. (a) – A terribly noisy low intensity image. (b) – denoised image. (c) – ground truth.

The way denoising was accomplished here shall remain unexplained as this is a Chapter about future work and the author would like to do this in the feature without anyone on the internet stealing this idea. It shall only be mentioned that the first step is to estimate the spatial resolution in Fourier space using the methods provided in this thesis. Figure 6-4 (a) shows the noisy image, Figure 6-4 (b) the denoised image and Figure 6-4 (c) shows the ground truth image. Spatial resolution estimates can therefore not only be useful for comparing instruments and optimising experiments – the impact of measuring spatial resolution can be extended to interpreting biological data. For example, consider the following figure.

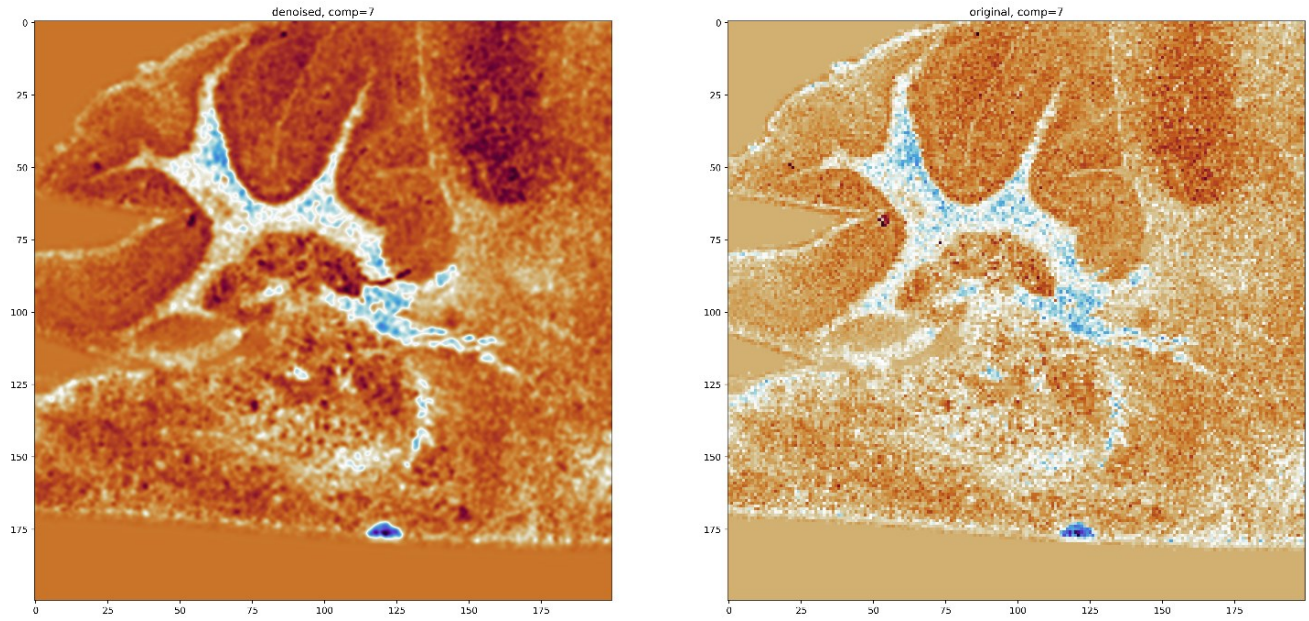


Figure 6-5 Denoising effects on PCA. Left – PCA on denoised datacube. Right – PCA on original data.

After calculating the spatial resolution in each single ion image of that datacube, an adaptive denoising step was performed. PCA was then performed on the original and denoised data. The left hand side panel in Figure 6-5 shows the results of applying PCA on a denoised datacube; the right hand side shows PCA on the original datacube. The benefits of being able to measure spatial resolution are clearly demonstrated with this example.

6.2.4 Future ways of measuring spatial resolution

The methods outlined in this thesis are limited to step edge samples. It becomes very difficult to measure the spatial resolution of a tissue imaging data set precisely because the lack of well-defined step edges. This also limits the resolution measurement in the direction of the edge. There are a several of possible ways of overcoming the edge-induced limitations. Now some more elegant methods for obtaining the blurring parameter than the one used in Chapter 5 are proposed. One possible approach would be to implement a Richardson-Lucy (RL) blind deconvolution[167]. This is Bayesian iterative method that when optimised appropriately can approximate the ground truth PSF and thus MTF; this will be a 2D estimate as well! The original RL method assumes Poisson noise so with some appropriate changes the RL method could be used to obtain an MTF. The other tricky thing is finding a metric for evaluating the optimal number of iterations. Another route that can be taken is to use an edge detection step, combined with an edge sharpening step; the PSF is then recovered based on a *maximum a posteriori* (MAP) estimation using the original (blurry) edge and the idealised (sharpened) edge[168]; this also yields a 2D PSF. It is also possible to use machine learning methods to recover the blurring parameter – for example a support vector machine has been used to do this[169]. Neural networks can also be a powerful tool for the quick estimation of the MTF[170–172].

Of course, all of the machine learning methods can be trained on data created by the image formation model and real data. This would be a fantastic way of generating robust MTF descriptors across various different instruments.

Finally, it is worth mentioning some other beautiful methods for measuring spatial resolution. These methods originate from imaging modalities that cannot obtain a PSF measurement due to how good their spatial resolution can be. One such example is cryo-electron microscopy. In a recent publication a parameter free single image method was proposed, which the authors named decorrelation analysis[173]. Unfortunately, the authors of this method were kind enough to thoroughly investigate how robust their method is with respect to image SNR. They show decorrelation analysis fails at low SNR values ($SNR \approx 5$ and smaller). It was shown in Chapter 4 and Chapter 5 that this is around the range of the highest achievable SNR values for some MSI modalities; only a handful of images within a datacube could potentially have their resolution measured with this metric. However, other modalities, such as NanoSIMS and OrbiSIMS could have their resolutions measured using decorrelation analysis, as they do not exhibit combined noise and their SNR values are not limited to a low number at high intensities. The method described here was inspired by an older method called Fourier ring correlations (FRC)[174]. This is an incredibly beautiful algorithm. The idea is to obtain two images of the same object. The two images will have independent noise realisations. The two images are then Fourier transformed. A ring mask is applied on both images and the correlation between them is computed. Starting at low frequencies, the two ring masks will correlate highly as at low frequencies the noise levels are low. As the rings expand the correlation will decrease. Once the signal is dominated by noise, since the noise realisations are independent, the FRC will vanish. The frequency at which this happens is the spatial resolution! In practice, the FRC curve fluctuates around zero and often an effective threshold is used. There are multiple such threshold metrics and selecting an appropriate one is an important part of the FRC resolution measurement[175]. Sadly, most MSI modalities are destructive and alter the state of the object that is imaged. Thus it would be difficult to acquire two images of the same object experimentally. It is possible to develop standards that allow to do this. In the case of tissue images perhaps consecutive sections can be used. In general FRC is a fantastic way to measure resolution when no step edge is available. More recently, single image FRC algorithm was proposed[176]. This is a really neat idea that splits a single image into two images by subsampling. The FRC curve is then computed. The authors show that the subsampling process introduces a shift in the FRC curve and propose a method for correcting for this shift. In general, if this were to be applied in MSI, a similar calibration step ought to be repeated. The experiments presented in Chapter 4 could be a good way of achieving this. The single image FRC method may be applied on tissue imaging datasets. The FRC method is a beautiful one and ought to be integrated in MSI resolution measurements. Future work may involve a comparison between the method outlined here and the FRC method.

To conclude, the future work ideas discussed in this section are enough to keep someone busy for the foreseeable future.

Bibliography

(1) Karas, M.; Bachmann, D.; Hillenkamp, F. Influence of the Wavelength in High-Irradiance Ultraviolet Laser Desorption Mass Spectrometry of Organic Molecules. *Anal. Chem.* **1985**, *57* (14), 2935–2939. https://doi.org/10.1021/ac00291a042.

(2) Tanaka, K.; Waki, H.; Ido, Y.; Akita, S.; Yoshida, Y.; Yoshida, T.; Matsuo, T. Protein and Polymer Analyses up to m/z 100 000 by Laser Ionization Time-of-flight Mass Spectrometry. *Rapid Commun. Mass Spectrom.* **1988**, *2* (8), 151–153. https://doi.org/10.1002/rcm.1290020802.

(3) Caprioli, R. M.; Farmer, T. B.; Gile, J. Molecular Imaging of Biological Samples: Localization of Peptides and Proteins Using MALDI-TOF MS. *Anal. Chem.* **1997**, *69* (23), 4751–4760. https://doi.org/10.1021/ac970888i.

(4) Brown, A.; van den Berg, J. A.; Vickerman, J. C. The Application of Secondary Ion Mass Spectrometry to Surface Analysis of Semiconductor Substrates and Devices. *Surf. Interface Anal.* **1986**, *9* (5), 309–317. https://doi.org/10.1002/sia.740090508.

(5) Roggli, V. L.; Ingram, P.; Linton, R. W. New Techniques for Imaging and Analyzing Lung Tissue. *Environ. Health Perspect.* **1984**, *VOL. 56*, 163–183. https://doi.org/10.2307/3429844.

(6) Dreisewerd, K.; Schürenberg, M.; Karas, M.; Hillenkamp, F. Influence of the Laser Intensity and Spot Size on the Desorption of Molecules and Ions in Matrix-Assisted Laser Desorption/Ionization with a Uniform Beam Profile. *Int. J. Mass Spectrom. Ion Process.* **1995**, *141* (2), 127–148. https://doi.org/10.1016/0168-1176(94)04108-J.

(7) Schürenberg, M.; Dreisewerd, K.; Kamanabrou, S.; Hillenkamp, F. Influence of the Sample Temperature on the Desorption of Matrix Molecules and Ions in Matrix-Assisted Laser Desorption Ionization. *Int. J. Mass Spectrom. Ion Process.* **1998**, *172* (1–2), 89–94. https://doi.org/10.1016/s0168-1176(97)00253-x.

(8) Zhigilei, L. V.; Kodali, P. B. S.; Garrison, B. J. Molecular Dynamics Model for Laser Ablation and Desorption of Organic Solids. *J. Phys. Chem. B* **1997**, *101* (11), 2028–2037. https://doi.org/10.1021/jp9634013.

(9) Zhigilei, L. V.; Kodali, P. B. S.; Garrison, B. J. A Microscopic View of Laser Ablation. *J. Phys. Chem. B* **1998**, *102* (16), 2845–2853. https://doi.org/10.1021/jp9733781.

(10) Bencsura, A.; Vertes, A. Dynamics of Hydrogen Bonding and Energy Transfer in Matrix-Assisted Laser Desorption. *Chem. Phys. Lett.* **1995**, *247* (1–2), 142–148. https://doi.org/10.1016/0009-2614(95)01179-1.

(11) Zhigilei, L. V.; Yingling, Y. G.; Itina, T. E.; Schoolcraft, T. A.; Garrison, B. J. Molecular Dynamics Simulations of Matrix-Assisted Laser Desorption - Connections to Experiment. *Int. J. Mass Spectrom.* **2003**, *226* (1), 85–106. https://doi.org/10.1016/S1387-3806(02)00962-4.

(12) Perez, D.; Lewis, L. J.; Lorazo, P.; Meunier, M. Ablation of Molecular Solids under Nanosecond Laser Pulses: The Role of Inertial Confinement. *Appl. Phys. Lett.* **2006**, *89* (14), 45–48. https://doi.org/10.1063/1.2358941.

(13) Miotello, A.; Kelly, R. Critical Assessment of Thermal Models for Laser Sputtering at High Fluences. *Appl. Phys. Lett.* **1995**, *67*, 3535. https://doi.org/10.1063/1.114912.

(14) Rohlfing, A.; Leisner, A.; Hillenkamp, F.; Dreisewerd, K. Investigation of the Desorption Process in UV Matrix-Assisted Laser Desorption/Ionization with a Liquid 3-Nitrobenzyl Alcohol Matrix by Photoacoustic Analysis, Fast-Flash Imaging, and UV-Laser Postionization. *J. Phys. Chem. C* **2010**, *114* (12), 5367–5381. https://doi.org/10.1021/jp905251r.

(15) Niehaus, M.; Soltwisch, J. New Insights into Mechanisms of Material Ejection in MALDI Mass Spectrometry for a Wide Range of Spot Sizes. *Sci. Rep.* **2018**, *8* (1), 7755. https://doi.org/10.1038/s41598-018-25946-z.

(16) Allwood, D. A.; Dyer, P. E.; Dreyfus, R. W.; Perera, I. K. Plasma Modelling of Matrix Assisted UV Laser Desorption Ionisation (MALDI). *Appl. Surf. Sci.* **1997**, *109–110*, 616–620. https://doi.org/10.1016/S0169-4332(96)00643-5.

(17) Allwood, D. A.; Dyer, P. E.; Dreyfus, R. W. Ionization Modelling of Matrix Molecules in Ultraviolet Matrix-Assisted Laser Desorption/Ionization. *Rapid Commun. Mass Spectrom.* **1997**, *11* (5), 499–503. https://doi.org/10.1002/(SICI)1097-0231(199703)11:5<499::AID-RCM880>3.0.CO;2-2.

(18) Knochenmuss, R. MALDI Ionization Mechanisms: The Coupled Photophysical and Chemical Dynamics Model Correctly Predicts 'Temperature'-Selected Spectra. *J. Mass Spectrom.* **2013**, *48* (9), 998–1004. https://doi.org/10.1002/jms.3248.

(19) Knochenmuss, R.; Karbach, V.; Wiesli, U.; Breuker, K.; Zenobi, R. The Matrix Suppression Effect in Matrix-Assisted Laser Desorption/Ionization: Application to Negative Ions and Further Characteristics. *Rapid Commun. Mass Spectrom.* **1998**, *12* (9), 529–534. https://doi.org/10.1002/(SICI)1097-0231(19980515)12:9<529::AID-RCM188>3.0.CO;2-E.

(20) Knochenmuss, R. A Quantitative Model of Ultraviolet Matrix-Assisted Laser Desorption/Ionization. *J. Mass Spectrom.* **2002**, *37* (8), 867–877. https://doi.org/10.1002/jms.349.

(21) Knochenmuss, R. A Quantitative Model of Ultraviolet Matrix-Assisted Laser Desorption/Ionization Including Analyte Ion Generation. *Anal. Chem.* **2003**, *75* (10), 2199–2207. https://doi.org/10.1021/ac034032r.

(22) Setz, P. D.; Knochenmuss, R. Exciton Mobility and Trapping in a MALDI Matrix. *J. Phys. Chem. A* **2005**, *109* (18), 4030–4037. https://doi.org/10.1021/jp050622c.

(23) Knochenmuss, R.; Zhigilei, L. V. Molecular Dynamics Model of Ultraviolet Matrix-Assisted Laser Desorption/Ionization Including Ionization Processes. *J. Phys. Chem. B* **2005**, *109* (48), 22947–22957. https://doi.org/10.1021/jp052945e.

(24) Knochenmussa, R.; Zhigilei, L. V. Molecular Dynamics Simulations of MALDI: Laser Fluence and Pulse Width Dependence of Plume Characteristics and Consequences Formatrix and Analyte Ionization. *J. Mass Spectrom.* **2010**, *45* (4), 333–346. https://doi.org/10.1002/jms.1732.

(25) Lai, Y. H.; Wang, C. C.; Lin, S. H.; Lee, Y. T.; Wang, Y. S. Solid-Phase Thermodynamic Interpretation of Ion Desorption in Matrix-Assisted Laser Desorption/Ionization. *J. Phys. Chem. B* **2010**, *114* (43), 13847–13852. https://doi.org/10.1021/jp104250g.

(26) Zhigilei, L. V.; Leveugle, E.; Garrison, B. J.; Yingling, Y. G.; Zeifman, M. I. Computer Simulations of Laser Ablation of Molecular Substrates. *Chem. Rev.* **2003**, *103* (2), 321–347. https://doi.org/10.1021/cr010459r.

(27) McDonald, F. A.; Wetsel, G. C. Generalized Theory of the Photoacoustic Effect. *J. Appl. Phys.* **1978**, *49* (4), 2313–2322. https://doi.org/10.1063/1.325116.

(28) Chu, K. Y.; Lee, S.; Tsai, M. T.; Lu, I. C.; Dyakov, Y. A.; Lai, Y. H.; Lee, Y. T.; Ni, C. K. Thermal Proton Transfer Reactions in Ultraviolet Matrix-Assisted Laser Desorption/Ionization. *J. Am. Soc. Mass Spectrom.* **2014**, *25* (3), 310–318. https://doi.org/10.1007/s13361-013-0792-9.

(29) Chu, K. Y.; Lee, S.; Tsai, M. T.; Lu, I. C.; Dyakov, Y. A.; Lai, Y. H.; Lee, Y. T.; Ni, C. K. Erratum: Thermal Proton Transfer Reactions in Ultraviolet Matrix-Assisted Laser Desorption/Ionization (Journal of the American Society for Mass Spectrometry DOI 10.1007/S13361-013-0792-9). *J. Am. Soc. Mass Spectrom.* **2014**, *25* (6), 1087. https://doi.org/10.1007/s13361-014-0879-y.

(30) Lin, H. Y.; Song, B. F.; Ni, C. K. Fluorescence Quantum Yields of Matrices Used in Ultraviolet Matrix-Assisted Laser Desorption/Ionization. *Rapid Commun. Mass Spectrom.* **2020**, *34* (18), 0–1. https://doi.org/10.1002/rcm.8846.

(31) Lin, H. Y.; Song, B.; Lu, I. C.; Hsu, K. T.; Liao, C. Y.; Lee, Y. Y.; Tseng, C. M.; Lee, Y. T.; Ni, C. K. Is

Energy Pooling Necessary in Ultraviolet Matrix-Assisted Laser Desorption/Ionization? *Rapid Commun. Mass Spectrom.* **2014**, *28* (1), 77–82. https://doi.org/10.1002/rcm.6765.

(32) Lu, I. C.; Lee, C.; Chen, H. Y.; Lin, H. Y.; Hung, S. W.; Dyakov, Y. A.; Hsu, K. T.; Liao, C. Y.; Lee, Y. Y.; Tseng, C. M.; Lee, Y. T.; Ni, C. K. Ion Intensity and Thermal Proton Transfer in Ultraviolet Matrix-Assisted Laser Desorption/Ionization. *J. Phys. Chem. B* **2014**, *118* (15), 4132–4139. https://doi.org/10.1021/jp5008076.

(33) Lin, H. Y.; Dyakov, Y. A.; Lee, Y. T.; Ni, C. K. Temperature Dependence of Desorbed Ions and Neutrals and Ionization Mechanism of Matrix-Assisted Laser Desorption/Ionization. *J. Am. Soc. Mass Spectrom.* **2021**, *32* (1), 95–105. https://doi.org/10.1021/jasms.0c00101.

(34) Yamashita, M.; Fenn, J. B. Electrospray Ion Source. Another Variation on the Free-Jet Theme. *J. Phys. Chem.* **1984**, *88* (20), 4451–4459. https://doi.org/10.1021/j150664a002.

(35) FENN, J. B.; MANN, M.; MENG, C. K.; WONG, S. F.; WHITEHOUSE, C. M. ChemInform Abstract: Electrospray Ionization for Mass Spectrometry of Large Biomolecules. *ChemInform* **1990**, *21* (5). https://doi.org/10.1002/chin.199005359.

(36) Takáts, Z.; Wiseman, J. M.; Gologan, B.; Cooks, R. G. Mass Spectrometry Sampling Under Ambient Conditions with Desorption Electrospray Ionization. *Science (80-.).* **2004**, *306* (5695), 471–473. https://doi.org/10.1126/science.1104404.

(37) Collins, R. T.; Jones, J. J.; Harris, M. T.; Basaran, O. A. Electrohydrodynamic Tip Streaming and Emission of Charged Drops from Liquidcones. *Nat. Phys.* **2008**, *4* (2), 149–154. https://doi.org/10.1038/nphys807.

(38) Takáts, Z.; Wiseman, J. M.; Cooks, R. G. Ambient Mass Spectrometry Using Desorption Electrospray Ionization (DESI): Instrumentation, Mechanisms and Applications in Forensics, Chemistry, and Biology. *J. Mass Spectrom.* **2005**, *40* (10), 1261–1275. https://doi.org/10.1002/jms.922.

(39) Ifa, D. R.; Manicke, N. E.; Rusine, A. L.; Cooks, R. G. Quantitative Analysis of Small Molecules by Desorption Electrospray Ionization Mass Spectrometry from Polytetrafluoroethylene Surfaces. *Rapid Commun. Mass Spectrom.* **2008**, *22* (4), 503–510. https://doi.org/10.1002/rcm.3377.

(40) Costa, A. B.; Graham Cooks, R. Simulated Splashes: Elucidating the Mechanism of Desorption Electrospray Ionization Mass Spectrometry. *Chem. Phys. Lett.* **2008**, *464* (1–3), 1–8. https://doi.org/10.1016/j.cplett.2008.08.020.

(41) Bereman, M. S.; Muddiman, D. C. Detection of Attomole Amounts of Analyte by Desorption Electrospray

Ionization Mass Spectrometry (DESI-MS) Determined Using Fluorescence Spectroscopy. *J. Am. Soc. Mass Spectrom.* **2007**, *18* (6), 1093–1096. https://doi.org/10.1016/j.jasms.2007.03.006.

(42) Venter, A.; Sojka, P. E.; Cooks, R. G. Droplet Dynamics and Ionization Mechanisms in Desorption Electrospray Ionization Mass Spectrometry. *Anal. Chem.* **2006**, *78* (24), 8549–8555. https://doi.org/10.1021/ac0615807.

(43) Costa, A. B.; Cooks, R. G. Simulation of Atmospheric Transport and Droplet-Thin Film Collisions in Desorption Electrospray Ionization. *Chem. Commun.* **2007**, No. 38, 3915–3917. https://doi.org/10.1039/b710511h.

(44) Nefliu, M.; Smith, J. N.; Venter, A.; Cooks, R. G. Internal Energy Distributions in Desorption Electrospray Ionization (DESI). *J. Am. Soc. Mass Spectrom.* **2008**, *19* (3), 420–427. https://doi.org/10.1016/j.jasms.2007.11.019.

(45) Drahos, L.; Heeren, R.; Collette, C.; De Pauw E; Vekey, K. Thermal Energy Distribution Observed in Electrospray Ionization. *J. Mass Spectrom.* **1999**, *34* (12), 1373–1379. https://doi.org/10.1002/(SICI)1096-9888(199912)34:12<1373::AID-JMS907>3.0.CO;2-#.

(46) Gabelica, V.; De Pauw, E.; Karas, M. Influence of the Capillary Temperature and the Source Pressure on the Internal Energy Distribution of Electrosprayed Ions. *Int. J. Mass Spectrom.* **2004**, *231* (2–3), 189–195. https://doi.org/10.1016/j.ijms.2003.10.010.

(47) Konermann, L.; Ahadi, E.; Rodriguez, A. D.; Vahidi, S. Unraveling the Mechanism of Electrospray Ionization. *Anal. Chem.* **2013**, *85* (1), 2–9. https://doi.org/10.1021/ac302789c.

(48) Iribarne, J. V.; Thomson, B. A. On the Evaporation of Small Ions from Charged Droplets. *J. Chem. Phys.* **1976**, *64* (6), 2287–2294. https://doi.org/10.1063/1.432536.

(49) Ahadi, E.; Konermann, L. Surface Charge of Electrosprayed Water Nanodroplets: A Molecular Dynamics Study. *J. Am. Chem. Soc.* **2010**, *132* (32), 11270–11277. https://doi.org/10.1021/ja1041989.

(50) Ahadi, E.; Konermann, L. Ejection of Solvated Ions from Electrosprayed Methanol/Water Nanodroplets Studied by Molecular Dynamics Simulations. *J. Am. Chem. Soc.* **2011**, *133* (24), 9354–9363. https://doi.org/10.1021/ja111492s.

(51) Heck, A. J. R.; Van Den Heuvel, R. H. H. Investigation of Intact Protein Complexes by Mass Spectrometry. *Mass Spectrom. Rev.* **2004**, *23* (5), 368–389. https://doi.org/10.1002/mas.10081.

(52) Fernandez De La Mora, J. Electrospray Ionization of Large Multiply Charged Species Proceeds via Dole's

Charged Residue Mechanism. *Anal. Chim. Acta* **2000**, *406* (1), 93–104. https://doi.org/10.1016/S0003-2670(99)00601-7.

(53) Kaltashov, I. A.; Mohimen, A. Estimates of Protein Surface Areas in Solution by Electrospray Ionization Mass Spectrometry. *Anal. Chem.* **2005**, *77* (16), 5370–5379. https://doi.org/10.1021/ac050511+.

(54) Ahadi, E.; Konermann, L. Modeling the Behavior of Coarse-Grained Polymer Chains in Charged Water Droplets: Implications for the Mechanism of Electrospray Ionization. *J. Phys. Chem. B* **2012**, *116* (1), 104–112. https://doi.org/10.1021/jp209344z.

(55) Bonnin, E. A.; Rizzoli, S. O. Novel Secondary Ion Mass Spectrometry Methods for the Examination of Metabolic Effects at the Cellular and Subcellular Levels. *Front. Behav. Neurosci.* **2020**, *14* (July), 1–13. https://doi.org/10.3389/fnbeh.2020.00124.

(56) Davies, M. C.; Lynn, R. A. P. A Review: Secondary Ion Mass Spectrometry (SIMS of Polymeric Biomaterials. *Clin. Mater.* **1990**, *5* (2–4), 97–114. https://doi.org/10.1016/0267-6605(90)90010-S.

(57) Passarelli, M. K.; Ewing, A. G. Single-Cell Imaging Mass Spectrometry. *Curr. Opin. Chem. Biol.* **2013**, *17* (5), 854–859. https://doi.org/10.1016/j.cbpa.2013.07.017.

(58) Slodzian, G.; Daigne, B.; Girard, F.; Boust, F.; Hillion, F. Scanning Secondary Ion Analytical Microscopy with Parallel Detection. *Biol. Cell* **1992**, *74* (C), 43–50. https://doi.org/10.1016/0248-4900(92)90007-N.

(59) Paruch, R. J.; Postawa, Z.; Wucher, A.; Garrison, B. J. Steady-State Statistical Sputtering Model for Extracting Depth Profiles from Molecular Dynamics Simulations of Dynamic SIMS. *J. Phys. Chem. C* **2012**, *116* (1), 1042–1051. https://doi.org/10.1021/jp2098075.

(60) Cumpson, P. J.; Jaskiewicz, M.; Kim, W. K. Argon Cluster-Ion Sputter Yield: Molecular Dynamics Simulations on Silicon and Equation for Estimating Total Sputter Yield. *Surf. Interface Anal.* **2022**, *54* (4), 341–348. https://doi.org/10.1002/sia.6996.

(61) Zirakparvar, N. A.; Spano, T. L.; Miskowiec, A.; Smith, J. B.; Hexel, C. R.; Ambrogio, M.; Kapsimalis, R. Nuclear Inst . and Methods in Physics Research , B Insights into Secondary Ion Formation during Dynamic SIMS Analysis : Evidence from Sputtering of Laboratory Synthesized Uranium Compounds with a High-Energy O − Primary Beam on a NanoSIMS 50L. *Nucl. Inst. Methods Phys. Res. B* **2021**, *502* (December 2020), 164–175. https://doi.org/10.1016/j.nimb.2021.06.007.

(62) Aoki, T.; Chiba, S.; Matsuo, J.; Yamada, I.; Biersack, J. P. Molecular Dynamics and Monte-Carlo Simulation of Sputtering and Mixing by Ion Irradiation. In *Nuclear Instruments and Methods in Physics Research, Section B: Beam Interactions with Materials and Atoms*; 2001; Vol. 180, pp 312–316.

https://doi.org/10.1016/S0168-583X(01)00437-2.

(63) Yang, L.; Seah, M. P.; Anstis, E. H.; Gilmore, I. S.; Lee, J. L. S. Sputtering Yields of Gold Nanoparticles by C 60 Ions. *J. Phys. Chem. C* **2012**, *116* (16), 9311–9318. https://doi.org/10.1021/jp300900j.

(64) Seah, M. P. Argon Cluster Size-Dependence of Sputtering Yields of Polymers: Molecular Weights and the Universal Equation. *Surf. Interface Anal.* **2015**, *47* (1), 169–172. https://doi.org/10.1002/sia.5656.

(65) Seah, M. P. Universal Equation for Argon Gas Cluster Sputtering Yields. *J. Phys. Chem. C* **2013**, *117* (24), 12622–12632. https://doi.org/10.1021/jp402684c.

(66) Seah, M. P.; Havelund, R.; Gilmore, I. S. Universal Equation for Argon Cluster Size-Dependence of Secondary Ion Spectra in Sims of Organic Materials. *J. Phys. Chem. C* **2014**, *118* (24), 12862–12872. https://doi.org/10.1021/jp502646s.

(67) Passarelli, M. K.; Wang, J.; Mohammadi, A. S.; Trouillon, R.; Gilmore, I.; Ewing, A. G. Development of an Organic Lateral Resolution Test Device for Imaging Mass Spectrometry. *Anal. Chem.* **2014**, *86* (19), 9473–9480. https://doi.org/10.1021/ac501228x.

(68) Seah, M. P. Resolution Parameters for Model Functions Used in Surface Analysis. *Surf. Interface Anal.* **2002**, *33* (12), 950–953. https://doi.org/10.1002/sia.1452.

(69) Senoner, M.; Wirth, T.; Unger, W. E. S. Imaging Surface Analysis: Lateral Resolution and Its Relation to Contrast and Noise. *J. Anal. At. Spectrom.* **2010**, *25* (9), 1440–1452. https://doi.org/10.1039/c004323k.

(70) Dowsett, M. G.; Barlow, R. D.; Allen, P. N. Secondary Ion Mass Spectrometry Analysis of Ultrathin Impurity Layers in Semiconductors and Their Use in Quantification, Instrumental Assessment, and Fundamental Measurements. *J. Vac. Sci. Technol. B Microelectron. Nanom. Struct. Process. Meas. Phenom.* **1994**, *12* (1), 186–198. https://doi.org/10.1116/1.587180.

(71) Lee, J. L. S.; Ninomiya, S.; Matsuo, J.; Gilmore, I. S.; Seah, M. P.; Shard, A. G. Organic Depth Profiling of a Nanostructured Delta Layer Reference Material Using Large Argon Cluster Ions. *Anal. Chem.* **2010**, *82* (1), 98–105. https://doi.org/10.1021/ac901045q.

(72) Shard, A. G.; Brewer, P. J.; Green, F. M.; Gilmore, I. S. Measurement of Sputtering Yields and Damage in C60 SIMS Depth Profiling of Model Organic Materials. *Surf. Interface Anal.* **2007**, *39* (4), 294–298. https://doi.org/10.1002/sia.2525.

(73) Shard, A. G.; Green, F. M.; Brewer, P. J.; Seah, M. P.; Gilmore, I. S. Quantitative Molecular Depth Profiling of Organic Delta-Layers by C 60 Ion Sputtering and SIMS. *J. Phys. Chem. B* **2008**, *112* (9),

2596–2605. https://doi.org/10.1021/jp077325n.

(74) Sjövall, P.; Rading, D.; Ray, S.; Yang, L.; Shard, A. G. Sample Cooling or Rotation Improves C60 Organic Depth Profiles of Multilayered Reference Samples: Results from a VAMAS Interlaboratory Study. *J. Phys. Chem. B* **2010**, *114* (2), 769–774. https://doi.org/10.1021/jp9095216.

(75) Steven, R. T.; Niehaus, M.; Taylor, A. J.; Nasif, A.; Elia, E.; Goodwin, R. J. A.; Takats, Z.; Bunch, J. Atmospheric-Pressure Infrared Laser-Ablation Plasma-Postionization Mass Spectrometry Imaging of Formalin-Fixed Paraffin-Embedded (FFPE) and Fresh-Frozen Tissue Sections with No Sample Preparation. *Anal. Chem.* **2022**, *94* (28), 9970–9974. https://doi.org/10.1021/acs.analchem.2c00690.

(76) Vande Voorde, J.; Steven, R. T.; Najumudeen, A. K.; Ford, C. A.; Dexter, A.; Gonzalez-Fernandez, A.; Nikula, C. J.; Xiang, Y.; Ford, L.; Maneta Stavrakaki, S.; Gilroy, K.; Zeiger, L. B.; Pennel, K.; Hatthakarnkul, P.; Elia, E. A.; Nasif, A.; Murta, T.; Manoli, E.; Mason, S.; Gillespie, M.; Lannagan, T. R. M.; Vlahov, N.; Ridgway, R. A.; Nixon, C.; Raven, A.; Mills, M.; Athineos, D.; Kanellos, G.; Nourse, C.; Gay, D. M.; Hughes, M.; Burton, A.; Yan, B.; Sellers, K.; Wu, V.; De Ridder, K.; Shokry, E.; Huerta Uribe, A.; Clark, W.; Clark, G.; Kirschner, K.; Thienpont, B.; Li, V. S. W.; Maddocks, O. D. K.; Barry, S. T.; Goodwin, R. J. A.; Kinross, J.; Edwards, J.; Yuneva, M. O.; Sumpton, D.; Takats, Z.; Campbell, A. D.; Bunch, J.; Sansom, O. J. Metabolic Profiling Stratifies Colorectal Cancer and Reveals Adenosylhomocysteinase as a Therapeutic Target. *Nat. Metab.* **2023**, *5* (8), 1303–1318. https://doi.org/10.1038/s42255-023-00857-0.

(77) Kreuzaler, P.; Inglese, P.; Ghanate, A.; Gjelaj, E.; Wu, V.; Panina, Y.; Mendez-Lucas, A.; MacLachlan, C.; Patani, N.; Hubert, C. B.; Huang, H.; Greenidge, G.; Rueda, O. M.; Taylor, A. J.; Karali, E.; Kazanc, E.; Spicer, A.; Dexter, A.; Lin, W.; Thompson, D.; Silva Dos Santos, M.; Calvani, E.; Legrave, N.; Ellis, J. K.; Greenwood, W.; Green, M.; Nye, E.; Still, E.; Kreuzaler, P.; Barry, S.; Goodwin, R. J. A.; Bruna, A.; Caldas, C.; MacRae, J.; de Carvalho, L. P. S.; Poulogiannis, G.; McMahon, G.; Takats, Z.; Bunch, J.; Yuneva, M. *Vitamin B5 Supports MYC Oncogenic Metabolism and Tumor Progression in Breast Cancer*; 2023; Vol. 5. https://doi.org/10.1038/s42255-023-00915-7.

(78) Lok, M. *The IUPAC Compendium of Chemical Terminology*; Gold, V., Ed.; International Union of Pure and Applied Chemistry (IUPAC): Research Triangle Park, NC, 2019. https://doi.org/10.1351/goldbook.

(79) Wolff, M. M.; Stephens, W. E. A Pulsed Mass Spectrometer with Time Dispersion. *Rev. Sci. Instrum.* **1953**, *24* (8), 616–617. https://doi.org/10.1063/1.1770801.

(80) Alikhanov, S. G. A New Impulse Technique for Ion Mass Measurements. *Sov. Phys. JETP* **1957**, *4* (3), 452–453.

(81) Mamyrin, B. A.; Karataev, V. I.; Shmikk, D. V.; Zagulin, V. A. The Mass-Reflectron, a New Nonmagnetic Time-of-Flight Mass Spectrometer with High Resolution. *Sov Phys JETP* **1973**, *37* (1), 45–48.

(82) Coombes, K. R.; Koomen, J. M.; Baggerly, K. A.; Morris, J. S.; Kobayashi, R. Understanding the Characteristics of Mass Spectrometry Data through the Use of Simulation. *Cancer Inform.* **2007**, *1* (1), 41–52. https://doi.org/10.1177/117693510500100103.

(83) Comisarow, M. B.; Marshall, A. G. Fourier Transform Ion Cyclotron Resonance Spectroscopy. *Chem. Phys. Lett.* **1974**, *25* (2), 282–283. https://doi.org/10.1016/0009-2614(74)89137-2.

(84) Marshall, A. G.; Hendrickson, C. L.; Jackson, G. S. Fourier Transform Ion Cyclotron Resonance Mass Spectrometry: A Primer. *Mass Spectrom. Rev.* **1998**, *17* (1), 1–35. https://doi.org/10.1002/(SICI)1098-2787(1998)17:1<1::AID-MAS1>3.0.CO;2-K.

(85) Makarov, A. Electrostatic Axially Harmonic Orbital Trapping: A High-Performance Technique of Mass Analysis. *Anal. Chem.* **2000**, *72* (6), 1156–1162. https://doi.org/10.1021/ac991131p.

(86) Makarov, A.; Denisov, E.; Kholomeev, A.; Balschun, W.; Lange, O.; Strupat, K.; Horning, S. Performance Evaluation of a Hybrid Linear Ion Trap/Orbitrap Mass Spectrometer. *Anal. Chem.* **2006**, *78* (7), 2113–2120. https://doi.org/10.1021/ac0518811.

(87) Makarov, A.; Denisov, E.; Lange, O.; Horning, S. Dynamic Range of Mass Accuracy in LTQ Orbitrap Hybrid Mass Spectrometer. *J. Am. Soc. Mass Spectrom.* **2006**, *17* (7), 977–982. https://doi.org/10.1016/j.jasms.2006.03.006.

(88) Makarov, A.; Denisov, E.; Lange, O.; Horning, S. Erratum to: Dynamic Range of Mass Accuracy in LTQ Orbitrap Hybrid Mass Spectrometer. *J. Am. Soc. Mass Spectrom.* **2006**, *17* (12), 1758–1758. https://doi.org/10.1016/j.jasms.2006.09.022.

(89) Rosas-Román, I.; Winkler, R. Contrast Optimization of Mass Spectrometry Imaging (MSI) Data Visualization by Threshold Intensity Quantization (TrIQ). *PeerJ Comput. Sci.* **2021**, *7*, 1–16. https://doi.org/10.7717/peerj-cs.585.

(90) Krutchinsky, A. N.; Chait, B. T. On the Nature of the Chemical Noise in MALDI Mass Spectra. *J. Am. Soc. Mass Spectrom.* **2002**, *13* (2), 129–134. https://doi.org/10.1016/S1044-0305(01)00336-1.

(91) Boskamp, T.; Lachmund, D.; Casadonte, R.; Hauberg-Lotte, L.; Kobarg, J. H.; Kriegsmann, J.; Maass, P. Using the Chemical Noise Background in Maldi Mass Spectrometry Imaging for Mass Alignment and Calibration. *Anal. Chem.* **2020**, *92* (1), 1301–1308. https://doi.org/10.1021/acs.analchem.9b04473.

(92) Allen, J. S. An Improved Electron Multiplier Particle Counter. *Rev. Sci. Instrum.* **1947**, *18* (10), 739–749. https://doi.org/10.1063/1.1740838.

(93) Shockley, W.; Pierce, J. R. A Theory of Noise for Electron Multipliers. *Proc. Inst. Radio Eng.* **1938**, *26* (3), 321–332. https://doi.org/10.1109/JRPROC.1938.228127.

(94) Burroughs, E. G. Collection Efficiency of Continuous Dynode Electron Multiple Arrays. *Rev. Sci. Instrum.* **1969**, *40* (1), 35–37. https://doi.org/10.1063/1.1683743.

(95) Ladislas Wiza, J. Microchannel Plate Detectors. *Nucl. Instruments Methods* **1979**, *162* (1–3), 587–601. https://doi.org/10.1016/0029-554X(79)90734-1.

(96) Daly, N. R. Scintillation Type Mass Spectrometer Ion Detector. *Rev. Sci. Instrum.* **1960**, *31* (3), 264–267. https://doi.org/10.1063/1.1716953.

(97) Brown, K. L.; Tautfest, G. W. Faraday-Cup Monitors for High-Energy Electron Beams. *Rev. Sci. Instrum.* **1956**, *27* (9), 696–702. https://doi.org/10.1063/1.1715674.

(98) Peterson, D. W.; Hayes, J. M. Signal-to-Noise Ratios in Mass Spectroscopic Ion-Current-Measurement Systems. In *Contemporary Topics in Analytical and Clinical Chemistry*; Springer US: Boston, MA, 1978; pp 217–252. https://doi.org/10.1007/978-1-4615-6734-9_5.

(99) Gedcke, D. A. How Counting Statistics and the ADC Sampling Interval Control Mass Accuracy in Time-of-Flight Mass Spectrometry. *ORTEC Appl. Notes* **2001**, *AN61*.

(100) Ipsen, A. Derivation from First Principles of the Statistical Distribution of the Mass Peak Intensities of MS Data. *Anal. Chem.* **2015**, *87* (3), 1726–1734. https://doi.org/10.1021/ac503554u.

(101) Ipsen, A. Derivation of the Statistical Distribution of the Mass Peak Centroids of Mass Spectrometers Employing Analog-to-Digital Converters and Electron Multipliers. *Anal. Chem.* **2017**, *89* (4), 2232–2241. https://doi.org/10.1021/acs.analchem.6b02446.

(102) Shin, H.; Mutlu, M.; Koomen, J. M.; Markey, M. K. Parametric Power Spectral Density Analysis of Noise from Instrumentation in MALDI TOF Mass Spectrometry. *Cancer Inform.* **2007**, *3*, 219–230. https://doi.org/10.1177/117693510700300019.

(103) Rocke, D. M.; Lorenzato, S. A Two-Component Model for Measurement Error in Analytical Chemistry. *Technometrics* **1995**, *37* (2), 176–184. https://doi.org/10.1080/00401706.1995.10484302.

(104) Rocke, D. M.; Durbin, B. A Model for Measurement Error for Gene Expression Arrays. *J. Comput. Biol.* **2001**, *8* (6), 557–569. https://doi.org/10.1089/106652701753307485.

(105) Anderle, M.; Roy, S.; Lin, H.; Becker, C.; Joho, K. Quantifying Reproducibility for Differential Proteomics: Noise Analysis for Protein Liquid Chromatography-Mass Spectrometry of Human Serum. *Bioinformatics* **2004**, *20* (18), 3575–3582. https://doi.org/10.1093/bioinformatics/bth446.

(106) Du, P.; Stolovitzky, G.; Horvatovich, P.; Bischoff, R.; Lim, J.; Suits, F. A Noise Model for Mass Spectrometry Based Proteomics. *Bioinformatics* **2008**, *24* (8), 1070–1077. https://doi.org/10.1093/bioinformatics/btn078.

(107) Deepaisarn, S.; Tar, P. D.; Thacker, N. A.; Seepujak, A.; McMahon, A. W. Quantifying Biological Samples Using Linear Poisson Independent Component Analysis for MALDI-ToF Mass Spectra. *Bioinformatics* **2018**, *34* (6), 1001–1008. https://doi.org/10.1093/bioinformatics/btx630.

(108) Alexandrov, T.; Becker, M.; Deininger, S. O.; Ernst, G.; Wehder, L.; Grasmair, M.; Von Eggeling, F.; Thiele, H.; Maass, P. Spatial Segmentation of Imaging Mass Spectrometry Data with Edge-Preserving Image Denoising and Clustering. *J. Proteome Res.* **2010**, *9* (12), 6535–6546. https://doi.org/10.1021/pr100734z.

(109) Trede, D.; Kobarg, J. H.; Oetjen, J.; Thiele, H.; Maass, P.; Alexandrov, T. On the Importance of Mathematical Methods for Analysis of MALDI-Imaging Mass Spectrometry Data. *J. Integr. Bioinform.* **2012**, *9* (1), 189. https://doi.org/10.1515/jib-2012-189.

(110) Zavalin, A.; Yang, J.; Haase, A.; Holle, A.; Caprioli, R. Implementation of a Gaussian Beam Laser and Aspheric Optics for High Spatial Resolution MALDI Imaging MS. *J. Am. Soc. Mass Spectrom.* **2014**, *25* (6), 1079–1082. https://doi.org/10.1007/s13361-014-0872-5.

(111) Zavalin, A.; Yang, J.; Caprioli, R. Laser Beam Filtration for High Spatial Resolution MALDI Imaging Mass Spectrometry. *J. Am. Soc. Mass Spectrom.* **2013**, *24* (7), 1153–1156. https://doi.org/10.1007/s13361-013-0638-5.

(112) Dueñas, M. E.; Carlucci, L.; Lee, Y. J. Matrix Recrystallization for MALDI-MS Imaging of Maize Lipids at High-Spatial Resolution. *J. Am. Soc. Mass Spectrom.* **2016**, *27* (9), 1575–1578. https://doi.org/10.1007/s13361-016-1422-0.

(113) Ščupáková, K.; Balluff, B.; Tressler, C.; Adelaja, T.; Heeren, R. M. A.; Glunde, K.; Ertaylan, G. Cellular Resolution in Clinical MALDI Mass Spectrometry Imaging: The Latest Advancements and Current Challenges. *Clinical Chemistry and Laboratory Medicine*. June 25, 2020, pp 914–929. https://doi.org/10.1515/cclm-2019-0858.

(114) Feenstra, A. D.; Dueñas, M. E.; Lee, Y. J. Five Micron High Resolution MALDI Mass Spectrometry

Imaging with Simple, Interchangeable, Multi-Resolution Optical System. *J. Am. Soc. Mass Spectrom.* **2017**, *28* (3), 434–442. https://doi.org/10.1007/s13361-016-1577-8.

(115) Angerer, T. B.; Bour, J.; Biagi, J. L.; Moskovets, E.; Frache, G. Evaluation of 6 MALDI-Matrices for 10 Mm Lipid Imaging and On-Tissue MSn with AP-MALDI-Orbitrap. *J. Am. Soc. Mass Spectrom.* **2022**, *33* (5), 760–771. https://doi.org/10.1021/jasms.1c00327.

(116) Li, B.; Bhandari, D. R.; Römpp, A.; Spengler, B. High-Resolution MALDI Mass Spectrometry Imaging of Gallotannins and Monoterpene Glucosides in the Root of Paeonia Lactiflora. *Nat. Publ. Gr.* **2016**, No. May, 1–12. https://doi.org/10.1038/srep36074.

(117) Spraggins, J. M.; Caprioli, R. M. High-Speed MALDI-TOF Imaging Mass Spectrometry: Rapid Ion Image Acquisition and Considerations for Next Generation Instrumentation. *J. Am. Soc. Mass Spectrom.* **2011**, *22* (6), 1022–1031. https://doi.org/10.1007/s13361-011-0121-0.

(118) Yin, R.; Burnum-Johnson, K. E.; Sun, X.; Dey, S. K.; Laskin, J. High Spatial Resolution Imaging of Biological Tissues Using Nanospray Desorption Electrospray Ionization Mass Spectrometry. *Nat. Protoc.* **2019**, *14* (12), 3445–3470. https://doi.org/10.1038/s41596-019-0237-4.

(119) He, M. J.; Pu, W.; Wang, X.; Zhang, W.; Tang, D.; Dai, Y. Comparing DESI-MSI and MALDI- MSI Mediated Spatial Metabolomics and Their Applications in Cancer Studies. **2022**, *12* (July), 1–13. https://doi.org/10.3389/fonc.2022.891018.

(120) Campbell, D. I.; Ferreira, C. R.; Eberlin, L. S.; Cooks, R. G. Improved Spatial Resolution in the Imaging of Biological Tissue Using Desorption Electrospray Ionization. In *Analytical and Bioanalytical Chemistry*; 2012; Vol. 404, pp 389–398. https://doi.org/10.1007/s00216-012-6173-6.

(121) Barré, F.; Rocha, B.; Dewez, F.; Towers, M.; Murray, P.; Claude, E.; Cillero-Pastor, B.; Heeren, R.; Porta Siegel, T. Faster Raster Matrix-Assisted Laser Desorption/Ionization Mass Spectrometry Imaging of Lipids at High Lateral Resolution. *Int. J. Mass Spectrom.* **2019**, *437*, 38–48. https://doi.org/10.1016/j.ijms.2018.09.015.

(122) Good, C. J.; Neumann, E. K.; Butrico, C. E.; Cassat, J. E.; Caprioli, R. M.; Spraggins, J. M. High Spatial Resolution MALDI Imaging Mass Spectrometry of Fresh-Frozen Bone. *Anal. Chem.* **2022**, *94* (7), 3165–3172. https://doi.org/10.1021/acs.analchem.1c04604.

(123) Bowman, A. P.; Bogie, J. F. J.; Hendriks, J. J. A.; Haidar, M.; Belov, M.; Heeren, R. M. A.; Ellis, S. R. Evaluation of Lipid Coverage and High Spatial Resolution MALDI-Imaging Capabilities of Oversampling Combined with Laser Post-Ionisation. *Anal. Bioanal. Chem.* **2020**, *412* (10), 2277–2289.

https://doi.org/10.1007/s00216-019-02290-3.

(124) Zhu, X.; Xu, T.; Peng, C.; Wu, S. Advances in MALDI Mass Spectrometry Imaging Single Cell and Tissues. *Front. Chem.* **2022**, *9* (February), 1–27. https://doi.org/10.3389/fchem.2021.782432.

(125) Prentice, B. M.; Chumbley, C. W.; Caprioli, R. M. High-speed MALDI MS/MS Imaging Mass Spectrometry Using Continuous Raster Sampling. *J. Mass Spectrom.* **2015**, *50* (4), 703–710. https://doi.org/10.1002/jms.3579.

(126) Shannon, C. E. Communication in the Presence of Noise. *Proc. IRE* **1949**, *37* (1), 10–21. https://doi.org/10.1109/JRPROC.1949.232969.

(127) Buchberger, A. R.; DeLaney, K.; Johnson, J.; Li, L. Mass Spectrometry Imaging: A Review of Emerging Advancements and Future Insights. *Anal. Chem.* **2018**, *90* (1), 240–265. https://doi.org/10.1021/acs.analchem.7b04733.

(128) O'Rourke, M. B.; Raymond, B. B. A.; Padula, M. P. The Characterization of Laser Ablation Patterns and a New Definition of Resolution in Matrix Assisted Laser Desorption Ionization Imaging Mass Spectrometry (MALDI-IMS). *J. Am. Soc. Mass Spectrom.* **2017**, *28* (5), 895–900. https://doi.org/10.1007/s13361-017-1632-0.

(129) Li, S.; Zhang, Y.; Liu, J.; Han, J.; Guan, M.; Yang, H.; Lin, Y.; Xiong, S.; Zhao, Z. Electrospray Deposition Device Used to Precisely Control the Matrix Crystal to Improve the Performance of MALDI MSI. *Sci. Rep.* **2016**, *6* (November), 1–10. https://doi.org/10.1038/srep37903.

(130) Jurchen, J. C.; Rubakhin, S. S.; Sweedler, J. V. MALDI-MS Imaging of Features Smaller than the Size of the Laser Beam. *J. Am. Soc. Mass Spectrom.* **2005**, *16* (10), 1654–1659. https://doi.org/10.1016/j.jasms.2005.06.006.

(131) Kuznetsov, I.; Filevich, J.; Dong, F.; Woolston, M.; Chao, W.; Anderson, E. H.; Bernstein, E. R.; Crick, D. C.; Rocca, J. J.; Menoni, C. S. Three-Dimensional Nanoscale Molecular Imaging by Extreme Ultraviolet Laser Ablation Mass Spectrometry. *Nat. Commun.* **2015**, *6* (1).

(132) Zavalin, A.; Todd, E. M.; Rawhouser, P. D.; Yang, J.; Norris, J. L.; Caprioli, R. M. Direct Imaging of Single Cells and Tissue at Sub-Cellular Spatial Resolution Using Transmission Geometry MALDI MS. *Journal of Mass Spectrometry*. November 7, 2012, pp 1473–1481. https://doi.org/10.1002/jms.3108.

(133) Metodiev, M. D.; Steven, R. T.; Loizeau, X.; Takats, Z.; Bunch, J. Modality Agnostic Model for Spatial Resolution in Mass Spectrometry Imaging: Application to MALDI MSI Data. *Anal. Chem.* **2021**, *93* (46), 15295–15305. https://doi.org/10.1021/acs.analchem.1c02470.

(134) Zubair, F.; Prentice, B. M.; Norris, J. L.; Laibinis, P. E.; Caprioli, R. M. Standard Reticle Slide to Objectively Evaluate Spatial Resolution and Instrument Performance in Imaging Mass Spectrometry. *Analytical Chemistry*. 2016, pp 7302–7311. https://doi.org/10.1021/acs.analchem.6b01655.

(135) Fagerer, S. R.; Römpp, A.; Jefimovs, K.; Brönnimann, R.; Hayenga, G.; Steinhoff, R. F.; Krismer, J.; Pabst, M.; Ibáñez, A. J.; Zenobi, R. Resolution Pattern for Mass Spectrometry Imaging. *Rapid Commun. Mass Spectrom.* **2015**, *29* (11), 1019–1024. https://doi.org/10.1002/rcm.7191.

(136) Kertesz, V.; Cahill, J. F.; Van Berkel, G. J. Quantitative Metrics for Assessment of Chemical Image Quality and Spatial Resolution. *Rapid Commun. Mass Spectrom.* **2016**, *30* (7), 927–932. https://doi.org/10.1002/rcm.7519.

(137) Van Elteren, J. T.; Izmer, A.; Šelih, V. S.; Vanhaecke, F. Novel Image Metrics for Retrieval of the Lateral Resolution in Line Scan-Based 2D LA-ICPMS Imaging via an Experimental-Modeling Approach. *Anal. Chem.* **2016**, *88* (14), 7413–7420. https://doi.org/10.1021/acs.analchem.6b02052.

(138) Rose, A. Human and Electronic Vision. *Vis. Hum. Electron.* **1973**, 1–28.

(139) Unger, W. E. S.; Senoner, M.; Wirth, T.; Bütefisch, S.; Busch, I. Lateral Resolution of Imaging Surface-Analytical Instruments as SIMS, AES and XPS: Application of the BAM-L200 Certified Reference Material and Related ISO Standards. *J. Surf. Anal.* **2017**, *24* (2), 123–128. https://doi.org/10.1384/jsa.24.123.

(140) Unger, W. E. S.; Senoner, M.; Stockmann, J. M.; Fernandez, V.; Fairley, N.; Passiu, C.; Spencer, N. D.; Rossi, A. Summary of ISO/TC 201 International Standard ISO 18516:2019 Surface Chemical Analysis—Determination of Lateral Resolution and Sharpness in Beam-Based Methods with a Range from Nanometres to Micrometres and Its Implementation for Imaging Laboratory X-Ray P. *Surf. Interface Anal.* **2022**, *54* (4), 320–327. https://doi.org/10.1002/sia.7025.

(141) Scott, D.; Weston, K. Cancer Grand Challenges—a Call to Reunify the Physical and Life Sciences Communities. *Converg. Sci. Phys. Oncol.* **2016**, *1* (2), 026002. https://doi.org/10.1088/2057-1739/1/2/026002.

(142) West, J.; Newton, P. K. Cellular Interactions Constrain Tumor Growth. *Proc. Natl. Acad. Sci. U. S. A.* **2019**, *116* (6), 1918–1923. https://doi.org/10.1073/pnas.1804150116.

(143) Yang, M.; Brackenbury, W. J. Membrane Potential and Cancer Progression. *Frontiers in Physiology*. 2013, pp 1–10. https://doi.org/10.3389/fphys.2013.00185.

(144) Sunshine, H.; Iruela-Arispe, M. L. Membrane Lipids and Cell Signaling. *Current Opinion in Lipidology*.

2017, pp 408–413. https://doi.org/10.1097/MOL.0000000000000443.

(145) Lucia, U.; Grisolia, G. How Life Works-a Continuous Seebeck-Peltier Transition in Cell Membrane? *Entropy* **2020**, *22* (9), 1–5. https://doi.org/10.3390/e22090960.

(146) Squires, G. Francis Aston and the Mass Spectrograph. *J. Chem. Soc. - Dalt. Trans.* **1998**, No. 23, 3893–3899. https://doi.org/10.1039/a804629h.

(147) Soltwisch, J.; Göritz, G.; Jungmann, J. H.; Kiss, A.; Smith, D. F.; Ellis, S. R.; Heeren, R. M. A. MALDI Mass Spectrometry Imaging in Microscope Mode with Infrared Lasers: Bypassing the Diffraction Limits. *Anal. Chem.* **2014**, *86* (1), 321–325. https://doi.org/10.1021/ac403421v.

(148) Smith, A. R. A Pixel Is Not a Little Square. *Pixar Tech. Memo* **1995**, No. 6, 1–11.

(149) Tirunelveli, G.; Gordon, R.; Pistorius, S. Comparison of Square-Pixel and Hexagonal-Pixel Resolution in Image Processing. *Can. Conf. Electr. Comput. Eng.* **2002**, *2*, 867–872. https://doi.org/10.1109/ccece.2002.1013056.

(150) Fadaei, S.; Rashno, A. A Framework for Hexagonal Image Processing Using Hexagonal Pixel-Perfect Approximations in Subpixel Resolution. *IEEE Trans. Image Process.* **2021**, *30*, 4555–4570. https://doi.org/10.1109/TIP.2021.3073328.

(151) Jurchen, J. C.; Rubakhin, S. S.; Sweedler, J. V. MALDI-MS Imaging of Features Smaller than the Size of the Laser Beam. *J. Am. Soc. Mass Spectrom.* **2005**, *16* (10), 1654–1659. https://doi.org/10.1016/j.jasms.2005.06.006.

(152) Efron, B.; Tibshirani, R. J. An Introduction to the Bootstrap. Monographs on Statistics and Applied Probability, No. 57. Chapman and Hall, London, 436 P. *Monogr. Stat. Appl. Probab.* **1993**, *57* (1989), 436.

(153) Zavalin, A.; Yang, J.; Haase, A.; Holle, A.; Caprioli, R. Implementation of a Gaussian Beam Laser and Aspheric Optics for High Spatial Resolution MALDI Imaging MS. *J. Am. Soc. Mass Spectrom.* **2014**, *25* (6), 1079–1082. https://doi.org/10.1007/s13361-014-0872-5.

(154) Bock, M.; Tyagi, A. K.; Kreft, J.-U.; Alt, W. Generalized Voronoi Tessellation as a Model of Two-Dimensional Cell Tissue Dynamics. *Bull. Math. Biol.* **2010**, *72* (7), 1696–1731. https://doi.org/10.1007/s11538-009-9498-3.

(155) Race, A. M.; Styles, I. B.; Bunch, J. Inclusive Sharing of Mass Spectrometry Imaging Data Requires a Converter for All. *J. Proteomics* **2012**, *75* (16), 5111–5112. https://doi.org/10.1016/j.jprot.2012.05.035.

(156) Race, A. M.; Palmer, A. D.; Dexter, A.; Steven, R. T.; Styles, I. B.; Bunch, J. SpectralAnalysis: Software for the Masses. *Anal. Chem.* **2016**, *88* (19), 9451–9458. https://doi.org/10.1021/acs.analchem.6b01643.

(157) Waters. High Definition Imaging (HDI) Software. *Online Broch.* https://doi.org/https://www.waters.com/webassets/cms/library/docs/720005652en.pdf.

(158) Sutour, C.; Deledalle, C. A.; Aujol, J. F. Estimation of the Noise Level Function Based on a Nonparametric Detection of Homogeneous Image Regions. *SIAM J. Imaging Sci.* **2015**, *8* (4), 2622–2661. https://doi.org/10.1137/15M1012682.

(159) CAMECA Application Laboratory. NanoSIMS 50L User's Guide. *NanoSIMS 50L users Guid.* **2021**, 1–410. https://doi.org/https://presolar.physics.wustl.edu/Laboratory_for_Space_Sciences/docs/NanoSIMS50LusersguideAug2020V1.pdf.

(160) Forbes, T. P.; Brewer, T. M.; Gillen, G. Desorption Electro-Flow Focusing Ionization of Explosives and Narcotics for Ambient Pressure Mass Spectrometry. *Analyst* **2013**, *138* (19), 5665–5673. https://doi.org/10.1039/c3an01164j.

(161) CARO, A.; RODRÍGUEZ, P. G.; ÁVILA, M. M.; RODRÍGUEZ, F.; RODRÍGUEZ, F. J.; PALACIOS, R. ACTIVE CONTOURS USING WATERSHED SEGMENTATION. In *Recent Trends in Multimedia Information Processing*; WORLD SCIENTIFIC, 2002; pp 340–345. https://doi.org/10.1142/9789812776266_0052.

(162) Barnes, R.; Lehman, C.; Mulla, D. Priority-Flood: An Optimal Depression-Filling and Watershed-Labeling Algorithm for Digital Elevation Models. *Comput. Geosci.* **2014**, *62* (2), 117–127. https://doi.org/10.1016/j.cageo.2013.04.024.

(163) Sobel, I.; Feldman, G. An Isotropic 3x3 Image Gradient Operator. *Stanford Artif. Intell. Proj.* **2015**, No. June, 271–272.

(164) Wang, X.; Jenner, A. L.; Salomone, R.; Drovandi, C. Calibration of a Voronoi Cell-Based Model for Tumour Growth Using Approximate Bayesian Computation Calibration of a Voronoi Cell-Based Model. *bioRxive* **2023**. https://doi.org/10.1101/2022.09.13.507714.

(165) Yuan, Y. Spatial Heterogeneity in the Tumor Microenvironment. *Cold Spring Harb. Perspect. Med.* **2016**, *6* (8). https://doi.org/10.1101/cshperspect.a026583.

(166) Cerutti, G.; Ribes, S.; Godin, C.; Galvan-Ampudia, C.; Vernoux, T. 3-d Tessellation of Plant Tissue-A Dual Optimization Approach to Cell-Level Meristem Reconstruction from Microscopy Images. *Proc.* -

2015 Int. Conf. 3D Vision, 3DV 2015 **2015**, 443–451. https://doi.org/10.1109/3DV.2015.57.

(167) Richardson, W. H. Bayesian-Based Iterative Method of Image Restoration*. *J. Opt. Soc. Am.* **1972**, *62* (1), 55. https://doi.org/10.1364/JOSA.62.000055.

(168) Joshi, N.; Szeliski, R.; Kriegman, D. J. PSF Estimation Using Sharp Edge Prediction. *26th IEEE Conf. Comput. Vis. Pattern Recognition, CVPR* **2008**. https://doi.org/10.1109/CVPR.2008.4587834.

(169) Zhang, Z.; Chen, Y.; Feng, H.; Xu, Z.; Li, Q. Modulation Transfer Function (MTF) Measurement Method Based on Support Vector Machine (SVM). *Sel. Pap. Chinese Soc. Opt. Eng. Conf. held Oct. Novemb. 2016* **2017**, *10255* (March 2017), 1025535. https://doi.org/10.1117/12.2266630.

(170) Delvit, J. M.; Léger, D.; Roques, S.; Valorge, C. Modulation Transfer Function and Noise Measurement Using Neural Networks. *Neural Networks Signal Process. - Proc. IEEE Work.* **2003**, *2003-Janua*, 131–140. https://doi.org/10.1109/NNSP.2003.1318011.

(171) Bauer, M.; Volchkov, V.; Hirsch, M.; Schcolkopf, B. Automatic Estimation of Modulation Transfer Functions. *IEEE Int. Conf. Comput. Photogr. ICCP 2018* **2018**, 1–12. https://doi.org/10.1109/ICCPHOT.2018.8368467.

(172) Kim, K. B.; Jeong, S. H.; Lee, S. H.; Kim, K. Investigation of Patch-Based Modulation Transfer Function (MTF) Prediction Framework in Radiography. *Radiat. Phys. Chem.* **2021**, *189* (March), 109728. https://doi.org/10.1016/j.radphyschem.2021.109728.

(173) Descloux, A.; Grußmayer, K. S.; Radenovic, A. Parameter-Free Image Resolution Estimation Based on Decorrelation Analysis. *Nat. Methods* **2019**, *16* (9), 918–924. https://doi.org/10.1038/s41592-019-0515-7.

(174) Saxton, W. O.; Baumeister, W. The Correlation Averaging of a Regularly Arranged Bacterial Cell Envelope Protein. *J. Microsc.* **1982**, *127* (2), 127–138. https://doi.org/10.1111/j.1365-2818.1982.tb00405.x.

(175) Van Heel, M.; Schatz, M. Fourier Shell Correlation Threshold Criteria. *J. Struct. Biol.* **2005**, *151* (3), 250–262. https://doi.org/10.1016/j.jsb.2005.05.009.

(176) Koho, S.; Tortarolo, G.; Castello, M.; Deguchi, T.; Diaspro, A.; Vicidomini, G. Fourier Ring Correlation Simplifies Image Restoration in Fluorescence Microscopy. *Nat. Commun.* **2019**, *10* (1), 3103. https://doi.org/10.1038/s41467-019-11024-z.